Development of A Fully Coupled, Unstructured Grid, Coastal Morphodynamic Model System

Thesis submitted in accordance with the requirements of
the University of Liverpool for the degree of Doctor in Philosophy
by

PENG ZHENG

September 2017

Abstract

A new fully coupled, unstructured grid, three-dimensional coastal morphodynamic model system is developed in this research. Based on two original independent models, i.e. the original unstructured-grid version of the third generation spectral wave model Simulating WAves Nearshore (UnSWAN) and the original Finite Volume Coastal Ocean Model (FVCOM), the development of this model system is achieved by accomplishing the following procedures: Coupling UnSWAN with FVCOM to enable the full representation of the wave-current interaction in the nearshore region, by building a new wave-current coupling scheme based on the vortex-force (VF) approach to represent the wave-current interaction and developing a new coupling module to facilitate the communication between UnSWAN and FVCOM in the parallel computing and realise the model coupling procedure. A GLS turbulence model is also modified to better reproduce wave-breaking generated turbulence, together with a roller transport model to account for the effects of surface wave roller. An alternative wave model based on Mellor et al. [1] is also implemented in the present model system. The original advection-diffusion (AD) module is modified for the representation of particle suspension and subsequent transport under the combined flows. In this module, the contribution of wave-induced stokes drift to particle transport is included which is absent in the original FVCOM model. A new bed load transport module based on the SANTOSS formulae is built to represent various processes within the oscillatory boundary layer. Based on the semi-unsteady "half-cycle" concept, this SANTOSS formulae distinguish the sediment transports during the positive “crest” and the negative “trough” half-cycles and have the advantages over the traditional steady 'equilibrium' transport formula that many wave-induced unsteadiness effects are included, including the wave asymmetry, sediment grain size effects and etc. Finally, the wave, circulation, suspended sediment and bed-load transport modules are integrated into the fully coupled, three-dimensional coastal morphodynamic model system, in which a sediment continuity (Exner) equation is also included to resolve the morphology evolution.

A detailed validation of the hydrodynamic part of the model system is firstly conducted against four different cases with different spatial scales and both 2D and 3D complex hydrodynamic conditions. Overall, the model predictions agree well with the

available measurements in these tests in all aspects, illustrating the robustness and efficiency of the present model for very different spatial scales and hydrodynamic conditions. Model simulations of the Duck 94 experiment clearly indicate that the VF is important in determining the two levels of momentum balance in both cross-shore and longshore flows. Further tests results indicate the importance of roller effects and wave energy dissipation on the mean flow (undertow) profile over the depth and suggest to adopt a spatially varying value for roller effects across the beach. In addition, the parameter values in the GLS turbulence model are suggested to be spatially inhomogeneous, which can lead to better prediction of the turbulent kinetic energy and an improved prediction of the undertow velocity profile.

The developed morphodynamic model system is further applied to a laboratory scale mobile bed experiment, in which a detailed measurement of the hydrodynamics (water level, flow velocity and turbulent kinematic energy, etc.), sand transport processes and bed profiles are obtained with a high spatial resolution. With these measurements, the performance of all the modules in the developed morphodynamic model are evaluated in detail, either as a stand alone part or a whole system. The following conclusions and finding are obtained: Although breaking waves may directly entrain large amounts of sand from the bed (Nielsen [2]), the predicted suspended sediment concentrations using the wave-averaged bed shear stress (τ_{cw}) alone without the additional wave breaking effects on the sediment concentration agree fairly well with the measurements. Quasi-steady bedload transport formulae fail to, but the semi-unsteady SANTOSS model succeed to, reproduce all the important features of (measured) bedload transport ($q_{bed,e}$). However, some discrepancies are still present in the detailed magnitude of the predicted bedload transport by SANTOSS model. Further sensitivity analysis shows that the effect of surface progressive waves and phase-lag are vitally important in determining the (right) features of $q_{bed,e}$. Suspended load and bedload have opposite contributions to the final principal morphology evolution characteristics, the contributions of suspended load transport exceed those by bedload; therefore it is the suspended load that decides the bar morphodynamics shown in this lab experiment. Further sensitivity tests show that the effects of bed level changes on the hydrodynamics are very important to the final beach evolution predictions; a reasonable prediction of the hydrodynamic processes is the prerequisite to obtain reliable bed profile changes in the present experiment application and excluding the wave breaking induced turbulence can significantly change the correct cross-shore distribution features of the predicted bed profile. However, it's important to be noted that an accurate prediction of TKE in the surf zone is still a challenge for the presently adopted turbulence closure (RANS) model in this research and also commonly used models in the academic community, further studies on the fundamental turbulence dynamics are thus suggested to be implemented.

Contents

Abstract **i**

Contents **viii**

List of Figures **xv**

List of Tables **xvi**

Nomenclature **xvii**

Acknowledgement **xxix**

1 Introduction **1**

1.1 Research Context 1

1.2 Coastal Processes 3

1.2.1 Waves 3

1.2.2 Mean Currents 5

1.2.3 Wave-Current Interaction 7

1.2.4 Sediment Transport 9

1.3 Coastal Models 12

1.3.1 Wave Models 12

1.3.2 Wave-Current Coupled Models 14

1.3.3 Turbulence Closure Models 15

1.3.4 Sediment Transport Models 16
1.4 Aims and Objectives 18
1.5 Outline 19

2 Modelling System – Part I: Existed Modules 21

2.1 Introduction 21
2.2 Hydrodynamic Module 22
2.2.1 Wave Module 22
2.2.2 Circulation Module 26
2.2.3 Turbulence Closure Model 28
2.3 Sediment Module 32
2.3.1 Suspended Sediment Transport Module 32
2.3.2 Bedload Module 33
2.4 Bottom Boundary Layer Module 34
2.5 Discretisation 38
2.6 Summary 39

3 Modelling System – Part II: Model Development 41

3.1 Introduction 41
3.2 Hydrodynamic Module 42
3.2.1 Wave Module 42
3.2.2 Circulation Module 50
3.2.3 Turbulence Closure Model 61
3.3 Bottom Boundary Layer Module — A Modification of The Original *mb_bbl* 63
3.4 Suspended Sediment Transport Module 67
3.5 A New Bedload Module – SANTOSS 69
3.5.1 General 69

3.5.2 The sand entrainment during each half-cycle with phase lag effect 72
3.5.3 Bed shear stress . . . 74
3.5.4 Velocities and orbital characteristics . . . 77
3.5.5 Ripple dimensions . . . 81
3.5.6 Sheet-flow layer thickness . . . 82
3.5.7 Effect of bed slope . . . 82
3.5.8 Effect of wave breaking induced turbulence on bedload transport 83
3.6 Morphology Evolution Module . . . 84
3.7 Coupling Procedure and Parallelization . . . 84
3.7.1 The New Coupler Module . . . 85
3.7.2 Mesh Decomposition and Parallelization . . . 85
3.8 Conclusions . . . 88

4 Model Validation 90

4.1 Introduction . . . 90
4.2 Obliquely Incident Waves on A Planar Beach . . . 91
4.2.1 Wave Parameters and Two-Dimensional Domain . . . 92
4.2.2 Three-Dimensional Velocities . . . 92
4.2.3 Model Convergence . . . 94
4.3 Wave Breaking over Breaker Bar at Laboratory Scale . . . 96
4.3.1 Wave Height and Water Surface Elevation . . . 97
4.3.2 Velocities . . . 99
4.3.3 Turbulent Kinetic Energy . . . 104
4.4 Obliquely Incident Waves on A Natural, Barred Beach (DUCK' 94 experiment) . . . 105
4.4.1 Wave Parameters . . . 108
4.4.2 Cross-Shore and Vertical Structure of Velocity . . . 109

4.4.3 Horizontal Momentum Balance 113
4.5 Normally Incident Waves on A Plane Beach with Shore-Parallel Breakwater 118
4.6 Conclusions 125

5 Model Application **127**

5.1 Introduction 127
5.2 The experiment 127
5.3 Model setup 129
5.4 Hydrodynamics 129
5.4.1 Wave Height and Water Surface Elevation 129
5.4.2 Velocities 133
5.4.3 Turbulent Kinetic Energy 139
5.4.4 Discussion 150
5.5 Suspended Sediment Transport 152
5.5.1 Suspended Sediment Concentrations 153
5.5.2 Representation of Wave Breaking Effects 155
5.5.3 Suspended Sediment Transport Rate 158
5.6 Bedload Transport 160
5.6.1 Approximation of The Measured Bedload Transport Rate 160
5.6.2 Bedload Transport Prediction with MPM 162
5.6.3 Bedload Transport Prediction with Soulsby and Damgaard . . . 164
5.6.4 Bedload Transport Prediction with SANTOSS Model 165
5.7 Total Load Transport 172
5.8 Morphology Development 175
5.8.1 Prediction of The Morphology Evolution 175
5.8.2 The Effect of Several Bedload Processes on The Morphology Evolution 178

5.8.3 Contributions of Suspended Load and Bedload Transport to The Bar Morphodynamics 181

5.9 Conclusions 186

6 Discussion, Conclusion and Recommendations 190

6.1 Discussions 191

6.1.1 Modelling approaches 191

6.1.2 Sensitivity analysis justification 193

6.2 Conclusion 195

6.2.1 On Morphodynamic Model System Development 196

6.2.2 On Physical Processes 198

6.3 Suggestions for Future Work 200

A A Parallel, Computation Economical Unstructured Wave Model 203

A.1 Theory sketch 204

A.2 Discretization approach 207

A.3 Parallelization 211

B Wave skewness and asymmetry 213

B.1 Analytical expression of wave orbital velocity 213

B.2 Parameterizations for the parameter of waveform (ϕ) and skewness (r) . 213

C Adaption of the SANTOSS model in the current dominated flow 216

D Comparison of the new and original methods used to define the periods of crest/trough half-cycles in SANTOSS model 219

E Using the Maximum Bed Shear Stress (τ_{cwmax}) in pick-up function 222

E.1 Enhance Shields Parameter with The Predicted Near-Bed TKE 222

E.2 Enhance Shields Parameter with Wave Dissipation Energy 225

E.3 Suspended Sediment Transport Rate 226

F Publications **228**

Bibliography **246**

Index **246**

List of Figures

1.1 Schematic diagram of a sinusoidal wave, a skewed wave, and a skewed and asymmetric wave. (After Grasmeijer [3]). 3

1.2 Breaker Types (After Fredsøe and Deigaard [4]). 4

1.3 A conceptual 2D (cross-shore) overview of sediment processes in the near-shore region (After van der Zanden [5]). 9

2.1 Illustration of the FVCOM unstructured triangular grid. 38

2.2 The location of the model variables in the vertical Sigma coordinate. . . 39

3.1 A schematic figure on the update of the wave action at vertex 1 in a triangle $\triangle 123$. 45

3.2 The shaded directional sector in spectral space (After Zijlema [6]). . . . 46

3.3 Ordering of vertices along spherical wave fronts indicated by different colour points. 47

3.4 A schematic diagram of the vertex-based approach used in partitioning the UnSWAN model 48

3.5 Definition sketch of near-bed velocity time-series in wave direction. . . . 71

3.6 Flow chart of the coupled model system. 87

4.1 Simulation results and analytical solutions of the obliquely incident waves on a plane beach test case. 93

4.2 Cross-shore section of Eulerian and Stokes velocities from the simulation. 93

4.3 Simulated and measured results of the large-scale breaking wave experiment with a naturally shaped breaker bar. 98

4.4 Model simulated distribution of cross-shore velocity u in the large-scale wave flume experiment with a naturally shaped breaker bar. 100

4.5 Comparison of simulated (lines) with observed vertical profiles (circles and diamonds) for cross-shore velocities. 101

4.6 Comparison of simulations (lines) with measurements (circles and diamonds) in terms of cross-shore TKE (a, b) and time-averaged velocities (c). 103

4.7 Results of Duck94 simulation. 107

4.8 Model simulated cross-shore distribution results for Duck94 experiment. 110

4.9 Comparison of simulation results (solid lines) with observed vertical profiles (red circles). 112

4.10 Cross-shore profiles of depth-averaged (a) cross-shore and (b) longshore momentum balance terms; (c) decomposed PGF terms in cross-shore direction as described in Eq. (4.3) 115

4.11 Cross-shore and vertical distribution of the terms contributing to the cross-shore (x) and longshore (y) momentum balance. 116

4.12 Experimental layout of Hamm et al. [7] 119

4.13 (a) Model domain and measurement profiles and points of Hamm et al. [7], the open boundary is located at Y = 12 m; (b) the horizontal unstructured triangular grids used for the simulations of the breakwater case. 120

4.14 The wave height (colour) and depth-averaged velocity (vector) 122

4.15 Comparison of model predicted and measured wave height (a-d), alongshore and cross-shore velocity distribution (e-h) along a number of transects in the Hamm et al. [7] experiment, test REG0107 123

4.16 Comparison of model predicted and measured velocity vertical profiles at a number of positions in the Hamm et al. [7] experiment, test REG0107 124

5.1 Experimental set-up and measurement locations (After van der Zanden [5]). 128

5.2 Cross-shore distribution of the significant wave height H_{sig} and five times of sea surface elevation $\zeta^c \times 5.0$ for the SINBAD mobile bed test. 130

5.3 Model predicted wave height with different approaches for the SINBAD mobile bed test. 131

5.4 Cross-shore distribution of the depth-averaged cross-shore Eulerian velocity UA (solid line) and Stokes velocity $-UA_{stokes}$ (red circles) for the SINBAD mobile bed test. 132

5.5 Model simulated distribution of cross-shore velocity u in the SINBAD mobile bed test; contour lines explicitly show the velocity value 134

5.6 Comparison of simulation results (solid black lines) with observed vertical profiles (red circles and short near-bed blue lines) for the cross-shore velocity. 135

5.7 Comparison of simulation results (solid lines) with observed vertical profiles (red circles and short near-bed magenta lines) of the cross-shore velocity (u) for the sensitivity to the parameter α_r. 136

5.8 Comparison of simulation results (solid lines) with observed vertical profiles (red circles and short near-bed magenta lines) of the cross-shore velocity (u) for the sensitivity to the parameter C_1. 137

5.9 Comparison of simulation results (solid black lines) with observed vertical profiles (red circles and short near-bed blue lines) for the TKE. The vertical black dashed lines indicate the profile measurement locations and zero value for each profile. 139

5.10 Comparison of simulation results (solid lines) with observed vertical profiles (red and blue circles) of TKE for the sensitivity to the parameter C_1. 140

5.11 Comparison of simulation results (solid lines) with observed vertical profiles (red and blue circles) of TKE for the sensitivity to the parameter D_w. While $H_w = 0.1$. 144

5.12 Comparison of simulation results (solid lines) with observed vertical profiles (red and blue circles) of TKE for the sensitivity to the parameter D_w. While $H_w = 0.6$. 144

5.13 Comparison of simulation results (solid lines) with observed vertical profiles (red and blue circles) of the cross-shore velocity (u) for the sensitivity to the parameter D_w. While $H_w = 0.1$ 145

5.14 Comparison of simulation results (solid lines) with observed vertical profiles (red and blue circles) of the cross-shore velocity (u) for the sensitivity to the parameter D_w. While $H_w = 0.6$ 145

5.15 Comparison of simulation results (solid lines) with observed vertical profiles (red and blue circles) of TKE for the sensitivity to the parameter H_w. While $D_w = 0.3$. 146

5.16 Comparison of simulation results (solid lines) with observed vertical profiles (red and blue circles) of TKE for the sensitivity to the parameter H_w. While $D_w = 0.001$. 146

5.17 Comparison of simulation results (solid lines) with observed vertical profiles (red and blue circles) of the cross-shore velocity (u) for the sensitivity to the parameter H_w. While $D_w = 0.3$. 147

5.18 Comparison of simulation results (solid lines) with observed vertical profiles (red and blue circles) of the cross-shore velocity (u) for the sensitivity to the parameter H_w. While $D_w = 0.001$. 147

5.19 Comparison of simulation results (solid black lines) from Run II with observed vertical profiles (red circles and short near-bed blue lines) for the cross-shore velocity u (a) and the TKE (b). 149

5.20 The value of cross-shore varying H_w used in Run II. 150

5.21 Comparison of simulation results (solid lines) with observed vertical profiles (red and blue circles) of suspended sediment concentration. 155

5.22 Comparison of simulation results (solid lines) with observed vertical profiles (red and blue circles) of suspended sediment concentration. 157

5.23 Suspended sediment transport rate q_s calculated from the sediment concentration shown in Figure 5.21. 159

5.24 Suspended sediment transport rate q_s calculated from the sediment concentration shown in Figure 5.22. 159

5.25 Total sediment transport rate calculated from the bed profile measurements at t=30 and 60 mins through the Eq.(5.10). 161

5.26 Total ($q_{tot,m}$, red dashed line), suspended (q_s, blue dashed line) and bedload ($q_{bed,e}$, black line) sediment transport rate. 163

5.27 The cross-shore distribution of the bedload transport rate that estimated from Eq.(5.8) ($q_{bed,e}$,red dashed line) and that predicted by MPM formulation with τ_{cw} ($q_{bed,p}$,black line). 163

5.28 The cross-shore distribution of the bedload transport rate estimated from Eq.(5.8) ($q_{bed,e}$,red dashed line) and that predicted by MPM formulation with τ_{cwmax} ($q_{bed,p}$,black line). 164

5.29 The cross-shore distribution of the bedload transport rate that estimated from Eq.(5.8) ($q_{bed,e}$,red dashed line) and that predicted by the formulation of Soulsby and Damgaard ($q_{bed,p}$,black line). 165

5.30 The cross-shore distribution of the bedload transport rate that estimated from Eq.(5.8) ($q_{bed,e}$, red dashed line) and that predicted by the SANTOSS model with all above mentioned effects but not the effect of wave-breaking induced turbulence ($q_{bed,ps0}$, black line). 166

5.31 The cross-shore distribution of the bedload transport rate that estimated from Eq.(5.8) ($q_{bed,e}$, red dashed line) and that predicted by the SANTOSS model with all above mentioned effects, including the effect of wave-breaking induced turbulence ($q_{bed,ps}$, black line). 167

5.32 (a) Measured(stars and crosses) and model calculated (red and blue lines) peak crest (red crosses and line) and trough (blue stars and line) wave orbital velocities. Panel (b) shows the bed profile at t = 30 min. 168

5.33 Wave orbital velocity skewness (a) and asymmetry (b) around breaker bar 169

5.34 The cross-shore distribution of the bedload transport rate predicted by the SANTOSS model: with all above mentioned effects ($q_{bed,ps}$, red dashed line); with all above mentioned effects but not the effect of surface progressive waves ($q_{bed,ps1}$, black line). 170

5.35 The cross-shore distribution of the bedload transport rate that predicted by the SANTOSS model: with all above mentioned effects ($q_{bed,ps}$, red dashed line); with all above mentioned effects but not the effect of phase-lag ($q_{bed,p}$, black line). 170

5.36 The cross-shore distribution of the bedload transport rate that predicted by the SANTOSS model: with all above mentioned effects ($q_{bed,ps}$, red dashed line); with all above mentioned effects but not the effect of acceleration skewness ($q_{bed,p}$, black line). 171

5.37 The cross-shore distribution of the bedload transport rate that predicted by the SANTOSS model: with all above mentioned effects ($q_{bed,ps}$, red dashed line); with all above mentioned effects but not the effect of bed slope ($q_{bed,p}$, black line). 171

5.38 Cross-shore variation in sediment transport rates. 173

5.39 Comparison of model predicted (black line) and measured (red line) bed profiles at the experiment time of $t = 60$ min. 176

5.40 Comparison of model predicted (black line) and measured (red line) bed profiles at the experiment time of $t = 90$ min. 176

5.41 The difference between the model predicted and measured bed level at $t = 60$ min (blue stars) and $t = 90$ min (red stars). 177

5.42 Comparison of model predicted (black line, without the effect of surface progressive waves on the bedload transport) and measured (red line) bed profiles at the experiment time of $t = 90$ min. 179

5.43 Comparison of model predicted (black line, without the phase-lag effect on the bedload transport) and measured (red line) bed profiles at the experiment time of $t = 90$ min. 179

5.44 Comparison of model predicted (black line, without the effect of acceleration skewness on the bedload transport) and measured (red line) bed profiles at the experiment time of $t = 90$ min. 180

5.45 Comparison of model predicted (black line, without the effect of bed slope on the bedload transport) and measured (red line) bed profiles at the experiment time of $t = 90$ min. 180

5.46 Cross-shore variation in sediment transport rates. 182

5.47 Comparison of model predicted in the scenario A1 (black line, without bedload transport component and the effect of bed profile change on the hydrodynamics) and measured (red line) bed profiles at the experiment time of $t = 90$ min. 183

5.48 Comparison of model predicted in the scenario A2 (black line, without bedload transport component but the bed profile is evolving instantly with time) and measured (red line) bed profiles at the experiment time of $t = 90$ min. 183

5.49 Comparison of model predicted in the scenario A3 (black line, without the wave breaking induced turbulence in the turbulent closure model) and measured (red line) bed profiles at the experiment time of $t = 90$ min. 184

5.50 The difference between the model predicted and measured bed level at $t = 90$ min for three scenarios. 185

A.1 Schematic of the model horizontal unstructured grid 210

A.2 Schematic of the angle grid and the cyclic boundary conditions 211

A.3 A schematic diagram of the cell-centered portioning approach. 212

D.1 A sketch on the method used to definite the crest and trough periods for SANTOSS model in situations when only waves are present. 220

D.2 A sketch on the method used to definite the crest and trough periods for SANTOSS model in situations when both wave and mean current are present. 220

E.1 Comparison of simulation results (solid lines) with observed vertical profiles (red and blue circles) of suspended sediment concentration. The model results are from the Run #10.1. 223

E.2 Comparison of simulation results (solid lines) with observed vertical profiles (red and blue circles) of suspended sediment concentration. The model results are from the Run #10.2. 224

E.3 The value of cross-shore varying e_k. 225

E.4 Comparison of simulation results (solid lines) with observed vertical profiles (red and blue circles) of suspended sediment concentration. 226

E.5 Suspended sediment transport rate q_s calculated from the sediment concentration shown in Figure E.2. 227

List of Tables

4.1 Wave time step and convergence time of 6 test cases 95

4.2 Model parameters for Duck94 simulation 106

4.3 Normalized root mean square error $\epsilon_j = \left\{ \frac{\sum_{i=1}^{nsen(j)} (d_{ij} - m_{ij})^2}{\sum_{j=1}^{nsen(j)} (d_{ij})^2} \right\}^{1/2}$ for the cross-shore and longshore velocity estimates for Duck94 experiment for various locations across the profile. 108

4.4 Normalized root mean square error analysis for cross-shore velocity with different values of C_1 111

4.5 List of symbols used for representing the momentum balances 114

5.1 Model parameters of the baseline test for the SINBAD mobile bed experiment 130

5.2 Model configurations of the sensitivity tests for the parameter α_r and C_1 138

5.3 Model configurations of the sensitivity tests for the parameter D_w and H_w. 142

5.4 Summarization of the values of parameter D_w and H_w with which a numerical simulation obtains reasonable well results against the measured TKE or/and cross-shore velocity at the twelve profiles. These values are obtained from the modeled results of simulation Group $\#3 - \#6$ 148

5.5 The variable used in calculating the pick-up rate in the simulations for modeling the suspended sediment concentration. 154

Nomenclature

Symbol	Description
$\boldsymbol{B}^{wcap}$	White-capping induced acceleration
$\boldsymbol{B}^{b}$	$\boldsymbol{B}^{b} = \boldsymbol{B}^{db} + \boldsymbol{B}^{r}$
$\boldsymbol{B}^{db}$	Depth-induced breaking accelerations
$\boldsymbol{B}^{r}$	Roller accelerations
$\boldsymbol{B}^{bf}$	Accelerations due to bottom streaming
$\boldsymbol{B}^{sf}$	Accelerations due to surface streaming
$\boldsymbol{B}^{swb}$	Total force induced by surface wave breaking (i.e. white-capping, depth-induced wave breaking and surface wave rollers)
$\boldsymbol{C}_g$	Wave group velocity vector
$\boldsymbol{C}_t = (C_x,\ C_y)$	$\boldsymbol{C}_g + \boldsymbol{V}$
$\boldsymbol{C}_p = (C_{px},\ C_{py})$	$\boldsymbol{V} + \frac{\sigma}{k}\frac{\boldsymbol{k}}{k}$
$\boldsymbol{F} = (F_x,\ F_y)$	The horizontal momentum diffusion term
$\boldsymbol{F^w} = (F_x^w,\ F_y^w)$	Wave-induced non-conservative forces
$(\boldsymbol{J},\ \mathrm{K})$	Vortex Force
$\boldsymbol{J'}$	Horizontal component of Modified Vortex Force
$\boldsymbol{P}^{tot}$	Total pressure gradient force $\boldsymbol{P}^{tot} = \boldsymbol{P}^{c} + \boldsymbol{P}^{wec}$
$\boldsymbol{P}^{c}$	Pressure gradient force result from the non-WEC terms
$\boldsymbol{P}^{wec}$	Pressure gradient force result from the WEC terms
$\boldsymbol{P}^{qs}$	Quasi-static response
$\boldsymbol{P}^{bh}$	Bernoulli head contribution to $\boldsymbol{P}^{wec}$
$\boldsymbol{P}^{pc}$	WEC surface pressure boundary correction term
$\boldsymbol{U}^{r}$	Stokes transport induced by wave roller
$\boldsymbol{U}^{st}$	Total Stokes transport
$\boldsymbol{V} = (u, v)$	Eulerian mean horizontal velocity vector

$\boldsymbol{V}^{st} = (u^{st}, v^{st})$	Stokes horizontal velocity vector
$\boldsymbol{V}^{l} = (u^{l}, v^{l})$	Wave-averaged Lagrangian horizontal velocity vector
$\overline{\boldsymbol{V}}^{l}$	Depth integral of $\boldsymbol{V}^{l}$
$\overline{\boldsymbol{V}}$	Depth-averaged Eulerian mean horizontal velocity vector
$\overline{\boldsymbol{V^{st}}}$	Depth-averaged Stokes horizontal velocity vector
$\boldsymbol{S}_x = (S_{xx},\ S_{xy})$	Depth-dependent radiation stresses induced by surface waves
$\boldsymbol{S}_y = (S_{yx},\ S_{yy})$	
$\boldsymbol{X(\xi)}$	A mapping transformation from $\boldsymbol{\xi}$ to $\boldsymbol{X}$
$\boldsymbol{\xi} = (\xi, \eta)$	A local coordinate system
$\boldsymbol{X} = (x, y)$	The Cartesian coordinate system
$\boldsymbol{e}_{(1)},\ \boldsymbol{e}_{(2)}$	Base vectors tangential to the local coordinate lines ξ and η, respectively
$\boldsymbol{e}^{(1)},\ \boldsymbol{e}^{(2)}$	$\boldsymbol{e}^{(\alpha)} \cdot \boldsymbol{e}_{(\beta)} = \delta^{\beta}_{\alpha}, \quad \alpha, \beta = [1, 2]$
$\boldsymbol{k}$	Wave number vector
$\boldsymbol{\tau}^{wind}_{sur}$	surface wind stress
$\boldsymbol{\tau}^{swb}_{sur}$	Surface boundary stress induced by surface wave breaking
$\boldsymbol{\tau}^{wave}_{sur}$	Momentum flux from atmosphere to wave
$\boldsymbol{\tau}^{str}_{sur}$	Surface boundary stress due to surface streaming
$\boldsymbol{\tau}_{sur}$	Total surface boundary stress $\boldsymbol{\tau}_{sur} = \boldsymbol{\tau}^{wind}_{sur} + \boldsymbol{\tau}^{swb}_{sur} - \boldsymbol{\tau}^{wave}_{sur}$
$\boldsymbol{\tau}_{bot}$	Bottom boundary stress used in the momentum equations
A_b	Wave near-bottom orbital excursion amplitude
A_R	Wave roller area
A_m	Horizontal diffusion coefficient for momentum equations
A_h	Horizontal diffusion coefficient for scalar equations
C	Tracer (temperature, salt, or suspended-sediment concentration)
$C_1,\ C_2,\ C_3$	Coefficients used in the GLS model.
C_b	Bottom friction coefficient used to calculate $S_{ds,b}$
C_c	A constant parameter used to calculate A_m and A_h
C_d	Bedform drag coefficient
C_{dBF}	Bedform drag coefficient for unseparated flow
C_{fw}	Collins bottom friction coefficient
C_{source}	Tracer source/sink term
D	Total water depth

D_s^*	Dimensionless grain size (particle parameter)
D_{50}	Median grain diameter
D_{tot}	Mean rate of energy dissipation per unit horizontal area due to wave breaking
D_w	Empirical constants
E	Wave total energy per unit surface area
E_{tot}	Wave total variance per unit surface area
E^r	Surface roller energy
$E(\sigma, \theta)$	Wave variance density spectrum
E_s	Erosion source term
E_0	Erosion rate for each sediment class (bed erodibility constant)
E_{va}	Mass of evaporation per unit surface area
$F_{CC}, F_{CS}, F_{SS}, F_{SC}$	Hyperbolic functions
F_C	The horizontal diffusion term of the tracer equation
F_{k}	The surface flux of energy injected into water column
F_q	The horizontal diffusion term of TKE
F_l	The horizontal diffusion term of turbulent marcroscale
F_{bs}^i	Fraction of the ith sediment in the bottom
F_{wall}	Wall function
G_b	Groundwater volume flux at the bottom
H_z	Grid cell thickness
H_{max}	Maximum wave height that can exist at a given depth
H_{rms}	Root-Mean-Square wave height
H_s	Significant wave height
H_w	Tuning Parameter
K_h	Vertical eddy diffusivity coefficient
K_m	Vertical eddy viscosity coefficient
K_q	Vertical eddy diffusivity coefficient for turbulent closure model
K_N	Bottom roughness length scale
L	Wave length
$N(\sigma, \theta)$	Wave action density spectrum
N_{bed}	Number of bed layers
P_{atm}	Atmospheric pressure

P_r	Prandtl number
P_{re}	Mass of precipitation per unit surface area
P_s	Shear production term of turbulent kinetic energy
P_b	Buoyancy production term of turbulent kinetic energy
P_{bs}	Porosity (volume of voids/total volume) of the top bed layer
P_c	The phase lag parameter for the crest half-cycle
P_t	The phase lag parameter for the trough half-cycle
Q_b	Fraction of breaking waves
R	The degree of velocity skewness $(= \hat{u}_c/(\hat{u}_c + \hat{u}_t))$
R_z	Wave roller shape function
S_w	Wave energy source/sink term
S_{px}, S_{py}	Vertically varying vertical radiation stresses
$S_{xx}, S_{xy}, S_{yx}, S_{yy}$	Vertically varying horizontal radiation stresses
$\overline{S_{xx}}, \overline{S_{xy}}, \overline{S_{yx}}, \overline{S_{yy}}$	Vertically integrated horizontal radiation stresses
S_{tot}	Source-sink term of the wave action balance equation
S_{in}	Wave growth by the wind
S_{nl3}	Nonlinear transfer of wave energy through three-wave interactions
S_{nl4}	Nonlinear transfer of wave energy through four-wave interactions
$S_{ds,w}$	Wave energy dissipation caused by white-capping
$S_{ds,b}$	Wave energy dissipation caused by bottom friction
$S_{ds,br}$	Wave energy dissipation caused by depth-induced wave breaking
S_m, S_h	Stability functions used in the MY-2.5 $\mathrm{k}-\mathrm{k}l$ model
T_*	Ratio of τ_{wc}/τ_{ce}
T_w	wave period T
T_{orb}^w	Near-bottom average wave period
T_c	The duration of the crest (positive) half cycle
T_{cu}	The duration of accelerating flow within the crest half cycle
T_t	The duration of the trough (negative) half cycle
T_{tu}	The duration of accelerating flow within the trough half cycle.
U_{rms}	Root-mean-square value of the wave orbital motion near the bottom.
W_{sc}	The sediment settling velocity within the crest half cycle
W_{st}	The sediment settling velocity within the trough half cycle
W_s	The still-water settling velocity

W_{min}	The peak negative vertical water particle velocities
W_{max}	The peak positive vertical water particle velocities
$A_1, A_2, B_1, B_2, C_1, E_1, E_2$	Parameters used in the MY-2.5 $\mathrm{k}-\mathrm{k}l$ model
a_1, a_2, a_r, α	Parameters used to calculate bottom roughness height
a_b, a_{bf}	Empirical constants
$\hat{a}$	The representative orbital excursion amplitude for the whole flow cycle
c	Wave phase speed
c_g	Wave group celerity
c_p	Wave phase speed at the dominant frequency
c_w	empirical constants
c_x	Wave celerity x-direction
c_y	Wave celerity y-direction
c_θ	Wave celerity in directional (θ) space
c_σ	Wave celerity in frequency (σ) space
c'	Turbulent concentration
c_μ^0	Stability coefficient based on experimental data for non-stratified channel flow
d_0	Wave orbital diameter
e_k	A numerical coefficient
f	Coriolis parameter
$\tilde{f}$	$\tilde{f} = \tilde{\sigma}/2\pi$
$f^b(z)$	Empirical vertical distribution function that quantifies the vertical penetration of momentum associated with breaking waves from the surface
$f^{\mathrm{bf}}(z)$	An upward decaying vertical distribution function
$f_{w\delta i}$	Wave-current friction factor
f_{wi}	Wave friction factor
f_δ	Current friction factor
f_w	The full-cycle wave friction factor
$f_{w\delta}$	The full-cycle wave-current friction factor: $f_{w\delta} = \alpha_f f_\delta + (1-\alpha_f) f_w$
g	Gravity
h	Mean water depth
k	Turbulent kinetic energy

k	Wave number (1/wave length)
k_b	Decay parameter: $k_b^{-1} = a_b H_{rms}$
k_{bf}	Decay parameter: $k_{\mathrm{bf}}^{-1} = a_{\mathrm{bf}} \delta_w$
k_x	Wave number in x-direction
ky	Wave number in y-direction
k_1, k_2	Active layer thickness coefficients
k_N	Nikuradse bottom roughness
$k_{s\delta}$	Current-related bed roughness
k_{sw}	Wave-related bed roughness
l	Turbulent marcroscale
l_z	"conventional" empirical turbulent length scale
m	Index for each sediment class
$m_\eta,\ m_\lambda,\ n_\eta,\ n_\lambda$	Intermediate factors to calculate η_r and λ_r by the ripple predictor of O'Donoghue et al. [8]
n	The nth time step
q_{bl}	Bedload transport rate
q_{blx}	Bedload transport rate in x-direction
q_{bly}	Bedload transport rate in y-direction
q_{bl_slope}	Bedload slope factor
$q_{tot,x}$	Total sediment transport rates (in m^3/ms) in x direction
$q_{tot,y}$	Total sediment transport rates (in m^3/ms) in y direction
q_{slp}	Bed slope factor multiplied on the transport rate calculated in horizontal bed condition to accounted for the bed slope effect
$\overrightarrow{q_s}$	The volumetric net transport rate per unit width
s	Vertical Sigma coordinate
s	Specific gravity
t	Time
Δt	Time interval
$t_{0_{pn}}$	The time of zero crossing from the positive to negative velocity
$t_{0_{np}}$	The time of zero crossing from the negative to positive velocity
$t_{u_{max}}$	The time when the velocity reaches its maximal value
$t_{u_{min}}$	The time when the velocity reaches its minimal value
u	Velocity x-direction

u_b	Bottom wave-orbital velocity
$u_{\tau s}$	Friction velocity associated with the surface
$u_{\tau b}$	Friction velocity associated with the bottom
u_*	Friction velocity
u_{*air}	Air friction velocity
u_{*c}	Friction velocity due to currents
u_{*wc}	Friction velocity due to combined waves and currents
u_*^s	Surface wind friction velocity
u'	Turbulent velocity x-direction
u_s	Vertically varying stokes velocity x-direction
$\bar{u}$	Depth-integrated velocity x-direction
$\overline{u_s}$	Depth-integrated stokes velocity x-direction
$\vec{u}_w(t)$	The time-varying free-stream orbital velocity vector
$\vec{u}_\delta$	The steady current velocity vector.
$\vec{u}(t)$	The near bed velocity at the edge of the wave boundary layer due to combined wave and current motion ($= \vec{u}_w(t) + \vec{u}_\delta$)
$\vec{u}_{c,r} = \{u_{c,rx},\ u_{c,ry}\}$	The representative combined wave-current velocity vectors for the crest half cycle
$\vec{u}_{t,r} = \{u_{t,rx},\ u_{t,ry}\}$	The representative combined wave-current velocity vectors for the trough half cycle
$\vec{u}_c = \{u_{cx},\ u_{cy}\}$	The combined wave-current velocity vectors at moments of maximum orbital velocity
$\vec{u}_t = \{u_{tx},\ u_{ty}\}$	The combined wave-current velocity vectors at moments of minimum orbital velocity
$\tilde{u}_{c,r}$	The representative half-cycle orbital velocity for the wave crest
$\tilde{u}_{t,r}$	The representative half-cycle orbital velocity for the wave trough
$\hat{u}_c$	The maximum wave orbital velocity in one wave period
$\hat{u}_t$	The minimum wave orbital velocity in one wave period
$\hat{u}$	The representative orbital velocity amplitude for the whole flow cycle
v	Velocity y-direction
v'	Turbulent velocity y-direction
v_s	Vertically varying stokes velocity y-direction
$\bar{v}$	Depth-integrated velocity y-direction
$\overline{v_s}$	Depth-integrated stokes velocity x-direction

w	Wave-averaged Eulerian velocity z-direction
w^{st}	Stokes velocity z-direction
w^{l}	Wave-averaged Lagrangian velocity z-direction
w'	Turbulent velocity s-direction
w_s	Sediment settling velocity
x	Horizontal direction
y	Horizontal direction
z	Vertical elevation
$\hat{z}$	Unit vector in the vertical direction
z_a	Active layer thickness
z_{air}	Air side roughness parameter
z_0	Total bottom roughness length
z_{0N}	Grain size bottom roughness
z_{0ST}	Sediment transport bottom roughness
z_{0BF}	Bedform bottom roughness
z_{0MIN}	Minimum bottom roughness
z_{0s}	Surface roughness
z_r	Reference elevation
z_w	Wave-related surface roughness height
z_{bed}	The bed level elevation (positive upwards)

Φ	Non-dimensional bedload transport rate
Ω	Area of the groundwater source
Ω^u	The area of the individual momentum control element
Ω^ζ	The area of the individual tracer control element
Ω_c	The sand load that is entrained during the wave crest period
Ω_t	The sand load that is entrained during the wave trough period
Ω_{cc}	The sand load that is entrained during the wave crest period and transported during the crest period
Ω_{tc}	The sand load that is entrained during the wave trough period and transported during the crest period
Ω_{tt}	The sand load that is entrained during the wave trough period and transported during the trough period

Ω_{ct}	The sand load that is entrained during the wave crest period and transported during the trough period
Υ	$\boldsymbol{k}\cdot\boldsymbol{V}$
$\mathcal{H}$	$\mathcal{H} = k\left(h + \zeta + \hat{\zeta}\right) = kD$
$\mathcal{P}$	The wave-averaged forcing surface boundary condition
$\mathcal{Z}$	$\mathcal{Z} = k\left(z + h\right)$
$\hat{\Psi}$	Mobility number
$\hat{\Psi}_c$	The maximum mobility number at crest half cycle
$\hat{\Psi}_t$	The maximum mobility number at trough half cycle
$\tilde{W}$	A wall proximity function
$\mathcal{K}$	The lower order Bernoulli head (after removing quasi-static terms)
$\mathcal{L}$	Slope of the turbulent length scale in the wave-enhanced layer
α_{de}	Spatial decay rate of TKE in the wave-enhanced layer
α_f	$\frac{\lvert u_\delta\rvert}{\lvert u_\delta\rvert+\hat{u}}$
α_{pl}	A calibration coefficient for calculating the phase lag parameter
α_r	Roller parameter
α_{BJ}	A parameter used to calculate D_{tot} (=1.0 in SWAN)
α_{CB}	A parameter related to the wave age
$\alpha_r^s,\ \alpha_r^0$	Parameters used to calculate A_R
α_{slp}	Tuning parameter with a default value of 1.0
β	The degree of acceleration skewness ($= a_{max}/(a_{max} - a_{min})$)
β_{sl}	Local bed sloping angle
β_w	The ratio of H_{rms} to H_{max}
β_{zw}	A parameter used to calculate the wave-related roughness height (i.e. z_{0s})
γ	The ratio of maximum possible wave height to water depth
γ_w	Wave asymmetry factor
γ_1	Linear drag coefficient
γ_2	Quadratic drag coefficient
γ_k	Numerical calibration factor
δ_w	Wave boundary layer height
δ_{wbl}	Wave boundary layer height
δ_{sc}	Sheet flow layer thickness for the crest half cycle

δ_{st}	Sheet flow layer thickness for the trough half cycle
ε	Turbulent kinetic energy dissipation rate
ε^{b}	Depth-induced wave breaking induced dissipation
$\varepsilon^{\mathrm{bf}}$	Bottom friction induced wave dissipation
ε^{r}	Roller energy dissipation rate
$\varepsilon^{\mathrm{wcap}}$	White-capping induced wave dissipation
ε_0	The sediment porosity
ζ	Wave averaged mean surface elevation
$\hat{\zeta}$	Quasi-static surface elevation
ζ^c	The composite sea level: $\zeta^c = \zeta + \hat{\zeta}$
η_r	Ripple wave height
θ	Wave direction
θ_m	Shields parameter (uses τ_m)
θ_{sf}	Shields parameter (uses τ_{sf})
θ_{cr}	Critical shields parameter (uses τ_{ce})
$\overrightarrow{\theta}$	Directional shields parameter
$\overrightarrow{\theta_c} = \{\theta_{cx}, \theta_{cy}\}$	Non-dimensional total bed shear stress (Shields parameter) vector for the crest half cycle
$\overrightarrow{\theta_t} = \{\theta_{tx}, \theta_{ty}\}$	Non-dimensional total bed shear stress (Shields parameter) vector for the trough half cycle
$\hat{\theta}_i$	Shields parameter based on the crest/trough velocity amplitude $\hat{u}_i$
$\langle\|\theta\|\rangle$	The time-averaged absolute Shields parameter
κ	von Karman's constant
λ_r	Ripple wave length
μ	A factor
ν	Molecular kinematic viscosity
ν_0	Molecular tracer kinematic diffusivity
ξ_s	A coefficient accounting for the shape of the velocity and concentration profile
ρ	Total density
ρ_0	Reference density of sea water
ρ_s	Sediment density
ρ_w	Water density
σ	Wave radian frequency (relative to currents)

$\tilde{\sigma}$	Mean wave frequency (relative to currents)
σ_{k}	Turbulent Schmidt numbers for k
σ_{ψ}	Turbulent Schmidt numbers for ψ
τ_t	Total bottom stress exerted on the flow
τ_{sed}	Bottom stress used for the sediment-transport formulations
τ_b	Mean (over many wave periods) bottom stress associated with mean current above the wave-boundary layer
τ_{bx}	Skin friction component of bottom stress in x-direction
τ_{by}	Skin friction component of bottom stress in y-direction
τ_c	Bottom stress due to currents alone
τ_{ce}	Bottom critical erosion stress
τ_{sx}	Surface stress x-direction
τ_{sy}	Surface stress y-direction
τ_{sf}	Total skin friction bottom stress (maximum combined wave + current)
τ_{sfm}	Skin friction component due to form drag
τ_w	Bottom stress due to waves alone
τ_{wc}	Combined bottom stress due to waves and currents
τ_{cw}	Mean bed shear stresses during a wave cycle, beneath the combined effect of waves and currents
τ_{cwmax}	Maximum bed shear stresses during a wave cycle, beneath the combined effect of waves and currents
τ_{wRe}	A stress contribution induced by surface progressive waves
$\tau_{cr,0}$	Critical bed shear stress for sand on a horizontal bed
$\tau_{cr,slp}$	Critical bed shear stress for sand on a sloping bed
$\phi_p(\theta)$	Sediment pickup function
ϕ	Dynamic pressure (normalized by the density ρ_0)
ϕ^c	$\phi^c = \phi + \mathcal{K}$
ϕ_r	The angle of repose of the sediment at which slope the sediment will avalanche in a zero flow
ψ	A generic turbulence length scale
ψ_{sl}	Flow angle to the up-slope direction
ω	Vertical Eulerian velocity in Sigma coordinates
ω^{st}	Vertical Stokes velocity in Sigma coordinates
ω^l	Vertical Lagrangian velocity in Sigma coordinates

E-B	Element-based sub-meshes (e.g. Figure A.3)
V-B	Node-based sub-meshes (e.g. Figure 3.4)
MPM	Meter-Peter M*ü*eller [9] formulation
WEC	The wave effects on current
FVCOM	Finite Volume Coastal Ocean Model
UnSWAN	Unstructured version of the SWAN model
SANTOSS	SANd Transport in OScillatory flows in the Sheet flow regime (a semi-unsteady sand transport formula)

Acknowledgement

I would like to express my gratitude to my primary supervisor Dr. Ming Li of School of Engineering, University of Liverpool for his guidance, focus, advice and continuous support throughout this research. I would also like to thank my secondary supervisor Dr. Judith Wolf of National Oceanography Center for her valuable advice and guidance.

I would like to thank Dr. Joep van der Zanden of University of Twente for his discussions and providing the detailed measurement data of the SINBAD mobile bed experiment. I would like to thank Dr. Dominic A. van der A of University of Aberdeen for providing me the measurement data of the SINBAD fixed bed experiment. I am also indebted to Dr. Jebbe J. van der Werf of Deltares for providing me the Fortran version of original SANTOSS model code. I would like to thank Prof. Xueen Chen of Ocean University of China for teaching me Physical Oceanography, and for his care, patient mentoring, and invaluable support and guidance.

I would like to thank my family, especially my wife Mrs. Caixia Wang, for putting up with me when I have been stressed, depressed and being amazingly supportive, loving and caring. Without you I don't think I can finish this research. Thank you so much! I would also like to thank my friends, roommates and colleagues for their support and for all the great times we have had over the last few years. I am also sincerely grateful to the China Scholarship Council and the School of Engineering, University of Liverpool for their financial support.

At last, I would like to thank Prof. C.S. Chen of the University of Massachusetts-Dartmouth for providing the source code of FVCOM and also the SWAN developers for developing and providing this open source code. I would also like to thank the staff and personnel involved in collecting and maintaining the DUCK'94 experiment dataset. Furthermore, this research is aided by the computational support from the Chadwick High Performance Computer at University of Liverpool, and also the facilities of N8 HPC Centre of Excellence, provided and funded by the N8 consortium and EPSRC (EP/K000225/1).

Chapter 1

Introduction

1.1 Research Context

Coastal regions occupy less than 15% of the Earth's land area, while they host more than 40% of the world population. Nearly 1.2 billion people live within 100 km of a shoreline and below 100 m of sea level, with an average density nearly 3 times higher than the global average for population (Small and Nicholls [10]). Coastal regions also contain rich resources to produce goods and services and are home to most commercial and industrial activities.

In the face of rising sea level and changing climate (e.g. storminess increase), however, the coastlines are facing increasing threat to be eroded. Furthermore, human interferences, e.g. damming of rivers and estuaries, the application of hard structures for coastal reinforcement, and sand and gas mining, may alter the sediment budget and enhance (local) coastal erosion (Giardino et al. [11]). Therefore, efficient and effective management strategies for these coastal regions are urgently in need.

The coasts are dynamic areas (van der Zanden [5]), the evolution of which contains complex sediment transport processes and interactions between the combined flows due to wind waves and bed morphological features. The proposal of coastal management strategy must be based on a detailed and fundamental understanding of those complicated processes, which is far from satisfactory, especially on the dynamic interactions between hydrodynamics and sediment movement on the continental shelf and within the nearshore region (van Rijn et al. [12]).

To fill in these knowledge gaps, a collective work on laboratory experiments, field observations and detailed model simulation are crucial in present day researchs. In particular, the laboratory measurements are capable of providing very detailed information on specific variables under controlled condition, which is ideal to investigate the roles

from different mechanisms on the sand transport and quantify their effects. However, due to the limitation of measuring technique, some quantities, such as turbulence characteristics and processes around individual particles are still not available or at the level can be applied to the general practice. Similarly, the field measurements are able to reveal certain fundamental insights into the fluid-sediment interactions. But the complication of the uncontrolled natural environment often means the uncertainties in these measured data are high, and the quality of the data are often not as good as that from the laboratory study.

The numerical modelling approach, on the other hand, is able to provide much detailed information which the laboratory and field measurements are not able to. But the assumptions and theory involved in any model have to be validated and the numerical scheme used in the simulation need to be calibrated against available data. Therefore, the three study approaches are complementary to each other and the combination of these different methods is now regarded as the way forward to advance our current knowledge and understanding of those complicated processes in the dynamic coastal areas.

However, it is widely recognised that many important physical processes influencing sediment transport and coastal morphology, are still missing from the present day practical engineering morphological models, such as the wave non-linearity, wave induced bottom streaming, sediment grains size effects. Many recent laboratory and field studies have demonstrated the critical role these processes play in determining the sediment motion in the coastal zone (van Rijn [12]).

The present study therefore focuses on the development of a new 3D cross-shore sediment transport model based on several important progresses in recent years, including the Vortex Force formalism of wave-current interactions and comprehensive measurements of sediment suspension under breaking waves that are not available before, with the aim to represent wave-breaking induced hydrodynamics, turbulence and sediment suspension in a more inclusive approach than the previous studies. The developed new model is particularly suitable for the investigation of sediment transport across the shore-face under progressive and breaking waves, which is regarded as one of the paramount important processes to quantify the sediment motion in the coastal region. A detailed literature review on coastal processes and modelling technique is given in the following section. The model development, calibration and validations are presented in the following chapters.

1.2 Coastal Processes

1.2.1 Waves

When waves approach the shore, the wave height decreases initially due to bottom friction induced energy dissipation and wave shoaling, and then increases due to shoaling as the wave celerity decreases. Waves approaching the shore at an angle gradually change their direction and eventually become perpendicular to the shoreline near the beach (refraction). Along the geometric shadow line of obstacles (e.g. islands, headlands and breakwaters) strong diffraction occurs, i.e. turning of waves towards areas with lower amplitudes due to amplitude changes along the wave crest (Holthuijsen, [13]).

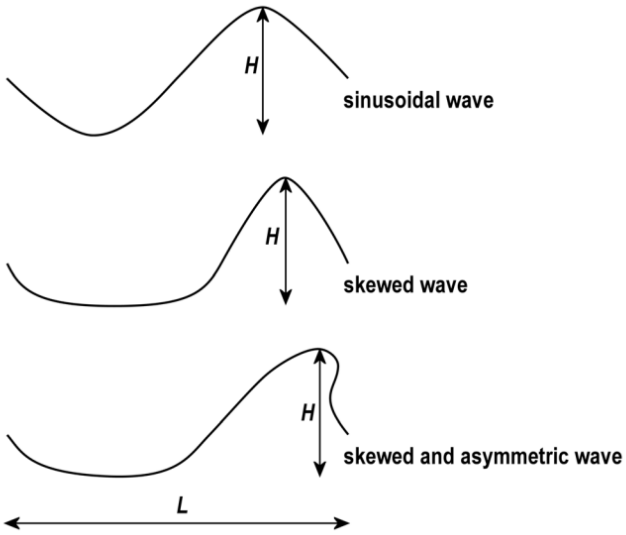

Figure 1.1: Schematic diagram of a sinusoidal wave, a skewed wave, and a skewed and asymmetric wave. (After Grasmeijer [3]).

In deep waters, the wave shape is very close to the sine curve. While approaching the shore, the non-linearity becomes more apparent due to energy transfer from the primary wave components to their higher harmonics in the shoaling process (Phillips [14]). The wave shape therefore becomes skewed, i.e. horizontally asymmetric with sharply peaked crests and broad flat troughs. Further shoreward, the higher harmonic constituents partially act as 'free' superimposed waves that lag the primary waves (ver der Zanden [5]). This leads to the commonly referred wave asymmetry, i.e. the waves show a vertical asymmetry or a tendency to become pitched forward (Grasmeijer [3]). A schematic diagram of a sinusoidal wave, a skewed wave and a skewed and asymmetric wave is shown in Figure 1.1. These changes in wave form have significant impacts on the flow dynamics and particularly the near bed boundary layer processes. Specially, Longuet-Higgins [15] has shown that for real fluids with viscosity effects, there is a

time-averaged net transfer of momentum into boundary layer and causes a net onshore streaming. Under an asymmetrical wave, there is also a net mass transport due to the wave shape asymmetry during the onshore phase and offshore phase of the wave, which also leads to a wave-shape induced streaming opposite to the wave propagation direction, see Ribberink and Al-Salem [16]. These processes are expected to have impact on the local sand transport within the boundary layer.

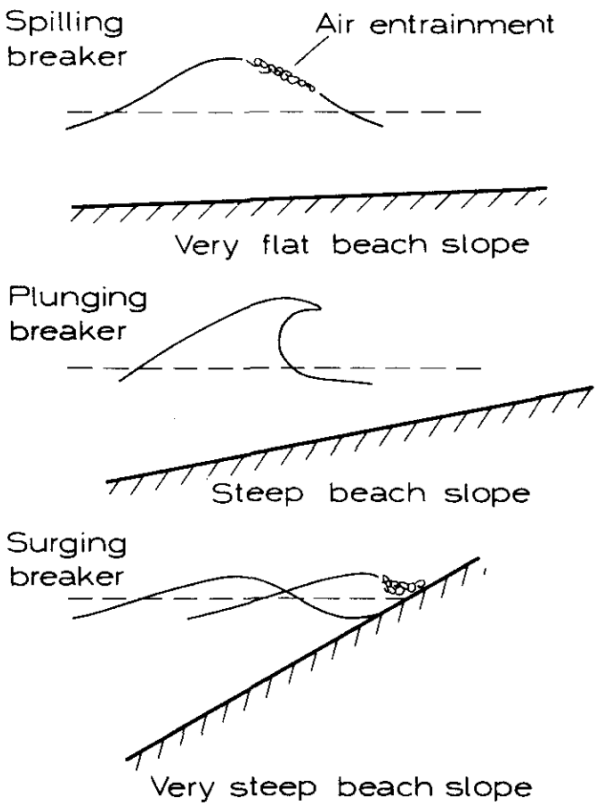

Figure 1.2: Breaker Types (After Fredsøe and Deigaard [4]).

With the increasing height and the steepness of front, the wave eventually breaks at a location where it cannot maintain its form any further. Depending on the characteristics of the incoming waves and bed slope, breaking waves can be classified into three types, i.e. spilling breakers, plunging breakers and surging breakers (Fredsøe and Deigaard [4]). A diagram of these three breaker types is shown in Figure 1.2, in which totally different characteristics can be observed: in spilling breakers, a plume of water and air bubbles slide down the forward slope of the wave top; in plunging breakers, the wave crest moves forward and falls down at the trough in front of it as a single structured mass of water or a jet; in surging breakers, the foot of the steep front rushes forward, leading to the decrease and disappearance of the wave crest.

After breaking, part of the broken primary waves transforms into a surface wave

roller (i.e. bore-like broken waves) which continues to propagate shoreward while gradually dissipating wave energy at the same time. This causes a lag in the transfer of momentum and has an important effect on the mean flow (Svendsen [17]; Nairn et al. [18]).

1.2.2 Mean Currents

In deep waters, the observed currents are usually generated by a number of physical processes, such as tides, winds and density gradients. In the coastal region, surface wind waves also can produce mean current. As these processes typically work at different depth across the water column, the flows in the coastal areas are therefore found to have a complicated 3D structure. The wave-driven currents can be very strong in the surf zone, e.g. after wave breaking, which significantly affects the sediment transport processes and morphological evolutions, therefore they are one of the main focuses in the present research. Generally, the wave-induced mean flow in the nearshore region can be divided into a cross-shore and a longshore component.

Cross-Shore Mean Current

The cross-shore mean current relates to the mass compensation to the wave-induced onshore mass flux (Stokes drift) that occurs especially above the wave trough level (van der Zanden [5]). It is characterized by an onshore directed mass flux near the water surface and an offshore directed return flow (i.e. undertow) in the lower part of the water column. This characteristic can be explained by an analysis of the change of radiation stress along the cross-shore direction with waves propagate from the breaking location towards the shoreline: the wave height reduction after wave breaking leads to a decrease of the radiation stress, the horizontal gradient of radiation stress (i.e. radiation force; onshore directed) is balanced by a offshore-directed horizontal pressure gradient force due to a set-up of the mean water level; however, the radiation force gradually decreases from the water surface to the bottom while the pressure gradient force is vertically uniform; therefore the momentum balance can only be obtained if there is an onshore-directed shear stress along the bottom, which is brought about by an offshore-directed velocity or undertow. The presence of undertow can also be explained by the mass conservation: as the coastline is a closed boundary, the vertically integrated net transport at the coastline must be zero; therefore the onshore directed wave mass flux near the water surface must be compensated by an offshore directed flow in the lower part of the water column.

Observations in a barred profile (Garcez Faria et al. [19]; van der Zanden [5]; van der A et al. [20]) show that the vertical structure of the undertow has a parabolic

shape with relatively large offshore-directed velocities in the lower part of the water column and small offshore-directed or even onshore-directed velocities in the upper part. This vertical shape of undertow profile can significantly affect the suspended sediment transport and therefore is also very important for the morphological changes. However, the vertical structure of the undertow profile is determined by the depth-varying momentum equations which include, in addition to the horizontal gradients in momentum and pressure, terms related to vertical exchange of horizontal momentum by orbital and turbulent velocities (van der Zanden [5]). An appropriate 3D wave-current interaction theory is thus needed to be implemented in the morphodynamic model in order to have a reasonable prediction of the undertow profile. This is discussed in much more details in Section 1.2.3

Traditionally, it was assumed that the transfer of momentum from the waves to the current occurs instantaneously (Grasmeijer [3]). The models with this assumption tend to predict narrow jets over the bar where momentum input is concentrated by breaking (Grasmeijer [3]), which, however, does not agree with some field observations, e.g. Gallagher et al. [21] show the maximum longshore current in the trough of the bar with a broad distribution. It is then realized that the wave roller is an effective mechanism for spreading and delaying the input of momentum from the incident wave to the water column, as the turbulent kinetic energy produced by wave breaking continues carrying momentum in the form of a roller and the dissipation of this kinetic energy (roller dissipation) drives the mean flow. In other words, the advection of the roller causes shoreward shifts of the current forcing patterns leading to the shifting of the peak in current speed into the bar trough (e.g. Ruessink et al. [22]; Uchiyama et al. [23]; Zheng et al. [24]). A wave roller model or parameterization method that can provide reasonable prediction of roller characteristics is thus needed to be implemented in a practical morphodynamic model.

Longshore Mean Current

When approaching the shoreline at an angle (obliquely incident waves), the wave excess longshore momentum flux can generate a shore parallel currents i.e. wave-driven longshore current. As there is no boundary in the longshore direction of the coast, the longshore current has the same direction in the whole water column. In the coastal region, other shore parallel currents driven by wind or tides may coexist with wave driven longshore currents.

1.2.3 Wave-Current Interaction

The interaction of wind-generated surface gravity waves with slowly varying ocean currents in shallow coastal areas can create unique flow patterns (e.g. longshore current, rip current and undertow) in both inner shelf and surf zone environments. The main effects of currents on the waves are the current-induced refraction and Doppler frequency shift (Kumar et al. [25]). The wave effects on current (hereinafter WEC) are more complicated and diverse, ranging from wave-induced upper-ocean mixing and current profiles to littoral flow, sea level set-up/set-down and near bed streaming. This important role of the surface wave effects in shallow coastal and nearshore regions have been verified by different observations. Wolf and Prandle [26] concluded that the maximum effects of waves with periods longer than 6s take place in depths shallower than 20 m. These effects often play a important role in determining local sediment transport and hence the overall morphological evolution (van Rijn et al. [12]). However, the widely used practical coastal circulation models based on a wave-period-averaged mean flow concept could not resolve the dynamics of surface ocean waves directly. Thus, the effects of waves on currents can only be added and represented in the wave-averaged circulation equations as additional forcing terms, which could be obtained with corresponding wave properties provided by a wave model.

In 1964, Longuet-Higgins and Stewart firstly identified that the presence of surface waves will result in an excess flow of momentum. From the hydraulics point of view, a horizontal momentum flux transports to one area via an interface will increase the total momentum of the water body in this area, whose effect is same with a horizontal external force acts on this water body. Hence, this excess flow of momentum resulting from the surface waves is regarded as a horizontal force, the so-called radiation stresses. This radiation stresses (excess flux of momentum) is formed by two contributions: one due to the wave-induced velocities of the water particles and another one due to the pressure, especially the wave-induced pressure.

Since the fundamental work of Longuet-Higgins and Stewart [27] in the last century, a large number of theoretical approaches and implementations have been proposed for coupling the surface wind waves with ocean circulation (Bowen [28]; Hasselmann [29]; Craik and Leibovich [30]; Garrett [31]; Phillips [32]). Most of these early studies investigated the interactions between waves and currents in forms that the additional wave forcing for the total momentum (i.e. including waves and currents), derived as a net wave-induced momentum flux, is represented as the divergence of the radiation stress tensor (the radiation stress scheme; Longuet-Higgins and Stewart [27]; Smith [33]; and Mellor [1, 34, 35, 36]). In the present research, the term of radiation-stress scheme is used to encompass equations that include wave effects on currents using the divergence

of either a radiation or an interaction stress, or a three-dimensional analog, following the work of Longuet-Higgins and Stewart [27] and Hasselmann [29].

It is also noted that before the pioneer work of Mellor [1], most of the early theories and model developments mainly investigated the interaction between waves and currents in one- or two-dimensional, depth-averaged forms, in which the additional wave forcing, derived as a net wave-induced momentum flux, is represented as the divergence of a 2D radiation stress tensor (Longuet-Higgins and Stewart [27]). Then Mellor [1] extended the 2D radiation stress tensor into a depth-varying form (i.e. the depth-varying radiation stress) within a closed set of equations for describing the 3D wave-current interactions. However, Ardhuin et al. [37] pointed out that this radiation stress tensor is not correct when applying it for shallow water ($kD \cong 1$), due to a mistake in the treatment of wave pressure. Further testing reveals the Mellor [1] scheme can produce mean currents over uneven bottom even for deep waters (say, $kD \cong 10$). Thus in 2008, Mellor [38], based on a z-coordinate, derived another depth-dependent wave radiation stress, including a Dirac delta function at the sea surface. When depth-integrated, this radiation stress, however, is not consistent with the radiation stress tensor of Longuet-Higgins and Stewart [27], which may result from an inconsistent treatment of the pressure (Bennis and Ardhuin [39]). As a result, the depth-integrated momentum equations are also inconsistent with Phillips [32]. Based on the corrected horizontal pressure gradient and radiation stress tensor of Mellor [38], Mellor [35] presented a closed set of equations in Sigma-coordinates that is consistent with Longuet-Higgins and Stewart [27] and Phillips [32]. However, the vertical flux in Mellor's approach (and also those use a Lagrangian mean velocity as the prognostic variable in the momentum equation, e.g. Andrews and McIntyre [40]; Moghimi et al. [41]) requires an approximation to first order in the wave-induced pressure and velocities, which is often difficult to resolve (Ardhuin et al. [42]; Bennis et al. [39]). Therefore, the ability, theory scope and limitations of this approach are still in debate in the literature (Bennis et al [39]; Moghimi et al [41]; Aiki and Greatbatch [43]; Ardhuin et al. [44]). Despite the issues mentioned above, the theory framework proposed by Mellor is widely used (Sheng and Liu [45]; Wang and Shen [46]; Warner et al [47]). Kumar et al. [48] implemented the radiation stress formulation of Mellor [35] into ROMS and confirmed that the equations captured the dynamics in the surf zone; while at the same time they also stressed the occurrence of spurious flows in shoaling regions due to the singular surface term in the Radiation stress tensor.

In recent years, many other theories are also proposed for the wave-current interactions, see McWilliams et al. [49]; Ardhuin et al. [37]; AiKi and Greatbatch [43]. Among them, a method based on the fluid momentum only (i.e. use Eulerian velocity as the prognostic variable in the momentum equation) are developed that is typically written in a form of Vortex Force (VF), e.g. Craik and Leibovich [30], McWilliams et al. [49],

Ardhuin et al. [37], Aiki and Greatbatch [43], though they are also equivalently cited in a different form (Suzuki and Fox-Kemper [50]). The VF approach arose to explain Langmuir circulations through wave vorticity generation by the currents and vortex stretching by the wave's Lagrangian mean flow, the Stokes drift (Craik and Leibovich [30]), but the representation is more generally germane. So far, the VF scheme has been widely used to represent the additional terms corresponding to WEC in the momentum equations.

Within asymptotic approximations the radiation-stress and vortex-force schemes are equivalent (Uchiyama et al. [23]), related through two alternative representations of the inertial acceleration (i.e., advection). The radiation-stress scheme arises from the identity, $\boldsymbol{V}\cdot\nabla\boldsymbol{V} = \nabla\cdot(\boldsymbol{V}\boldsymbol{V}) + \boldsymbol{V}(\nabla\cdot\boldsymbol{V})$, together with incompressibility $\nabla\cdot\boldsymbol{V} = 0$, while the VF scheme comes from the identity, $\boldsymbol{V}\cdot\nabla\boldsymbol{V} = \nabla|\boldsymbol{V}|^2/2 + (\nabla\times\boldsymbol{V})\times\boldsymbol{V}$, where $\boldsymbol{V}$ is the Eulerian velocity vector. However, as it splits the wave effects into gradients of Bernoulli head and a vortex force, an primary advantage of the VF formalism is that it explicitly includes a type of wave-current interaction that is not available in the radiation stress concept (Uchiyama et al. [23]; McWilliams et al. [49]; Newberger and Allen [51, 52]). As a result, the VF method is able to separate the different contributions in pressure distribution that is particularly important to verify the model's characteristics through the momentum balance as demonstrated by Uchiyama et al [23] and Zheng et al [24]. Based on the above analysis, the wave-current interaction scheme based on a VF approach (Uchiyama et al. [23]; McWilliams et al. [49]) is finally selected to be implemented in the newly developed model system in the present research.

1.2.4 Sediment Transport

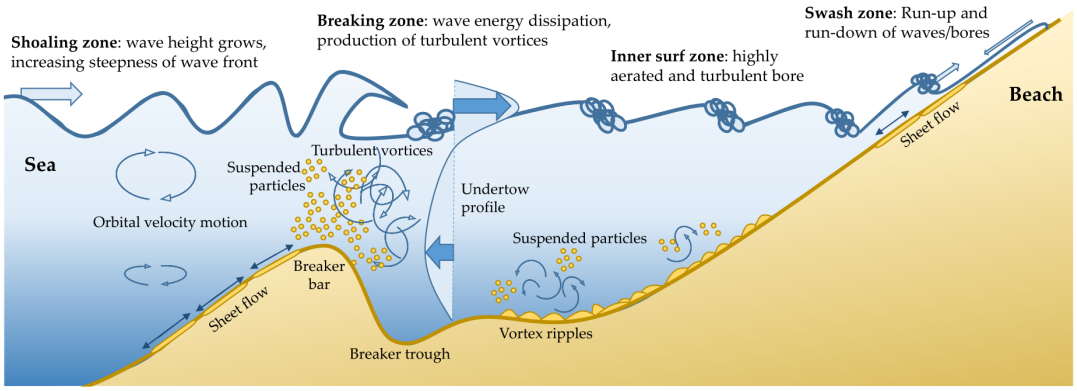

Figure 1.3: A conceptual 2D (cross-shore) overview of sediment processes in the near-shore region (After van der Zanden [5]).

Figure 1.3 shows a simplified 2D overview of the sediment transport processes in

the nearshore region. In deep waters where waves hardly affect the bed, all of the sediment transport is driven by the ocean currents generated by tides, winds and density gradients. Close to the shore, as water depth gradually decreases and wave height increases, the wave motion gradually dominates the flow in the water column and thus the sediment transport. Close to the breaking point, wave induced fluid motions are very vigorous due to the relative shallow depth and the strong oscillations; the bed will have megaripples or be almost perfectly flat in this region, where the sediment grains are transported essentially in a very thin ($O(mm)$) but high-concentration (100-1600 g/L) layer near the bed (i.e. the 'Sheet flow' region in the offshore slope of the breaker bar)(van der Zanden [5]; van der Zanden et al. [53, 54]). Around the breaking point, the wave-breaking induced vortices bring large amounts of sediment towards the water surface, thus sediment transport occurs throughout the whole water depth (van der Zanden [5]; van der Zanden et al. [53, 55]). In the surf zone where the bed may be flat or covered by ripples, a considerable amount of sand will be suspended due to the continuation of strong turbulence in the water column.

Generally, the total sediment transport in the nearshore region is partitioned into a bedload and a suspended load component. Up to now no precise definitions of these two components have been given. Fredsøe and Deigaard [4] defined the bedload as the part of the total load that is in more or less continuous contact with the bed during the transport. It primarily includes grains that roll, slide, or jump along the bed. Thus the bed load transport rate mostly relies on the effective shear stress acting directly on the bed surface. The suspended load is defined as the part of the total load that is moving without continuous contact with the bed as a result of the agitation of fluid turbulence. The above classification is given based on the different transport mechanisms of bed materials. From a modelling point of view, the bed load can also be regarded as the moving sediment grains below a particular reference level above the bed (van Rijn [56]) and suspended load as those above this near-bed reference level (van Rijn [57])

Bedload Transport

In the nearshore region when the bed shear stress induced by waves and currents exceeds the critical value for initial motion, sandy particles begin to move along the bed surface and often ripples start to form. As the bed shear stress increases, ripples successively go through the equilibrium range, in which both the ripple height and ripple length tend to increase until ripple steepness and ripple roughness reach their maximum; and the break-off range, in which the ripple height decreases while the ripple length roughly stays constant or decreases slightly (Grasmeijer [3]). If the bed shear stress is further increased, the ripples can be wholly washed out leaving a plane seabed. Therefore, generally two distinct bedload transport regimes, i.e. the rippled-bed regime and the

flat-bed sheet flow regime, are commonly cited in the modelling of sand transport in the nearshore region. Practically, these two transport regimes are distinguished depending on the particle mobility number $\Psi_{max} = u_{max}^2/[(s-1)gd_{50}]$ (van Rijn [12]), where u_{max} is the maximum orbital velocity, $s = \rho_s/\rho$ the relative sand density, ρ_s and ρ the density of sand and water, g the gravity acceleration and d_{50} the median grain size of sediment.

The rippled-bed regime is generally observed for mildly energetic conditions (e.g. at deeper water more offshore and inner surf zone), while the flat-bed sheet-flow regime is usually observed under energetic waves with large orbital velocities, e.g. in the breaking region and the swash zone. Flow and sand dynamics over rippled beds differ strongly from flat-bed oscillatory flows (Ribberink et al. [58]), especially for relatively steep, vortex ripples with ripple steepness $\eta/\lambda > 0.1$ (van Rijn [12]), where η and λ are the ripple height and length, respectively. An accurate prediction of the bedload transport regimes is thus very important, e.g. Schnitzler [59] indicated that a difference in predicted transport regime can lead to large discrepancy in the overall bedload transport rate.

Apart from the wave-current combined flow induced different flow regimes, the other hydrodynamic processes as discussed in the previous section also have significant effects on the boundary layer processes and hence the bed load transport in particular. The boundary layer streaming due to progressive waves and wave shape (asymmetry) tends to affect the bed load transport direction in the offshore non-breaking zone and near shore shoaling area. When the wave-current induced flow is strong enough to cause sheet flows, then sediment becomes mobile within a thick layer (mm to cm) and often the wave asymmetry becomes very important in determining the direction of sediment transport.

Another important factor that has been identified recently is the grain size effect, i.e. for coarse sediment, the grain tends to respond to the flow instantaneously. However, for fine and median sediment, the particle tends to delay in responding to changing flow dynamics. The entrained fine particles can be lifted to higher in the water column and the slow settling means they will not settle back to the bed when the wave-induced oscillation has changed to opposite direction. Consequently, the particles will be transported in the opposite direction, i.e. the so called phase-lag effects, see Dohmen-Janssen [60].

For the cross-shore sediment transport, the bed slope effects have been identified in many literatures. The upslope and downslope effects can influence the grain's motion under the given flow induced drag force. As the slope of the beach can be sometime considerable, the local bed load transport will either be enhanced or reduced depending on the slope angle. When a breaking bar is present, such effects can dominate around

the steep side of the bar and even lead to avalanche.

Suspended Sediment Transport

When the bed shear stress is large enough, the sediment grains sitting on the bed can be lifted into suspension. The lift is driven by an upward-directed pressure gradient that is associated with bed-shear-induced ejected vortices (van der Zanden, [5]). The equilibrium concentration profiles in the vertical direction generally follow an exponential or power-function distribution, depending on the distribution of mixing coefficient. This is a result of the combined effects of sediment pick-up from the bed, vertical advection, diffusive mixing and gravitational settling. Under non-breaking waves over a horizontal bed, the suspended sediment concentrations at a particular cross-shore location can be largely determined by the local vertical processes. This is not the case under the breaking waves where breaking induced strong spatial non-uniformity of the sediment concentration is found; the advection (i.e. incoming sediment fluxes from adjacent locations with different hydrodynamics) can also contribute to the local suspended sediment concentration.

Breaking waves in the surf zone generate an additional sediment stirring effect, caused by the breaking-induced flows and enhanced turbulent kinetic energy in the water column (van Rijn et al. [12]). The enhanced turbulence from the water surface may also penetrate through the water column and invade, often in an intermittent way, the wave bottom boundary layer, leading to increased bed shear stresses and additional bedload transport, pick-up and turbulent mixing of suspended sediments. Compared with shoaling locations, much increased suspended sediment concentrations are thus found in the breaking region.

1.3 Coastal Models

The typical coastal morphodynamic model used by engineering design includes several interactive models, e.g. the wave model, current model, sediment transport and morphological model. The following review will examine the currently well developed models in these categories.

1.3.1 Wave Models

In vast majority practical works, the wave characteristics at a given site need to be known or predicted under real conditions, which involves a mixture of swell and local generated wind waves, under spatially and temporally varying winds and irregu-

lar bathymetry and coastlines. Apparently, in these complicated conditions, the wave spectra and their integral properties can not be simply acquired by empirically based knowledge or algorithms, but only from the computation results of operational numerical models.

Generally speaking, there are two classes of surface ocean wave models: the phase-resolving models and the phase-averaging models. These two kinds of wave models have their own application remits: within a small regional scale, such as simulation for waves around harbours and beach processes, a phase resolving model can be used; when simulating wave dynamics around larger domains, such as regional processes and global oceans, the phase-averaging models are more suitable. In the present study, the new cross-shore sediment transport model is based on a phase-averaging wave model, aiming for practical engineering morphological predictions over large areas.

Phase Resolving Wave Models

By tracing the instantaneous water surface elevation and thus predicting the amplitude and phase of individual waves, the phase resolving model is suitable for situations where phase averaged properties vary rapidly over a few wavelengths.

In comparing with the phase-averaged models, the phase resolving model can usually represent many important wave processes directly in the model solutions, including wave-wave interactions, wave non-linearities, wave-structural interactions. However, a major difficulty involved in applying this type of model is the large computational cost which in many cases is prohibitive to any large regional simulation with realistic simulation scenarios.

Phase-Averaging Wave Models

In contrast to the phase resolving models, the phase-averaging models concentrate on phase-averaged properties of waves: the spectrum and its integral properties (H_s, f_p, etc.) and should be limited to applications in which the phase averaged properties vary slowly. Based on the manner of the source terms being included in the model, three generations of phase-averaging models have been developed. Almost all of the phase-averaging wave models used in the present scientific community belong to the third generation wave models, among which WAM, WAVEWATCHIII and SWAN are the most widely used. The SWAN (Simulating WAves Nearshore), by containing some additional formulations for shallow water, is designed specifically for modelling the wave propagation from deep water to the surf zone (i.e. the main research area of this study) and thus is preferred in this research.

Comparing with the phase-resolving models, the phase-averaged model is simple to use and does not require a large amount of computing power, which makes it ideal for engineering practical work. However, to resolve the necessary wave characters based on the computed wave energy at a given site, a linear wave theory (Airy wave theory) is often employed. Although such an approach has been proven acceptable in terms of the model's accuracy in most practical applications, the wave non-linearity, skewness and other related wave characteristics as shown in the previous section are not available and certain high order non-linear wave theories have to be used, which introduces uncertainties in the wave-current interactions and sediment transport predictions.

1.3.2 Wave-Current Coupled Models

In the last two decades, along with the development of theory for wave-current interactions, a number of numerical models have been developed and widely adopted in the present day engineering applications. Among them, the phase-averaged model in 1-D (across surf zone) or 2-D plane (depth-integrated) are dominant in the simulation of alongshore currents or rip current circulation. Although the 1-D and 2-D model could provide some information on the current patterns, intrinsically they are not applicable in resolving the 3-D dynamics (see Section 1.2.2) that are needed in investigating the effects of 3-D currents on the nearshore physical processes, such as the sediment transport, the morphological developments and the water quality simulations.

In recent years, several full 3-D wave-current coupled models have been developed. It is noted that the majority of these models are mainly based on two types of theory frameworks for wave-current interactions (see Section 1.2.3): the depth-varying radiation stress concept and the Vortex Force approach. Groeneweg and Klopman [61] used the approximate Generalized Lagrangian Mean (GLM) approach with the DELFT three-dimensional flow model. Sheng and Liu [45] used a 3D current-wave modelling system, by coupling the SWAN wave model with the Curvilinear-grid Hydrodynamics 3D (CH3D) model, to compare the performances of three radiation stress formulations: two depth-dependent formulations proposed by Mellor [38] and Xia et al. [62] and one depth-independent formulation proposed by Longuet-Higgins and Stewart [27]. Warner et al. [47] and Kumer et al. [48] adopted the wave radiation stress formulation which was initially proposed in a two-dimensional form by Longuet-Higgins and Stewart [27], Phillips [32] and then extended by Mellor [1, 34, 35, 38] into three-dimensional form, to couple ROMS and SWAN models. In above 3D models, the wave-current interaction terms are represented as the radiation stress gradient, at the same time many models based on the Vortex Force approach have also been developed. For example, Newberger and Allen [51, 52] accounted in the wave effects on the current within the Princeton Ocean Model (POM) in form of surface stress and body forces; Uchiyama et al. [23]

and Kumar et al. [25] used the vortex force approach proposed by McWilliams et al. [49] with Regional Ocean Modeling System (ROMS).

For reasons that indicated in Section 1.2.3, the Vortex Force approach is finally adopted to developed the new model system in the present research. However, most of the existing studies that use the VF methods are limited to structured grid models (e.g. Uchiyama et al. [23]; Kumar et al. [25]; Sheng and Liu [45]; Kumar et al. [48]; Newberger and Allen [51, 52]), which can be effectively applied into open seas or coastal areas with simple geometry. For sites with complex geometry and rapidly varying bathymetry, for instance around structures, setups with nested fine grids are necessary to achieve the high resolution required to accurately simulate hydrodynamic processes, sediment transport rates, and morphodynamic evolution. However, this involves a large amount of information exchange between different models and different sets of numerical mesh grids which increases the model complexity and decreases the computational efficiency.

Therefore in practical engineering applications, an unstructured grid model is in much demand, as it has distinct advantages in dealing with the complicated domain and local refinement around rapidly varying bathymetry (e.g. around structures) that are not easily achievable in a structured grid (Wang and Shen, [46]). With the potential of dynamic mesh adaptation using an unstructured grid, the model is also able to deal with simulations involving strong spatial and temporal variations, as shown in Huang et al [63].

It should be noted that the third-generation wave model solves an action balance equation where the action density spectrum is a function of five independent variables, wave propagation angle θ, frequency σ, and horizontal space coordinates X, Y and time t, while the circulation model only has four independent variables. In a typical simulation, the wave model requires larger computational efforts. As a result, in comparison with a sole circulation model, the total computation time is expected to increase up to two orders for the coupled wave-current model. For example, Mellor et al. [64] indicated that the CPU time required by SWAN simulation is about 86 times that for POM circulation calculation, under the same horizontal grid and length of run.

1.3.3 Turbulence Closure Models

As demonstrated by many existing studies, a proper description of turbulence generation and dissipation is crucial for the simulation of WEC under breaking waves. However, most of the existing studies are based on models such as k-ε or k-kl that are calibrated for an equilibrium turbulence production and dissipation state, which are strictly speaking not applicable for the simulation of the wave breaking process (Burchard [65];

Umlauf and Burchard [66]). The K-profile parameterization (KPP) is also found difficult to accurately represent the mixing in the bottom boundary layer in nearshore regions (Durski et al. [67]). This is partly due to the fact that to develop and verify the suitability of a turbulence scheme in modelling wave breaking, much detailed measurements in controlled laboratory conditions are required in both flow hydrodynamics and turbulence characteristics, as well as free surface variations. Due to the limitations in the measuring technique, such comprehensive datasets are still scarce in the literature. With few most recent experimental studies, e.g. van der A. et al [20] and van der Zanden et al [53], it is now possible to verify a turbulence closure in the details required for simulating wave breaking and wave-current interactions.

1.3.4 Sediment Transport Models

Suspended Sediment Transport Models

Similar to the current model, a wave-averaged advection-diffusion (AD) model is commonly used by the morphodynamic model systems to calculate the suspended sediment concentration distribution. The diffusion term in the AD model represents the sediment fluxes in horizontal and vertical directions, which are modelled as a diffusive process based on the sediment diffusivity that is determined either purely empirical or based on (separately calculated) turbulent viscosities (van der Zanden [5]). Most of the existing AD models use the Eulerian mean flow velocities in the horizontal and vertical advection terms that represent the current-related (wave-averaged) sand flux (i.e. the product of wave-averaged velocities and concentrations). Such a model, however, does not account for the wave-related suspended sediment transport, including that resulting from the non-closed trajectory of wave orbital motions in a wave cycle (Stokes drift) and that resulting from the lagging of particle reaction to the wave oscillation (phase lag). To take these into account, the wave-averaged Lagrangian mean velocity (i.e. the sum of Eulerian mean and Stokes velocities) should be used in the AD model (e.g. Uchiyama et al. [23]; Kumar et al. [25]). In addition, the phase lag effects should be considered in the model, particularly for the fine grains which are affected by such an effect more apparently.

The AD model requires a bottom boundary condition to describe the vertical sediment exchange between the suspension and the bedload layers. This boundary condition is generally given as semi-empirical formulations in forms of a reference concentration at an elevation above the bed (reference level), or a pick-up function that determines the upward sand flux brought from the bed into suspension. Such pick-up/reference concentration models are generally developed only for non-breaking waves in which the bed shear stress by waves and currents are used as the driving force for sediment sus-

pension (e.g. Nielsen [68]; van Rijn [69, 70, 57]). However, these formulations may not be applicable in wave breaking condition (Aagaard and Jensen [71]), as breaking waves, especially strongly plunging waves, may directly affect the near bed flow and turbulence that can entrain large amounts of sediment from the bed (Nielsen [2]). Several parameterizations are thus developed to account for the wave breaking turbulence effects in the pick-up/reference concentration models, some of which use the near-bed Turbulence Kinetic Energy (TKE) as an additional parameter to increase the bed shear stress and thus the sediment concentrations (e.g. Hsu and Liu [72]; Okayasu et al. [73]), while others using the local (breaking) wave parameters, such as the wave height at breaking (Jayaratne and Shibayama [74]) and the wave or roller energy dissipation (Kobayashi and Johnson [75]; Spielmann et al. [76]), to calculate the reference concentrations. Recently, van der Zanden [77] proposed a new method in which the near-bed TKE (include the breaking wave induced component) is the sole parameter used to calculate the reference concentration or sand pick-up rate. However, these formulations are not as thoroughly supported by experimental data and are not as widely applied as formulations based on horizontal bed shear.

Bedload Transport Models

Generally speaking, two kinds of predictive approaches, i.e. process-based numerical models and parameterised formulae, have been used for bed load transport predictions. The process-based numerical models explicitly include many of the detailed physical processes involved in the sediment transport by waves and currents, and resolve the vertical and sometimes also the horizontal structure of the time-dependent, intra-wave velocity and sand concentration fields (van der A et al. [78]). Such models therefore require large computational resources and are generally not implemented in practical coastal morphodynamic models. In contrast, the parameterised formulae only include a set of simple equations and require very little computational times, so can be easily implemented in coastal morphodynamic models (van Rijn et al. [12]).

In the coastal marine environment, three kinds of parameterised (practical) formulae, i.e. the formulae of time-averaged, quasi-steady and semi-unsteady, are developed for bed load transport predictions. Based on wave-averaged flow velocity and sand concentrations, the time-averaged formulae predict sand transport at a timescale that is much longer than the wave period. The total sand transport predicted by such formulae is always in the direction of the mean current which omits the wave-related sand transport contributions (van der A et al. [78]).

In most of the present morphodynamics model systems, quasi-steady formulae are commonly implemented, which calculate intra-wave sand transport with the assumption

that the instantaneous sand transport relates only to the instantaneous forcing parameter, e.g. the flow velocity or bed shear stress. The assumption of quasi-steadiness only holds for conditions for which the pick-up and settling of sand particles must take place in a much shorter time than the wave period. However, for fine sand sheet-flow conditions and ripple bed conditions, the phase-lag effect[1] can significantly affect the magnitude and even the direction of the net sediment transport rate; therefore the quasi-steadiness assumption is not correct in these conditions. In addition, most of the quasi-steady formulae do not account for sediment transport resulting from acceleration skewness, as occurs under sawtooth-shaped waves (van der A et al. [79]; Watanabe and Sato [80]).

To account for the phase lag effects, semi-unsteady formulae are thus proposed. In the past decade, a number of such models have been developed based on such an idea, e.g. for sheet-flow condition (Camenen and Larson [81]), rippled bed conditions (van der Werf et al. [82]) and for both sheet-flow and ripple conditions (Silva et al. [83]; van Rijn [56, 57, 84]). Experiments carried out in large wave flumes indicate that the progressive surface wave effects can be important in determining the net sand transport (van der A et al. [78]) due to the added complexities in the hydrodynamics of surface waves compared to tunnel flows, which however are not accounted for in most of the proposed semi-unsteady transport formulae. van der A et al. [78] present a new practical model for the net sand transport induced by non-breaking waves and currents (i.e. SANTOSS model). It not only includes phase-lag effects for rippled beds and fine sand, but also explicitly accounts for the progressive surface wave effects, as well as the effects of velocity skewness and acceleration skewness. Therefore the SANTOSS model is the best candidate to be implemented in the morphodynamic model system developed in this research.

1.4 Aims and Objectives

Based on the above discussions, the main aim of this research is to develop a new fully coupled, unstructured grid, three-dimensional coastal morphodynamic model system, with the most recent progresses in laboratory and theoretical study. This is achieved by accomplishing the following specific objectives (a more detailed description is displayed in Chapter 3):

1. Development of a new three-dimensional coastal hydrodynamic model system with fully coupled 3D wave-current interactions on an unstructured grid, which is used

[1] Sediments entrained from the bed during one half-cyle do not resettle to the bed before flow reversal, being still in the water column during the next half-cycle and transported in the opposite direction (van Rijn et al. [12])

as a basis for the morphodynamic model system developed in the present research.

2. Development of a new advection-diffusion (AD) suspended sediment transport module for the morphodynamic model system.

3. Development of a bedload transport module for the morphodynamic model system following the SANTOSS formulae.

4. Integration of the wave, circulation, suspended sediment and bedload transport modules into the the fully coupled, three-dimensional coastal morphodynamic model system.

5. Validation and application of the developed morphodynamic model system.

The other aim of this research is to improve the understanding of the hydrodynamics (waves and currents) and sediment transport processes involved in a cross-shore morphology evolution, by applying the developed morphodynamic model system into a recently conducted large-scale laboratory experiment (van der Zanden [5, 53, 55]). This target is assessed through the following research questions (RQs):

RQ1 How does wave breaking affect the undertow, turbulence, sediment transport and morphology evolutions?

RQ2 Which processes are important in determining the dynamics of local waves, fluid flow and sediment transport under the breaking waves?

RQ3 Which transport mode, e.g. bedload and the suspended load transport, has the decisive contribution to the cross-shore bar morphodynamics?

1.5 Outline

The outline of this thesis is presented as follows:

Chapter 1 (i.e. the present chapter) gives the context of the present research, briefly introduces the latest research progress of various processes involved in the coastal morphodynamics, and raises the questions and aims/objectives need to answered and accomplished in the present study.

Chapter 2 introduces the basic theories of the existed models (e.g. FVCOM circulation model, SWAN wave model, etc.) based on which the morphodynamic model system is developed in this research.

Chapter 3 describes the details on the development of the new fully coupled, unstructured grid, three-dimensional coastal morphodynamic model system, including the various adopted theories (e.g. wave-current interaction approach, turbulent , practical bedload transport formulae, etc.), the numerical implementation, coupling procedure and code parallelization.

Chapter 4 presents the validation of the model against several cases with different spatial scales and both 2D and 3D complex hydrodynamic conditions: (a) a theoretical case of obliquely incident waves on a planar beach; (b) a large-scale laboratory experiment involving normal incident wave breaks over a naturally formed breaker bar; (c) a real field experiment of obliquely incident waves on a natural, sandy, barred beach (Duck'94 experiment); and (d) a laboratory scale experiment of normally incident waves on plane beach with a shore-parallel breakwater.

Chapter 5 applies the developed morphodynamic model system into a recently conducted large-scale laboratory experiment (van der Zanden [5, 53, 55]) in which detailed measurements of the wave parameters, current and TKE profiles, suspended sediment concentration and bed profiles are conducted. The hydrodynamics (waves and currents) and sediment transport processes involved in the cross-shore morphology evolution are analysis in detail, along which several physical parameters are calibrated to obtain best model performances. Furthermore, the four questions raised above are investigated in detail.

Chapter 6 summarises the main conclusions and contributions of the overall research, addresses the limitations of the present study and highlights recommendations for future research.

Chapter 2

Modelling System – Part I: Existed Modules

2.1 Introduction

A coastal morphodynamic model is a complex system, including various sub-models to solve specific physical process, e.g. a wave model is used for predicting the wave parameters while a turbulent model describes the sub-scale turbulence. This is because the physical processes involved have very different spatial and temporal scales and are difficult to resolve at the same time by a single numerical model. Over the last few decades, a large number of numerical models, including coastal circulation models, wave propagation models, and sediment transport models have been developed for different purposes, with their own particular research or application area. Many of these well tested models provide a good platform to develop a new morphodynamic model system for understanding sediment suspension under breaking waves and the overall cross-shore sediment transport process.

In this chapter, the existing near shore wave propagation model SWAN and circulation model FVCOM are presented briefly. The further developments, based on the latest theories and techniques, on these models, and the details of numerical implementation, coupling procedure and code parallelization in order to integrate them into a new morphodynamic model system are described in the next chapter (i.e. Chapter 3).

2.2 Hydrodynamic Module

2.2.1 Wave Module

SWAN (Simulating WAves Nearshore) is a third-generation spectra surface wave model developed originally by Booij et al. [85] and improved over a number of years since then (The SWAN Team [86]). For given wind, bathymetry and current conditions, SWAN resolves the spectral and integral wave properties of random short-crested wind-generated waves by solving a spectral action balance equation, includes wave energy dissipation due to bottom friction, triad and quadruplet wave–wave interactions and shallow water wave-breaking, without any *a priori* restrictions on the spectrum for the evolution of wave growth. The wave action balance equation is represented as

$$\frac{\partial N\left(\sigma,\theta;x,y,t\right)}{\partial t}+\nabla_{\perp}\cdot\left[\left(\boldsymbol{C}_{g}+\boldsymbol{V}\right)N\left(\sigma,\theta;x,y,t\right)\right] + \frac{\partial\ c_{\theta}\ N\left(\sigma,\theta;x,y,t\right)}{\partial\theta}+\frac{\partial\ c_{\sigma}\ N\left(\sigma,\theta;x,y,t\right)}{\partial\sigma}=\ \frac{S_{tot}\left(\sigma,\theta;x,y,t\right)}{\sigma} \tag{2.1}$$

where $N(\sigma,\theta)$ is the action density spectrum, it is defined as $N=E/\sigma$; c_{θ} and c_{σ} are propagation velocities in spectral space (θ, σ);θ is wave propagation direction and σ is wave radian frequency; $\boldsymbol{C}_{g}=\partial\sigma/\partial\boldsymbol{k}$ is the group velocity, $\boldsymbol{k}$ is the wave number vector, $\boldsymbol{V}$ is the ambient water current vector, $S_{tot}\left(\sigma,\theta\right)$ is the source-sink term which could be represented as

$$S_{tot}=S_{in}+S_{nl3}+S_{nl4}+S_{ds,w}+S_{ds,b}+S_{ds,br} \tag{2.2}$$

where the first term denotes the wind energy input, the second and third terms represent the wave energy distribution through three-wave (triad) and four-wave (quadruplet) interactions, and the last three terms represent the wave energy dissipation caused by white-capping, bottom friction and depth-induced wave breaking.

In the SWAN model, the resonance mechanism of Phillips [87] and feed-back mechanism of Miles [88] are used to describe the wave energy transform from wind to waves. Two optional expressions for white-capping are formulated, including a commonly used pulse-based model (Hasselmann [89]) and a saturation-based model (Van der Westhuysen et al. [90]). In addition, several other alternative expressions are also proposed in the scientific community to improve the model perfomance, including alternative calibrations of the Komen [91] expression (e.g. Rogers et al [92]) and alternative ways of calculating mean spectral steepness (e.g. Van Vledder and Hurdle [93]). Several bottom

friction models are employed, including an empirically obtained constant suggested by Hasselmann et al. [94]; a nonlinear formulation proposed by Hasselmann and Collins [95]; and eddy viscosity models developed by Madsen et al. [96] and by Weber [97]. To model the energy dissipation in random waves due to depth-induced breaking, the bore-based model of Battjes and Janssen [98] is used in SWAN. In the following section, the formulations of bottom friction and depth-induced wave breaking are introduced in detail; while for further details of the parameterization of other terms, people can refer to Booij et al. [85] and The SWAN Team [86].

Bottom Friction

The surface-wave-induced orbital motions extend down to the sea floor in the shallow water, which can cause an interaction between the surface wave and the bottom. This wave-bottom interaction could be mainly divided into four kinds, i.e. scattering on bottom irregularities, percolation into a porous bottom, motion of a soft bottom and friction in the turbulent bottom boundary layer. For continental shelf seas with sandy bottoms, the bottom friction should be the dominant mechanism (Bertotti and Cavaleri [99]) which can generally be expressed as:

$$S_{ds,b} = -C_b \frac{\sigma^2}{g^2 \sinh^2 kD} E(\sigma, \theta) \tag{2.3}$$

in which C_b is a bottom friction coefficient that generally depends on the bottom orbital motion represented by U_{rms}:

$$U_{rms}^2 = \int_0^{2\pi} \int_0^{\infty} \frac{\sigma^2}{\sinh^2 kD} E(\sigma, \theta) d\sigma d\theta \tag{2.4}$$

Several bottom friction models are employed for the value of C_b :

1. An empirically obtained constant suggested by Hasselmann et al [94].

   $C_b = 0.038\ m^2 s^{-3}$ (Hasselmann et al [94]), which is in agreement with the JONSWAP results for swell dissipitation.

2. A nonlinear formulation proposed by Hasselmann and Collins [95] and later simplified by Collins [100].

   This is based on a conventional bottom friction formulation for periodic waves, the drag law, with appropriate parameters adapted to suit a random wave field, in which the bottom friction coefficient is $C_b = gC_{fw}U_{rms}$. C_{fw} is the Collins bottom friction coefficient with a default value of 0.015 (Collins [100]) .

3. Eddy viscosity models developed by Madsen et al. [96] and by Weber [97].

   It is expressed as $C_b = f_w g/\sqrt{2}U_{rms}$ in which f_w is a non-dimensional friction factor estimated by using the formulation of Madsen et al. [96], as a function of the bottom roughness height and the actual wave conditions:

$$\frac{1}{4\sqrt{f_w}} + \log_{10}\left(\frac{1}{4\sqrt{f_w}}\right) = -0.08 + \log_{10}\left(\frac{A_b}{k_N}\right) \tag{2.5}$$

   in which A_b is a representative near-bottom excursion amplitude represented with: $A_b^2 = 2\int_0^{2\pi}\int_0^{\infty}\frac{1}{\sinh^2 kD}E(\sigma,\theta)d\sigma d\theta$ and K_N is the bottom roughness length scale.

Depth-induced Wave Breaking

Eldeberky and Battjes [101] formulated a spectral version of the bore model of Battjes and Janssen [98] that conserves the spectral shape. In the SWAN model, their expression is expanded to include directions:

$$S_{ds,br}(\sigma,\theta) = \frac{D_{tot}}{E_{tot}}E(\sigma,\theta) = -\frac{\alpha_{BJ}Q_b\tilde{\sigma}}{\beta_w^2\pi}E(\sigma,\theta) \tag{2.6}$$

in which E_{tot} is the total wave energy and $D_{tot} < 0$ is the mean rate of energy dissipation of the total energy due to wave breaking :

$$D_{tot} = -\frac{1}{4}\alpha_{BJ}Q_b\left(\frac{\tilde{\sigma}}{2\pi}\right)H_{max}^2 = -\alpha_{BJ}Q_b\tilde{\sigma}\frac{H_{max}^2}{8\pi} \tag{2.7}$$

in which $\alpha_{BJ} = 1$ in SWAN and Q_b is the fraction of breaking waves, determined by:

$$\frac{1-Q_b}{\ln Q_b} = -8\frac{E_{tot}}{H_{max}^2} \tag{2.8}$$

in which H_{max} is the maximum wave height that can exist at the given depth and $\tilde{\sigma}$ iss a mean frequency defined as:

$$\tilde{\sigma} = E_{tot}^{-1}\int_0^{2\pi}\int_0^{\infty}\sigma E(\sigma,\theta)\ d\sigma d\theta \tag{2.9}$$

The fraction of depth-induced breakers (Q_b) is determined in SWAN with

$$Q_b = \begin{cases} 0 & ;\ \text{for } \beta_w \le 0.2 \\ Q_0 - \beta_w^2\frac{Q_0 - \frac{exp(Q_0-1)}{\beta_w^2}}{\beta_w^2 - \frac{exp(Q_0-1)}{\beta_w^2}} & ;\ \text{for } 0.2 < \beta_w < 1.0 \\ 1 & ;\ \text{for } \beta_w \ge 1.0 \end{cases} \tag{2.10}$$

where $\beta_w = H_{rms}/H_{max}$ and

$$Q_0 = \begin{cases} 0 & ; \text{ for} \beta_w \leq 0.5 \\ (2\beta_w - 1)^2 & ; \text{ for} 0.5 < \beta_w < 1.0 \end{cases} \tag{2.11}$$

The value of D_{tot} depends critically on the breaker parameter $\gamma = H_{max}/D$ (in which H_{max} is the maximum possible individual wave height in the local water depth). In SWAN, both a constant value and a variable value are available. The constant value, $\gamma = 0.73$, is used as the default value.

Discrete Approach

Initially, SWAN was developed on a structured grid system. A challenge for SWAN is to configure its curvilinear-structured grid to resolve realistic coastal geometry. Qi et al. [102] developed FVCOM-SWAVE surface wave model by converting the structured-grid SWAN wave model into an unstructured-grid finite-volume version under the FVCOM framework for applications in coastal ocean regions with complex irregular geometry. The implementation is made using the implicit Crank-Nicolson method in directional space, the Flux-Corrected Transport (FCT) algorithm in frequency space, and options of explicit or implicit second-order upwind finite-volume schemes in geographic space.

Following the discrete approach used in FE-WAVE (Hsu et al. [103]), Eq. (2.1) is split into four equations given as

$$\frac{N^{n+\frac{1}{4}} - N^n}{\Delta t} + \frac{\partial (c_\sigma N)}{\partial \sigma} = 0 \tag{2.12}$$

$$\frac{N^{n+\frac{2}{4}} - N^{n+\frac{1}{4}}}{\Delta t} + \frac{\partial (c_\theta N)}{\partial \theta} = 0 \tag{2.13}$$

$$\frac{N^{n+\frac{3}{4}} - N^{n+\frac{2}{4}}}{\Delta t} + \nabla_\perp \cdot [(\boldsymbol{C}_g + \boldsymbol{V})\, N] = 0 \tag{2.14}$$

$$\frac{N^{n+1} - N^{n+\frac{3}{4}}}{\Delta t} = \frac{S_{tot}}{\sigma} \tag{2.15}$$

where n denotes the nth time step, and Δt is the time interval for the numerical integration. Eqs. (2.12) and (2.13) describe the change of action density spectrum in spectral space, which are solved by the Flux Corrected Transport method (FCT) (Boris

and Book [104]; Hsu et al. [103]) and the Crank-Nicolson method (Crank and Nicolson [105]), respectively. Eq. (2.14) describes the propagation of the waves in geographic space. Two methods are provided in FVCOM to solve this equation, an explicit finite-volume upwind advection scheme or a semi-implicit finite-volume upwind advection scheme. Eq. (2.15) represents the growth, transfer and decay of the waves driven by the source terms. It is solved by a semi-implicit integration scheme as used in the WAM model (WAMDI Group [106]) and WAVEWATCH III model (Tolman [107]).

The detailed description of the used discrete algorithms are given in Qi et al. [102].

2.2.2 Circulation Module

In the present study, the prognostic, unstructured-grid, three-dimensional oceanic circulation model, Finite Volume Coastal Ocean Model (FVCOM; Chen et al. [108]) is used as the basis for the circulation module. It uses non-overlapped triangular grids in the horizontal to resolve the complex shoreline and geometry, and the generalized terrain-following Sigma coordinate in the vertical direction. The present version of FVCOM (version 4.0) includes both hydrostatic and non-hydrostatic schemes (Lai et al. [109, 110]) and wetting/drying treatment. The mode-split approach is used for the solution of the circulation model, in which currents are divided into external and internal modes and computed using an external and internal time step respectively (Chen et al. [108]).

In Cartesian coordinates, without taking snow and ice into consideration, the governing equations of FVCOM are:

$$\begin{aligned}
&\frac{\partial \boldsymbol{V}}{\partial t} + (\boldsymbol{V}\cdot\nabla_\perp)\,\boldsymbol{V} + w\frac{\partial \boldsymbol{V}}{\partial z} + f\hat{z}\times\boldsymbol{V} + \nabla_\perp\phi - \boldsymbol{F} - \frac{\partial}{\partial z}\left(K_m\frac{\partial \boldsymbol{V}}{\partial z} + \nu\frac{\partial \boldsymbol{V}}{\partial z}\right) \\
&= -\frac{\partial \boldsymbol{S}_x}{\partial x} - \frac{\partial \boldsymbol{S}_y}{\partial y} \\
&\frac{\partial \phi}{\partial x} + \frac{g\rho}{\rho_0} = 0 \\
&\nabla_\perp\cdot\boldsymbol{V} + \frac{\partial w}{\partial z} = 0 \\
&\frac{\partial C}{\partial t} + (\boldsymbol{V}\cdot\nabla_\perp)\,C + w\frac{\partial C}{\partial z} - \frac{\partial}{\partial z}(K_h\frac{\partial C}{\partial z}) - F_{_C} = C_{source}
\end{aligned} \tag{2.16}$$

In these equations the boldface typesets are used for horizontal vectors, while the

vertical components are represented by a normal typeset so that 3D vectors are designated by (**horizontal**, vertical). $(\boldsymbol{V}, w)$ is the Eulerian mean velocity; f is the Coriolis parameter; ϕ is the dynamic pressure (normalized by the density ρ_0); $\boldsymbol{F}$ represents the horizontal momentum diffusion term; K_m is the vertical eddy viscosity coefficient; ρ and ρ_0 are total and reference densities of sea water, respectively; g is the gravity acceleration; and ν_0 is the molecular diffusivity. C represents a tracer quantity (e.g. temperature, salinity); C_{source} are tracer source/sink terms; K_h is the thermal vertical eddy diffusion coefficient. $\boldsymbol{S}_x = (S_{xx},\ S_{xy})$, $\boldsymbol{S}_y = (S_{yx},\ S_{yy})$, represent the depth-dependent radiation stresses induced by surface waves. Within FVCOM, the used wave-current interaction theory is given by Mellor [1, 35, 38] and the radiation stress terms are computed as:.

$$
\begin{aligned}
\S_{xx} &= \frac{kE}{\rho_0}\left[\frac{k_x k_x}{k^2}F_{CS}F_{CC} - F_{SC}F_{SS}\right] + \frac{E_D}{\rho_0} \\
S_{yy} &= \frac{kE}{\rho_0}\left[\frac{k_y k_y}{k^2}F_{CS}F_{CC} - F_{SC}F_{SS}\right] + \frac{E_D}{\rho_0} \\
S_{xy} &= S_{yx} = \frac{kE}{\rho_0}\left[\frac{k_x k_y}{k^2}F_{CS}F_{CC}\right]
\end{aligned}
\tag{2.17}
$$

where k is the wave number, k_x and k_y are the wave number components in the x and y directions and E is the wave energy; the parameter F denotes the vertical distribution defined as:

$$
\begin{aligned}
F_{CS} &= \frac{coshkD(1+s)}{sinhkD} \\
F_{CC} &= \frac{coshkD(1+s)}{coshkD} \\
F_{SC} &= \frac{sinhkD(1+s)}{coshkD} \\
F_{SS} &= \frac{sinhkD(1+s)}{sinhkD} \\
E_D &= 0 \text{ if } z \neq \zeta \text{ and } \int_{-h}^{\zeta} E_D\, dz = E/2
\end{aligned}
\tag{2.18}
$$

in which h is the mean water depth, ζ is the sea surface elevation and $D = h + \zeta$ is the

total water column depth; s $=\frac{z-\zeta^c}{D}$ is the vertical Sigma coordinate, ranges from s $=-1$ at the bottom to s $=0$ at the free surface.

The surface and bottom boundary conditions for $(\boldsymbol{V}, w)$ are:

$$\begin{cases} K_m(\frac{\partial \boldsymbol{V}}{\partial z}) = \frac{1}{\rho_0}\boldsymbol{\tau}_{sur}, \text{ and } w = \frac{\partial \zeta}{\partial t} + \boldsymbol{V}\cdot\nabla_\perp\zeta + \frac{E_{va}-P_{re}}{\rho} & , \quad \text{when } z = \zeta(x,y,t) \\ K_m(\frac{\partial \boldsymbol{V}}{\partial z}) = \frac{1}{\rho_0}\boldsymbol{\tau}_{bot}, \text{ and } w = -\boldsymbol{V}\cdot\nabla_\perp h + \frac{G_b}{\Omega} & , \quad \text{when } z = -h(x,y) \end{cases} \tag{2.19}$$

where $\boldsymbol{\tau}_{sur}$ and $\boldsymbol{\tau}_{bot} = \rho_0 C_d|\boldsymbol{V}|\boldsymbol{V}$ are surface wind and bottom stresses, respectively; G_b is the groundwater volume flux at the bottom and Ω is the area of the groundwater source. The drag coefficient C_d is determined by matching a logarithmic bottom layer to the model at a height of z_r above the bottom:

$$C_d = max\left(\frac{\kappa^2}{ln^2\left(\frac{z_r}{z_0}\right)},\ 0.0025\right) \tag{2.20}$$

where $\kappa = 0.4$ is the von Karman constant, z_0 is the bottom roughness parameter, and z_r is a reference height above the bed, nominally equivalent to half the height of the first grid cell above the bed.

2.2.3 Turbulence Closure Model

The primitive equations described above are not mathematically closed unless horizontal and vertical diffusion for momentum, temperature and salinity are determined.

The Horizontal Diffusion Coefficients

In FVCOM, it is possible to choose between a constant value or the Smagorinsky eddy parameterization method (Smagorinsky [111]) for horizontal diffusion coefficient. The Smagorinsky horizontal diffusion for momentum is given as

$$A_m = \frac{1}{2}C_c\Omega^u\sqrt{\left(\frac{\partial u}{\partial x}\right)^2 + \frac{1}{2}\left(\frac{\partial v}{\partial x}+\frac{\partial u}{\partial y}\right)^2 + \left(\frac{\partial v}{\partial y}\right)^2} \tag{2.21}$$

where C_c is a constant parameter and Ω^u is the area of the individual momentum control element. The value of A_m varies with the model resolution and the gradient of horizontal velocities: decreasing as the grid size or horizontal velocity gradients are reduced.

A similar formula is also used for scalars, which is proportional to the area of the individual tracer control element and the horizontal gradient of the tracer concentration. For water temperature, for example, it is given as

$$A_h = \frac{1}{2}\frac{C_c \Omega^{\zeta}}{P_r}\sqrt{\left(\frac{\partial u}{\partial x}\right)^2 + \frac{1}{2}\left(\frac{\partial v}{\partial x} + \frac{\partial u}{\partial y}\right)^2 + \left(\frac{\partial v}{\partial y}\right)^2} \tag{2.22}$$

where Ω^{ζ} is the area of the individual tracer control element and P_r is the Prandtl number.

The Vertical Eddy Viscosity

For the parameterization of the vertical eddy viscosity (K_m), the most popular k-kl (where k is the turbulent kinetic energy and l is the turbulent macro length scale) turbulent model, Mellor and Yamada level 2.5 (MY-2.5) model [112], is included in the FVCOM. The MY-2.5 model in FVCOM is updated from its original form by a) the upper and lower bounds of the stability function proposed by Galperin et al. [113]; b) the wind-driven surface wave breaking-induced turbulent energy input at the surface and internal wave parameterization by Mellor and Blumberg [114]; and c) the improved parameterization of pressure-strain covariance and shear instability-induced mixing in the strongly stratified region by Kantha and Clayson [115, 116].

In the boundary layer approximation where the shear production of turbulent kinetic energy is produced by the vertical shear of the horizontal flow near the boundary, the equations for k and kl can be simplified as:

$$\begin{aligned}
&\frac{\partial \mathrm{k}}{\partial t} + \boldsymbol{V}\cdot\nabla_{\perp}\mathrm{k} + w\frac{\partial \mathrm{k}}{\partial z} = (P_s + P_b - \varepsilon) + \frac{\partial}{\partial z}(K_q\frac{\partial \mathrm{k}}{\partial z}) + F_q \\
&\frac{\partial \mathrm{k}l}{\partial t} + \boldsymbol{V}\cdot\nabla_{\perp}(\mathrm{k}l) + w\frac{\partial \mathrm{k}l}{\partial z} = \frac{1}{2}lE_1(P_s + P_b - \frac{\tilde{W}}{E_1}\varepsilon) + \frac{\partial}{\partial z}(K_q\frac{\partial \mathrm{k}l}{\partial z}) + F_l
\end{aligned} \tag{2.23}$$

where $\mathrm{k} = 1/2\left(u'^2 + v'^2\right)$ is the turbulent kinetic energy; l is the macroscale; K_q is the vertical eddy diffusion coefficient of the turbulent kinetic energy; F_q and F_l represent the horizontal diffusion of the turbulent kinetic energy and marcroscale; $P_s = K_m\left[(\partial u/\partial z)^2 + (\partial v/\partial z)^2\right]$ and $P_b = gK_h(\partial\rho/\partial z)/\rho_0$ are the shear and buoyancy production terms of turbulent kinetic energy; $\varepsilon = 2\mathrm{k}\sqrt{2\mathrm{k}}/B_1 l$ is the turbulent kinetic energy dissipation rate; $\tilde{W} = 1 + E_2 l^2/(\kappa L)^2$ is a wall proximity function where $L^{-1} = (\zeta - z)^{-1} + (h + z)^{-1}$; $\kappa = 0.4$ is the von Karman constant; h is the mean water

depth; and ζ is the free surface elevation. In FVCOM, F_q and F_l are parameterized using the Smagorinsky eddy parameterization method shown above (Smagorinsky [111]). However, the turbulent closure model can be run with both F_q and F_l set to zero (or a small constant value).

The turbulent kinetic energy and macroscale equations are closed by defining:

$$K_m = \sqrt{2\mathrm{k}}\, lS_m, \quad K_h = \sqrt{2\mathrm{k}}\, lS_h, \quad K_q = \frac{\sqrt{2\mathrm{k}}}{5} l \tag{2.24}$$

in which S_m and S_h are defined as the stability functions:

$$S_m = \frac{0.4275 - 3.354G_h}{(1 - 34.676G_h)(1 - 6.127G_h)} \text{ and } S_h = \frac{0.494}{1 - 34.676G_h} \tag{2.25}$$

where $G_h = \frac{l^2 g}{2\mathrm{k}\rho_0}\rho_z$. In the original MY-2.5 turbulent closure model (Mellor and Yamada [112, 117]), S_m and S_h are functions of the gradient Richardson number. By removing a slight inconsistency in the scaling analysis, Galperin et al. [113] simplified the MY-2.5 turbulent closure model so that S_m and S_h depend only on G_h. G_h has an upper bound of 0.023 for the case of unstable ($\partial\rho/\partial z > 0$) stratification and a lower bound of -0.28 for the case of stable ($\partial\rho/\partial z < 0$) stratification. Parameters A_1, A_2, B_1, B_2, and C_1 are given as 0.92, 16.6, 0.74, 10.1, and 0.08, respectively.

In the original MY-2.5 model, the surface and bottom boundary conditions for the turbulent kinetic energy and macroscale equations are given as:

$$\begin{cases} \mathrm{k}l = 0, \quad 2\mathrm{k} = B_1^{\frac{2}{3}} u_{\tau s}^2, & z = \zeta(x, y, t) \\ \\ \mathrm{k}l = 0, \quad 2\mathrm{k} = B_1^{\frac{2}{3}} u_{\tau b}^2, & z = -h(x, y) \end{cases} \tag{2.26}$$

where $u_{\tau s}$ and $u_{\tau b}$ are the water friction velocities associated with the surface and bottom. Since $\mathrm{k} \neq 0$ at the surface and bottom, $l = 0$ at both boundaries, which means K_m, K_h and K_q are always 0 at the surface and bottom. This simplification is reasonable for the bottom but ignores the turbulent energy flux due to surface waves during windy conditions.

Mellor and Blumberg [114] introduced a new turbulent kinetic flux surface boundary condition into the MY-2.5 model, in which

$$\frac{\partial \mathrm{k}}{\partial z} = \frac{\alpha_{CB}\, u_{\tau s}^3}{K_q}, \text{ and } l = max(kz_{0s},\ l_z); \text{ at } z = \zeta(x, y, t) \tag{2.27}$$

where α_{CB} is a parameter related to the wave age; l_z is the "conventional" empirical length scale; $\kappa = 0.4$ is the von Karman constant and z_{0s} is the wave-related roughness height. According to the best fit to available observational data (Terray et al. [118]), α_{CB} can be approximated by

$$\alpha_{CB} = 15\frac{c_p}{u_{*air}} \exp\left[-\left(\frac{0.04c_p}{u_{*air}}\right)^4\right] \tag{2.28}$$

where c_p is the phase speed of wave at the dominant frequency, u_{*air} is the air friction velocity ($u_{*air} = 30u_{\tau s}$), and c_p/u_{*air} is the "wave age". The value of α_{CB} changes significantly with the wave age:

$$\alpha_{CB} \cong \begin{cases} 0 & ; \text{ for} c_p/u_{*air} = 0 \text{ no waves: original MY-2.5 model} \\ 146 & ; \text{ for} c_p/u_{*air} = 10 \text{ younger waves} \\ 57 & ; \text{ for} c_p/u_{*air} = 30 \text{ mature waves} \end{cases} \tag{2.29}$$

In general, l_z is proportional to z, which can be approximately estimated by

$$l_z = \kappa z \tag{2.30}$$

Based on available observational data (Terray et al. [119]; Mellor and Blumberg [114]), z_{0s} can be determined by

$$z_{0s} = 0.85H_s \tag{2.31}$$

where H_s is the significant wave height. As suggested by Smith et al. [120], H_s can be estimated based on the wave age and air side roughness parameter (z_{air}) in a form of

$$H_s = 2.0\left(\frac{c_p}{u_{*air}}\right)^{2.5} z_{air} \tag{2.32}$$

Specifying $z_{air} = \alpha_{CH}\ u_{*air}/g$, $\alpha_{CH} = 0.45u_{*air}/c_p$ and $u_{*air}^2 = (\rho_w/\rho_a)u_{\tau s}^2$, z_{0s} can be rewritten as

$$z_{0s} = \beta_{zw}\frac{u_\tau^2}{g}; \qquad \beta_{zw} = 665\left(\frac{c_p}{u_{*air}}\right)^{1.5} \tag{2.33}$$

According to observational data, $\beta_{zw} = 2.0 \times 10^5$

2.3 Sediment Module

The sediment transport model in FVCOM is based on the Community Model for Coastal Sediment Transport (CMCST) developed by the USGS and other researchers[1], which includes suspended sediment and bedload transport, bed evolution based on the active layer concept, flux-limited solution of sediment settling, unlimited number of sediment classes and bed layers and cohesive sediment erosion/deposition algorithms.

Based on Warner et al. [47], the same scheme as that in the structured-grid Regional Ocean Modeling System (ROMS) is adopted and converted into unstructured-grid code in FVCOM by using mass conservative finite-volume approach.

2.3.1 Suspended Sediment Transport Module

The suspended sediment transport model is based on an advection-diffusion equation to compute the suspended sediment concentration (Warner et al. [47]):

$$\frac{\partial C^i}{\partial t} + (\boldsymbol{V} \cdot \nabla_\perp) C^i + w\frac{\partial C^i}{\partial z} - \frac{\partial}{\partial z}(K_h \frac{\partial C^i}{\partial z}) - F_{C^i} = C^i_{source} \tag{2.34}$$

where i is an index for the ith sediment class; C^i is the concentration of the $i-th$ sediment class; K_h is the vertical eddy viscosity; F_{C^i} represents the horizontal diffusion of the sediment concentration; C^i_{source} is the source/sink term (for the ith sediment class), which contains the process of vertical settling and sediment exchange with the bed, given as:

$$C^i_{source} = -\frac{\partial w^i_s C_i}{\partial z} + E^i_s \tag{2.35}$$

where w^i_s is the vertical settling velocity (positive upwards) of the ith sediment class. E^i_s is the erosion source, parameterized following Ariathurai and Arulanandan [121] as

$$E^i_s = E^i_0(1 - P_{bs})F^i_{bs}\left(\frac{\tau_{sf}}{\tau^i_{ce}} - 1\right), \quad \text{when } \tau_{sf} > \tau^i_{ce} \tag{2.36}$$

where E^i_s is the surface erosion mass flux ($kg\ m^{-2}s^{-1}$), E^i_0 is a bed erodibility constant ($kg\ m^{-2}s^{-1}$), P_{bs} is the porosity (volume of voids/total volume) of the top bed layer, F^i_{bs} is the fraction of the ith sediment in the bottom. τ_{sf} is the bottom shear stress, and τ^i_{ce} is the critical shear stress for erosion of the ith sediment. The erosional flux for each sediment class is limited by the availability of that class in the top layer of the bed

[1] http://woodshole.er.usgs.gov/project-pages/sediment-transport/

model. The source or sink term in the equation represents the net downward settling and upward flux of eroded material.

Zero-flux boundary conditions for the sediment concentration are imposed at both the surface and bottom in the vertical diffusion equation:

$$\begin{cases} K_h \frac{\partial C_i}{\partial z} = 0 \quad , \text{ when } z = \zeta \\ \\ K_h \frac{\partial C_i}{\partial z} = 0 \quad , \text{ when } z = -h \end{cases} \tag{2.37}$$

Sediment is scoured when the local bottom shear stress exceeds a critical value and the material is removed at a rate defined by the user. The resulting concentration profile is dependent on a balance between advection, and vertical diffusion process in the water column, as well as the entrainment and settling close to the bed surface. A constant, user-defined sink rate w_s^i is used to model settling for each sediment type. The settling term (i.e. the first term in r.h.s of Eq.(2.35)) must be carefully calculated due to the sharp gradients in the concentration profile near the bottom. In FVCOM, a piecewise parabolic method (Colella and Woodward [122]) and a weighted essentially non-oscillatory (WENO) scheme (Liu et al. [123]) are used for the settling equation. This method integrates depositional flux over multiple grid cells, so it is not constrained by the CFL criterion.

2.3.2 Bedload Module

Similar to that in ROMS, two methods for computing bedload transport are implemented in FVCOM: (1) Meyer-Peter and M*ü*eller [9] formulation for unidirectional flow and (2) the formulae of Soulsby and Damgaard [124] that account for combined effects of currents and waves. Depending on the characteristics of individual sediment classes, including size D_{50}, density ρ_s , specific density in water s $(= \rho_s/\rho)$, these two formulae firstly calculate the non-dimensional transport rates Φ for each sediment class and then convert it into dimensional bedload transport rates q_{bl} as

$$q_{bl} = \Phi \sqrt{(s-1) g D_{50}^3} \rho_s \tag{2.38}$$

Only the first method is described here; for a detailed introduction of the second method, one can refer to Warner et al. [47]. The formulation of Meyer-Peter and Mueller [9] is

$$\Phi = max \left[8 \left(\theta_{sf} - \theta_c \right)^{1.5} , \quad 0 \right] \tag{2.39}$$

where Φ is the magnitude of the non-dimensional transport rate for each sediment class, θ_{sf} is the non-dimensional Shields parameter for skin stress

$$\theta_{sf} = \frac{\tau_{sf}}{\rho(s-1)gD_{50}} \tag{2.40}$$

$\theta_c = 0.047$ is the critical Shields parameter, and τ_{sf} is the magnitude of total skin-friction component of bottom stress computed from

$$\tau_{sf} = \sqrt{\tau_{bx}^2 + \tau_{by}^2} \tag{2.41}$$

where τ_{bx} and τ_{by} are the skin-friction components of bed stress, from currents alone or the maximum wave-current combined stress, in the x and y directions. The bedload transport vectors are partitioned into x and y components based on the magnitude of the bed shear stress as

$$q_{blx} = q_{bl}\frac{\tau_{bx}}{\tau_{sf}}, \qquad q_{bly} = q_{bl}\frac{\tau_{by}}{\tau_{sf}} \tag{2.42}$$

2.4 Bottom Boundary Layer Module

The bottom boundary layer (BBL) is intuitively defined as the layer inside which the flow is significantly influenced by the bed. The velocity, Reynolds stresses, production and dissipation of turbulent kinetic energy, and suspended-sediment concentrations can vary rapidly over very short vertical distances inside the BBL. However, in regional circulation models (e.g. FVCOM, ROMS) these processes cannot be resolved due to the limitation in vertical grid spacing used. Therefore, parameterization algorithms are utilized to represent some of these subgrid-scale processes inside the BBL. In particular, the parameterization of the BBL is very important in terms of two aspects:

- It determines the shear stress exerted on the flow by the bed (hereinafter τ_t). In a circulation model, τ_t is used in bottom boundary conditions for Reynolds-averaged momentum equations;
- It calculates the bottom stress used in the sediment-transport formulations (hereinafter τ_{sed}). τ_{sed} is used to calculate the bedload transport and reference concentration or pick-up rate for sediment in suspension.

It should be noted that the above two bottom stresses (τ_t and τ_{sed} are generally different, i.e. τ_t is the total bed shear stress that corresponds to the overall resistance of the flow

(Soulsby [125]), while τ_{sed} is the part of τ_t that only results from the skin friction (grain-related contribution).

In the absent of surface waves, a simple drag-coefficient expression (Eq. (2.20)) is implemented in FVCOM by assuming a logarithmic velocity profile near the bed. However, in the presence of surface waves and/or mobile sediment, more complex algorithms are needed to simulate BBL processes:

- Surface progressive waves induce short oscillatory motions in the wave BBL, which could produce extra turbulence and generate large instantaneous shear stresses compared to that due to current alone. Wave induced turbulence enhances momentum transfer, thus effectively increasing the coupling between the flow and the bottom and increasing the frictional drag exerted on the mean flow.
- The large instantaneous shear stresses often dominate sediment resuspension and enhance bedload transport.
- Sediment transport can produce ripples and other bedforms, which increase the bottom roughness height and enhances the stress exerted on the flow.
- Bedload transport can also induce extra drag on the flow and damp the turbulence when the local concentration level is high enough.

In order to represent the complex interactions of wave and currents in the BBL, Warner et al. [47] implements three different wave-current BBL models (i.e. *sg_bbl*, *mb_bbl* and *ssw_bbl*), coupled with the calculations of bottom roughness, into the ROMS model. Similar formulations are also adopted and modified in FVCOM to be consistent with the unstructured grid framework, which are also used in the present research.

In this section, only the procedure in *ssw_bbl* that was used for the bottom-boundary layer calculations is briefly described. For a detailed description on this and the other two methods, one can refer to Warner et al. [47] and also the ROMS and FVCOM codes.

(1) The input variables required for the parameterization of BBL

- velocities u and v at reference elevation z_r; representative wave-orbital velocity amplitude u_b, wave period T_w, and wave-propagation direction θ (degrees, in nautical convention).

  These wave parameters should represent the full spectrum of motion near the bed, which could either be obtained from a wave model (e.g. SWAN) or simpler calculations based on a particular wave theory.

- bottom sediment characteristics (median grain diameter D_{50}, mean sediment density ρ_s and representative settling velocity w_s).

  These are based on the composition of the uppermost active layer of the bed sediment during the previous time step (Warner et al. [47]).

(2) Calculate the Ripple height η_r and wavelength λ_r

Using information from the previous time step and the Malarkey and Davies [126] implementation of the Wiberg and Harris [127] formulation, which is valid for wave-dominated conditions, the ripple wavelength is approximated as $535D_{50}$ and ripple steepness is given as

$$\frac{\eta_r}{\lambda_r} = \exp\left\{-0.095\left[ln\left(\frac{d_0}{\eta_r}\right)\right]^2 + 0.442\left[ln\left(\frac{d_0}{\eta_r}\right)\right] - 2.28\right\} \tag{2.43}$$

where $d_0 = u_b T^w_{orb}/\pi$ is the wave-orbital diameter. When transport stage is below the threshold for sediment transport ($T_* = \tau_{wc}/\tau_{ce} < 1$), ripple dimensions from the previous time step are retained.

(3) Calculate the bottom roughness height: $z_0 = max[z_{0N} + z_{0ST} + z_{0BF},\ z_{0MIN}]$

z_{0N}, z_{0ST} and z_{0BF} are roughness lengths associated with grain roughness, sediment transport and bedform respectively. They are estimated as:

$$z_{0N} = 2.5D_{50}/30 \tag{2.44}$$

$$z_{0ST} = \alpha D_{50} a_1 \frac{T_*}{1 + a_2 T_*} \tag{2.45}$$

$$z_{0BF} = a_r \eta_r^2/\lambda_r \tag{2.46}$$

where $a_1 = 0.068$, $a_2 = 0.0204\ln(100D_{50}^2) + 0.0709\ln(100D_{50})$ and $\alpha = 0.056$ (Wiberg and Rubin [128]) are the sediment-transport coefficients; D_{50} is the median grain diameter (expressed in meters); a_r is a coefficient that may range from 0.3 to 3 (Soulsby [125]). Grant and Madsen [129] proposed $a_r = 27.7/30$, however Nielsen [130] suggested $a_r = 0.267$ which is used as the default value. z_{0MIN} allows setting a lower limit on bottom drag (default $z_{0MIN} = 5e^{-5}m$).

(4) Initial estimates of (kinematic) bottom stresses

For pure currents τ_c ($= \tau_b$), and pure waves τ_w ($\tau_b = 0$), it is assumed

$$\tau_c = \rho \frac{\left(u^2 + v^2\right) \kappa^2}{ln^2(z_r/z_0)} \tag{2.47}$$

and $\tau_w = \frac{1}{2}\rho f_w u_b^2$, where f_w is the Madsen [131] wave-friction factor, which depends on the ratio of the wave-orbital excursion amplitude to the bottom roughness length A_b/k_N, where $A_b = u_b T_{orb}^w/(2\pi)$ and $k_N = 30 z_0$:

$$f_w = \begin{cases} 0.3 & , A_b/k_N \leq 0.2 \\ \exp\left(-8.82 + 7.02(A_b/k_N)^{-0.078}\right) & , 0.2 < A_b/k_N \leq 100 \\ \exp\left(-7.30 + 5.61(A_b/k_N)^{-0.109}\right) & , 100 < A_b/k_N \end{cases} \tag{2.48}$$

(5) The pure currents and pure wave limits are used as initial estimates for calculations towards consistent profiles for eddy viscosity and velocity between z_0 and z_r, using either the model of Madsen [131] or Styles and Glenn [132]. Both of these models assume eddy viscosity profiles scaled by $u_{*wc} = \sqrt{\tau_{wc}/\rho}$ in the wave-boundary layer (WBL) and $u_{*c} = \sqrt{\tau_b/\rho}$ in the current boundary layer, calculated as

$$K_m = \begin{cases} \kappa u_{*cw} z, & z < \delta_{wbl} \\ \kappa u_{*c} z, & z > \delta_{wbl} \end{cases} \tag{2.49}$$

where δ_{wbl} is the thickness of the WBL, which scales as $u_{*cw} T_{orb}^w/(2\pi)$. τ_{wc} represents the maximum vector sum of wave- and current-induced stress, but the τ_b is influenced by the elevated eddy viscosity in the WBL, and must be determined through an iterative process. The shape and elevation of the transition between these profiles and other details differ among the two models, but both the models of Madsen [131] or Styles and Glenn [132] return values for the horizontal vectors τ_b, τ_w, and τ_{wc}. The parameter τ_b is the mean (over many wave periods) stress used as the bottom-boundary condition in the momentum equations, and $\tau_{wc}$is the maximum instantaneous stress exerted over the bottom by representative waves and currents.

(6) When ripples are present, τ_{wc} is a combination of form drag, which does not directly contribute to sediment transport, and skin friction, which does. The next step in the BBL calculations is to estimate the skin-friction component of τ_{wc} using the ripple dimensions and a bedform drag-coefficient approach (Wiberg and Nelson [133]), as follows.

$$\tau_{sfm} = \tau_{wc} \left[1 + 0.5 C_{dBF} \frac{\eta_r}{\lambda_r \kappa^2} \left(ln \frac{\eta_r}{z_{0N} + z_{0ST}} - 1 \right)^2 \right]^{-1} \tag{2.50}$$

where $C_{dBF} \approx 0.5$ is a bedform drag coefficient for unseparated flow.

(7) Finally, because shear stress varies between ripple crests and troughs, an estimate of the maximum shear stress at the crests τ_{sfm} is calculated for use in sediment-transport algorithms as

$$\tau_{sf} = \tau_{sfm}\left(1 + 8\frac{\eta_r}{\lambda_r}\right) \tag{2.51}$$

In summary, the more advanced BBL routines calculate current and wave-boundary layer bottom stresses under the combined influence of wave, currents, and mobile sediments. These stresses directly influence flow near the bottom and act as agents for sediment resuspension and bedload transport.

2.5 Discretisation

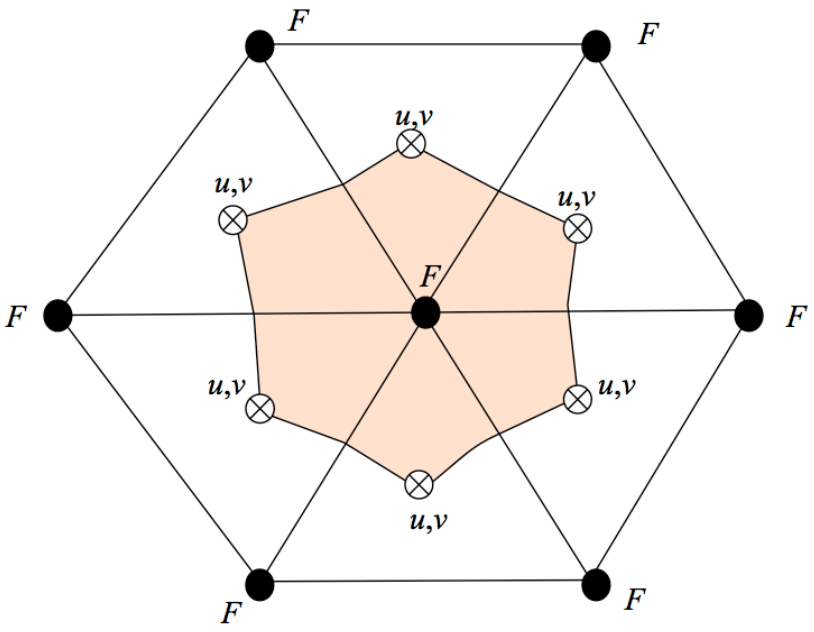

Figure 2.1: Illustration of the FVCOM unstructured triangular grid. Variable locations: Node •: h, D, ω, S, T, ρ, K_m, K_h, A_m and A_h; Centroid ⊗: u, v. F represents all tracer variables.

In FVCOM, the computational domain is subdivided into a set of non-overlapping unstructured triangular cells in the horizontal direction, which is particularly suitable for resolving the complex coastal geometries. As shown in Figure 2.1, an unstructured triangle is comprised of three nodes, a centroid, and three sides in FVCOM. To provide a more accurate estimation of the sea-surface elevation, currents and salt and temperature fluxes, u and v are placed at centroids and all scalar variables, such as ζ, h, D, ω, S,

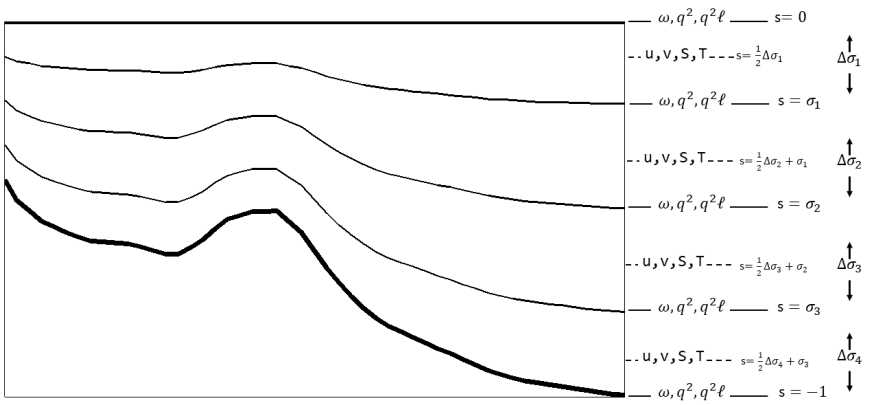

Figure 2.2: The location of the model variables in the vertical Sigma coordinate.

T, ρ, K_m, K_h, A_m and A_h, are placed at nodes. Scalar variables at each node are determined by a net flux through the sections linked to centroids and the mid-point of the adjacent sides in the surrounding triangles (called the "tracer control element" or TCE, shaded area in Figure 2.1), while u and v at the centroids are calculated based on a net flux through the three sides of that triangle (called the "momentum control element" or MCE).

Similar to finite-difference models such as POM and ROMS, all the model variables except ω (vertical velocity on the Sigma-layer surface) and turbulence quantities (such as k and kl) are placed at the mid-level of each Sigma layer (Figure 2.2). There are no restrictions on the thickness of the Sigma layer, which allows users to use either uniform or non-uniform Sigma layers.

2.6 Summary

This chapter introduces several existing models which will be used as the basis to build the morphodynamic model system shown in Chapter 3.

The nearshore spectral wave model SWAN is briefly described as the basis for the simulation of wave dynamics in the new morphological model system. The necessary wave processes, such as shoaling, bed friction, wave-wave interactions and wave-current interaction, and more importantly wave breaking are included in SWAN's solution through a conservation of energy density equation.

A 3D, unstructured-grid, finite-volume coastal ocean circulation model, FVCOM, is used as the hydrodynamic module and the basic framework (i.e. all other sub-models are modified to be consistent with the program framework of FVCOM; see details in

Chapter 3) of the morphodynamic model system. It uses non-overlapped triangular grids in the horizontal to resolve the complex shoreline and geometry, and the generalized terrain-following Sigma coordinate in the vertical direction.

The horizontal diffusion coefficient can be set as a constant value or be calculated by the Smagorinsky eddy parameterization method (Smagorinsky [111]); while the parameterization of the vertical eddy viscosity (K_m) and vertical thermal diffusion coefficient (K_h) is via a popular k-kl (where k is the turbulent kinetic energy and l is the turbulent macroscale) turbulent closure model, the MY-2.5 model (Mellor and Yamada [112, 117]; Galperin et al. [113]; Mellor and Blumberg [114]).

The sediment transport model in FVCOM is based on the Community Model for Coastal Sediment Transport (CMCST), which includes suspended and bedload transport, layered bed dynamics based on the active layer concept and flux-limited solution of sediment setting. The advection and transport of sediment follows similar approach as Warner et al. [47] for the CMCST in the Regional Ocean Modeling System (ROMS).

Chapter 3

Modelling System – Part II: Model Development

3.1 Introduction

The previous chapter briefly introduces the existing spectral wave model SWAN and the coastal ocean model FVCOM, which are used as the basis of the newly developed morphodynamic model system in this research.

This chapter describes the details on the development of the new fully coupled, un-structured grid, three-dimensional coastal morphodynamic model system. The un-structured version of SWAN is adopted to couple with the current model as described in Section 3.2. Details of various adopted theories into FVCOM, e.g. wave-current interaction approach, turbulent closure model, new treatment of suspended load transport and a new practical bedload transport formulae, are introduced, which are not available in the existing FVCOM system before. The special treatment of numerical implementation, coupling procedure and code parallelization are also presented.

The wave model, wave roller model, circulation model and turbulent closure model contained in this hydrodynamic model system are described in Section 3.2.1 - 3.2.3 respectively. Section 3.3 shows the detailed calculation procedure of the improved *mb_bbl* BBL module. The suspended sediment transport module is modified from the original implemented CMCST and is described in Section 3.4. A new semi-unsteady bedload transport model SANTOSS is described in detailed in Section 3.5 and implemented into the morphodynamic system. The final morphology evolution is solved by the sediment continuity (Exner) equation displayed in Section 3.6. Details of the coupling procedure between various models and the corresponding parallelization method are described in Section 3.7. The conclusions are drawn in Section 3.8.

3.2 Hydrodynamic Module

3.2.1 Wave Module

As introduced in the previous chapter, the widely-used third generation SWAN (Booij et al. [85]) spectral wave model is adapted to provide the predictions for the wave characteristics. To be consistent with FVCOM, the unstructured version of the SWAN model (hereinafter refer as UnSWAN) developed by Zijlema [6] is employed. This is due to the fact that UnSWAN is able to compute the wave propagation, breaking and dissipation processes on the same unstructured triangular mesh as in FVCOM, which minimises the necessary data interpolation and hence improves the model's efficiency and accuracy considerably. For example, the solution of the wave energy density function, wave height and dominant period can be found at each vortex of a triangle element, so they can be used by FVCOM straightforwardly.

It should be noted that the FVCOM-SWAVE model developed by Qi et al. [102] includes a wave model SWAVE that can couple with FVCOM directly. However, practical experience in using FVCOM-SWAVE suggests that for the same simulation, the required computing effort to run SWAVE is significantly larger than that for the original SWAN, in addition to the uncertainties in the model's accuracy. Though two alternative numerical schemes are provided in SWAVE, e.g. an explicit approach and an implicit approach, to solve the term of action density propagation in the geographic space, it is found that both schemes are very time-consuming: the explicit scheme only permits a much smaller time step than that in SWAN, and the implicit scheme requires solving very large linear equations which also needs much more CPU time. In addition, many important wave dynamic processes, e.g. wave refraction-diffraction, are still not included in FVCOM-SWAVE, which apparently limit its implementation in coastal areas. Therefore, the UnSWAN is the preferred wave model to couple with FVCOM in this research.

The details of the theory involved in UnSWAN has been presented in previous chapter. The following sections focus on the numerical implementation of UnSWAN and the coupling between UnSWAN and FVCOM.

Unstructured SWAN Model (UnSWAN)

The solution techniques of UnSWAN are tailored from that used in the structured SWAN, namely the four-direction Gauss-Seidel iteration technique and implicit temporal discretization. As these numerical propagation schemes have been proven to be able to provide a stable solution for structured SWAN model for any given time step, a

good performance is also be expected on the UnSWAN. In this research, much effort is therefore made to incorporate the UnSWAN model into FVCOM, with all of the original numerical propagation schemes of UnSWAN retained.

Numerical techniques For the sake of completeness, the numerical methods and techniques used in UnSWAN are described in brief here; more detailed and comprehensive discussion could be found in Zijlema [6].

Firstly, using the term $F(\boldsymbol{X};\sigma,\theta)$ to represent all the terms except the time derivative and propagation terms in the geographical space of Eq.(2.1), the wave action balance equation would become:

$$\frac{\partial N\left(\sigma,\theta;x,y,t\right)}{\partial t}+\nabla_{\perp}\cdot\left[\boldsymbol{C}_{t}N\left(\sigma,\theta;x,y,t\right)\right]=F \tag{3.1}$$

where $\boldsymbol{C}_t=\boldsymbol{C}_g+\boldsymbol{V}$ is the geographic velocity vector.

A vertex-based scheme is utilized to solve Eq. (3.1), in which the wave action N is stored and updated at the vertices. As with the structured version, the UnSWAN model also uses the first order implicit Euler scheme for the time integration (Eq. (3.2)), so that large time steps can be used without violating the stability restriction imposed by the CFL condition as in an explicit method, e.g. the explicit scheme of FVCOM-SWAVE model. In general, its time step is limited only by the desired temporal accuracy.

$$\frac{N^{n}-N^{n-1}}{\Delta t}+\nabla_{\perp}\cdot\left[\boldsymbol{C}_{t}N^{n}\left(\sigma,\theta;x,y,t\right)\right]=F^{n} \tag{3.2}$$

For the term of action density propagation in the geographic space, a point-by-point multi-directional Gauss-Seidel iteration technique is employed. As this scheme could make use of the newly acquired vertex values during an iteration, it has a very unique characteristic, i.e. it is locally implicit but globally explicit. This means that such a procedure could circumvent the need to build or store large matrices, which is common in other models using implicit integration schemes such as FVCOM-SWAVE, and still remain stable at any given time step size. By applying this numerical procedure, UnSWAN is able to converge to steady state much more rapidly than explicit schemes but at the same time without demanding too much computational efforts.

As an example of describing this Gauss-Seidel iteration technique, the update process of the vertex 1 in the triangle $\triangle 123$ of Figure 3.1 is described in detail here. This involves looping over each cell of this vertex.

Firstly, applying a mapping transformation $\boldsymbol{X}(\boldsymbol{\xi})$ from a local coordinate system

$\boldsymbol{\xi} = (\xi, \eta)$ to the Cartesian system $\boldsymbol{X} = (x, y)$, the following base vectors could be obtained, which are tangential to the coordinate lines ξ and η:

$$\boldsymbol{e}_{(1)} = \frac{\partial \boldsymbol{X}}{\partial \xi} \qquad \text{and} \qquad \boldsymbol{e}_{(2)} = \frac{\partial \boldsymbol{X}}{\partial \eta} \tag{3.3}$$

The vectors normal to the coordinate surface of constant ξ and η are:

$$\boldsymbol{e}^{(1)} = \nabla \xi \qquad \text{and} \qquad \boldsymbol{e}^{(2)} = \nabla \eta \tag{3.4}$$

Moreover, these two vectors are reciprocal to the base vectors, i.e.

$$\boldsymbol{e}^{(\alpha)} \cdot \boldsymbol{e}_{(\beta)} = \delta^{\beta}_{\alpha}, \quad \alpha, \beta = [1, 2], \tag{3.5}$$

where δ^{β}_{α} is Kronecker delta (which is unity if $\alpha = \beta$, and zero otherwise). Using Cramer's rule, the following equations are obtained:

$$\boldsymbol{e}^{(1)} = \frac{1}{|D|} \left(e^2_{(2)}, \ -e^1_{(2)} \right)^{\mathrm{T}} \qquad \text{and} \qquad \boldsymbol{e}^{(2)} = \frac{1}{|D|} \left(e^2_{(1)}, \ -e^1_{(1)} \right)^{\mathrm{T}} \tag{3.6}$$

in which $|D| = e^2_{(2)} e^1_{(1)} - e^2_{(1)} e^1_{(2)}$.

Secondly, expanding the propagation term in Eq. (3.2) and using the chain rule, one could obtain:

$$\nabla_{\perp} \cdot [\boldsymbol{C}_t \ N \ ] = \frac{\partial C_x N}{\partial x} + \frac{\partial C_y N}{\partial y} = e^{(1)}_1 \frac{\partial C_x N}{\partial \xi} + e^{(2)}_1 \frac{\partial C_x N}{\partial \eta} + e^{(1)}_2 \frac{\partial C_y N}{\partial \xi} + e^{(2)}_2 \frac{\partial C_y N}{\partial \eta} \tag{3.7}$$

Then using the one-sided first order difference scheme to discrete the Eq. (3.7):

$$\frac{\partial C_x N}{\partial \xi} \approx \frac{C_x N_1 - C_x N_2}{\Delta \xi} \qquad \text{and} \qquad \frac{\partial C_x N}{\partial \eta} \approx \frac{C_x N_1 - C_x N_3}{\Delta \eta} \tag{3.8}$$

$$\frac{\partial C_y N}{\partial \xi} \approx \frac{C_y N_1 - C_y N_2}{\Delta \xi} \qquad \text{and} \qquad \frac{\partial C_y N}{\partial \eta} \approx \frac{C_y N_1 - C_y N_3}{\Delta \eta} \tag{3.9}$$

where N_1, N_2, N_3 represent the action densities at vertices of 1, 2 and 3, respectively. Although this geophysical space discretization is very simple, it has the following advantages: firstly, it forces the propagation of wave action to follow the characteristics; secondly, it is monotonous (i.e. guaranteeing $N > 0$ everywhere) and compact (i.e. operating on one triangle only), while sufficiently accurate for near shore applications.

Here, by choosing a proper transformation $\boldsymbol{X}(\boldsymbol{\xi})$ that makes $\Delta\xi = \Delta\eta = 1$, and substituting Eq. (3.8) and Eq. (3.9) into Eq. (3.7) , the following equation is obtained:

$$\nabla_{\perp} \cdot [\boldsymbol{C}_t \; N \;] \approx C_x N|_2^1 \; e_1^{(1)} + C_x N|_3^1 \; e_1^{(2)} + C_y N|_2^1 \; e_2^{(1)} + C_y N|_3^1 \; e_2^{(2)} \tag{3.10}$$

where the components of vectors $\boldsymbol{e}^{(1)}$ and $\boldsymbol{e}^{(2)}$ are given by Eq. (3.6) and the base vectors are calculated as $\boldsymbol{e}_{(1)} = \boldsymbol{x}_1 - \boldsymbol{x}_2$ and $\boldsymbol{e}_{(2)} = \boldsymbol{x}_1 - \boldsymbol{x}_3$ with $\boldsymbol{x}_i = (x_i, \; y_i)$ the position vector of vertex i in the Cartesian coordinate system.

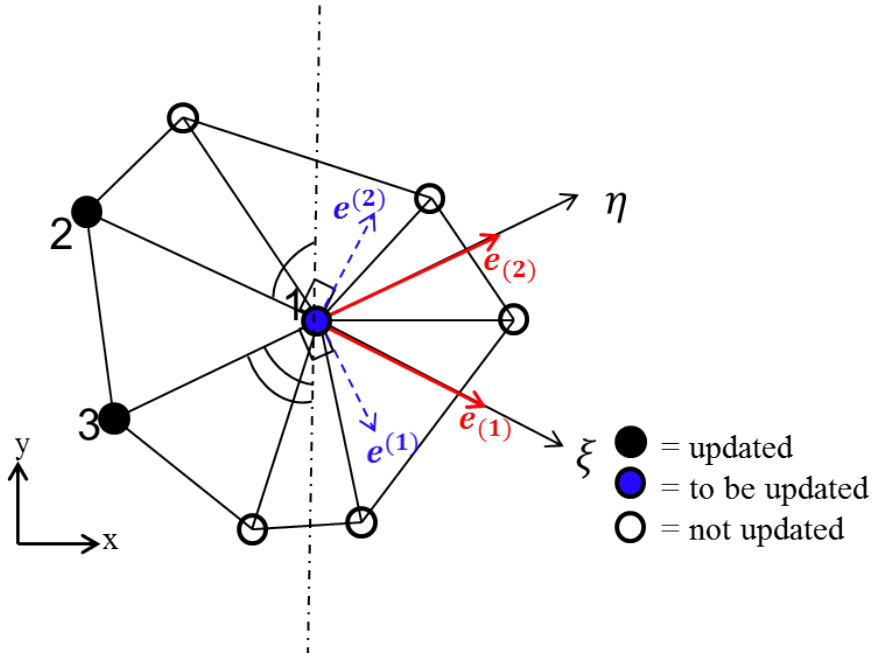

Figure 3.1: A schematic figure on the update of the wave action at vertex 1 in a triangle $\triangle 123$.

Assuming the action densities N_2^n and N_3^n at vertices 2 and 3 of the triangle $\triangle 123$ have been updated, the action density N_1^n at vertex 1 could then be easily determined from

$$\begin{aligned} &\left[\frac{1}{\Delta t} + C_{x,1}\left(e_1^{(1)} + e_1^{(2)}\right) + C_{y,1}\left(e_2^{(1)} + e_2^{(2)}\right)\right] N_1^n \\ &= \frac{N_1^{n-1}}{\Delta t} + \left(C_{x,2} e_1^{(1)} + C_{y,2} e_2^{(1)}\right) N_2^n + \left(C_{x,3} e_1^{(2)} + C_{y,3} e_2^{(2)}\right) N_3^n + F^n \end{aligned} \tag{3.11}$$

The term of F^n in Eq. (3.11) is discretized implicitly in the shaded sector considered (Figure 3.2), and the approximation methods used in the spectral space and the linearization techniques of the source terms are the same as those of the structured SWAN.

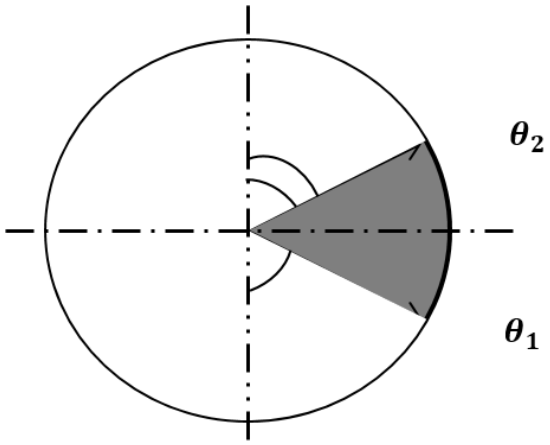

Figure 3.2: The shaded directional sector in spectral space (After Zijlema [6]).

All of the incoming wave energy between the directions θ_1 and θ_2 as indicated by the shaded sector in Figure 3.2 would be enclosed by the waves whose directions locate between the faces $\boldsymbol{e}_{(1)}$ and $\boldsymbol{e}_{(2)}$ in Figure 3.1. In other words, this shaded sector is actually the domain of dependence of Eq. (3.11) in vertex 1, which means, after the integration of the Eq. (3.11), part of wave action density at vertex 1, which located between θ_1 and θ_2 in the direction space, is updated. Since, the wave characteristics lie within this directional sector, this ensures that the CFL number used will properly capture the propagation of wave action towards vertex 1. Therefore, propagation is not subjected to a CFL stability criterion.

As the integration of Eq. (3.11) in triangle $\triangle 123$ indicates the update of wave energy located between directions θ_1 and θ_2, after all the surrounding cells have been treated, the wave action density in the whole 360 degrees at vertex 1 would be updated. This procedure ensures that waves could be transmitted from all directions. Due to the bathymetry and current refraction and nonlinear interactions, wave energy shifts in the spectral space from one directional sector to another. In order to take those effects into account properly, the whole procedure will be repeated several times until converging results obtained.

The update of vertex 1 could only be finished when all of its upwind vertices have

already been updated. For regular grids, the grid points are ordered in a natural manner, e.g. left to right and bottom to top during the first sweep, right to left and bottom to top during the second sweep, right to left and top to bottom during the third sweep and left to right and top to bottom during the fourth sweep. The updated values will be used immediately for updating the next unknown. Thus in the structured version of SWAN, the so-called four sweep technique based on the four-direction Gauss-Seidel relaxation is employed to solve this kind of problem. However, in an unstructured mesh there are no distinct directions, resulting in the consequence that the latest obtained solution will be not necessarily used for updating surrounding vertices.

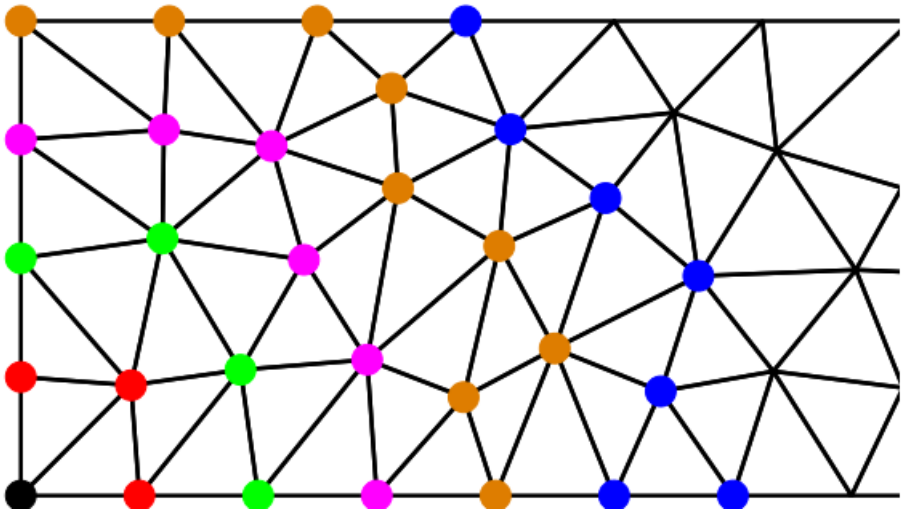

Figure 3.3: Ordering of vertices along spherical wave fronts indicated by different colour points. The black point in left-bottom corner is chosen as reference point (After Zijlema [6]).

A specific ordering scheme is then specifically designed for the unstructured version of SWAN, in which the solution of each vertex will tend to ensure that updated values from the surrounding vertices are used as soon as they are available. By first introducing a reference point on the boundary where the incoming wave energy is imposed and then ordering all the vertices in ascending order according to their distances to the reference point, this scheme would obtain a particular ordering list of vertices. The action density will then be updated along this ordering of vertices. As illustrated in Figure 3.3, this procedure can be interpreted as propagation of spherical wave fronts with a center on the upwave boundary through the domain. It is expected that this specific ordering should result in a faster convergence than a random ordering of vertices.

Discretization and parallelization In order to take advantage of the high-performance computer, UnSWAN also needs to be parallelized, and also to be compatible with the FVCOM model. This procedure is more complicated than that used in the FVCOM

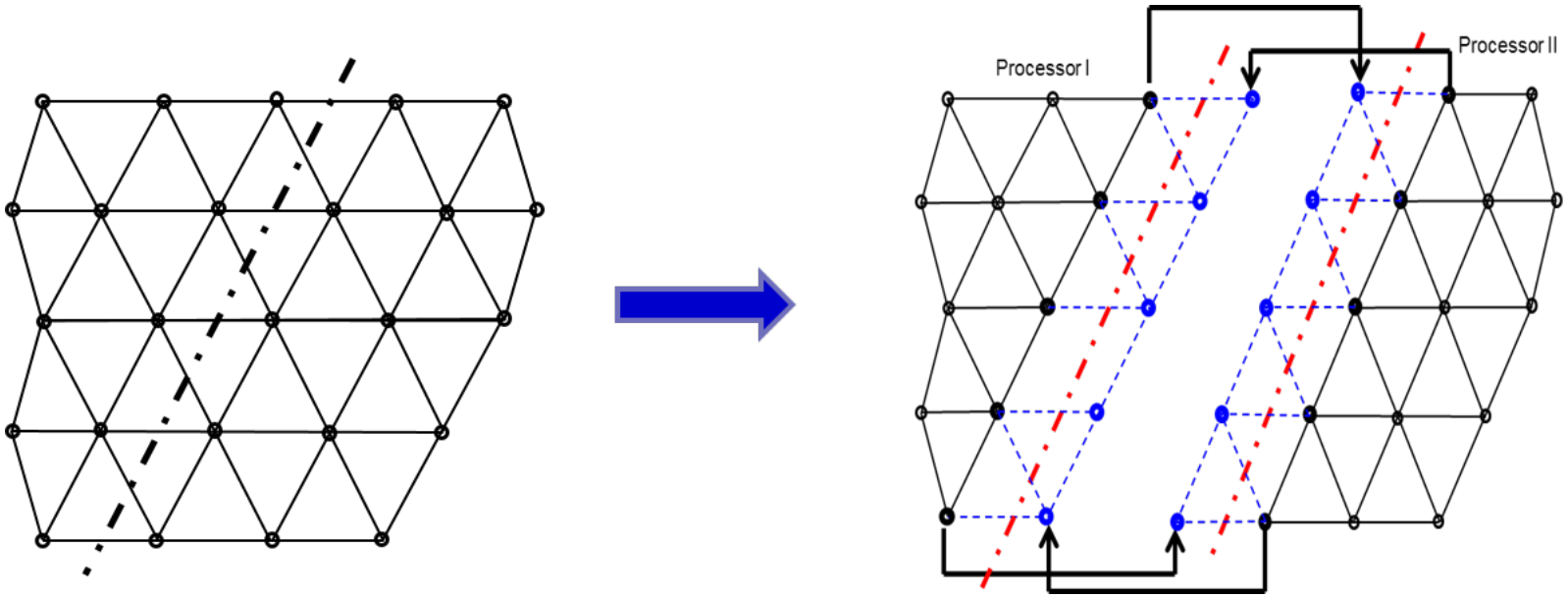

Figure 3.4: A schematic diagram of the vertex-based approach used in partitioning the UnSWAN model: the blue circles in the right figure represents the halo nodes which are computation vertices from the neighbour processors.

model (e.g. Figure A.3). It should be noted here, although the UnSWAN model is discretised in the unstructured triangular grid in geographic space, strictly speaking, the numerical method employed is a finite-difference approach, not a finite-volume method as used in FVCOM. Hence, the parallelization procedure of the UnSWAN model would be very different to that used for the FVCOM. As shown in Figure 3.4, all of the variables including the wave action density of UnSWAN are located at the vertices of the triangles, no variables located at the central nodes of the triangles, different from that in FVCOM model as shown in Figure 2.1.

The triangulation geographical space is firstly decomposed into N equal subdomains by using the METIS graph partitioning library. However, different from the procedure used in FVCOM (e.g. Figure A.3), this decomposition is based on the vertices, not the triangle elements. In other words, in two adjacent sub-domains of different processors, no vertices are duplicated, i.e. no vertices are shared with two different sub-domains.

The UnSWAN code is parallelized using the Single Processor Multiple Data (SPMD) approach, and using the Massage Passing Interface (MPI) to define the inter-processor communications. In order to facilitate this communication between different processors, besides the computation vertices, some halo nodes are also set up in each sub-domain (the blue circles in Figure 3.4). These halo nodes are actually computation vertices belonging to neighbouring processors. Before the computation proceeds onto the next time step, variables values on these nodes will be transferred between processors, and then used to update the wave action density in the subdomains.

In the present wave-current fully coupled system, some specific variables from the wave model and the circulation model need to be transferred into the other model. As the decomposition procedures used in parallelizing the codes of UnSWAN model and FVCOM circulation model are very different from each other, the decomposed corresponding sub-domains in the same processor are also different from each other. Hence, some specific techniques are needed to deal with the wave-current inter-model interactions. In the present study, a simple but efficient approach is implemented. This procedure includes two steps: at the time of transferring, the variables required by these two models are firstly collected to an aggregate array by the master processor, and then distributed into the corresponding sub-domains that belong to the two models. This coupling procedure is implemented directly at the bottom code level. This needs far less time and memory than those of approaches which employ specific toolkits, e.g. the Model-Coupling Toolkit (MCT) used by the ROMS model system. Some more descriptions on the coupling procedure can be found in Section 3.7.

Wave Roller Module

As introduced in the previous chapter, within the surf zone, the bathymetry-dependent breaking is the dominant form of wave energy dissipation. However, after breaking, the wave rollers also play an important role in this process. As the onshore-travelling bores of broken primary waves, the wave roller stores the dissipated wave energy and transfers it gradually into the mean flow, causing a lag in the transfer of momentum (Svendsen [17]; Nairn et al. [18]). There is no roller model available in the existing UnSWAN and FVCOM. A new surface wave roller model is therefore developed in the present fully coupled 3D model system to improve calculations of the surf zone currents.

The surface roller model in the present study is based on the approaches of Stive and De Vriend [134] and Reniers et al. [135]. Analogous to the spectral wave evolution equation, the evolution equation for the wave roller energy is represented as:

$$\frac{\partial \mathrm{E}^r}{\partial \mathrm{t}} + \frac{\partial}{\partial \mathrm{x}}\left(C_{px}\mathrm{E}^r\right) + \frac{\partial}{\partial \mathrm{y}}\left(C_{py}\mathrm{E}^r\right) = \ \alpha_r \varepsilon^{\mathrm{b}} - \varepsilon^{\mathrm{r}} \tag{3.12}$$

where E^r is the surface roller energy; $\boldsymbol{C}_p = (C_{px},\ C_{py})$ is the phase speed of the primary wave, given by $\boldsymbol{V} + \frac{\sigma}{k}\frac{\boldsymbol{k}}{k}$; $\boldsymbol{V}$ is the current velocities, k is the wave number vector; ε^{b} is the dissipation of wave energy which is a source term for the roller energy; ε^{r} is the roller energy dissipation rate; α_r is an *ad hoc* empirical parameter introduced by Tajima and Madsen [136], denoting the fraction of wave dissipation feeding the wave roller (value between 0 and 1). As suggested by Uchiyama et al. [23], α_r provides some flexibility to depict different beach forms and wave breaking types (i.e. spilling, plunging, surging). The roller dissipation rate can be parameterized by $\varepsilon^{\mathrm{r}} = \frac{gsin\beta \mathrm{E}^r}{c}$, where c is the phase speed and $sin\beta$ (=0.1) is an empirical constant (Reniers et al. [135]).

In addition to the UnSWAN model described above, a theoretically much simpler wave model proposed by Mellor et al. [64] is also implemented in the present model system. It is named as the 'wave model A' and introduced in much detail in the Appendix A.

3.2.2 Circulation Module

As discussed in the previous chapter, the FVCOM flow model is adopted in the present study as basis for the circulation model. The Vortex Force concept of Uchiyama et al. [23] and McWilliams et al. [49] is used to facilitate the wave-current interactions. Following Uchiyama et al. [23], the hydrodynamic model equations, including the Vortex Force formalism and the newly included WEC terms (at right-hand side of equation), are given by:

$$
\begin{aligned}
&\frac{\partial \boldsymbol{V}}{\partial \mathrm{t}}+\left(\boldsymbol{V} \cdot \nabla_{\perp}\right) \boldsymbol{V}+w \frac{\partial \boldsymbol{V}}{\partial \mathrm{z}}+f \hat{z} \times \boldsymbol{V}+\nabla_{\perp} \phi-\boldsymbol{F}-\frac{\partial}{\partial \mathrm{z}}\left(K_m \frac{\partial \boldsymbol{V}}{\partial \mathrm{z}}+\nu \frac{\partial \boldsymbol{V}}{\partial \mathrm{z}}\right) \\
&=-\nabla_{\perp} \mathcal{K}+\boldsymbol{J}+\boldsymbol{F}^{\boldsymbol{w}} \\
&\frac{\partial \phi}{\partial \mathrm{z}}+\frac{g \rho}{\rho_0}=-\frac{\partial \mathcal{K}}{\partial \mathrm{z}}+K \\
&\nabla_{\perp} \cdot \boldsymbol{V}+\frac{\partial w}{\partial \mathrm{z}}=0 \\
&\frac{\partial C}{\partial \mathrm{t}}+\left(\boldsymbol{V} \cdot \nabla_{\perp}\right) C+w \frac{\partial C}{\partial \mathrm{z}}-C_{source}-\frac{\partial}{\partial \mathrm{z}}\left(K_h \frac{\partial C}{\partial \mathrm{z}}+\nu_0 \frac{\partial C}{\partial \mathrm{z}}\right)-F_C \\
&=-\left(\boldsymbol{V}^{\boldsymbol{st}} \cdot \nabla_{\perp}\right) C-w^{st} \frac{\partial C}{\partial \mathrm{z}}
\end{aligned}
\tag{3.13}
$$

In these equations the boldface typesets are used for horizontal vectors, while the vertical components are represented by a normal typeset so that 3D vectors are designated by (**horizontal**, vertical). $(\boldsymbol{V}, w)$ and $(\boldsymbol{V}^{st}, w^{st})$ are the Eulerian mean and Stokes velocities, respectively; f is the Coriolis parameter; ϕ is the dynamic pressure (normalized by the density ρ_0); $\boldsymbol{F}$ represents the non-wave non-conservative forces; $\boldsymbol{F}^{\boldsymbol{w}}$ represents the wave-induced non-conservative forces; $(\boldsymbol{J}, K)$ is the Vortex Force and $\mathcal{K}$ is the lower order Bernoulli head (after removing quasi-static terms, see Section 9.6 of McWilliams et al. [49]); ρ and ρ_0 are total and reference densities of sea water respectively; g is the gravity acceleration; C is any material tracer concentration (e.g. T and S); C_{source} is tracer source/sink term and ν_0 is the molecular diffusivity. An overbar represents time average, and a prime represents a turbulent fluctuating quantity. The vertical coordinate range is $-h\left(\mathbf{x}\right) \leq z \leq \zeta+\hat{\zeta}$, in which ζ and $\hat{\zeta}$ are the mean and quasi-static sea level components, respectively. All wave quantities are referenced to the local wave-averaged sea level, $z=\zeta+\hat{\zeta}$, rather than the mean sea level, z=0.

The three-dimensional Stokes velocity ($\boldsymbol{V}^{st}$, w^{st}) is defined for a spectral wave field as:

$$
\boldsymbol{V}^{st}(z)=\frac{2E}{c} \frac{\cosh\left[2\mathcal{Z}\right]}{sinh\left[2\mathcal{H}\right]} \boldsymbol{k} \tag{3.14}
$$

$$
w^{st}\left(z\right)=\ -\nabla_{\perp} \cdot \int_{-h}^{z} \boldsymbol{V}^{st} dz' \tag{3.15}
$$

where E is the wave energy; c is the phase speed of the waves; $\boldsymbol{k}$ is the wave number vector and k is its magnitude; $h(\mathbf{x})$ is the resting depth. $\mathcal{Z}$ and $\mathcal{H}$ are the normalized vertical lengths, defined as:

$$\mathcal{Z} = k\,(z+h)\,;\ \text{and}\ \mathcal{H} = k\left(h+\ \zeta+\hat{\zeta}\right) = kD \tag{3.16}$$

where $D = \ h+\zeta+\hat{\zeta}$ is the wave-averaged thickness of the water column. Finally, the wave energy E, phase speed c and intrinsic frequency σ are given by:

$$E = \frac{1}{8}\rho g H_{rms}^2\ ;\ c = \frac{\sigma}{k}\ ;\ \ \sigma = \ \sqrt{gk\ \tanh\left[\mathcal{H}\right]} \tag{3.17}$$

where H_{rms} is the root-mean-square wave height.

The Vortex Force $(\boldsymbol{J}, K)$ and the Bernoulli head term $(\mathcal{K})$ are expressed as:

$$\begin{aligned}
\boldsymbol{J} &= \ -\hat{z}\times\boldsymbol{V^{st}}\ \left(f+\left(\hat{z}\cdot\nabla_{\perp}\times\boldsymbol{V}\right)\right) - w^{st}\frac{\partial \boldsymbol{V}}{\partial \mathrm{z}} \\
\mathrm{K} &= \boldsymbol{V^{st}}\cdot\frac{\partial \boldsymbol{V}}{\partial \mathrm{z}} \\
\mathcal{K} &= \ \frac{1}{32}\frac{\sigma H_s^2}{k\sinh^2\left[kD\right]}\ \int_{-h}^{z}\frac{\partial^2\Upsilon}{\partial z'^2}\sinh\left[2k\left(z-z'\right)\right]\ dz'
\end{aligned} \tag{3.18}$$

where Υ=$\boldsymbol{k}$·$\boldsymbol{V}$, and $\hat{z}$ is the unit vector in the vertical direction.

The quasi-static sea level component is expressed as:

$$\hat{\zeta} = -\frac{P_{atm}}{g\rho_0} - \frac{H_s^2 k}{16\sinh[2\mathcal{H}]}, \tag{3.19}$$

in which an inverse barometric response to changes in atmospheric pressure P_{atm} and a phase-averaged set-up/set-down (with respect to the still water) are included.

For random waves, the wave energy E is replaced by the elementary variance, $E\,(\sigma,\theta)\,d\sigma d\theta$, and the entire expressions (e.g. Eq. (3.14)) are integrated over the spectrum of the relative frequencies and angles of wave propagation of the wave model. It should be noted that the expression of Stokes drift (Eq. (3.14)) in strongly nonlinear waves can be different from the second-order approximation (Grue and Kolaas [137]), which is outside the scope of the present study.

With the additional WEC terms on the right-hand side, the boundary conditions

for the newly developed model are expressed as:

$$w|_{-h} + \boldsymbol{V}|_{-h} \cdot \nabla_\perp h = 0$$

$$w|_{\zeta+\hat{\zeta}} - \frac{\partial \zeta}{\partial t} - \left(\boldsymbol{V}|_{\zeta+\hat{\zeta}} \cdot \nabla_\perp\right) \zeta = \nabla_\perp \cdot \overline{\boldsymbol{V^{st}}} + \frac{\partial \hat{\zeta}}{\partial t} + \left(\boldsymbol{V}|_{\zeta+\hat{\zeta}} \cdot \nabla_\perp\right) \hat{\zeta} \tag{3.20}$$

$$g\zeta - \phi|_\zeta + \hat{\zeta} = \mathcal{P}$$

where $\overline{\boldsymbol{V^{st}}}$ is the depth-averaged Stokes velocity and $\mathcal{P}$ is the wave-averaged forcing surface boundary condition, defined as:

$$\mathcal{P} = \frac{gH_s^2}{16\sigma} \left\{ \frac{\tanh[kD]}{\sinh[2kD]} \left(-\frac{\partial \Upsilon}{\partial z} \,|_{\zeta+\hat{\zeta}} + \cosh[2kD] \frac{\partial \Upsilon}{\partial z} \,|_{-h} + \int_{-h}^{\zeta+\hat{\zeta}} \frac{\partial^2 \Upsilon}{\partial z'^2} \cosh[2kz'] dz' \right) \right.$$
$$\left. -2k \tanh[kD] \Upsilon|_{\zeta+\hat{\zeta}} \right\} \tag{3.21}$$

Parameterization of Non-Conservative Wave Acceleration, $\boldsymbol{F}^w$

The non-conservative wave acceleration/forcing term, $\boldsymbol{F}^w$, originates from the fact that surface gravity waves lose energy when propagating towards the shoreline. This phenomenon includes four different dissipation processes: (a) white-capping (ε^{wcap}); (b) depth-induced wave breaking (ε^b); (c) bottom friction (ε^{bf}); and (d) surface streaming. Thus $\boldsymbol{F}^w$ is expressed as:

$$\boldsymbol{F}^w = \boldsymbol{B}^{wcap} + \boldsymbol{B}^b + \boldsymbol{B}^{bf} + \boldsymbol{B}^{sf} \tag{3.22}$$

where $\boldsymbol{B}^{wcap}$ is the white-capping induced acceleration; $\boldsymbol{B}^b$ contains both the depth-induced breaking ($\boldsymbol{B}^{db}$) and roller accelerations ($\boldsymbol{B}^r$); $\boldsymbol{B}^{bf}$ and $\boldsymbol{B}^{sf}$ denote accelerations due to bottom and surface streaming, respectively. These accelerations could either be represented as body forces, or as equivalent boundary stresses for the cases in which the associated turbulence boundary layers are too thin to be resolved.

Acceleration induced by whitecapping, ($\boldsymbol{B}^{wcap}$) White-capping is controlled by the wave steepness. In UnSWAN, many different expressions for white-capping have been formulated, e.g. the pulse-based model (Hasselmann [89]) that is commonly used in the third-generation operating wave model, and a saturation-based model (Alves and

Banner [138]; van der Westhuysen et al [139]). Taking the value of white-capping dissipation ($\varepsilon^{\text{wcap}}$) calculated in UnSWAN, the associated acceleration could be expressed either as a body force,

$$\boldsymbol{B}^{wcap} = \frac{\varepsilon^{\text{wcap}}}{\rho_0 \sigma} \boldsymbol{k} \cdot f^b(z) \tag{3.23}$$

or as a boundary stress,

$$\boldsymbol{\tau}_{sur}^{wcap} = \frac{\varepsilon^{\text{wcap}}}{\sigma} \boldsymbol{k} \tag{3.24}$$

where $f^b(z)$ is an empirical vertical distribution function that quantifies the vertical penetration of momentum associated with breaking waves from the surface, given by

$$f^b(z) = \frac{\cosh\left[k_b\left(h+z\right)\right]}{\int_{-h}^{\zeta_c} \cosh\left[k_b\left(h+z\right)\right] dz} \tag{3.25}$$

where $k_b^{-1} = a_b H_{rms}$ is a decay parameter that controls the penetration depth; H_{rms} is root mean square wave height; a_b is an empirical constant that is set to 0.2 in this study.

Depth-induced breaking (ε^{b}) and acceleration ($\boldsymbol{B}^{db}$) In UnSWAN, the bore model of Battjes and Janssen [98] is used to compute the depth-induced breaking (ε^b), given by

$$\varepsilon^{\text{b}} = -\frac{\rho g}{4} \alpha_{BJ} Q_b \tilde{f} H_{max}^2 \tag{3.26}$$

where $\alpha_{BJ} = O(1)$ is a tunable coefficient; Q_b is the fraction of breaking waves; $\tilde{f}$ is the mean wave frequency; and H_{max} is the maximum possible wave height at local water depth d, controlled by $H_{max} = \gamma d$ where γ is an adjustable breaking coefficient. In this study, γ is either given as a constant value (0.73) or determined by a recently proposed $\beta - kd$ parameterization (Salmon et al. [140]).

The depth-induced wave breaking acceleration ($\boldsymbol{B}^{db}$), as a body force, is provided by:

$$\boldsymbol{B}^{db} = \frac{\left(1-\alpha_r\right)\varepsilon^{\text{b}}}{\rho_0 \sigma} \boldsymbol{k} \cdot f^b(z) \tag{3.27}$$

where α_r is the fraction of wave dissipation converted into rollers (described in details later); $f^b(z)$ is an empirical vertical distribution function, which utilizes the same

function as defined in Eq. (3.25).

The depth-induced wave breaking acceleration ($\boldsymbol{B}^{db}$) could be alternatively incorporated into the momentum equation as an equivalent boundary stress,

$$\boldsymbol{\tau}^{b}_{sur} = \frac{(1-\alpha_r)\,\varepsilon^{\mathrm{b}}}{\sigma}\boldsymbol{k} \tag{3.28}$$

Acceleration induced by rollers ($\boldsymbol{B}^{r}$) Based on the wave roller model developed in the previous section, two kinds of method are utilized in this research to include the roller induced acceleration at the surface.

The first method is based on the formulation of Svendsen [17], in which the roller energy is given by:

$$E^r = \frac{\rho_0 c^2 A_R}{L} \tag{3.29}$$

where A_R is a roller area in the vertical plane estimated by either $A_R = \left(\frac{\alpha_r^0}{\sqrt{2.0}} H_s L Q_b\right)$ (Svendsen, [17]); or $A_R = \left(\frac{\alpha_r^s}{2.0} H_s^2 Q_b\right)$ (Okayasu et al. [141]), in which $\alpha_r^0 = 0.06$ and $\alpha_r^s = 0.9$, H_s is the significant wave height, L is wavelength and Q_b is the fraction of breaking waves.

Apart from the first method, a surface roller model is developed and incorporated into the model system to calculate the evolution of the roller energy, based on the existing approaches of Stive and De Vriend [134] and Reniers et al. [135]. The details of this roller model are described in Section 3.2.1.

Given the roller energy (E^r), the roller dissipation rate could be obtained from

$$\varepsilon^{\mathrm{r}} = \frac{g \sin\beta \mathrm{E}^r}{c}$$

where c is the phase speed and $\sin\beta$ (=0.1) is an empirical constant (Reniers et al. [135])

The acceleration induced by wave rollers can be given as, in the form of a body force,

$$\boldsymbol{B}^r = \frac{\varepsilon^{\mathrm{r}}}{\rho_0 \sigma}\boldsymbol{k} \cdot f^b(z) \tag{3.30}$$

and in the form of a boundary stress,

$$\boldsymbol{\tau}_{sur}^{r} = \frac{\varepsilon^{\mathrm{r}}}{\sigma}\boldsymbol{k} \tag{3.31}$$

Combining Eqs. (3.23), (3.27) and (3.30), the total force induced by surface wave breaking (i.e. white-capping, depth-induced wave breaking and surface wave rollers) reads

$$\boldsymbol{B}^{swb} = \frac{\varepsilon^{\mathrm{wcap}} + (1-\alpha_r)\,\varepsilon^{\mathrm{b}} + \varepsilon^{\mathrm{r}}}{\rho_0 \sigma}\boldsymbol{k} \cdot f^{b}(z) \tag{3.32}$$

and the corresponding boundary stress reads

$$\boldsymbol{\tau}_{sur}^{swb} = \frac{\varepsilon^{\mathrm{wcap}} + (1-\alpha_r)\,\varepsilon^{\mathrm{b}} + \varepsilon^{\mathrm{r}}}{\sigma}\boldsymbol{k} \tag{3.33}$$

This boundary stress could be taken as an augmentation to the usual oceanic-model representation of surface wind stress (τ_{sur}^{wind}), which at the same time the momentum flux from atmosphere to wave (τ_{sur}^{wave}) need to be subtracted. Hence, the total surface stress becomes

$$\boldsymbol{\tau}_{sur} = \boldsymbol{\tau}_{sur}^{wind} + \boldsymbol{\tau}_{sur}^{swb} - \boldsymbol{\tau}_{sur}^{wave} \tag{3.34}$$

Wave rollers also contribute to the Stokes transport. Following Svendsen [17], the roller Stokes transport is given by

$$\boldsymbol{U}^{r} = \frac{\mathrm{E}^{r}}{\rho_0 \sigma}\boldsymbol{k} \tag{3.35}$$

Thus the total Stokes transport becomes

$$\boldsymbol{U}^{st} = \frac{(E + \mathrm{E}^{r})}{\rho_0 \sigma}\boldsymbol{k} \tag{3.36}$$

If the same vertical distribution of the Stokes drift velocity (Eq. (3.14)) is assumed for the vertical profile of $\boldsymbol{U}^{r}$, the total Stokes drift velocity reads

$$\boldsymbol{V}^{st} = \frac{\cosh\left[2\mathcal{Z}\right]}{\sinh\left[2\mathcal{H}\right]}\frac{2\,(E + \mathrm{E}^{r})}{c}\boldsymbol{k} \tag{3.37}$$

As suggested by Uchiyama et al. [23] and Kumar et al. [25], a surface-intensified vertical structure (e.g. Haas and Warner [142]) may be more suitable for $\boldsymbol{U}^{r}$. However, the simulation results using these two vertical distributions are very similar (Kumar et

al. [25]). Hence, for simplicity, the Stokes velocity type of distribution is used in this study.

Bottom friction dissipation ($\varepsilon^{\mathrm{bf}}$) and accelerations due to bottom streaming ($\boldsymbol{B}^{\mathrm{bf}}$) The surface-wave-induced orbital motions extend down to the sea floor in shallow water, causing interactions between the surface waves and the bottom. In these wave-bottom interactions, the bottom friction is a dominant wave dissipation mechanism for continental shelf seas with sandy bottoms (Bertotti and Cavaleri [99]). Following Reniers et al. [143], the bottom friction induced wave dissipation (ε^{bf}) is parameterized by

$$\varepsilon^{\mathrm{bf}} = \frac{1}{2\sqrt{\pi}}\,\rho_0 f_w u_b^3 \tag{3.38}$$

where u_b is the wave bottom orbital velocity and $f_w = 1.39\left(\frac{\sigma z_0}{u_b}\right)^{0.52}$ is the wave friction factor (Soulsby [144]).

Dissipation of wave energy in the wave boundary layer causes the instantaneous, oscillatory wave bottom orbital velocities to be not exactly ninety degrees out of phase, resulting in a wave stress (bottom streaming) in the wave bottom boundary layer along the direction of wave propagation (Longuet-Higgins [15]). Similar to the wave breaking induced accelerations implemented above, this stress can be incorporated in the form of either a body force,

$$\boldsymbol{B}^{\mathrm{bf}} = \frac{\varepsilon^{\mathrm{bf}}}{\rho_0 \sigma}\boldsymbol{k}\cdot f^{\mathrm{bf}}(z) \tag{3.39}$$

or an equivalent bottom boundary stress

$$\boldsymbol{\tau}_{bot}^{\mathrm{bf}} = \frac{\varepsilon^{\mathrm{bf}}}{\sigma}\boldsymbol{k} \tag{3.40}$$

where $f^{\mathrm{bf}}(z)$ is an upward decaying vertical distribution function given by

$$f^{\mathrm{bf}}(z) = \frac{\cosh\left[k_{\mathrm{bf}}\ (\zeta^c - z)\ \right]}{\int_{-h}^{\zeta^c}\cosh\left[k_{\mathrm{bf}}\ (\zeta^c - z)\ \right]dz} \tag{3.41}$$

with a decay length $k_{\mathrm{bf}}^{-1} = a_{\mathrm{bf}}\delta_w$, where a_{bf} is an empirical constant which is equal to one under monochromatic waves and has a much larger value (e.g., $a_{\mathrm{bf}} = 3$ is used by Reniers et al. [143]) under random waves (Klopman [145]); δ_w is the wave bottom boundary layer thickness expressed as a function of the semi-orbital excursion

length (A_b), Nikuradse roughness (k_N) and bottom roughness length (z_0) (Fredsoe and Deigaard [4]):

$$\delta_w = 0.09 k_N \left(\frac{A_b}{k_N} \right)^{0.82} \tag{3.42}$$

where $A_b = u_b/\sigma$ and $k_N = 30 z_0$.

Acceleration due to surface streaming Due to the wave-viscous boundary layer at the water surface, surface streaming similar to the concept of bottom streaming occurs. As the thickness of this surface wave-viscous boundary layer ($\sqrt{2\nu/\sigma} \approx 1mm$) is usually too thin to be resolved, the acceleration due to surface streaming in the momentum balance is implemented only as a boundary stress in this study. It is parameterized as (Xu and Bowen [146]):

$$\boldsymbol{\tau}_{sur}^{str} = \frac{coth(kh)}{4} \rho_0 \, K_m \, H_s^2 \sigma k \cdot \boldsymbol{k} \tag{3.43}$$

Although many studies have omitted this effect of surface streaming (e.g. Uchiyama et al. [23]), the effect can be significant especially outside the surf zone (Lentz et al. [147]).

Wave-Enhanced Bottom Drag

The interactions of waves and currents in the bottom boundary layer can affect the hydrodynamic results in coastal circulation modelling, particularly in the surf zone. In order to parameterize the wave enhanced bottom shear stress, the drag law proposed by Soulsby [144] is used here in the coupled model system:

$$\boldsymbol{\tau}_{cw} = \boldsymbol{\tau}_c \left[1.0 + 1.2 \left(\frac{|\tau_w|}{|\tau_w| + |\tau_c|} \right)^{3.2} \right] \tag{3.44}$$

$$\boldsymbol{\tau}_c = \rho_0 \left[\frac{\kappa}{ln\,(z_r/z_0)} \right]^2 |\boldsymbol{V}| \, \boldsymbol{V}; \quad |\boldsymbol{\tau}_w| = \frac{1}{2} \rho_0 f_w u_b^2 \tag{3.45}$$

where τ_c and τ_w are bottom stresses due to current and waves; $\kappa = 0.4$ is the von Karman constant; z_r is a reference height above the bed, nominally equivalent to half the height of the first grid cell above the bed (in a barotropic model $z_r = D/2$; e.g.

Uchiyama et al. [148]); z_0 is the bed roughness length; f_w is the wave friction factor given by

$$f_w = Min\left\{0.3,\ 1.39\left(\frac{A_b}{z_0}\right)^{-0.52}\right\}\ ; \tag{3.46}$$

$$A_b = \frac{u_b}{\sigma} = \frac{u_b}{2\pi}T_{orb}^w = \sqrt{2\int_0^{2\pi}\int_0^{\infty}\frac{1}{sinh^2 kd}E\left(\sigma,\theta\right)d\sigma d\theta} \tag{3.47}$$

u_b is the bottom wave orbital velocity and T_{orb}^w is the near bottom wave period.

Model Transformation

Following the approach in FVCOM, the above current model equations are transformed into a topography-following coordinate system (Sigma coordinates, e.g. Figure 2.2).

Three new variables are defined,

$$\begin{aligned}\zeta^c &= \zeta + \hat{\zeta}\\ \phi^c &= \phi + \mathcal{K}\\ \left(\boldsymbol{V}^l, w^l\right) &= \left(\boldsymbol{V}^{st}, w^{st}\right) + \left(\boldsymbol{V}, w\right)\end{aligned} \tag{3.48}$$

where ζ^c is the composite sea level, ϕ^c is the sum of the dynamic pressure and the Bernoulli head, and $\left(\boldsymbol{V}^l, w^l\right)$ is the wave-averaged Lagrangian velocity.

Rewritten in a flux-divergence form, the momentum and continuity equations become

$$\begin{aligned}&\frac{\partial \boldsymbol{V}}{\partial \mathrm{t}} + \widetilde{\nabla}_\perp \cdot \left(\widetilde{\boldsymbol{V}}\boldsymbol{V}\right) + \frac{\partial}{\partial \mathrm{z}}\left(w^l \boldsymbol{V}\right) + f\hat{z}\times\boldsymbol{V}^l + \nabla_\perp \phi^c - \boldsymbol{F} - \frac{\partial}{\partial \mathrm{z}}\left(K_m\frac{\partial \boldsymbol{V}}{\partial \mathrm{z}} + \nu\frac{\partial \boldsymbol{V}}{\partial \mathrm{z}}\right)\\ &= \boldsymbol{J'} + \boldsymbol{F^w}\end{aligned}$$

$$\frac{\partial \phi^c}{\partial z} + \frac{g\rho}{\rho_0} = K$$

$$\nabla_\perp \cdot \boldsymbol{V}^l + \frac{\partial w^l}{\partial z} = 0$$

$$\frac{\partial C}{\partial \mathrm{t}} + \left(\boldsymbol{V}^l \cdot \nabla_\perp\right) C + w^l\frac{\partial C}{\partial \mathrm{z}} - C_{source} - \frac{\partial}{\partial \mathrm{z}}\left(K_h\frac{\partial C}{\partial \mathrm{z}} + \nu_0\frac{\partial C}{\partial \mathrm{z}}\right) - F_C = 0 \tag{3.49}$$

where $\boldsymbol{J'}$ is a modified VF, expressed as

$$\begin{aligned}\boldsymbol{J'} &= -\hat{z} \times \boldsymbol{V}^{st} \left(f + (\hat{z} \cdot \nabla_{\perp} \times \boldsymbol{V})\right) + \boldsymbol{V} \frac{\partial w^{st}}{\partial \mathrm{z}} \\ &= -\hat{z} \times \boldsymbol{V}^{st} \left(f + (\hat{z} \cdot \nabla_{\perp} \times \boldsymbol{V})\right) - \boldsymbol{V} \left(\nabla_{\perp} \cdot \boldsymbol{V}^{st}\right)\end{aligned} \tag{3.50}$$

After these steps the wave-induced terms are no longer only retained to the right hand side of equations. The boundary conditions become

$$\begin{aligned} & w^{l}|_{-h} + \boldsymbol{V}|_{-h} \cdot \nabla_{\perp} h = 0 \\ & w^{l}|_{\zeta^{c}} - \frac{\partial \zeta^{c}}{\partial \mathrm{t}} - \left(\boldsymbol{V}|_{\zeta^{c}} \cdot \nabla_{\perp}\right) \zeta^{c} = 0 \\ & \mathrm{g}\ \zeta^{c} - \ \phi^{c}|_{\ \zeta^{c}} = \mathcal{P} + g\hat{\zeta} - \mathcal{K}|_{\ \zeta^{c}} \end{aligned} \tag{3.51}$$

The depth-integrated continuity equation is given by

$$\frac{\partial \zeta^{c}}{\partial \mathrm{t}} + \nabla_{\perp} \cdot \overline{\boldsymbol{V}}^{l} = 0 \tag{3.52}$$

where $\overline{\boldsymbol{V}}^{l}$ is the depth integral of $\boldsymbol{V}^{l}$.

Subsequently, define

$$\left(\boldsymbol{V}^{l}, \omega^{l}\right) = \left(\boldsymbol{V}^{st}, \omega^{st}\right) + \left(\boldsymbol{V}, \omega\right) \tag{3.53}$$

where ω, ω^{st}, ω^{l} are the vertical Eulerian, Stokes and Lagrangian velocities in Sigma coordinates, respectively. The equations for the wave-averaged currents can then be transformed into the Sigma coordinates used by FVCOM:

$$\frac{\partial D}{\partial \mathrm{t}} + \frac{\partial u^l D}{\partial \mathrm{x}} + \frac{\partial v^l D}{\partial \mathrm{y}} + \frac{\partial \omega^l}{\partial \mathrm{s}} = 0$$

$$\begin{aligned}
&\frac{\partial uD}{\partial t} + \frac{\partial u^2 D}{\partial x} + \frac{\partial uvD}{\partial y} + \frac{\partial u\omega^l}{\partial s} - fv^l D + D\frac{\partial \phi^c}{\partial x} - DF_x - \frac{\partial}{\partial s}\left(\frac{K_m}{D}\frac{\partial u}{\partial s} + \frac{\nu}{D}\frac{\partial u}{\partial s}\right) \\
&= Dv^{st}\left(\frac{\partial v}{\partial x} - \frac{\partial u}{\partial y}\right) - u\left(\frac{\partial u^{st} D}{\partial x} + \frac{\partial v^{st} D}{\partial y}\right) + DF_x^w
\end{aligned}$$

$$\begin{aligned}
&\frac{\partial vD}{\partial t} + \frac{\partial uvD}{\partial x} + \frac{\partial v^2 D}{\partial y} + \frac{\partial v\omega^l}{\partial s} + fu^l D + D\frac{\partial \phi^c}{\partial y} - DF_y - \frac{\partial}{\partial s}\left(\frac{K_m}{D}\frac{\partial v}{\partial s} + \frac{\nu}{D}\frac{\partial v}{\partial s}\right) \\
&= -Du^{st}\left(\frac{\partial v}{\partial x} - \frac{\partial u}{\partial y}\right) - v\left(\frac{\partial u^{st} D}{\partial x} + \frac{\partial v^{st} D}{\partial y}\right) + DF_y^w
\end{aligned} \tag{3.54}$$

where $\boldsymbol{F} = (F_x, F_y)$ is the non-wave body force and parameterized horizontal momentum mixing term; $\boldsymbol{F^w} = \left(F_x^w, F_y^w\right)$ is the momentum flux from non-conservative wave terms described later in this section; the vertical Sigma coordinates $\mathrm{s} = \frac{z-\zeta^c}{D}$ ranges from $\mathrm{s} = -1$ at the bottom to $\mathrm{s} = 0$ at the free surface; the vertical Lagrangian velocity over the Sigma surface is given by

$$\omega^l = \left[w^l - \left(\frac{\partial z}{\partial t} + \boldsymbol{V}^l \cdot \nabla_\perp z\right)\right]\Bigg|_{\mathrm{s}} \tag{3.55}$$

The geopotential function, evaluated from integration of the vertical momentum equation, is given by

$$\phi^c = g\left(\zeta^c - \widehat{\zeta}\right) - \left(\mathcal{P}|_{\ \zeta^c} - \mathcal{K}|_{\ \zeta^c}\right) + \int_s^0 \left[\frac{g\rho}{\rho_0} - K\right] Dds \tag{3.56}$$

3.2.3 Turbulence Closure Model

Wave breaking leads to extra turbulence generation at the surface and enhances turbulent kinetic energy (TKE) levels in the water column (Thorpe [149]; Agrawal et al. [150]; Moghimi et al. [151]). Craig and Banner [152] accounted for this effect by implementing a new flux-type surface boundary condition for the TKE in a one-dimensional M-Y2.5 turbulence closure model. This approach has been implemented in the present study for incorporating the effects of wave breaking on vertical mixing, by adapting a generic length scale (GLS) two-equation turbulence closure model similar to approaches by Umlauf et al. [153].

The GLS model, introduced by Umlauf and Burchard [66], has been tested against measurements for oscillating grid generated turbulence which is considered to be similar to the wave-breaking induced turbulence. However, the original GLS model is modified in the present study to better account for the wave-enhanced vertical mixing. The two equations for k and for the GLS (ψ) read:

$$\begin{aligned}
\frac{\partial \mathrm{k}}{\partial t} + \boldsymbol{V} \cdot \nabla \mathrm{k} = & \frac{\partial}{\partial z}\left(\frac{K_m}{\sigma_{\mathrm{k}}} \frac{\partial \mathrm{k}}{\partial z}\right) + P_s + P_b - \varepsilon \\
\frac{\partial \psi}{\partial t} + \boldsymbol{V} \cdot \nabla \psi = & \frac{\partial}{\partial z}\left(\frac{K_m}{\sigma_{\psi}} \frac{\partial \psi}{\partial z}\right) + \frac{\psi}{\mathrm{k}}\left(C_1 P_s + C_3 P_b - C_2 \varepsilon F_{wall}\right)
\end{aligned} \tag{3.57}$$

where $P_s = K_m \left[\left(\frac{\partial u}{\partial z}\right)^2 + \left(\frac{\partial v}{\partial z}\right)^2\right]$ and $P_b = K_h \frac{g}{\rho_0} \frac{\partial \rho}{\partial z}$ represent the turbulence production rates by shear and buoyancy, respectively; K_m and K_h are the vertical eddy viscosity and vertical eddy diffusion coefficients, respectively; $\varepsilon = \left(c_\mu^0\right)^3 \mathrm{k}^{3/2}\, l^{-1}$ is the turbulence dissipation rate; σ_{k} and σ_ψ are the turbulent Schmidt numbers for k and ψ, respectively; F_{wall} is a wall function; and C_1, C_2 and C_3 are coefficients which can be found in Warner et al. [154]. The GLS (ψ) is defined as:

$$\psi = \left(c_\mu^0\right)^p \mathrm{k}^m\, l^n \tag{3.58}$$

where c_μ^0 is the stability coefficient based on experimental data for non-stratified channel flow, it takes on a specific value when used with a stability function and other model parameters (Warner et al. [154]); p=2.0, m=1.0 and n=-0.67 are coefficients, following suggestions by Umlauf and Burchard [66]. Note that many conventional turbulence schemes can also be derived from this GLS model by using specific combinations of values for p, m and n (e.g. a $\mathrm{k}-\varepsilon$ scheme is reproduced by p=3, m=1.5 and n=-1.0; a $\mathrm{k}-\psi$ scheme is reproduced by p=-1.0, m=0.5 and n=-1.0.).

The TKE injection due to wave breaking is provided by a flux boundary condition at the water surface (Craig and Banner [152]; Feddersen [155, 156]):

$$F_{\mathrm{k}} = \left.\frac{K_m}{\sigma_{\mathrm{k}}} \frac{\partial \mathrm{k}}{\partial z}\right|_{\zeta^c} \tag{3.59}$$

where F_{k} is the surface flux of turbulence energy injected into water column due to surface wave dissipation, which can be either parameterised in proportion to the cube of surface wind friction velocity (Craig and Banner [152]) as $F_{\mathrm{k}} = c_w (u_*^s)^3$, or directly obtained from a surface wave model as a fraction of the surface wave dissipation, i.e. $F_{\mathrm{k}} = D_w \left[(1-\alpha_r)\,\varepsilon^b + \varepsilon^{\mathrm{r}} + \varepsilon^{\mathrm{wcap}}\right]$; where u_*^s is the surface friction velocity and

c_w and D_w are empirical constants. The former formulation has been used at deep seas and open seas (Craig [157]; Terray et al. [118]) with $c_w \approx (100 \sim 150)$, while the latter formulation is more appropriate in the surf zone. $D_w(\approx 0.01 \sim 0.25)$ is used for depth-induced breaking (Govender et al. [158]; Huang et al. [159]; Feddersen and Trowbridge [160]; Feddersen [155, 156]) and $D_w \approx 1$ is for deep water white-capping (Paskyabi et al. [161]).

Neumann-type surface boundary conditions for k and ψ (following Umlauf and Burchard [66]) are applied at vertical position of z':

$$\begin{aligned} \frac{K_m}{\sigma_{\mathrm{k}}}\frac{\partial \mathrm{k}}{\partial z} &= -\frac{c_\mu}{\sigma_{\mathrm{k}}}(\mathbb{K})^{\frac{3}{2}}\ \mathcal{L}\cdot\alpha_{de}\left(z_{0s}-\mathrm{z}'\right)^{\frac{3}{2}\alpha_{de}} \\ \frac{K_m}{\sigma_\psi}\frac{\partial \psi}{\partial z} &= -\frac{c_\mu\left(c_\mu^0\right)^p}{\sigma_\psi}\left(m\alpha_{de}+n\right)(\mathbb{K})^{m+\frac{1}{2}}\ \mathcal{L}^{n+1}\left(z_{0s}-\mathrm{z}'\right)^{\left(m+\frac{1}{2}\right)\alpha_{de}+n} \end{aligned} \tag{3.60}$$

where $\alpha_{de}$is the spatial decay rate of TKE in the wave-enhanced layer; $\mathcal{L}$ is the slope of the turbulent length scale; $\mathbb{K} = \left(-\frac{\sigma_{\mathrm{k}}}{c_\mu\alpha_{de}\mathcal{L}}F_{\mathrm{k}}\right)^{\frac{2}{3}}\frac{1}{z_{0s}^{\alpha_{de}}}$ and F_{k} is the injection flux of TKE at the water surface.

In the present study, the surface roughness z_{0s} is connected to the length scale of injected turbulence which is determined uniquely by the spectral properties of turbulence at the source. This parameter directly affects the vertical distribution of TKE in the upper portion of the water column (Moghimi et al. [151]). However, due to the difficulty in measuring this parameter, a wide range of values have been proposed (e.g. Craig and Banner [152]; Terray et al. [119]; Umlauf et al. [162]; Stips et al. [163]; Feddersen and Williams [164]; Moghimi et al. [151]). In the present study, $z_{0s} = H_w H_s$, where H_w is kept as a tuning parameter which is adjusted to produce results closest to the available observations.

3.3 Bottom Boundary Layer Module — A Modification of The Original *mb_bbl*

As stated in Section 2.4, three BBL models (i.e. *sg_bbl*, *mb_bbl* and *ssw_bbl*) had been implemented in the original FVCOM codes. These three formulations use slightly different combinations of algorithms for the wave-current interactions and moveable bed, which could produce significantly different results (Warner et al. [47]). In this study, after some preliminary testing, the *mb_bbl* formulation is finally adopted (see Section 5.5), which uses wave-current BBL algorithms developed by Soulsby [144] in

combination with sediment and bedform roughness estimates of Grant and Madsen [129], Nielsen [68] and Li and Amos [165].

The procedure in *mb_bbl* used to solve the bottom-boundary layer processes is described here:

(1) The input variables required for the parameterization of BBL

- velocities u and v at reference elevation z_r; representative wave-orbital velocity amplitude u_b, wave period T, and wave-propagation direction θ (degrees, in nautical convention).

  These wave parameters should represent the full spectrum of motion near the bed, which could either be obtained from a wave model (e.g. SWAN) or simpler calculations based on specified surface wave parameters.

- bottom sediment characteristics (median grain diameter D_{50}, mean sediment density ρ_s and representative settling velocity w_s).

  These are based on the composition of the uppermost active layer of the bed sediment during the previous time step (Warner et al. [47]).

(2) The formulations shown in Eqs. (3.44) and (3.45) are used to calculate these shear stresses, which are repeated here as follows:

$$\begin{cases} \boldsymbol{\tau}_c = \rho_0 \left[\frac{\kappa}{ln(z_r/z_0)}\right]^2 |\boldsymbol{V}|\,\boldsymbol{V}; \\ \tau_w = \frac{1}{2}\rho_0 f_w u_b^2 \\ \boldsymbol{\tau}_{cw} = \boldsymbol{\tau}_c \left[1.0 + 1.2\left(\frac{\tau_w}{\tau_w+\tau_c}\right)^{3.2}\right] \\ \tau_{cwmax} = \left[(\tau_{cw} + \tau_w cos\phi_{wc})^2 + (\tau_w sin\phi_{wc})^2\right]^{1/2} \end{cases} \tag{3.61}$$

where $\boldsymbol{\tau}_c$, τ_w represent the bed shear stresses which would occur due to the current alone and the wave alone, respectively; $\boldsymbol{\tau}_{cw}$ and τ_{cwmax} are respectively the mean and maximum bed shear stresses during a wave cycle, beneath the combined effect of waves and currents; τ_{cw} and τ_c represent the magnitude of $\boldsymbol{\tau}_{cw}$ and $\boldsymbol{\tau}_c$.

(3) Calculate the skin friction contribution of bed shear stresses produced by (and acting on) the sediment grains.

Use $z_0 = z_{0N} = 2.5D_{50}/30$ (i.e. the grain roughness lengths) and Eq. (3.61), the calculated bed shear stresses due to skin friction are calculated and represented as τ_c^s, τ_w^s, τ_{cw}^s, τ_{cwmax}^s.

(4) Calculate the ripple height η_r and wavelength λ_r, based on the procedure adopted in Li and Amos [165].

Firstly, calculate several representative shear stresses used in the following formulas:

- The critical shear stress for transition to sheet flow:

$$\tau_{up} = 0.172\rho_w(s-1)g(D_{50})^{0.624} \tag{3.62}$$

- The break-off shear stress τ_{bf}, i.e. the critical shear stress beyond which significant sand by-passing occurs and ripple steepness η_r/λ_r starts to decrease from its maximum value obtained in the equilibrium range.

$$\tau_{bf} = 1.8\tau_{cr}\left(\frac{D_{50}}{4\nu}\right)^{0.6}[\rho_w(s-1)gD_{50}]^{0.3} \tag{3.63}$$

- The enhanced skin-friction shear stress at the ripple crest (τ_{cwe}), which determines when bedload transport and hence ripple movement will start.

$$\tau_{cwe} = Max\left\{\tau^s_{cwmax}, \tau^s_{cwmax}\left(\frac{\lambda_{rp}}{\lambda_{rp}-\pi\eta_{rp}}\right)^2\right\} \tag{3.64}$$

  where η_{rp} and λ_{rp} are height and wavelength of the pre-existing ripples, respectively.

- The maximum bedload shear stress (τ^b_{cwmax}) when bedload occurs.

  Calculate roughness lengths associated with bedload sediment transport (z_{0ST}):

$$z_{0ST} = 17.4D_{50}\left[\frac{\tau^s_{cwmax}-\tau_{cr}}{(s-1)gD_{50}}\right]^{0.75} \tag{3.65}$$

  Let $z_0 = z_{0N} + z_{0ST}$ and repeat the step (2), after which the bedload bed shear stresses, i.e. τ^b_c, τ^b_w, τ^b_{cw}, τ^b_{cwmax} are obtained

The detailed formulas to calculate ripple wavelength and ripple height are given as the following, in which ripples are separated into five categories: no transport, ripples in weak-transport range, ripples in equilibrium range, ripples in break-off range, and upper-plane bed sheet-flow.

$$
\begin{cases}
\left.\begin{aligned} \eta_r/D_{50} &= 19.6\sqrt{\tau^s_{cwmax}/\tau_{cr}} + 20.9 \\ \eta_r/\lambda_r &= 0.12 \end{aligned}\right\} & \text{, if } \tau^s_{cwmax} < \tau_{cr} \ \& \ \tau_{cwe} > \tau_{cr} \\
\left.\begin{aligned} \eta_r/D_{50} &= 22.15\sqrt{\tau^b_{cwmax}/\tau_{cr}} + 6.38 \\ \eta_r/\lambda_r &= 0.12 \end{aligned}\right\} & \text{, if } \tau^s_{cwmax} > \tau_{cr} \ \& \ \tau^b_{cwmax} < \tau_{bf} \\
\left.\begin{aligned} \eta_r &= 535 D_{50} \\ \eta_r/\lambda_r &= 0.15\frac{\sqrt{\tau_{up}}-\sqrt{\tau^b_{cwmax}}}{\sqrt{\tau_{up}}-\sqrt{\tau_{bf}}} \end{aligned}\right\} & \text{, if } \tau_{bf} < \tau^b_{cwmax} < \tau_{up} \\
\left.\begin{aligned} \eta_r &= 0 \\ \lambda_r &= 0 \end{aligned}\right\} & \text{, if } \tau_{up} < \tau^b_{cwmax} \\
\left.\begin{aligned} \eta_r &= \eta_{rp} \\ \lambda_r &= \lambda_{rp} \end{aligned}\right\} & \text{, else}
\end{cases}
\tag{3.66}
$$

Calculate the roughness lengths associated with bedform (z_{0BF}):

$$
z_{0BF} = a_r \eta_r^2/\lambda_r \tag{3.67}
$$

where a_r is a coefficient that may range from 0.3 to 3 (Soulsby [125]), $a_r = 27.7/30$ proposed by Grant and Madsen [129] is used in this formulation.

For a more detailed description on this process, one can refer to Li and Amos [165].

(5) Calculate the bottom roughness height: $z_0 = max[z_{0N} + z_{0ST} + z_{0BF},\ z_{0MIN}]$

z_{0N}, z_{0ST} and z_{0BF} are roughness lengths associated with grain roughness, sediment transport and bedform respectively.

(6) Calculate the total bed shear stresses.

Based on the newly acquired z_0 in step (5), repeat step (2) to calculate the final total bed shear stresses, i.e. τ^t_c, τ^t_w, τ^t_{cw}, τ^t_{cwmax}. τ^t_{cw} is used in the bottom boundary conditions for the momentum equations.

It should be noted that, Soulsby [125] suggested to use the maximum bed stress τ_{cwmax} (i.e. τ^s_{cwmax} or τ^b_{cwmax}) to determine the threshold of motion and entrainment rate of sediments. Therefore, only the maximum bed stress is stored and used in the original code. In the new model, the wave-averaged wave-current combined bed shear stress τ_{cw} (i.e. τ^s_{cw} or τ^b_{cw})) is treated as a global variable and could be selected to be

used in modelling the sediment transport processes. In Section E and 5.5.1, simulations using τ_{cwmax} and τ_{cw} are conducted respectively. The model results, however, suggest that using τ_{cw} to calculate the pick-up functions may be more reasonable.

3.4 Suspended Sediment Transport Module

As discussed in Section 2.3, the open-source community sediment transport model, CMCST, had been implemented into the FVCOM model based on Warner et al. [47]. However, in the present research, modifications are introduced for the simulation of effects due to surface wave propagation and breaking.

As indicated in Eqs. (3.13) and (3.49), the wave-induced Stokes drift could also contribute to transport of a tracer in the present of surface waves. The advection-diffusion equation for the sediment concentration, Eq. (2.34) in the Section 2.3.1, is thus replaced by the following equation:

$$\frac{\partial C^i}{\partial \mathrm{t}} + \left(\boldsymbol{V}^l \cdot \nabla_\perp\right) C^i + w^l \frac{\partial C^i}{\partial \mathrm{z}} - \frac{\partial}{\partial \mathrm{z}}\left(K_h \frac{\partial C^i}{\partial \mathrm{z}}\right) - F_{C^i} = C^i_{source} \tag{3.68}$$

where, with the same meaning of parameters in Eq. (2.34), i is an index for the ith sediment class; C^i is the concentration of the ith sediment class; K_h the vertical eddy viscosity; F_{C^i} represent the horizontal diffusion of the sediment concentration; C^i_{source} is the source/sink term (for the ith sediment class).

However, different from that in Eq. (2.34), the term of C^i_{source} here only contains a vertical settling process, whose expression is

$$C^i_{source} = -\frac{\partial w^i_s C_i}{\partial z} \tag{3.69}$$

where w^i_s the vertical settling velocity (positive upwards) of the ith sediment class, and can be given by the formula proposed by Soulsby [125]:

$$w^i_s = \frac{\nu}{D^i_{50}}\left(\sqrt{10.36^2 + 1.049 D^{i*3}_s} - 10.36\right) \tag{3.70}$$

in which $D^{i*}_s = D^i_{50}[\frac{(s-1)g}{\nu^2}]^{\frac{1}{3}}$ is dimensionless grain size (particle parameter).

Instead of being included in the source term, the process of sediment re-suspension from the bed is represented by a pick-up function in the bottom boundary condition

here. This is because the implementation of the erosion source term (E_s^i) in Eq. (2.34) needs a known bed erodibility constant (E_s^0) as the input parameter, which is hard to provide and largely determined by the human experiences. In addition, in situations with variable hydrodynamic conditions (e.g. surf zone), the sediment eroded from bed is generally not a constant but a complex function of the local hydrodynamic and sediment parameters (e.g. water diffusivity, bed stress, sediment diameter, etc.).

The bottom boundary condition is

$$K_h \frac{\partial C_i}{\partial z} = -\phi_p^i(\theta), \text{ when } z = -h \tag{3.71}$$

where $\phi_p^i(\theta)$ is a pickup function. Many different formulations had been proposed for the pickup function, and the formula suggested by van Rijn [69] is adopted in this research:

$$\frac{\phi_p^i(\theta)}{\sqrt{(s-1)gD_{50}^i}} = 3.3 \times 10^{-4} \left[\frac{\theta_{sf}^i - \theta_{cr}^i}{\theta_{cr}^i}\right]^{3/2} \left(D_s^{i*}\right)^{0.3} \tag{3.72}$$

where θ_{cr} is the critical Shields number determined by Soulsby [125]

$$\theta_{cr}^i = \frac{0.3}{1 + 1.2D_s^{i*}} + 0.055\left(1 - exp(-0.02D_s^{i*})\right) \tag{3.73}$$

and θ_{sf}^i is the Shields parameter (non-dimensional bed shear stress), given as

$$\theta_{sf}^i = \frac{\tau_{sf}}{\rho(s-1)gD_{50}^i} = \frac{u_*^2}{(s-1)gD_{50}^i} \tag{3.74}$$

where τ_{sf} is the skin-friction component of the total bed shear stress and could be determined from the BBL model (see the details in Section 2.4), u_* is the bed friction velocity (or bed shear velocity, $= \sqrt{\tau_{sf}/\rho}$).

A no-flux boundary condition, as that used in Section 2.3.1, is used at the surface boundary for the sediment concentration:

$$K_h \frac{\partial C_i}{\partial z} = 0, \text{ when } z = \zeta \tag{3.75}$$

The accuracy of the predicted suspended sediment transport relies on a reasonable estimate of the pickup flux, as it determines the amount of sediment eroded from the bed into the water column. The pickup flux is in turn mainly determined through Eq. (3.72) by the magnitude of Shields parameter (θ_{sf}^i). For sediment transport in a U tube or under non-breaking waves, the Shields parameter is often calculated from the

near-bed velocities without (Eq. (2.20)) or with representative wave characteristics and the bottom roughness z_0 (see the details in Section 2.4).

On the other hand, the near-bed sediment pickup under breaking waves can be enhanced by breaking wave induced turbulence, which may not be fully parameterized solely by the processes shown in Section 2.4. Following Hsu and Liu [72], a non-dimensional parameter based on breaking wave turbulence energy k_b is introduced to parameterize the effects of breaking wave turbulence:

$$\frac{e_k k_b}{(s-1)gD_{50}^i} \tag{3.76}$$

with e_k being a numerical coefficient, which is calibrated empirically on the basis of comparisons with the measured data. A generalized Shields parameter to calculate the sediment pickup is thus give as:

$$\theta_i = \frac{u_*^2 + e_k k_b}{(s-1)gD_{50}^i} \tag{3.77}$$

3.5 A New Bedload Module – SANTOSS

To improve the accuracy and reliability of bedload transport in the existing FVCOM model, and more importantly, to include several important physical processes influence sediment motion within the near bed region under progressive waves that have been identified in recent year of research, a new bedload module is added into the developed model system. The following introduction of this new bedload module is rewritten from van der A et al. [78].

3.5.1 General

Dibajnia and Watanabe [166] initially proposed the semi-unsteady "half-cycle" concept in which the sediment transport during the positive "crest" and the negative "trough" half-cycle are distinguished, the wave-averaged total net sand transport rate (bedload and suspended load) in a whole wave cycle is described as the sum of the contributions from the "crest" and "trough" half-cycles. Such an approach has the advantage over the traditional steady 'equilibrium' transport formula that many wave-induced unsteadiness effects can be included, including the wave asymmetry, sediment grain size effects and etc., by distinguishing the transport flux at each half cycle.

This concept further takes the unsteady phase lag effects into account by working out the amount of sand transported during each half-cycle, i.e. the sand entrained and transported during the present half-cycle, and the sand entrained during the previous half cycle but without settling out and being transported in the present half-cycle. Based on this concept, van der A et al. [78] further developed a new semi-unsteady sand transport formula, SANd Transport in OScillatory flows in the Sheet flow regime (hereinafter SANTOSS), for net sand transport induced by non-breaking waves and currents. In this sand transport formula, several important processes are recognised and incorporated, including the effects of wave acceleration skewness, the effects of progressive surface waves, distinguishing itself with former semi-unsteady formulaes(Dibajnia and Watanabe[167, 168]; Silva et al. [83]; Watanabe and Sato [80]).

The non-dimensional net transport rate is given by the following formula:

$$\overrightarrow{\Phi} = \frac{\overrightarrow{q_s}}{\sqrt{(s-1)gD_{50}^3}} = \frac{q_{slp1}\sqrt{|\theta_c|}T_c(\Omega_{cc} + \frac{T_c}{2T_{cu}}\Omega_{tc})\frac{\overrightarrow{\theta_c}}{|\theta_c|} + q_{slp2}\sqrt{|\theta_t|}T_t(\Omega_{tt} + \frac{T_t}{2T_{tu}}\Omega_{ct})\frac{\overrightarrow{\theta_t}}{|\theta_t|}}{T} \tag{3.78}$$

where $\overrightarrow{q_s}$ is the volumetric net transport rate per unit width, $s = (\rho_s - \rho)/\rho$ is the relative density in which ρ_s and ρ are the densities of sand and water respectively, g is acceleration due to gravity and D_{50} is the sand median diameter; q_{slp1} and q_{slp2} represent the bed slope effect on bedload transport rate (see Eq. (3.134)); $\overrightarrow{\theta}$ is the non-dimensional bed shear stress (Shields parameter), with subscripts "c" and "t" implying "crest" and "trough" half cycles respectively; T is wave period; T_c is the duration of the crest (positive) half cycle and T_{cu} is the duration of accelerating flow within the crest half cycle (Figure 3.5); similarly T_t is the duration of the trough (negative) half cycle and T_{tu} the period of accelerating flow within the trough half cycle. Ω_{cc}, Ω_{tc}, Ω_{tt}, Ω_{ct} are the four main contributions to the net transport rate with the following meanings:

- Ω_{cc} represents the sand load that is entrained during the wave crest period and transported during the crest period;
- Ω_{tc} represents the sand load that is entrained during the wave trough period and transported during the crest period;
- Ω_{tt} represents the sand load that is entrained during the wave trough period and transported during the trough period;
- Ω_{ct} represents the sand load that is entrained during the wave crest period and transported during the trough period.

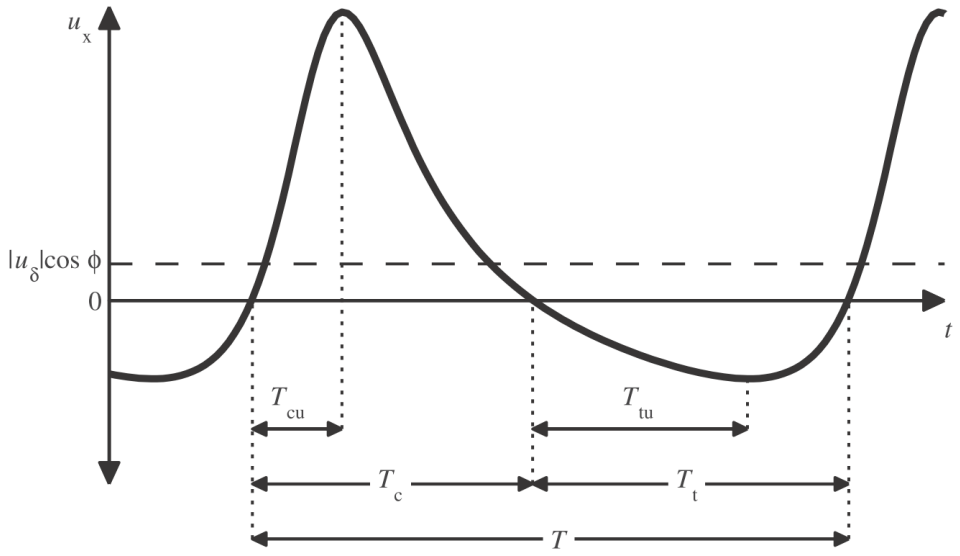

Figure 3.5: Definition sketch of near-bed velocity time-series in wave direction. The parameters T_c and T_t are the positive (crest) and negative (trough) flow durations. Similarly, $T_c u$ and $T_t u$ are the durations of flow acceleration in positive and negative x-directions (after van der A et al. [78]).

The total sand load in each half-cycle is multiplied by $\sqrt{\theta_i}$, representing a (non-dimensional) near-bed (friction) velocity, to obtain the non-dimensional half-cycle transport rate. Both half-cycle transport rates are weighted with their duration relative to the wave period (T_c/T and T_t/T respectively). Since Ω_{tc} and Ω_{ct} represent the sediment load remaining in the water column beyond the phase of flow reversal, the travel distance must be affected by the velocity shortly after flow reversal. For acceleration-skewed flow larger velocities are reached sooner after the flow reversal 'offshore-onshore', i.e. during the crest period, than after the flow reversal 'onshore-offshore', i.e. during the trough period; which means a greater travel distance for Ω_{tc} compared to Ω_{ct}. In Eq. (3.78) the travel distance $\sqrt{|\theta_c|}T_c$ for the load Ω_{tc} is therefore multiplied by the ratio $\frac{T_c}{2T_{cu}}$ (>1) while for the load Ω_{ct} the travel distance $\sqrt{|\theta_t|}T_t$ is multiplied by $\frac{T_t}{2T_{tu}}$ (<1). In the case of no acceleration skewness the effect disappears since $\frac{T_c}{2T_{cu}} = \frac{T_t}{2T_{tu}} = 1$.

In total, the SANTOSS formula is designed to predict the net sand transport for given sand characteristics and given current and wave-generated oscillatory flow at the top of the wave boundary layer ($z = \delta_{wbl}$). It can be therefore applied to the wave shoaling zone prior to wave breaking and the subsequent surf zone.

To facilitate the implementation of this formula (Eq. (3.78)) in oscillatory flow or

under progressive surface waves, a complete description on how to calculate Eq. (3.78) is given in the following sessions.

3.5.2 The sand entrainment during each half-cycle with phase lag effect

The four sand load contributions in Eq.(3.78), after considering the effect of phase lag, are given in the following manner:

$$\Omega_{cc} = \begin{cases} \Omega_c & \text{, if } P_c \leq 1 \\ \frac{1}{P_c}\Omega_c & \text{, if } P_c > 1 \end{cases} \tag{3.79}$$

$$\Omega_{ct} = \begin{cases} 0 & \text{, if } P_c \leq 1 \\ (1-\frac{1}{P_c})\Omega_c & \text{, if } P_c > 1 \end{cases} \tag{3.80}$$

$$\Omega_{tt} = \begin{cases} \Omega_t & \text{, if } P_t \leq 1 \\ \frac{1}{P_t}\Omega_t & \text{, if } P_t > 1 \end{cases} \tag{3.81}$$

$$\Omega_{tc} = \begin{cases} 0 & \text{, if } P_t \leq 1 \\ (1-\frac{1}{P_t})\Omega_t & \text{, if } P_t > 1 \end{cases} \tag{3.82}$$

where P_i (the subscript "i" represents either "c" for crest or "t" for trough) is the phase lag parameter for the corresponding half-cycles which controls how much of that sand is transported within the present half-cycle and how much remains in suspension to be transported in the following half-cycle.

The phase lag parameter is calculated according to:

$$P_c = \begin{cases} \alpha_{pl}(\frac{1-\xi_s\hat{u}_c}{c})\frac{\eta_r}{2(T_c-T_{cu})W_{sc}} & \text{, if } \eta_r > 0\text{(ripple regime)} \\ \alpha_{pl}(\frac{1-\xi_s\hat{u}_c}{c})\frac{\delta_{sc}}{2(T_c-T_{cu})W_{sc}} & \text{, if } \eta_r = 0\text{(sheet flow regime)} \end{cases} \tag{3.83}$$

$$P_t = \begin{cases} \alpha_{pl}(\frac{1+\xi_s\hat{u}_t}{c})\frac{\eta_r}{2(T_t-T_{tu})W_{st}} & \text{, if } \eta_r > 0\text{(ripple regime)} \\ \alpha_{pl}(\frac{1+\xi_s\hat{u}_t}{c})\frac{\delta_{st}}{2(T_t-T_{tu})W_{st}} & \text{, if } \eta_r = 0\text{(sheet flow regime)} \end{cases} \tag{3.84}$$

where α_{pl} is a calibration coefficient, η_r is ripple height, δ_{si} is sheet flow layer thickness for the half cycle (see the following details) and W_{si} is the sediment settling velocity within the half cycle. The phase lag effect results from the generation and ejection of sediment laden vortices on the ripple sides in the ripple regime, while mainly occur for fine sands in the sheet flow regime. Therefore, the ripple regime and sheet flow regime are distinguished in this approach.

The term $r_i/\left[2(T_i - T_{iu})W_{si}\right]$ represents the ratio of a representative sediment stirring height (r_i = ripple height η_r or sheet flow layer thickness δ_{si}) and the sediment

settling distance ($2(T_i - T_{iu})W_{si}$) within the half cycle. In this term, the half cycle period T_i is replaced with the deceleration time within each half cycle, $2(T_i - T_{iu})$, to account for the effect of acceleration skewness, indicating that an increasing (forward leaning) acceleration skewness leads to a smaller crest phase lag parameter P_c (larger P_t) as the settling time increases (decreases) during the crest (trough) half-cycle. In the absence of acceleration skewness $T_{iu} = T_i/2$, the settling time thus reduces to the commonly used half-cycle period since $2(T_i - T_{iu}) = T_i$. This effect had been observed in the fine sand sheet flow experiments of van der A et al. [169] and the 1DV model simulation of Ruessink et al. [170], and it is also expected to play a significant role under rippled bed conditions (Van der A et al. [78]).

The sand settling velocities during the crest (W_{sc}) and trough (W_{st}) half cycles are calculated as follows:

$$W_{sc} = W_s - W_{min}(r_c) \tag{3.85}$$

$$W_{st} = max(W_s - W_{max}(r_t), 0) \tag{3.86}$$

where $W_{min}(r_c)$ and $W_{max}(r_t)$ are the peak negative and peak positive vertical water particle velocities at the elevation of r_c and r_t, respectively; they are estimated using the Stokes 2nd order wave theory. W_s is the still-water settling velocity determined by the Soulsby [125] proposed formula as following:

$$W_s = \frac{\nu}{0.8D_{50}}(\sqrt{10.36^2 + 1.049D_s^{*3}} - 10.36) \tag{3.87}$$

in which the mean grain diameter of suspended sand is assumed to be 80% of that of the sand bed, i.e. $d_s = 0.8D_{50}$ (van Rijn [84]); $D_s^* = 0.8D_{50}[\frac{(s-1)g}{\nu^2}]^{\frac{1}{3}}$ is the dimensionless grain size. The selected elevation is $r_i = \eta_r$ in the ripple regime and $r_i = \delta_{si}$ in the sheet flow regime. The inclusion of $W_{min}(r_c)$ and $W_{max}(r_t)$ in Eqs. (3.85) and (3.86) accounts for an extra effect of surface progressive waves (not tunnel-type oscillatory flow) on the phase lag behaviour. Although wave-induced vertical orbital velocities are small near the bed, they can be of the same order of magnitude as the (still-water) sediment settling velocity, especially for fine sand and high waves. Therefore, the presence of a vertical orbital velocity leads to an asymmetry between the crest and trough half cycle: in the deceleration phase of the crest half cycle, wave-induced vertical particle velocities are increasing and are directed downwards, aiding the sediment settling process; in the trough half cycle, the increasing, upwards-directed wave-induced particle velocities reduce this sediment settling process. For tunnel-type oscillatory flows $W_{sc} = W_{st} = W_s$.

Wave non-uniformity produces horizontal gradients in the horizontal sediment flux, with the result that sediment concentration is no longer controlled by local vertical sediment fluxes alone (i.e. pick-up from and deposition to the bed). Kranenburg et al. [171] showed that, even for sinusoidal waves, the intra-wave horizontal sediment advection could lead to a net transport rate in the direction of wave propagation. This effect is accounted for in the present SANTOSS formula through a correction of the phase-lag parameters P_i (Eqs. (3.83) and (3.84)), by incorporating the factors of $(\frac{1-\xi_s \hat{u}_c}{c})$ and $(\frac{1+\xi_s \hat{u}_t}{c})$ for the crest load and trough load respectively, where c is wave speed, ξ_s is a calibration factor. This is a second effect of surface progressive waves on the phase lag behaviour.

The sand load entrained during each half-cycle is described with the Shields parameter as follows:

$$\Omega_i = \begin{cases} 0, & \text{if } |\theta_i| \leq \theta_{cr} \\ m_{st}(|\theta_i| - \theta_{cr})^{n_{st}}, & \text{if } |\theta_i| > \theta_{cr} \end{cases} \tag{3.88}$$

where the critical Shields number, θ_{cr}, is determined by Soulsby [125] as the following:

$$\theta_{cr} = \frac{0.3}{1 + 1.2D_s^*} + 0.055\,(1 - exp(-0.02D_s^*)) \tag{3.89}$$

in which $D_s^* = D_{50}\left[\frac{(s-1)g}{\nu^2}\right]^{\frac{1}{3}}$ is the dimensionless particle size; proportionality constant m_{st} and power of the excess Shields parameter n_{st} are two calibration coefficients. The process of how to calculate the non-dimensional Shields parameters is described in detail in Section 3.5.3.

3.5.3 Bed shear stress

The non-dimensional total bed shear stress (Shields parameter) vector is:

$$\overrightarrow{\theta_i} = \{\theta_{ix}, \theta_{iy}\} \tag{3.90}$$

where subscript "i" is either "c" for crest or "t" for trough. The x and y components of the Shields parameter are:

$$\theta_{ix} = |\theta_i| \frac{u_{i,rx}}{|u_{i,r}|} + \frac{\tau_{wRe}}{\rho(s-1)gD_{50}} \tag{3.91}$$

$$\theta_{iy} = |\theta_i| \frac{u_{i,ry}}{|u_{i,r}|} \tag{3.92}$$

where τ_{wRe} is a stress contribution induced by surface progressive waves (see the details below), which is not present in tunnel-type oscillatory flow situations. The magnitude of the Shields parameter is given by:

$$|\theta_i| = \frac{\frac{1}{2} f_{w\delta i} |u_{i,r}|^2}{(s-1)gD_{50}} \tag{3.93}$$

where $f_{w\delta i}$ is the wave-current friction factor. Following the approach of Ribberink [172], it is described as a linear combination of the wave friction factor f_{wi} (at crest and trough) and the current friction factor f_δ, as below :

$$f_{w\delta i} = \alpha_f f_\delta + (1 - \alpha_f) f_{wi} \tag{3.94}$$

in which

$$\alpha_f = \frac{|u_\delta|}{|u_\delta| + \hat{u}} \tag{3.95}$$

The relevant velocities (i.e. u_δ, $\hat{u}$, $u_{i,r}$, $u_{i,rx}$ and $u_{i,ry}$)) are described in detail in Section 3.5.4.

The current-related friction factor is calculated after a logarithmic velocity profile assumption:

$$f_\delta = 2 \left[\frac{0.4}{ln(30\delta/k_{s\delta})} \right]^2 \tag{3.96}$$

where $k_{s\delta}$ is the current-related bed roughness. It is calculated, based on grain roughness extended with additional mobile bed roughness for the presence of the wave ripples, as the following:

$$k_{s\delta} = max\{3d_{90}, D_{50}\left[\mu + 6(\langle|\theta|\rangle - 1)\right]\} + 0.4\eta_r^2/\lambda_r \tag{3.97}$$

Similar to f_δ, the wave-related bed roughness k_{sw} (used in calculating the wave friction factor f_{wi}) is given by:

$$k_{sw} = max\{D_{50}, D_{50}\left[\mu + 6(\langle|\theta|\rangle - 1)\right]\} + 0.4\eta_r^2/\lambda_r \tag{3.98}$$

in which η_r and λ_r are ripple height and ripple length respectively (described in detail in Section 3.5.5); the factor μ varies linearly between $\mu = 1$ for sand with $D_{50} \geq 0.2$ mm to $\mu = 6$ for sand with $D_{50} \leq 0.15$ mm:

$$\mu = \begin{cases} 6 & \text{, if } D_{50} \leq 0.15\text{mm} \\ 6 - \frac{5(D_{50}-0.15)}{0.20-0.15} & \text{, if } 0.15\text{mm} < D_{50} \leq 0.20\text{mm} \\ 1 & \text{, if } D_{50} \geq 0.20\text{mm} \end{cases} \tag{3.99}$$

in which D_{50} is entered in mm.

$\langle|\theta|\rangle$ is the time-averaged absolute Shields parameter given by:

$$\langle|\theta|\rangle = \frac{\frac{1}{2} f_\delta |u_\delta|^2}{(s-1)gD_{50}} + \frac{\frac{1}{4} f_w \hat{u}^2}{(s-1)gD_{50}} \tag{3.100}$$

where f_w is the full-cycle wave friction factor based on Swart [173]:

$$f_w = \begin{cases} 0.00251\ exp\left[5.21\left(\frac{\hat{a}}{k_{sw}}\right)^{-0.19}\right] & \text{, for } \frac{\hat{a}}{k_{sw}} > 1.587 \\ 0.3 & \text{, for } \frac{\hat{a}}{k_{sw}} \leq 1.587 \end{cases} \tag{3.101}$$

The calculation of the bed roughnesses ($k_{s\delta}$ in Eq. (3.97) and k_{sw} in Eq. (3.98)) need the value of Shield parameter $\langle|\theta|\rangle$, while $\langle|\theta|\rangle$ also depends on the bed roughnesses (through the calculation of f_δ and f_w by Eqs. (3.96) and (3.101)). Therefore, Eqs. (3.96) - (3.101) are solved in an iterative way.

The wave friction factor for the crest or trough half-cycle (f_{wi}, used in Eq. (3.94)) is separately calculated, with a formula similar to Eq. (3.101):

$$f_{wi} = \begin{cases} 0.00251\ exp\left[5.21\left(\frac{\left(\frac{2T_{iu}}{T_i}\right)^{c_1}\hat{a}}{k_{sw}}\right)^{-0.19}\right] & \text{, for } \frac{\hat{a}}{k_{sw}} > 1.587 \\ 0.3 & \text{, for } \frac{\hat{a}}{k_{sw}} \leq 1.587 \end{cases} \tag{3.102}$$

Following the approach of Silva et al. [83], Eq. (3.102) for f_{wi} includes an extra term $(\frac{2T_{iu}}{T_i})^{c1}$, the ratio of acceleration time-length over half cycle period (with a power of c_1), to account for the effects of acceleration skewness on the bed shear stress. This term $(\frac{2T_{iu}}{T_i})^{c1}$ has the effect of increasing f_{wi} for the flow half-cycle with higher acceleration $\left(\frac{2T_{iu}}{T_i} < 1\right)$ and decreasing f_{wi} for the half-cycle with lower acceleration $\left(\frac{2T_{iu}}{T_i} > 1\right)$. In sinusoidal or pure velocity-skewed flows, this term equals unity and then Eq. (3.102) reduces to the standard full-cycle wave friction factor equation (Eq. (3.101)). c_1 is a

parameter that has an optimal value of 2.6, which is obtained from the measurements of bed shear stress by van der A et al. [174] for a range of acceleration-skewed oscillatory flows.

For progressive surface waves, the vertical orbital water particle motions transfer horizontal momentum in and out of the wave boundary layer, leading to a wave-averaged (Reynolds) stress $-\rho\langle\tilde{u}\tilde{w}\rangle$ (Longuet-Higgins,[15] [175]). The vertical gradient of this stress drives a positive mean flow (boundary layer streaming) in the direction of the wave propagation. This is accounted for in the SANTOSS formula by adding a wave Reynolds stress τ_{wRe} to the x-component bed shear stress at the edge of the wave boundary layer, as per Eq.(3.91), following the approach of Nielsen [176]. It has the effect of increasing the total Shields stress under the wave crest and decreasing the stress under the wave trough. The wave Reynolds stress is estimated as follows:

$$\tau_{wRe} = \rho\frac{f_{w\delta}}{2c}\alpha_w\hat{u}^3 \tag{3.103}$$

with $\hat{u}$ determined according to Eq. (3.109), $\alpha_w = 4/(3\pi) = 0.424$ and c is the wave phase speed. Here $f_{w\delta}$ is the full-cycle wave-current friction factor, $f_{w\delta} = \alpha_f f_\delta + (1 - \alpha_f)f_w$, with f_δ calculated by Eq. (3.96) and f_w calculated by Eq. (3.101).

3.5.4 Velocities and orbital characteristics

The near bed velocity at the edge of the wave boundary layer, $z = \delta$, due to combined wave and current motion is:

$$\vec{u}(t) = \vec{u}_w(t) + \vec{u}_\delta \tag{3.104}$$

where $\vec{u}_w(t)$ is the time-varying free-stream orbital velocity vector and $\vec{u}_\delta$ is the steady current velocity vector. Without loss of generality, (in the following sections) the wave propagates in the x-direction and makes an angle of φ with the direction of obliquely-incident current, then the combined wave and current velocities in the x- and y-directions are:

$$u_x(t) = |u_\delta|cos\varphi + u_w(t) \tag{3.105}$$

$$u_y(t) = |u_\delta|sin\varphi \tag{3.106}$$

respectively. With reference to Figure 3.5, the combined wave-current velocity vectors at moments of maximum and minimum orbital velocity are:

$$\vec{u}_c = \{u_{cx},\ u_{cy}\} = \{\ \hat{u}_c + |u_\delta| cos\varphi, |u_\delta| sin\varphi\} \tag{3.107}$$

$$\vec{u}_t = \{u_{tx},\ u_{ty}\} = \{-\hat{u}_t + |u_\delta| cos\varphi, |u_\delta| sin\varphi\} \tag{3.108}$$

where $\hat{u}_c$ and $\hat{u}_t$ are the peak crest and peak trough orbital velocities (both are defined as positive quantities, i.e. $\hat{u}_c$ >0.0, $\hat{u}_t$ >0.0). The representative orbital velocity amplitude $\hat{u}$ and the representative orbital excursion amplitude $\hat{a}$ for the whole flow cycle are calculated in the following way:

$$\hat{u} = \sqrt{\frac{2}{T}\int_0^T u_w^2(t)dt} \tag{3.109}$$

$$\hat{a} = \frac{\hat{u}T}{2\pi} \tag{3.110}$$

In the calculation of Shields parameters during each half cycle of the wave (Eqs. (3.90) - (3.93)), the representative half-cycle orbital velocity for the wave crest ($\tilde{u}_{c,r}$) and the wave trough ($\tilde{u}_{t,r}$) are used. They are defined as the root mean square velocity of a sinusoidal flow with amplitude of $\hat{u}_c$ and $\hat{u}_t$ respectively, as follows:

$$\tilde{u}_{c,r} = \frac{1}{2}\sqrt{2}\hat{u}_c \tag{3.111}$$

$$\tilde{u}_{t,r} = \frac{1}{2}\sqrt{2}\hat{u}_t \tag{3.112}$$

The representative combined wave-current velocity vectors for each half-cycle are then given as:

$$\vec{u}_{c,r} = \{u_{c,rx},\ u_{c,ry}\} = \{\ \tilde{u}_{c,r} + |u_\delta| cos\varphi, |u_\delta| sin\varphi\} \tag{3.113}$$

$$\vec{u}_{t,r} = \{u_{t,rx},\ u_{t,ry}\} = \{-\tilde{u}_{t,r} + |u_\delta| cos\varphi, |u_\delta| sin\varphi\} \tag{3.114}$$

However, the orbital velocities $\hat{u}_c$, $\hat{u}_t$ and the time-varying free-stream orbital velocity ($\vec{u}_w(t)$) used in the above formulas are all unknown parameters in the present. In addition, the periods (T_c, T_{cu}, T_t, T_{tu}) are also needed in calculation of the phase lag parameters and the wave acceleration skewness which could significantly affect the predicted results of the final sand transport rate. These are all regarded as input parameters to the SANTOSS sand transport model, which however can not be provided by a time-averaged circulation model (e.g. FVCOM) or a spectral wave model (e.g. SWAN). To determine these parameters, an analytical expression for the near-bed wave orbital time series ($u_w(t)$) proposed by Abreu et al. [177] is utilized (see the details in

Appendix B). In this analytical expression, the parameter of skewness (non-linearity), r_{sk}, and the parameter of waveform, ϕ_{sk}, used to determine the velocity and acceleration skewness, are provided by a parametrization method proposed by Ruessink et al. [178].

After the implementation of the approach of Ruessink et al. [178] and Abreu et al. [177], a discrete time series of wave orbital velocity (in one wave period) is obtained:

$$u_w(t) = u_w(t_k); \quad t_k = \frac{k}{N}T \text{ and } k = [0, 1, 2, 3, ..., N-1] \tag{3.115}$$

where N (= 200)is total fraction number of the discrete series; T is the wave period. Based on this discrete wave orbital velocity time series, the orbital velocities $\hat{u}_c$, $\hat{u}_t$ and relevant wave periods (T_c, T_{cu}, T_t, T_{tu}) utilized in determining the sand transport rate are not difficult to be described.

The maximum and minimum orbital velocities are given as:

$$\begin{aligned} \hat{u}_c &= max[u_w(t_k)] \\ \hat{u}_t &= |min[u_w(t_k)]| \, ; k = [0, 1, 2, 3, ..., N-1] \end{aligned} \tag{3.116}$$

while the wave orbital accelerations are determined as follows:

$$a_k = \begin{cases} \frac{u_w(t_{k+1}) - u_w(t_N)}{2T/N} & , \text{ if } k = 1 \\ \frac{u_w(t_{k+1}) - u_w(t_{k-1})}{2T/N} & , \text{ if } 1 < k < N \\ \frac{u_w(t_1) - u_w(t_{k-1})}{2T/N} & , \text{ if } k = N \end{cases} \tag{3.117}$$

The degree of velocity skewness and acceleration skewness could be described respectively by $R = \hat{u}_c/(\hat{u}_c + \hat{u}_t)$ and $\beta = a_{max}/(a_{max} - a_{min})$, in which $a_{max} = max(a_k)$ and $a_{min} = min(a_k)$. Deep water waves could be approximately regarded as sinusoidal waves with vertically and horizontally symmetrical orbital velocities, i.e. $R = 0.5$ and $\beta = 0.5$. When propagate towards the shallow water, waves gradually have larger onshore orbital velocity (with shorter wave crest) and smaller offshore velocity (with longer wave trough), leading to $R > 0.5$. Close to the breaker point, waves could have forward-leaning crest (pitched forward shape) with higher acceleration under the crest when compared to the trough, resulting in $\beta > 0.5$.

The various kinds of period are described by the following formulas:

$$T_c = \begin{cases} t_{0_{pn}} - t_{0_{np}} & , \text{if } t_{0_{pn}} > t_{0_{np}} \\ t_{0_{pn}} - t_{0_{np}} + T & , \text{if } t_{0_{pn}} \leq t_{0_{np}} \end{cases} \tag{3.118}$$

$$T_{cu} = \begin{cases} t_{u_{max}} - t_{0_{np}} & , \text{if } t_{u_{max}} > t_{0_{np}} \\ t_{u_{max}} - t_{0_{np}} + T & , \text{if } t_{u_{max}} \leq t_{0_{np}} \end{cases} \tag{3.119}$$

$$T_{cd} = T_c - T_{cu} \tag{3.120}$$

$$T_t = \begin{cases} t_{0_{np}} - t_{0_{pn}} & \text{, if } t_{0_{pn}} \leq t_{0_{np}} \\ t_{0_{np}} - t_{0_{pn}} + T & \text{, if } t_{0_{pn}} > t_{0_{np}} \end{cases} \tag{3.121}$$

$$T_{tu} = \begin{cases} t_{u_{min}} - t_{0_{pn}} & \text{, if } t_{u_{min}} \leq t_{0_{np}} \\ t_{u_{min}} - t_{0_{pn}} + T & \text{, if } t_{u_{min}} > t_{0_{np}} \end{cases} \tag{3.122}$$

$$T_{td} = T_t - T_{tu} \tag{3.123}$$

where T_c, T_{cu} and T_{cd} respectively represent the duration of the crest (crest period), crest acceleration and crest deceleration; and T_t, T_{tu} and T_{td} respectively represent the duration of the trough (trough period), trough acceleration and trough deceleration; $t_{0_{pn}}$ and $t_{0_{np}}$ represent the time of zero crossing from the positive to negative velocity and that from the negative to positive velocity, respectively; $t_{u_{max}}$ and $t_{u_{min}}$ represent the time when the velocity reaches its maximal and minimal value respectively.

In the original version of the SANTOSS model (van der A et al. [78]; Veen [179]; Schnitzler [59]), the duration of the crest half-cycle (i.e. crest period, T_c) is determined as the part of the wave period (T) with a positive velocity, and the duration of the trough half-cycle (i.e. trough period, T_t) is determined as the part of the wave period (T) with a negative velocity. Therefore, the velocity used to determine the crest/trough periods is the wave orbital velocity (i.e. $\vec{u}_w(t)$ in Eq. (3.104)) in the absent of current; in the presence of a current, the relevant velocity is the combined wave and current velocity (i.e. $\vec{u}(t)$ in Eq. (3.104)). When strong currents are present, the combined wave-current velocity could be only positive or negative during the whole wave period, the zero crossings ($t_{0_{pn}}$ and $t_{0_{np}}$) are thus not present and the durations defined with the above formulas (Eqs. 3.118 - 3.123) are not appropriate any more. Therefore, some relevant changes are made by Veen [179] in order to adapt the SANTOSS model to the situations with strong currents (see details in Appendix C).

However, those adaptions introduced in Appendix C complicate the code of the SANTOSS model a lot and reduce its computational efficiency. More importantly, Eqs. (3.111) and (3.112) become invalid in situations where both waves and currents are present, i.e. new formulas are needed to calculate the representative half-cycle orbital velocities for the wave crest ($\tilde{u}_{c,r}$) and the wave trough ($\tilde{u}_{c,r}$), because the duration of crest (trough) periods are different from that in situations with waves only according to the above mentioned definitions. In the present study, a different definition method for the crest (trough) period is used, i.e. use only the wave orbital velocity ($\vec{u}_w(t)$) to

determine the crest (trough) period in both situations with or without current. The new definition method is compared with the original method in Appendix D, and it shows that the new method is physically more reasonable when the magnitude of mean current is very strong (i.e. close to or larger than the magnitude of peak crest/trough wave orbital velocity). With this new definition, the adaptions introduced in Appendix C are not necessary any more and Eqs. (3.111) and (3.112) are valid for all situations.

3.5.5 Ripple dimensions

In applications where the ripple dimensions are unknown, the ripple predictor of O'Donoghue et al. [8] is incorporated:

$$\frac{\eta_r}{\hat{a}} = m_\eta n_\eta \left(0.275 - 0.022\hat{\Psi}^{0.42}\right) \tag{3.124}$$

$$\frac{\lambda_r}{\hat{a}} = m_\lambda n_\lambda \left(1.97 - 0.44\hat{\Psi}^{0.21}\right) \tag{3.125}$$

where η_r and λ_r represent the ripple wave height and ripple wave length, respectively.

$$m_\eta = \begin{cases} 0.55 & \text{, if } D_{50} \leq 0.22\text{mm} \\ 0.55 + \frac{0.45(D_{50}-0.22)}{0.30-0.22} & \text{, if } 0.22\text{mm} \leq D_{50} < 0.30mm \\ 1.0 & \text{, if } D_{50} \geq 0.30\text{mm} \end{cases} \tag{3.126}$$

$$m_\lambda = \begin{cases} 0.73 & \text{, if } D_{50} \leq 0.22\text{mm} \\ 0.73 + \frac{0.27(D_{50}-0.22)}{0.30-0.22} & \text{, if } 0.22\text{mm} \leq D_{50} < 0.30mm \\ 1.0 & \text{, if } D_{50} \geq 0.30\text{mm} \end{cases} \tag{3.127}$$

with the mobility number $\hat{\Psi} = max\left(\hat{\Psi}_c, \hat{\Psi}_t\right)$ for regular flow, whereby the maximum mobility number at crest or trough is defined as $\hat{\Psi}_i = \frac{\hat{u}_i^2}{(s-1)gD_{50}}$, and for irregular flow $\hat{\Psi} = \hat{\Psi}_{1/10} = \hat{u}_{1/10}^2/(s-1)gD_{50}$. Since information on $\hat{u}_{1/10}$ (average of the highest one-tenth orbital velocities) is not available for most irregular flow datasets, it is for simplicity assumed that the irregular flows are Rayleigh distributed, therefore $\hat{u}_{1/10} = 1.27\hat{u}$.

To avoid strong discontinuities in the predicted net transport rates with increasing flow intensities, the factors n_η and n_λ are introduced to allow for a smooth transition between the ripple regime and the flat bed sheet flow regime:

$$n_\eta = n_\lambda = \begin{cases} 1 & \text{, if } \hat{\Psi} \leq 190 \\ \frac{1}{2}\left(1 + cos\left\{\pi \frac{\hat{\Psi}-190}{240-190}\right\}\right) & \text{, if } 190\hat{\Psi} < 240 \\ 0 & \text{, if } \hat{\Psi} \geq 240 \end{cases} \tag{3.128}$$

3.5.6 Sheet-flow layer thickness

The sheet flow layer thickness δ_{si} is calculated as following:

$$\frac{\delta_{si}}{D_{50}} = \begin{cases} 25\hat{\theta}_i & \text{, if } D_{50} \leq 0.15\text{mm} \\ 25 - \frac{12(D_{50}-0.15)}{0.20-0.15} & \text{, if } 0.15\text{mm} \leq D_{50} < 0.20mm \\ 13\hat{\theta}_i & \text{, if } D_{50} \geq 0.20\text{mm} \end{cases} \tag{3.129}$$

where $\hat{\theta}_i$ is Shields parameter based on the crest/trough velocity amplitude $\hat{u}_i$ as follows:

$$\hat{\theta}_i = \frac{\frac{1}{2} f_{w\delta i}\ \hat{u}_i^2}{(s-1)gD_{50}} \tag{3.130}$$

with $f_{w\delta i}$ the wave-current friction factor according to Eq. (3.94), wave and current related roughness are described in detail in Section 3.5.3. For fine sand ($D_{50} \leq 0.15$mm) Eq. (3.129) differs slightly from Dohmen-Janssen's [60] original equation since the constant is recalibrated (here 25 instead of 35 in the original) as a result of the increase in the wave related roughness for fine sands.

3.5.7 Effect of bed slope

Bed slope effect on the critical shear stress

When the sea floor is sloping, the gravity contribution to the net force on the sand grain can increase or decrease the critical shear-stress required from the flow. The gravity force can be added to the shear-stress force from the flow to calculate the critical condition for a grain on a bed of arbitrary stream-wise and cross-stream slopes. According to Soulsby [125], the critical bed shear stress ($\tau_{cr,slp}$) for sand on a bed sloping at an angle β_{sl} to the horizontal, in a flow making an angle ψ to the up-slope direction is related to the value $\tau_{cr,0}$ for the same sand on a horizontal bed by the expression:

$$\frac{\tau_{cr,slp}}{\tau_{cr,0}} = \frac{\cos\psi_{sl}\sin\beta_{sl} + \left(\cos^2\beta_{sl}\tan^2\phi_r - \sin^2\psi_{sl}\sin^2\beta_{sl}\right)^{1/2}}{\tan\phi_r} \tag{3.131}$$

where ϕ_r is the angle of repose of the sediment at which slope the sediment will avalanche in a zero flow (default value is 33°); the angle of the bed slope $\beta_{sl} = \tan^{-1}(dz_{bed}/dx_\alpha)$, positive in the upslope direction and negative in the down slope direction. When the flow is up or down the slope (i.e. longitudinal direction when $\psi_{sl} = 0°$ or 180°), Eq. (3.131) would reduce to

$$\frac{\tau_{cr,slp}}{\tau_{cr,0}} = \frac{\sin(\phi_r + \beta_{sl})}{\sin\phi_r} \tag{3.132}$$

If the flow is directed laterally across the slope (i.e. $\psi_{sl} = \pm 90°$), then

$$\frac{\tau_{cr,slp}}{\tau_{cr,0}} = \cos\beta_{sl}\left(1 - \frac{\tan^2\beta_{sl}}{\tan^2\phi_r}\right)^{1/2} \tag{3.133}$$

Bed slope effect on the sediment transport rate

The bed slope effect also affects the net bedload transport rate. Generally, the bed slope effect is accounted for by multiplying a bed slope factor on the transport rate calculated in horizontal bed condition. Following Bagnold [180], this factor is given as:

$$q_{slp} = 1 + \alpha_{slp}\left[\frac{\tan\phi_r}{(\tan\phi_r + \tan\beta_{sl})\cos\beta_{sl}} - 1\right] = 1 + \alpha_{slp}\left[\frac{\sin\phi_r}{\sin(\phi_r + \beta_{sl})} - 1\right] \tag{3.134}$$

where α_{slp} is a tuning parameter with a default value of 1.0. Thus, it is expected that the sediment transport rate increases in the down slope bed and decreases in the up-slope bed. The original SANTOSS model is calibrated with data that measured only in horizontal bed conditions (van der A et al.[78]). Therefore, the bed slope effect is absent in the original SANTOSS model and must be supplemented. Different from quasi-steady formulations, the SANTOSS model describes the wave-averaged total net sand transport rate in a whole wave cycle as the sum of the contributions from the "crest" and "trough" half-cycles. The sand transport from these two half-cycles generally (when the mean current is not very strong) have opposite directions. Therefore it is physically more reasonable to separately account for the bed slope effect on these two bed transports.

3.5.8 Effect of wave breaking induced turbulence on bedload transport

As introduced in Section 3.5.1, the SANTOSS model is originally developed for net sand transport induced by non-breaking waves and currents, while the effect of wave-breaking induced turbulence on sand entrainment is not accounted for. Therefore, it has limited predictive capability when applied to the wave breaking regions. To extend its application to breaking waves and within the surf zone, the representative half-cycle orbital velocity is extended following Reniers et al. [135]:

$$\tilde{u}_{i,r} = \sqrt{\tilde{u}_{i,rold}^2 + \gamma_k k_b} \tag{3.135}$$

$\tilde{u}_{i,rold}$ on the R.H.S. is calculated by Eq. (3.111) for wave crest half-cycle and Eq. (3.112) for wave trough half-cycle; k_b is the near-bed turbulence kinetic energy which

could be predicted from turbulence closure models or parameterization methods; γ_k is a numerical calibration factor.

One of the most widely used formulations for k_b is proposed by Roelvink and Stive [181] as follows:

$$k_b = \frac{(\epsilon_r/\rho)^{2/3}}{exp(D/H_{rms}) - 1} \tag{3.136}$$

where ϵ_r is the roller energy dissipation rate that defined in Section 3.2.1, D is the water depth and H_{rms} is the root mean square wave height.

3.6 Morphology Evolution Module

The morphology evolution module computes the morphological changes by solving the sediment continuity (Exner) equation, given by:

$$\frac{\partial z_{bed}}{\partial t} + \frac{1}{1-\varepsilon_0}\left(\frac{\partial q_{tot,x}}{\partial x} + \frac{\partial q_{tot,y}}{\partial y}\right) = 0 \tag{3.137}$$

where z_{bed} is the bed level elevation measured from the deepest water depth in the study area (positive upwards), ε_0 is the sediment porosity, $q_{tot,x}$ and $q_{tot,y}$ are the total sediment transport rates (in m^3/ms) in X and Y direction, respectively.

The morphological changes can have significant influence on hydrodynamic processes and sediment transport when they are larger than a few percent of the water depth. Following Warner et al. [47], the bottom boundary condition of the vertical velocity is equated to the rate of change of the bed elevation in order to account for the effect of morphological changes.

3.7 Coupling Procedure and Parallelization

In this section, the coupling procedure between the circulation and UnSWAN wave model is described in detail; the coupling procedure of other models is in a similar way and thus is not repeated (Figure 3.6). Furthermore, two types of parallelization method utilized in the developed model system are introduced: the V-B mesh (see details below) is exclusively designed for the UnSWAN wave model, while the E-B mesh is used by the other sub-models (including the wave model A) which is the same as that used by the original FVCOM model.

3.7.1 The New Coupler Module

To facilitate data exchange between the wave model and circulation model, a new coupler module is developed based on a two-way coupling scheme, similar to the approach employed by FVCOM-SWAVE (Wu et al. [182]). Due to the implicit scheme used in UnSWAN, the wave propagation time step could be generally much larger than the circulation time step. Therefore, the coupling interval is designed to be the same as the wave propagation time step, which is specified as a multiple of the internal time step of the circulation model. In the following tests in the present research, however, the default wave time step is taken as the same as the internal time step of the circulation model for simplicity reason.

At the beginning of the defined coupling cycle, the wave model runs first, with the specific sea surface elevation, current fields and bathymetric changes that were obtained directly from the circulation model at the end of previous cycle, to compute the required wave parameters, e.g. wave height, wave direction, wave relative peak period, wave bottom orbit velocity and wave dissipation variance. Based on this updated information, the coupler module then calculates the relevant WEC terms, including non-conservative wave accelerations, wave friction factor, which are then passed to the circulation model to solve the hydrodynamic variables. With these WEC terms, the circulation model runs several time steps to the end of this coupling cycle and provides data for solving the wave model at the next time interval, marks the end of a coupling cycle of wave and current models.

3.7.2 Mesh Decomposition and Parallelization

All of the sub-models, including the UnSWAN wave model, utilise the same set of global triangular mesh in this research, which avoids the interpolation between different sets of computational grids. However, two different types of local sub-mesh, i.e. node-based sub-meshes (V-B; Figure 3.4) for the UnSWAN wave model (Dietrich et al. [183]) and element-based sub-meshes (E-B; Figure A.3) for the other models (e.g. circulation model; Chen et al [108]; Wang and Shen [46]) following the original FVCOM decomposition approach, are employed in the developed parallel coupling scheme in the present research. This is determined by the different intrinsic characteristics of these two models, e.g. the locations (centroids or vertexes) of variables, discretization technique (finite volume or finite difference method) for partial differential equations. These two types of decomposed sub-mesh are both assigned to the same group of processors for calculation. However, it should be noted that due to the randomness in the mesh generation and processor assignment, the two sets of local mesh owned by the same processor do not necessarily consist of the same triangular elements and vertices. Therefore, the cou-

pling procedure of UnSWAN and the circulation sub-model, especially in the parallel situations, need to be specially designed. More explanations on this coupling procedure are depicted below.

- Data exchange

  A new coupler module is developed based on a two-way coupling scheme to facilitate the data exchange and parallel computing. Figure 3.6 shows the flow chart for the present model. The coupling interval is designed to be the same as the wave propagation time step, which is specified as a multiple of the internal time step of the circulation model. At the beginning of this coupling cycle, the variables obtained from FVCOM are firstly transferred onto the vertex-based mesh (the process of E-B to V-B shown in Figure 3.6), with which UnSWAN calculates the required wave parameters. These wave parameters are then transferred back to the element-based mesh (V-B to E-B as shown in Figure 3.6). After this process, the coupler module uses these wave parameters to calculate the relevant wave-current interaction terms which are then passed to the circulation model to solve the hydrodynamic variables.

  The same with the original FVCOM, the Single Processor Multiple Data (SPMD) approach is used to implement the parallelization. The method for inter-processor data exchange between the same types of mesh grids is that in the original FVCOM. The data communication between the FVCOM mesh and UnSWAN mesh is newly developed, which requires the information exchange between the E-B to V-B and V-B to E-B as described below.

- Communication management

  The technique to realise the communication between E-B mesh to V-B mesh and V-B mesh to E-B mesh follows the method for data I/O procedure in FVCOM. Taking V-B mesh to E-B mesh as an example, the wave parameters computed by the UnSWAN model are stored in the vertex-based sub-domain (V-B) mesh girds. In order to transfer these on the element-based (E-B) mesh grids as required; they are firstly collected by the master processor onto the global mesh grid and stored in the memory of the master processor. Then the master processor distributes these data onto the element-based sub-domain mesh grids for each processor. The procedure is very similar to the method for data I/O in FVCOM, i.e. the master processor collects the data from each sub-domain mesh gird (stored in multiple processors) and combine them onto the global mesh before outputting into NetCDF files; the forcing data is firstly read in by the master processor and then distributed into local sub-domain mesh grids.

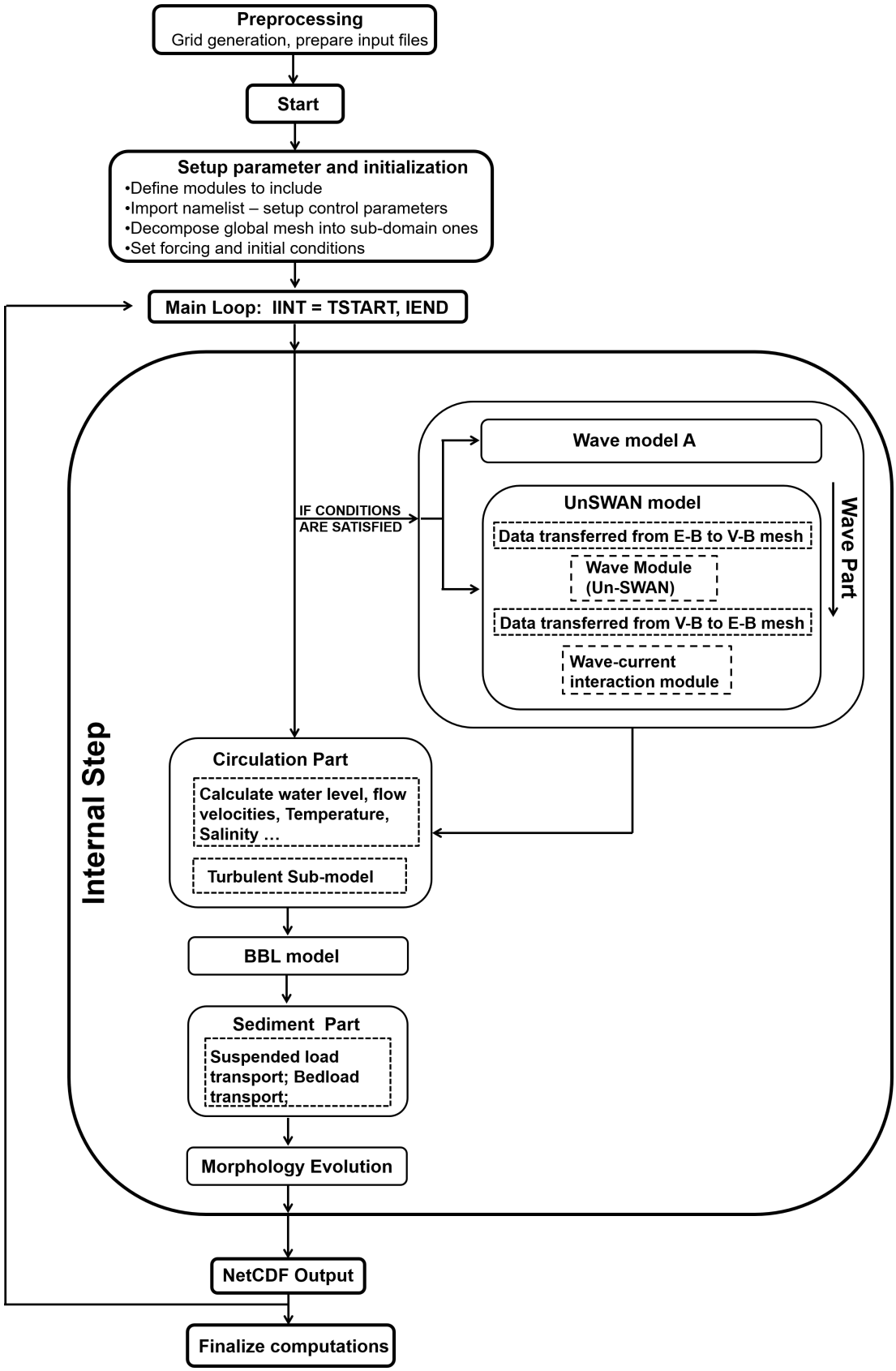

Figure 3.6: Flow chart of the coupled model system.

3.8 Conclusions

This chapter describes the new development in wave-current interaction, wave breaking modelling, turbulence modelling, sediment transport in both suspended load and bed load based on the existing UnSWAN and FVCOM models. Within this development, some of the most recent progress in coastal morphodynamics are implemented. The detailed development process contains the following portions:

1. Development of a new three-dimensional coastal hydrodynamic model system with fully coupled 3D wave-current interactions on an unstructured grid, which is used as a basis for the morphodynamic model system developed in the present research.

   This is achieved by coupling the unstructured version of the third generation wind wave model SWAN (hereinafter UnSWAN, Booij et al. [85]; Zijlema [6]), as the wave module, to the unstructured-grid, three-dimensional oceanic circulation model, Finite Volume Coastal Ocean Model (FVCOM, Chen et al. [108]). A wave-current interaction scheme based on the VF approach (Uchiyama et al. [23]; McWilliams et al. [49]) is developed and implemented into FVCOM to account for wave effects on currents (WEC). The Generic Length Scale (GLS; Umlauf and Burchard [66]) scheme is incorporated and modified to better account for the wave-enhanced turbulence generation, dissipation and vertical mixing in breaking-wave conditions. A wave roller transport model is added in this modelling system to account for wave breaking under influence of the surface roller, which is absent in the original FVCOM code. A new coupling module is also developed to facilitate the communication between UnSWAN and FVCOM, and realise the model coupling procedure

2. Development of the suspended sediment transport module.

   To be consistent with the wave-current interaction approach, the original advection-diffusion (AD) suspended sediment model is modified to account for the wave-related suspended sediment transport (i.e. the wave-averaged Lagrangian mean velocity is used in the advection terms of AD model). Several options are provided to calculate the sediment pick-up rates, including those parameterizations that account for the wave breaking turbulence effects (e.g. Hsu and Liu [72]; van der Zanden [77]). The approach proposed by van der Zanden [77] is, by the first time, used in a morphodynamic model with the model predicted TKE (see details in Section 5.5).

3. Development of the bedload transport module of the morphodynamic model system following the SANTOSS formulae. The semi-unsteady practical formulae

SANTOSS (van der A et al. [78]) is implemented in this developed morphodynamic model system as a further option (among those already existed quasi-steady models in the original FVCOM) to predict the bedload transport rate. Some adaptions, which are thought more reasonable, are made for some specific applications. By accounting for more physical processes (e.g. phase-lag effect, progressive surface wave effect, effect of velocity and acceleration skewness) explicitly, this model can significantly improve the model results (e.g. Section 5.6).

4. Integration of the wave, circulation, suspended sediment and bedload transport modules into the the fully coupled, three-dimensional coastal morphodynamic model system.

   Morphology evolutions thus can be predicted by the present model system as a result of interactions between the hydrodynamics (waves and currents), sediment transport and the morphology itself.

Chapter 4

Model Validation

4.1 Introduction

This chapter presents the detailed validation of the hydrodynamic part of the developed morphodynamic model system, against several cases with different spatial scales and both 2D and 3D complex hydrodynamic conditions.

In Section 4.2, the new model system is firstly validated against the analytical solutions for obliquely incident waves break on a constant mild sloping (1/80) planar beach. Then the model system is applied to several more complex cases with detailed measurements to test its efficiency and to examine the details of hydrodynamics under breaking waves on a beach at very different scales. Three further test cases are described in detail. The first case shown in Section 4.3 reproduces the breaking wave characteristics, wave-induced undertow and turbulence structures as measured in high detail around a fixed breaker bar during a recent laboratory experiment. In the second case (Section 4.4), the model system is applied to simulate field-scale measurements conducted during the DUCK94 experiment (e.g. Garcez Faria et al. [19, 184]), in which wave-induced undertow as well as alongshore currents are studied and further analysed through momentum balance. As these two cases largely focus on conditions of (approximate) alongshore uniformity, the third case described in Section 4.5 involves a laboratory experiment conducted on a beach with a shore-parallel breakwater, which introduces three-dimensionality in the domain and flow development. This case examines the model's ability of simulating complex three-dimensional flow around structures in coastal regions with desirable flexibility in the unstructured mesh.

4.2 Obliquely Incident Waves on A Planar Beach

The new model system is firstly validated against an analytical solution for obliquely incident waves breaking on a constant mild sloping (1/80) planar beach. This test case was initially posed by Haas and Warner [142] and later used as a benchmark in a series of numeric studies using different wave-current interaction approaches, e.g. the depth-dependent Radiation Stress formulation (N. Kumar et al. [48]; Haas and Warner [142]), the Vortex Force formulation (Uchiyama et al. [23]; Kumar et al. [25]) and the glm2z-RANS theory (Michaud et al. [185]).

The model domain covers a 1900 m long (cross-shore) by 300 m wide (alongshore) rectangular area, which is discretized using isosceles right triangles with grid size of 20 m in the horizontal and 31 vertical Sigma levels with uniform thickness, resulting in a total of 1536 nodes and 2850 elements. It has a west-east orientation with the offshore boundary open boundary located at $x = 100$m. The water depth varies from 12m below the still water level at the offshore boundary to 0.75m above at the shoreline. The boundary conditions include periodic boundaries in the alongshore direction, wetting/drying at the shoreline, and a clamped water level boundary condition (Chen et al. [108]) at the offshore boundary. Coriolis forces are excluded, and there is no lateral momentum diffusion, stratification, and surface wind/heat/freshwater fluxes. The roller waves and bottom streaming effects are also not included. The bottom stress is formulated using the quadratic bottom drag with a constant c_d value of 0.0015. The wave information is provided at the offshore boundary based on a JONSWAP spectrum with 2m significant wave height, 10sec peak wave period and a 10° angle of incidence. Both the barotropic and baroclinic time step in the standard test case is 0.1 sec, and results are used for the analysis in Section 4.2.1 and Section 4.2.2.

For this condition, Uchiyama et al. [148] showed that the barotropic continuity balance can be integrated in the cross-shore direction to yield a balance between depth-averaged Eulerian and Stokes velocities, i.e. $\overline{u} = -\overline{u}^{st}$. In addition, a dominant cross-shore barotropic momentum balance between the pressure gradient force (PGF) and breaking acceleration, i.e.

$$\rho_0 g \frac{\partial}{\partial x}\left(\zeta^c - \hat{\zeta}\right) = \frac{\varepsilon^b k_x}{D\sigma} \tag{4.1}$$

and an alongshore momentum balance between bottom drag and breaking acceleration, i.e.

$$\rho_0 c_d \left|\overline{\boldsymbol{V}}\right| \overline{v} = \frac{\varepsilon^b k_y}{\sigma} \tag{4.2}$$

can be obtained; where $\overline{\boldsymbol{V}} = \sqrt{\overline{u}^2 + \overline{v}^2}$. Along with the wave parameters and wave breaking induced dissipation (ε^b) produced by the UnSWAN, Eqs. (4.1) and (4.2) can be solved to obtain the analytical solutions for $\overline{\boldsymbol{V}}$ and $\zeta^c(x)$.

4.2.1 Wave Parameters and Two-Dimensional Domain

The computed cross-shore distributions of significant wave height, depth-induced breaking dissipation and water depth are shown in Figure 4.1(a). When propagating across the slope, waves shoal between x = 1000m and 1400m and begin to break around x = 1400m (indicated by the increase in breaking dissipation ε^b in Figure 4.1(a)). The wave energy dissipation rate remains zero during wave shoaling and has a maximum value of 75 kg/s^3 at about x = 1700m, which is identical to results in Uchiyama et al. [23] and Kumar et al. [25]. The computed free surface ζ^c(solid line in Figure 4.1(b)) gradually decreases landward from a small negative value at the offshore boundary to a maximum wave set-down at about x = 1500m, where it then increases monotonically to a maximum wave setup of approximately 0.22m at the shoreline. These results agree very well with the analytical solutions shown in Figure 4.1(b).

The predicted depth-averaged cross-shore Eulerian flow (solid line in Figure 4.1(c)) has equal magnitude and opposite sign to the depth-averaged Stokes flow (blue diamonds in Figure 4.1(c)), i.e. is in perfect agreement with $\overline{u}$= − $\overline{u}^{st}$. The depth-averaged longshore-shore velocity attains a maximum value of approximately 0.93m/s at about x = 1750m and decreases to zero towards the shoreline and offshore, which also agrees well with previous studies (Uchiyama et al. [23]; Kumar et al. [25]; Kumar et al. [48]). Because of a cross-shore momentum imbalance associated with the non-conservative wave accelerations and wave-enhanced vertical mixing (Uchiyama et al. [23]), the maximum value of the longshore-shore velocity is shifted shoreward compared to the analytical solution (Eq. (4.2), red circle in Figure 4.1(d)).

4.2.2 Three-Dimensional Velocities

The vertical structure of the simulated Eulerian mean and Stokes velocities are shown in Figure 4.2. Inside the surf zone (x > 1400 m; Figure 4.2(a)), the Eulerian mean cross-shore velocity shows a strong recirculation cell with velocities directed onshore near the water surface and directed offshore close to the sea bed. The longshore velocity attains the maximum value at the water surface and decreases slightly towards the sea bed, with a maximum value of approximately -1 m/s throughout the domain located at about x = 1750 m. Outside the surf zone (x < 1400 m) the cross-shore velocity is weak in magnitude, directed offshore and almost uniform over depth, and also the longshore velocity is much weaker throughout the entire water column.

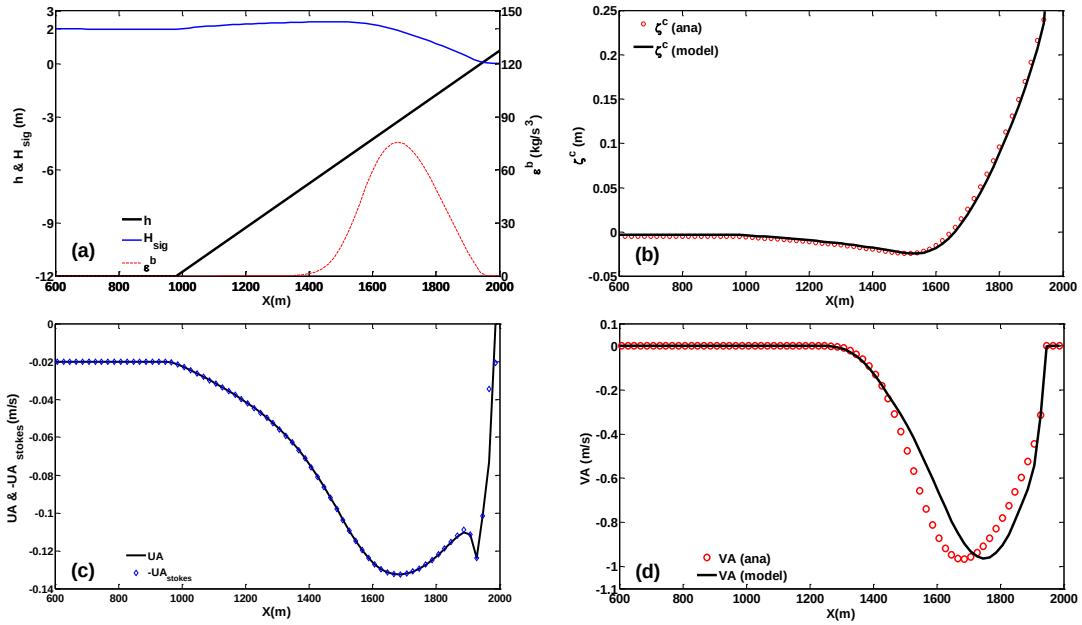

Figure 4.1: Simulation results and analytical solutions of the obliquely incident waves on a plane beach test case. Cross-shore distribution of (a) significant wave height H_{sig}, depth h and breaking dissipation rate ε^b; (b) sea surface elevation ζ^c; (c) depth-averaged cross-shore Eulerian velocity UA (solid line) and Stokes velocity -UA_{stokes} (blue diamonds); and (d) longshore velocity VA.

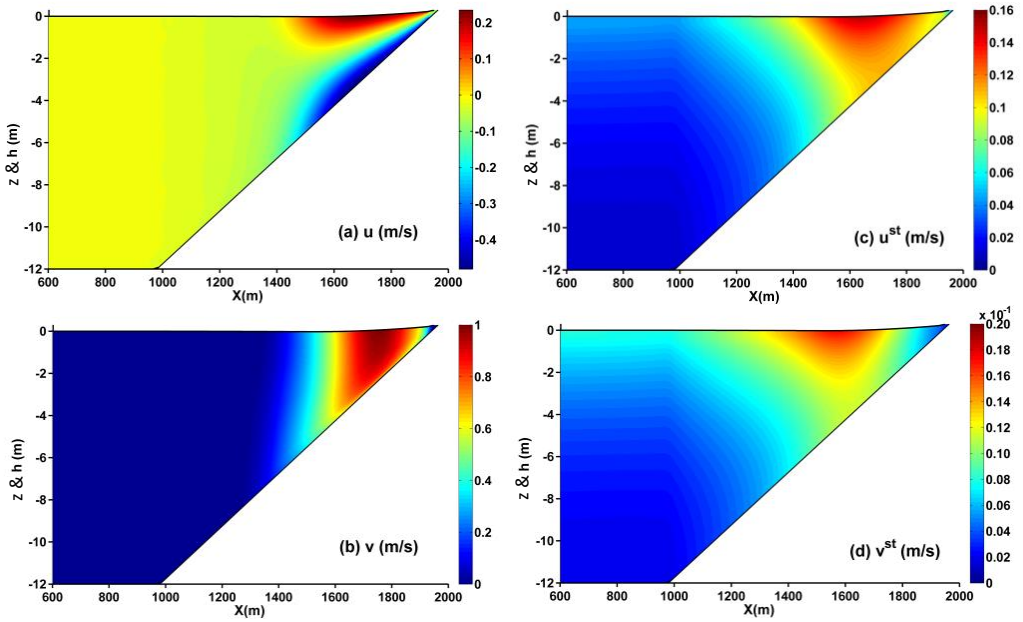

Figure 4.2: Cross-shore section of Eulerian and Stokes velocities from the simulation. (a) cross-shore (u); (b) longshore (v); and (c) cross-shore (u^{st}) and (d) longshore (v^{st}).

Near the sea surface, the computed cross-shore Stokes velocity (Figure 4.2(c)) increases from near zero at the offshore boundary and the shoreline to a maximum value of ~ 0.15m/s at the location of maximum wave breaking (i.e. $x = 1700$ m). Vertically, the velocity decreases from the sea surface towards the sea bed. The longshore Stokes velocity (Figure 4.2(d)) follows a similar distribution as the cross-shore Stokes velocity, but is about one order of magnitude weaker in strength because of the relatively small wave obliqueness.

The model results clearly follow the analytical solution for this particular condition and are consistent with previous similar research works in Uchiyama et al. [23] and Kumar et al. [25] despite different turbulence closure schemes being used in these models. This demonstrates the model's capability and accuracy for simulating coastal surface wave induced currents.

4.2.3 Model Convergence

Roland and Ardhuin [186] indicated that a large time step could affect the convergence of the SWAN solution. To test the effects of the time steps on the module solution, five sensitivity tests with increasing time steps were carried out, see Table 4.1. These tests are based on the same model setup as the above validation case. All tests are run with the nonstationary mode of UnSWAN, starting from 00:00:00 until convergent results are obtained. The model convergence time (Table 4.1) is defined as the time when the normalized root mean square error of wave height (WHNRMS) is less than 1.0 %. WHNRMS is defined as $\epsilon_j = \left\{ \frac{\sum_{i=1}^{NodeNum} (hs_{i,j} - hs_{i,0})^2}{\sum_{i=1}^{NodeNum} (hs_{i,0})^2} \right\}^{1/2}$, in which $hs_{i,0}$ represents the convergent wave height simulated in the standard case and $hs_{i,j}$ represents the wave height of test case j (j=1,2,3,4,5). It can be seen that the model convergence time of these six tests in Table 4.1 increases monotonously with increase time steps, which verifies that UnSWAN in the present study is able to remain stable and converge into a steady state at these given time step sizes.

The convergence steps in Table 4.1, defined as $\frac{Convergence\ Time}{Wave\ Time\ Step}$, reduce firstly as the time step increases but then remain approximately constant when the wave time step is larger than 100sec. The computational efforts are much less for the cases with large time steps and fewer convergence steps, in comparison with the cases with small time step and large number of convergence steps. On the other hand, the time step in the circulation model is unavoidably limited by the CFL criterion. For a given time step in the circulation model, a large time steps in the wave model means more internal mode calculations are required in the circulation model, which will increase the computation load. Therefore, when the whole coupled model system is implemented in practise, the time step for the wave model should be decided for the optimal operation for both wave

Table 4.1: Wave time step and convergence time of 6 test cases

Test Case #	#0 (standard case)	#1	#2	#3	#4	#5
Wave Time Step (sec)	0.1	1.0	10.0	100.0	1000.0	10000.0
Convergence Time(hh:mm:ss)	00:05:00	00:05:15	00:08:40	00:43:20	06:56:40	69:26:40
Convergence Steps	3000	315	52	26	25	25

and current models. In the present study, 10 seconds is used as a typical time step for the following cases.

Two tests with different spatial resolutions, i.e. 5m (run 6), 50m (run 7), are also carried out. Due to the large mesh size, the results in run 7 cannot capture all the characteristics. The difference between the results of run 6 and the base case run 0 are very small. Therefore, a spatial resolution of 20m is considered sufficient for this test case.

4.3 Wave Breaking over Breaker Bar at Laboratory Scale

Breaking wave characteristics over a barred profile can be significantly different from those on a plane sloping beach (Smith and Kraus [187]), and consequently the wave-induced velocities and turbulence will also differ considerably. Recently, hydrodynamics and sand transport processes were measured under a large-scale plunging breaking wave during a combined laboratory campaign involving experiments with a mobile medium-sand bed (van der Zanden et al. [53]; see detailed analysis in the Chapter 5) and with a rigidized fixed bed (van der A et al. [20]). Both campaigns involve the same wave conditions and barred beach profile, which developed from an initially flat horizontal test section. In this section, the numerical model is validated against measurements of hydrodynamics, including turbulence, obtained with high spatial coverage during the fixed-bed experiment.

The experiment was conducted in the 100 m long, 3 m wide, and 4.5 m deep wave flume at the Polytechnic University of Catalunya in Barcelona (van der A et al. [20]). The wave generation system consists of a wedge-type wave paddle and the steering signals were based on first-order wave generation. The coordinate system has its x origin at the toe of the wave paddle in its rest position and is positive in the direction of the waves; the vertical z coordinate has its origin at the still water level and is positive upward; the y coordinate has its origin on the right side wall of the flume when facing the beach and is positive toward the center of the flume.

Figure 4.3(a) shows the layout of the beach profile in the fixed bed experiment, consisting of a 1:12 offshore slope, a 0.6m high breaker bar (measured from crest to trough) with a lee-side slope of approximately 1:4, followed by a 10m long 1:125 slope and terminated by a fixed sloping beach. Regular waves ($H = 0.85$m and $T = 4$sec) were generated at the offshore boundary with a 2.65m water depth by a wedge-type wave paddle. The water surface elevations, used to quantify the wave height and mean surface elevation, were measured with sidewall-mounted resistive wave gauges at 19 locations covering the deep part of the flume to the shoaling zone and were measured with pressure

transducers at 37 locations for the remainder of the flume (i.e. at the breaking and inner surf zones). Instantaneous velocities were measured at 12 cross-shore locations along the bar region, covering the shoaling, breaking and inner surf zones, using a Laser Doppler Anemometer (LDA) and two Acoustic Doppler Velocimeters (ADV) deployed from a mobile frame. Velocities were measured over the entire water column with a vertical measurement separation distance of 0.10m. The instantaneous velocities were decomposed into a time-averaged, wave-related and turbulent component, following a Reynolds decomposition. Further details on the measurements and data processing can be found in van der A et al. [20].

The corresponding model domain covers an area of 70m in the cross-shore by 1m in the longshore direction. The spatial resolution is 0.1m in both directions, together with equally spaced 33 vertical Sigma layers, yielding a total of 14000 elements. The water depth at the offshore boundary is fixed at 2.65m in accordance with the experiment. At the offshore boundary, the model is forced with regular normally incident waves with a 4sec period and 0.85m wave height. In this study, the original code of UnSWAN is further developed to allow the simulation of normally incident regular waves, by limiting the wave propagation direction in exactly one direction bin, e.g. zero degree in this case, and one frequency bin. The recently developed β-kd approach in Salmon et al. [140] is chosen to account for the depth-induced wave breaking, as the numerical results improved significantly compared to that from the more widely used constant breaker index approach. Following the baseline numerical experiment of Uchiyama et al. [23], the shape function of Eq. (3.25) with $a_b = 0.2$ and of Eq. (3.41) with $a_{\mathrm{bf}} = 3.0$ are used for $f^b(z)$ and $f^{\mathrm{bf}}(z)$, respectively. Bottom stress due to the combined action of waves and currents is estimated using the formulation proposed by Soulsby [144] with $z_0 = 0.001$m which is representative for the roughness of the concrete rigidized bed. In order to obtain smooth solutions, a weak horizontal momentum diffusion coefficient of the order $0.10\mathrm{m}^2/\mathrm{s}$ is applied. The effect of wave rollers is considered in the simulation, with the roller evolution model (Eq. (3.12)) fed by the wave dissipation obtained from the UnSWAN wave module using $\alpha_r = 0.75$. $H_w = 0.3$ and $D_w = 0.01$ are chosen for a proper description of the turbulence under breaking waves.

Starting from still water, a standard simulation of this test condition lasts for 30 mins after which the results are found to be in hydrodynamic equilibrium using a barotropic and baroclinic time step of 0.01 sec and 0.1 sec respectively.

4.3.1 Wave Height and Water Surface Elevation

Figure 4.3(a) compares the model computed and measured wave height and mean water level. After propagating from the offshore boundary into the model domain, it can be

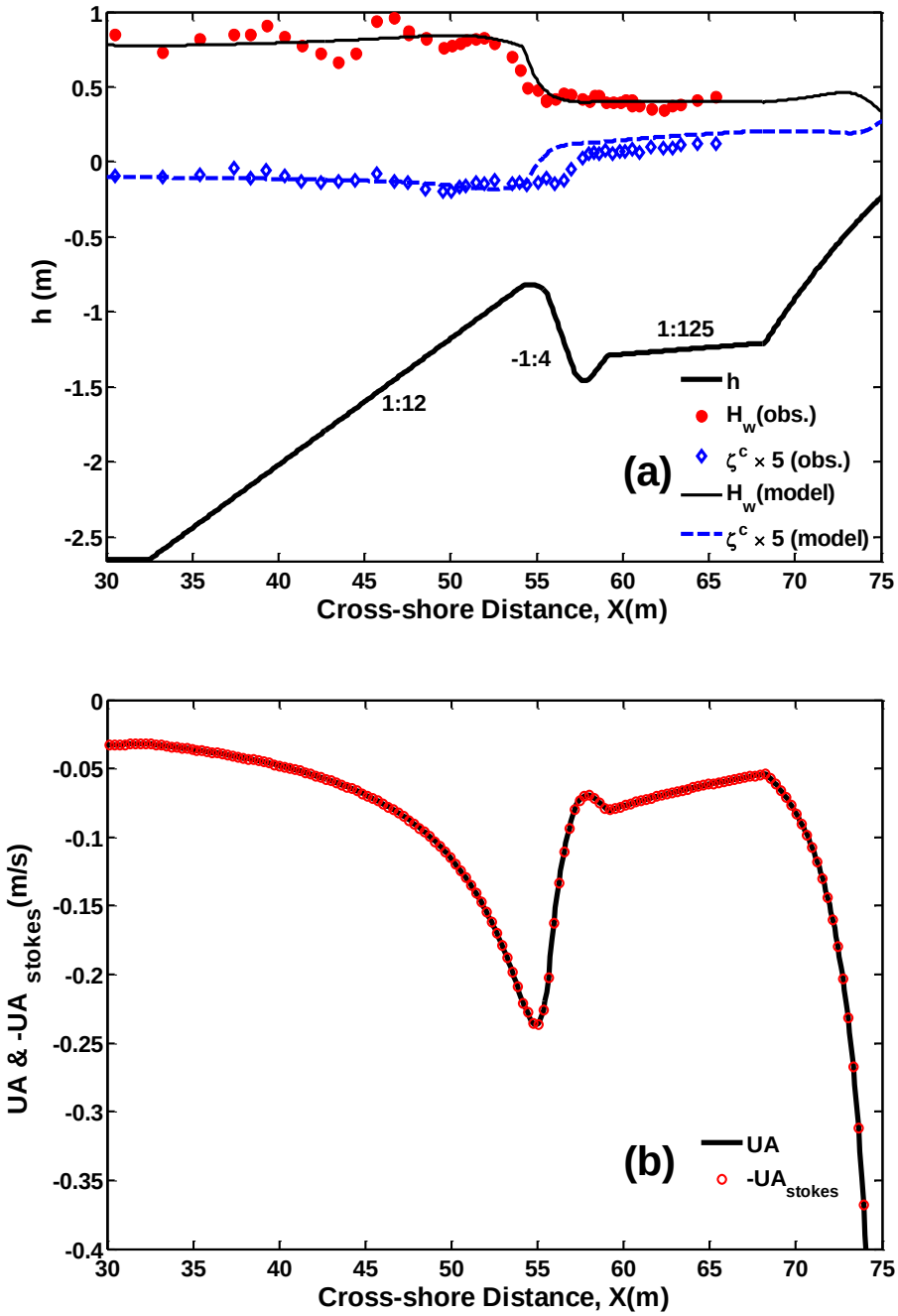

Figure 4.3: Simulated and measured results of the large-scale breaking wave experiment with a naturally shaped breaker bar. Cross-shore distribution of (a) significant wave height H_{sig} and five times of sea surface elevation $\zeta^c \times 5.0$; (b) depth-averaged cross-shore Eulerian velocity UA (solid line) and Stokes velocity -UA_{stokes} (red circles).

seen that the wave height decreases first due to the bottom friction induced wave attenuation and then increases gradually due to wave shoaling along the offshore bar slope. A maximum wave height is reached at $x \approx 52$m, where depth-induced wave breaking occurs, resulting in a rapid decrease in wave height. Overall the model computed wave height agrees well with the measurements in the breaking area and inner surf zone (i.e. $x > 52$ m), although the model predictions of the breaking point and the strong decrease in wave height are shifted by about 1 m shoreward compared to the measurements. In the deeper section of the flume and along the offshore bar slope, the oscillation in the measured wave height is due to wave reflection and/or spurious wave generation in the laboratory, which is not seen in the modelled results. A factor of 5.0 was multiplied with mean water level to facilitate the inter-comparisons of the simulation and observation. The simulated mean water level shows a continuous and near constant set-down of approximately 2.5 cm from $x = 0$ m (i.e. the offshore boundary) to $x \approx 55$ m, where it rapidly (within 1 m) turns into a set-up. The set-up value increases slowly throughout the inner surf zone, with a maximum value of about 3.5 cm at the end of the flume. The cross-shore behaviour and the quantitative set-down and set-up computed by the model are in good agreement with the measurements. However, a spatial lag of about 2 m is found in the simulated location where set-down changes to setup. This is closely related to the discrepancies of simulated wave breaking energy here (Eq. (4.1)), which in turn result from the overestimation of the wave height.

4.3.2 Velocities

The simulated depth-averaged Eulerian velocity as shown in Figure 4.3(b) complies well with the barotropic mass conservation law which, similar to the characteristic shown in Figure 4.1(c), has the same magnitude but opposite sign to the depth-averaged Stokes flow. The simulated cross-shore and vertical distribution of Eulerian velocity in Figure 4.4 is much more complicated than for the plane beach condition (Figure 4.2) due to the more complex barred bathymetry. From the offshore boundary until $x =$ 51m, the Eulerian velocities are offshore-directed over the entire water column with relatively small magnitudes ($x < 0.10$m/s) and are near uniform in cross-shore and vertical direction. In the remainder of the flume (i.e. $x > 51$m) current velocities increase in magnitude. Large onshore-directed velocities occur near the water surface due to the enhanced mass flux related to depth-induced wave breaking and wave roller effects (see details below). These velocities are balanced by a return flow (undertow) in the bottom part of the water column, leading to strong vertical shear. Maximum onshore velocities, reaching values of 0.3m/s, are located above the breaker bar, while maximum undertow velocities occur near the shoreline and above the breaker bar with values of about -1.4m/s and -0.4m/s respectively.

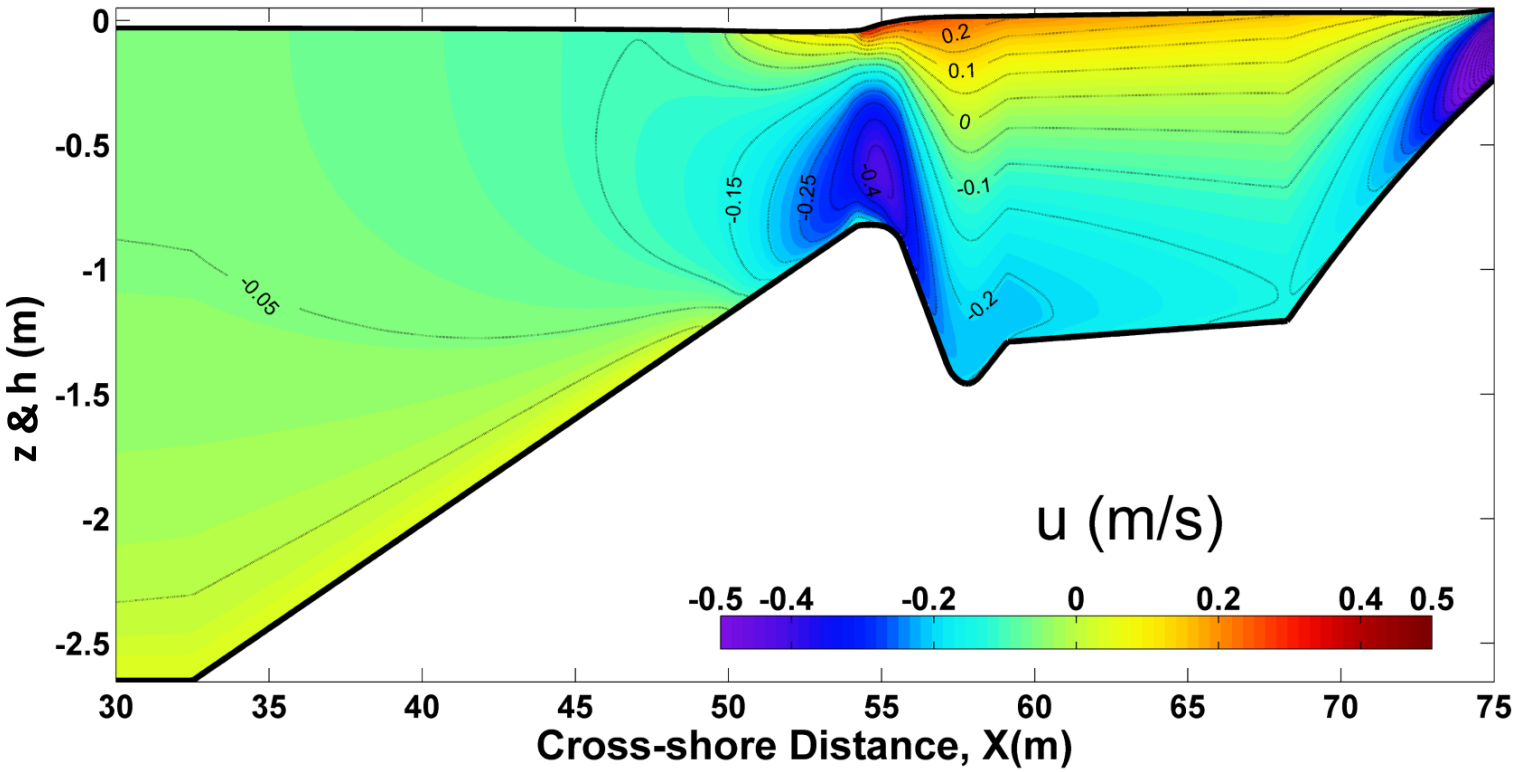

Figure 4.4: Model simulated distribution of cross-shore velocity u in the large-scale wave flume experiment with a naturally shaped breaker bar; contour lines explicitly show the velocity value.

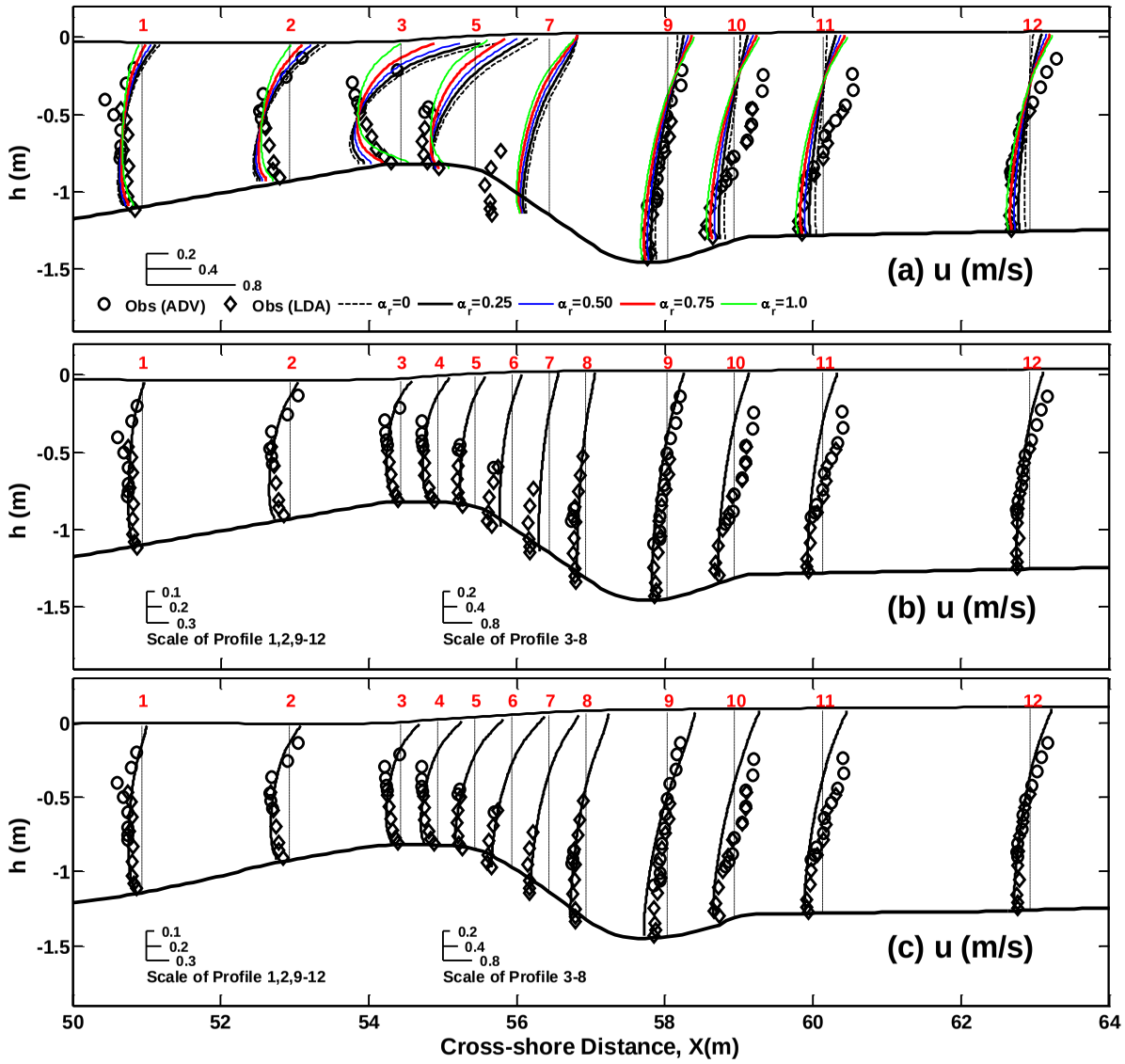

Figure 4.5: Comparison of simulated (lines) with observed vertical profiles (circles and diamonds) for cross-shore velocities. (a) five simulations with $\alpha_r = 0.0, 0.25, 0.50, 0.75, 1.0$; (b) the standard run with $\alpha_r = 0.75$; (c) the run with local enhanced wave dissipation at x=56 m $\sim$ 57 m; The vertical dashed lines indicate the profile measurement locations and zero value for each profile.

Eq. (3.32) suggests that the total wave dissipation, which induces a shear stress at the water surface, equals $\varepsilon^{tot} = (1 - \alpha_r)\,\varepsilon^b + \varepsilon^r + \varepsilon^{wcap}$ where α_r controls the fraction of the breaking waves turned into wave rollers that propagate toward the shore before dissipating. The value of α_r (between 0 and 1) can change the rate of wave dissipation which in turn reshapes the velocity profile inside the surf zone. In order to give an explicit presentation of the effect of the wave roller, five different numerical experiments are conducted with α_r values equal to 0, 0.25, 0.5, 0.75 and 1.0. The simulated profiles of velocity for different α_r values are shown in Figure 4.5(a), which also includes the measured velocities. With $\alpha_r = 0$, the simulated velocity shows a strong vertical shear on the breaker bar and along the offshore slope, due to a strong onshore flow near the water surface as well as a large undertow, while above the bar trough and further inshore the simulated velocities are nearly depth-uniform and onshore and offshore time-averaged velocity magnitudes are much lower. The resulting vertical shear overestimates the measured shear above the breaker bar. As the value of α_r progressively increases from 0 to 0.75, the computed velocity profiles tend to follow the measurements better, i.e. the velocity shear gradually decreases on the breaker bar and above the offshore slope while it increases in the bar trough and further shoreward. However, when α_r= 1 the simulated near surface velocities above the offshore slope of the breaker bar are too small in comparison with the measurements, while the improvement of vertical velocity structures in the bar trough and further shoreward is minor. Overall, the model results with the α_r value of 0.75 show the best agreement with the measured data in these five simulations as shown in Figure 4.5(b) and hence is used in this study. However, the local best fit value of α_r shown in Figure 4.5(a) is different at different cross-shore locations, which suggests that α_r is more appropriately regarded as a function of the cross-shore positions (i.e. a function of local bathymetry slope and/or local wave characteristics) in the surf zone. The results demonstrate that the inclusion of wave roller effects improves the model performance significantly.

Although Figure 4.5(b) shows a good agreement between the simulated and the measured Eulerian velocities, it is also noted that the simulated undertow is apparently underestimated along the steeper shoreward slope of the breaker bar (i.e. x = 56m and 56.5m), which is most likely caused by the underestimated surface wave dissipation and overestimation in wave height around the breaker bar (Figure 4.3(a)). To verify the guess, an additional simulation with locally enhanced wave dissipation (i.e. ε^{b} in Eq. (3.26)) in this region (x = 56m to 57m) was conducted. As shown in Figure 4.5(c), this leads to a much better agreement with the measurements.

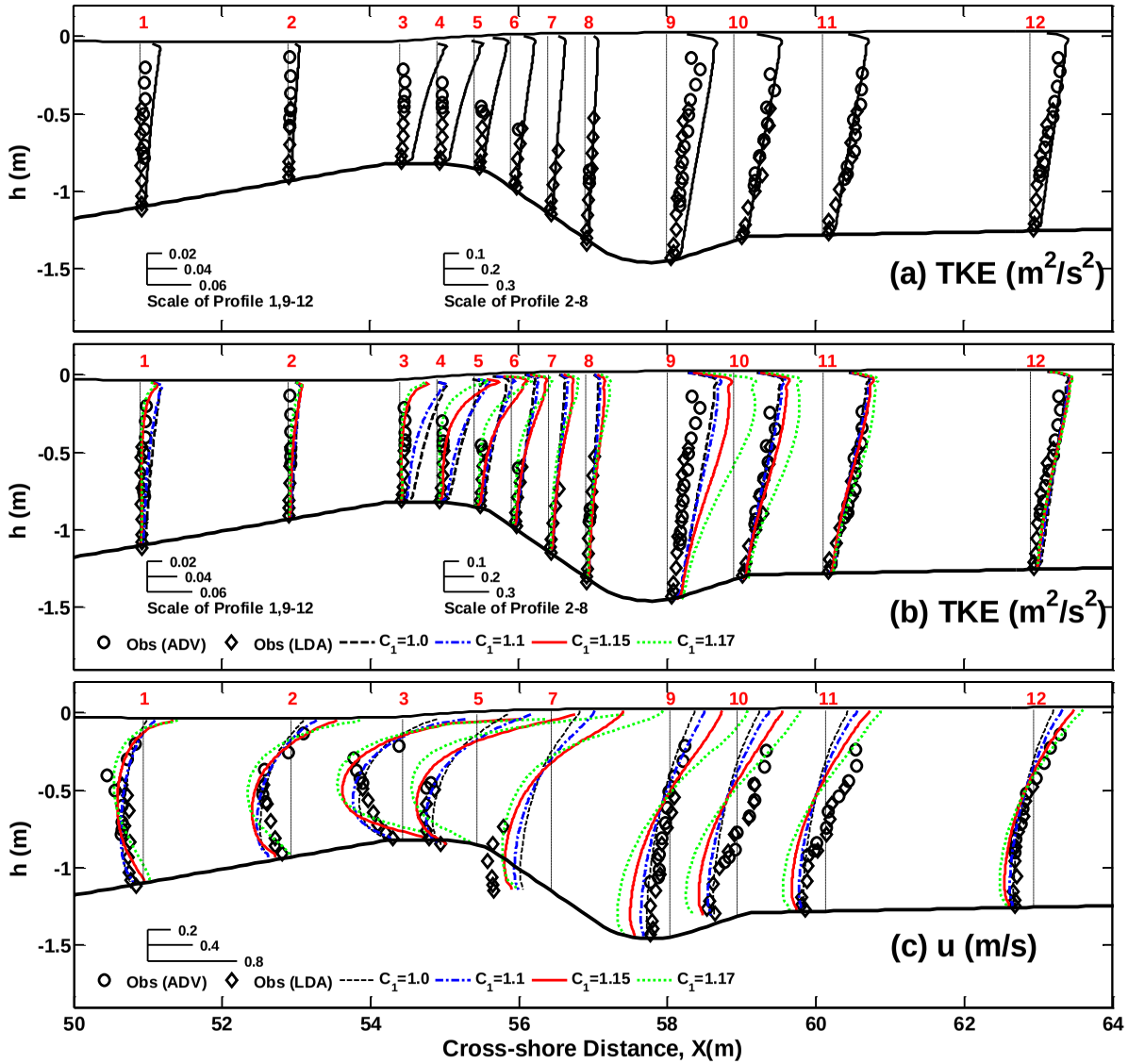

Figure 4.6: Comparison of simulations (lines) with measurements (circles and diamonds) in terms of cross-shore TKE (a, b) and time-averaged velocities (c). (a) the standard run with C_1= 1.0; (b) and (c) four simulations with C_1= 1.0, 1.1, 1.15,1.17. The vertical dashed lines indicate the profile measurement locations and zero value for each profile.

4.3.3 Turbulent Kinetic Energy

The model computed TKE is also compared with the measurements at the same 12 profiles (Figure 4.6(a)). Overall, fairly good simulation results are obtained except at the profile of 3 - 5 around the breaking point, where TKE is obviously over-predicted. Note that over-predictions of TKE in the breaking region have been reported in many 2D and 3D simulations using various turbulence closure models (Xie [188]; Brown et al. [189]). Various explanations for this overestimating have been given, e.g. the omission of TKE contained in the overturning jet during wave breaking (Lin and Liu [190]), the exclusion of air effects on turbulence production and dissipation before the impingement of the overturning jet (Christensen et al. [191]), the exclusion of air bubbles in conventional turbulence models (Xie [188]), and the invalidity of the turbulence model coefficients, that have been calibrated for quasi-steady turbulent flows rather than wave-induced oscillatory flows with strong free surface dynamics (Lin and Liu [190]; Shao [192]).

We conjecture an underestimated turbulence dissipation rate as the main cause of the over-prediction of TKE around the breaking point, which is likely due to inappropriate coefficients in the turbulence model. Therefore, four sensitivity simulations are conducted with a variation of the coefficient C_1 (= 1.0, 1.1, 1.15, 1.17) in Eq. (3.57). With increasing C_1, higher turbulence dissipation rates are expected. Simulation results are shown in Figure 4.6(b). As C_1 increases from the original default value (i.e. 1.0), the simulated TKE levels at the profiles of 3-5 gradually decrease and approach the measurements. Among these four simulations, the best fit is obtained for $C_1 = 1.15$. TKE at the profile locations 1, 2 and 6-8 are also reduced with a bigger C_1. However, at the profiles of 9-11, the reverse tendency occurs, i.e. higher TKE is obtained for larger C_1. This is understood from the resulting velocity profiles (Figure 4.6(c)). As C_1 increases, the vertical velocity gradients at profiles of 9-11 increase strongly due to decreased vertical momentum diffusivity. This implies an increased TKE shear production rate which explains the higher TKE at these locations.

Overall, an increased coefficient C_1 improves the model performance in terms of TKE in the breaking region. However, it also should be noted that this enlargement is not appropriate for all the locations in the surf zone. Apparently, similar to α_r, a cross-shore-varying rather than a constant value for C_1 seems more appropriate; the development of such a function could be a topic for further research. In addition, Figure 4.6(c) shows that the undertow magnitudes in the breaking region improve as C_1 increases, which implies that a proper description of the TKE can improve the mean flow results.

4.4 Obliquely Incident Waves on A Natural, Barred Beach (DUCK' 94 experiment)

The developed model system is further evaluated by comparing model simulated wave-induced currents to measurements obtained on a natural sandy beach at Duck, North Carolina, during the DUCK94 experiment (e.g., Garcez Faria et al., [184, 19]; Uchiyama et al. [23]; Kumar et al. [48]). Vertical profiles of velocities were obtained with a vertical stack of seven electromagnetic current meters (EMCs) located at elevations of 0.41, 0.68, 1.01, 1.46, 1.79, 2.24 and 2.57m above the bed, and measured at seven surf zone cross-shore locations for approximately one hour at each site. Directional wave spectra were measured using 10 pressure sensors on an alongshore line at 8 m water depth (Long [193]). Additionally, a spatially fixed cross-shore array of 11 EMCs and 13 pressure sensors were used to measure cross-shore variability of horizontal velocity and wave heights in the surf zone (Elgar et al. [194]). All data were collected on October 12 1994, when strong longshore and cross-shore currents occurred due to waves generated by winds associated with the passage of a low pressure storm system. During data collection, the tidal variability was minimal and the bathymetric contours were assumed alongshore uniform (Garcez Faria et al. [19]). Further details on the data acquisition and processing can be found in Gallagher et al. [21, 195] and Elgar et al. [194].

The bathymetry used in the calculation is shown in Figure 4.7(a), with the shoreline located near $x = 120$m and a nearshore bar located at about $x = 250$ m. With a horizontal resolution of 5 m in both x and y direction, the model domain is uniform alongshore and has a cross-shore (x) width of 800 m and an alongshore length (y) of 100m with origin at $x = 100$m and $y = 100$m. The water depth varies from 2.5m above the datum at the origin to 7.3m at the off-shore boundary. A tidal elevation, assumed constant over the simulation period, of 0.70 m is added to the water level. In total 31 vertical Sigma levels are used with grid-height refinement near the surface and bottom. A periodic boundary condition is imposed in the alongshore direction (i.e., north and south boundaries) and a wet/dry boundary condition is used at the shoreward boundary. At the offshore open boundary, the Flather radiation condition for the free surface is adapted with nudging towards the quasi-static sea level $\widehat{\zeta}$. The effect of earth rotation is included with a constant Coriolis frequency of 8.8695×10^{-5}/s. Wind stress forcing of -0.2532 and -0.1456N/m^2 is imposed in the cross-shore and longshore directions, respectively. At the offshore boundary, a JONSWAP wave spectrum with a root-mean-square wave height of 1.6m, a peak period of 6sec and a 13° angle of incidence is provided to the UnSWAN model to obtain the wave field. The wave roller effect is also enabled with $\alpha_r = 1.0$, as sensitivity tests (not shown here) present overall

Table 4.2: Model parameters for Duck94 simulation

Variable	Value	Unit
Horizontal resolution	5	m
Time step	0.1	s
Offshore wave height H_{rms}	1.6	m
Offshore peak wave period Tp	6.0	s
Offshore incident wave angle θ_o	193.0°	
Roller dissipation parameter sinβ	0.1	
Offshore tidal elevation ζ_{tide}	0.7	m
Cross-shore wind stress $\tau_{sur}^{wind,x}$	-0.2532	N/m^2
Alongshore wind stress $\tau_{sur}^{wind,y}$	-0.1456	N/m^2
Coriolis frequency f	8.5695×10^{-5}	s^{-1}
Lateral momentum diffusion coefficient Kh	0.1	m^2/s

best results with this value. However, as discussed in Section 4.3.2, this factor is more appropriate to be regarded as a function of the cross-shore positions. Instead of the β-kd parameterization, the constant breaker index (γ=0.73) is used in this case to calculate the wave dissipation. Other model settings are the same as those used in Section 4.2. Note that the shoreline is located in the left side of the coordinate in this case, opposite to the former ideal and lab cases, thus u $>$ 0 means velocity is offshore directed.

The model simulation is initiated with a resting state and carried out for a period of 6 h to obtain converged solutions with both baroclinic and barotropic time stepping of 0.1 sec. The relevant model parameters are summarized in Table 4.2.

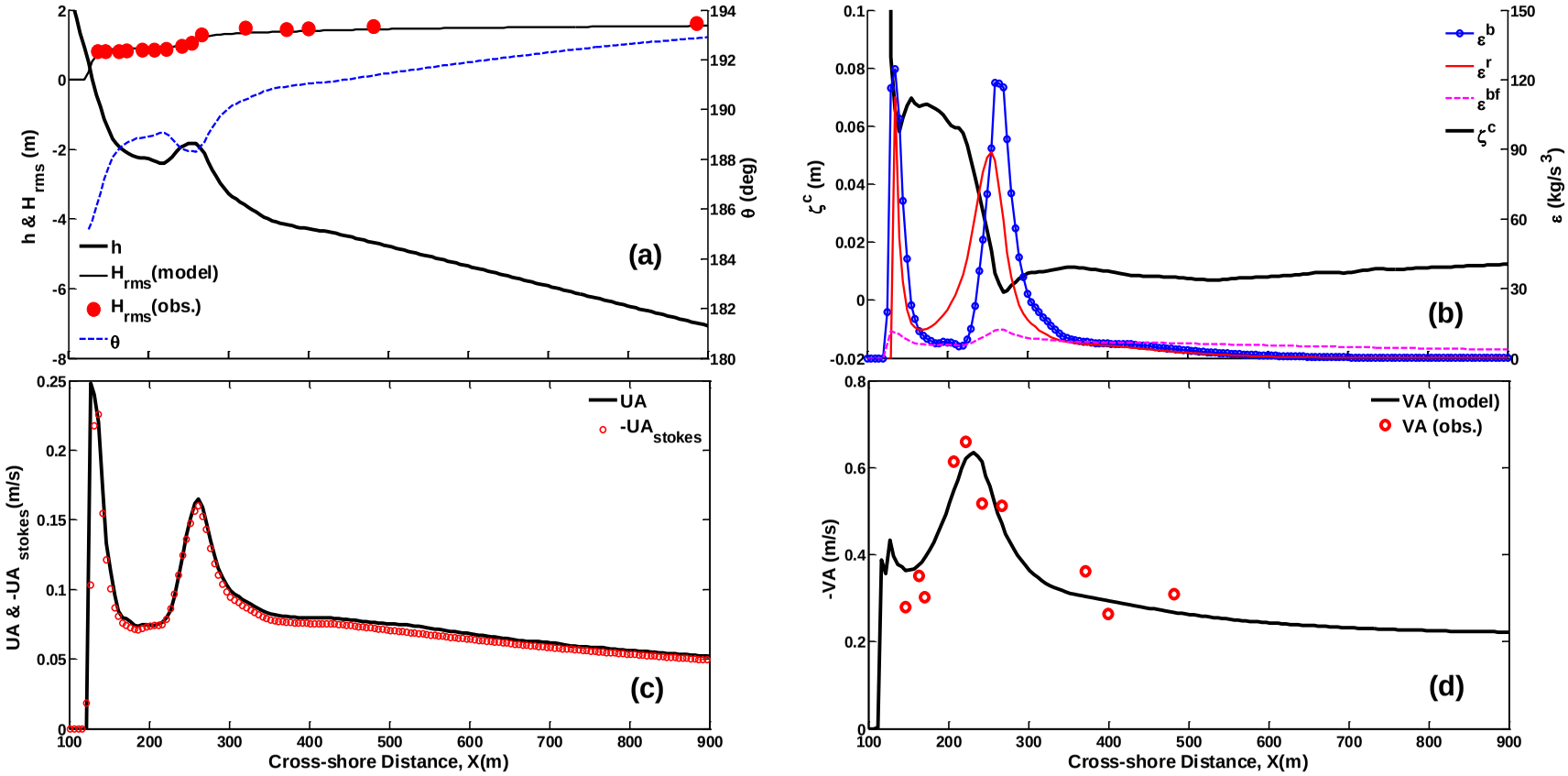

Figure 4.7: Results of Duck94 simulation. Cross-shore distribution of: (a) root-mean-square wave height (H_{rms}) from model simulation (solid line) and observation (from Elgar et al. [194]; red circles), water depth (h) and simulated wave direction (θ); (b) sea surface elevation ζ^c, wave dissipation rates by depth-induced breaking ε^b, roller ε^r and bottom stress ε^{wd}; (c) simulated depth-averaged cross-shore Eulerian velocity UA (solid line) and Stokes velocity -UA_{stokes} (red circles); (d) depth-averaged Eulerian longshore velocity VA from simulation (solid line) and observation (from Feddersen et al. [196]; red circles).

Table 4.3: Normalized root mean square error $\epsilon_j = \left\{ \frac{\sum_{i=1}^{nsen(j)} (d_{ij} - m_{ij})^2}{\sum_{j=1}^{nsen(j)} (d_{ij})^2} \right\}^{1/2}$ for the cross-shore and longshore velocity estimates for Duck94 experiment for various locations across the profile. d_{ij} and m_{ij} represent measured (from Garcez-Faria et al. [184, 19]) and model estimated velocity values at the 7 cross-shore locations (j) and various elevations (i) above the sea bed. Station 1 is closest to the shoreline

STN #	mean	#1	#2	#3	#4	#5	#6	#7
Cross-shore	0.392	0.585	0.567	0.272	0.478	0.126	0.328	0.388
Longshore	0.120	0.416	0.043	0.131	0.092	0.039	0.075	0.043

4.4.1 Wave Parameters

Figure 4.7(a) shows that the computed wave height H_{rms} is in close agreement with the measured wave height (Elgar et al. [194]) throughout the beach profile. The wave direction, demonstrating clearly the effect of depth-induced refraction, turns from 193° at the offshore boundary to about 185° at the shoreline. The three dissipation terms calculated from the model (Figure 4.7(b)) demonstrate that the depth-induced breaking (ε^b) occurs predominantly at the bar crest and at the nearshore region close to the shoreline. Over the bar trough, the wave dissipation is very small, which leads to the relatively stable wave height in this region (Figure 4.7(a)). The roller dissipation (ε^r) peaks more shoreward than ε^b; the bottom friction dissipation (ε^{bf}) is about one order of magnitude smaller than the other dissipation terms in the breaking region while it is dominant at the offshore region (x > 500 m). The sea surface elevation (ζ^c) presents an overall trend of wave set-up outside and wave setup inside the surf zone (Figure 4.7(b)), while around the breaking point a small decrease occurs due to the dominant contribution by the Bernoulli head (see details below), consistent with simulation results by Uchiyama et al. [23] and Kumar et al. [25]. The depth-averaged Eulerian cross-shore velocity (Figure 4.7(c)) is directed offshore and strongest over the bar crest and further shoreward. Similarly, to the plane beach test in Section 4.2.1, it also has the same magnitude but opposite sign to the depth-averaged Stokes flow, agreeing well with the barotropic mass conservation principle in alongshore-uniform, steady-state cases. The depth-averaged alongshore velocity (Figure 4.7(d)) corresponds to the measurements (Feddersen et al. [196]) reasonably well, showing a general increase towards the shore with a peak value located over the bar trough and then a diminishing magnitude toward the shore.

4.4.2 Cross-Shore and Vertical Structure of Velocity

Figure 4.8 presents the computed horizontal and vertical distribution of ($\mathbf{V}$,w) and ($\mathbf{V}^{st}$,wst) in the x-z plane. Similar to the plane beach case, the distribution pattern of cross-shore velocity $u(x,z)$ shows an overturning circulation in the surf zone, with an onshore directed flow near the surface and offshore directed undertow near the bottom (Figure 4.8(a)). This circulation cell has maximum strengths over the bar crest and close to the shoreline while being relatively weaker over the inner surf zone (x = 150m to 200m). Outside the surf zone, currents are offshore directed and generally weak. In the lower layer of the water column the current reaches a maximum value which monotonically decrease to zero at the sea bed, while near the sea surface there is a small onshore directed contribution. In the horizontal x direction, the longshore velocity $v(x,z)$ (Figure 4.8(b)) has a maximum negative value in the trough region shoreward of the bar. Vertically, the strongest longshore velocity occurs at the water surface and magnitudes decrease monotonically towards the sea bed.

The computed vertical velocity (Figure 4.8(c)) shows upward directed velocities shoreward from the bar crest and downward directed velocities offshore from the bar-crest (x = 250m), with maximum values located near the bottom. This pattern along with onshore flows near the surface and offshore directed undertow in the lower layers of the water column creates an anticlockwise circulation cell pattern over the bar trough inshore of the bar crest.

In accordance with the cosh($2kz$) distribution suggested by Eq. (3.14), the 3D wave-induced cross-shore and longshore Stokes drift (u^{St}, v^{St}) are strongest near the surface and weakest near the sea bed, with maximum u^{St} and v^{St} above the bar crest and near the shoreline at shallow water (Figure 4.8(d) and Figure 4.8(e)). Due to the small obliqueness of the incident waves, v^{St} is almost an order of magnitude weaker than u^{St}. The distribution pattern of vertical Stokes velocity $w^{St}$is characterized by two pairs of upward and downward directed w^{St} dipole circulations, with the upward directed velocities located near the shoreline and shoreward from the bar crest, while downward directed velocities occurs offshore to these locations. The vertical Stokes velocity w^{St} is of the same magnitude as its Eulerian mean counterpart w, but has its maximum strength near the water surface. Additionally, Figure 4.8(d) - (f) show that the Stokes drifts have vertical variations even in water depth < 1m, which confirms the presence of a vertically varying VF. As indicated by Uchiyama et al. [23], the use of vertically varying VF in the model could lead to a simulation improvement compared to simulations (e.g. Newberger and Allen [52]) using vertically uniform VF.

A further model-data comparison is made for the cross-shore and longshore velocity at seven different surf zone locations in Figure 4.9, which shows fairly good agreement

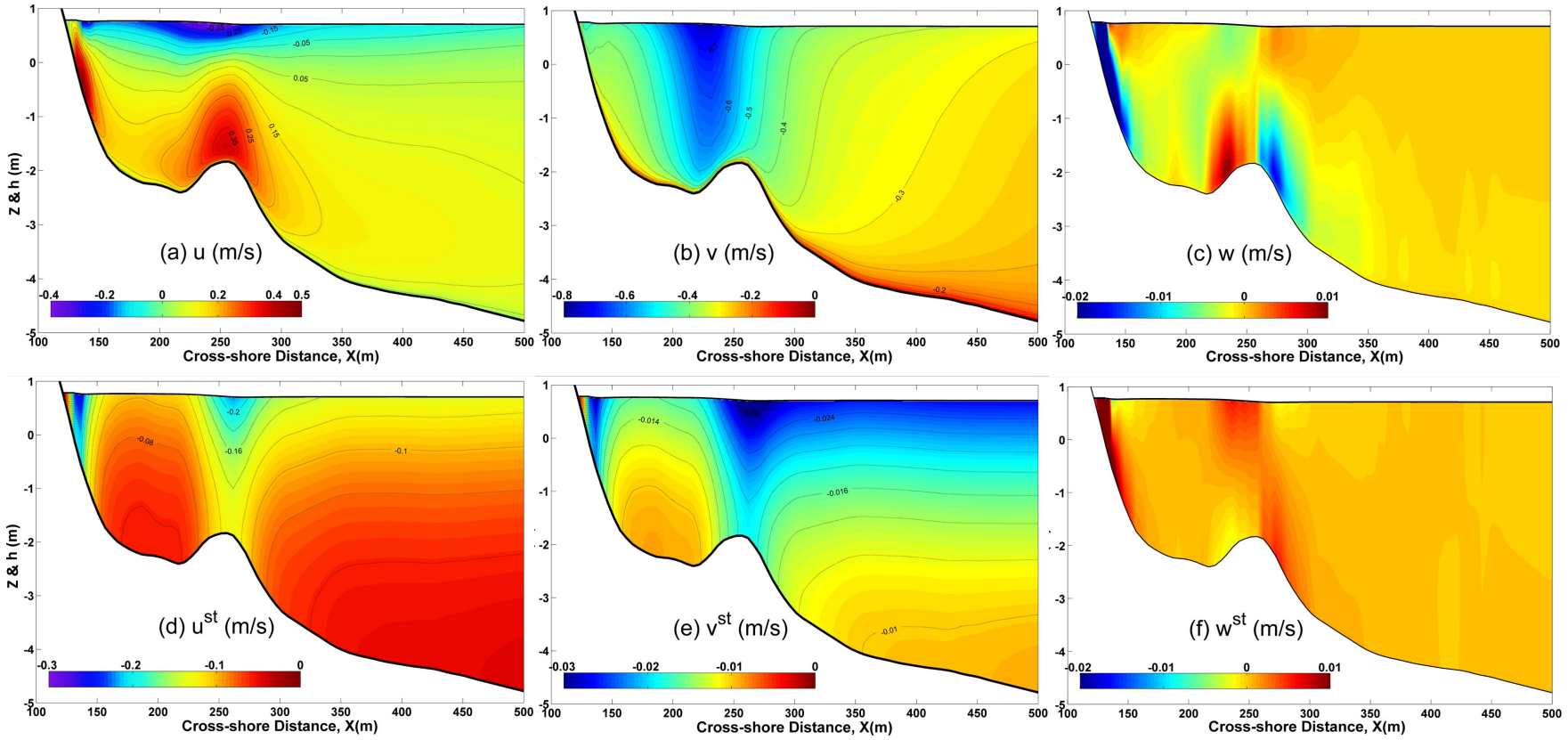

Figure 4.8: Model simulated cross-shore distribution of (a) cross-shore velocity u; (b) alongshore velocity v; (c) vertical velocity w; (d) cross-shore Stokes velocity u^{st}; (e) alongshore Stokes velocity v^{st}; and (f) vertical Stokes velocity w^{st}, for Duck94 experiment. Contour lines are used to show the velocity value explicitly

Table 4.4: Normalized root mean square error analysis for cross-shore velocity with different values of C_1

RUN#	**STN**# #1	#2	#3	#4	#5	#6	#7	Mean	C_1
1	0.515	0.565	0.615	0.871	0.082	0.238	0.303	0.456	0.80
2	0.529	0.562	0.546	0.792	0.073	0.256	0.319	0.440	0.85
3	0.544	0.560	0.468	0.703	0.076	0.276	0.337	0.423	0.90
4	0.562	0.561	0.378	0.601	0.094	0.299	0.360	0.408	0.95
5	0.585	0.567	0.272	0.478	0.126	0.328	0.388	0.392	1.00
6	0.609	0.579	0.154	0.334	0.170	0.364	0.420	0.376	1.05
7	0.640	0.598	0.131	0.166	0.220	0.403	0.467	0.375	1.10
8	0.674	0.634	0.351	0.181	0.275	0.457	0.531	0.443	1.15
9	0.506	0.560	0.135	0.215	0.080	0.238	0.303	0.291	*

* $C_1 = 1.10$ at cross-shore locations between the 3^{rd} and 4^{th} profiles and 0.80 at the remainder locations

between the simulated results and the observations. The normalized r.m.s. errors for u and v (as defined in Uchiyama et al. [23] and Newberger and Allen [52]) at a total of 42 measurement positions are summarized in Table 4.3. The mean r.m.s. errors at 7 locations are 0.39 for u and 0.12 for v, which is similar to those shown by Uchiyama et al. [23] (u error and v error range 0.45–0.70 and 0.10–0.40, respectively) and slightly better than those in Kumar et al. [25] (u error and v error range 0.54–0.66 and 0.21–0.30, respectively). These simulated results show that the developed model system in this study is capable of creating realistic velocity profiles in a surf zone environment.

Similar to the laboratory breaking wave test case in Figure 4.5(b), the computed cross-shore velocity magnitudes at the shoreward side of the breaker bar (the 3^{rd} and 4^{th} profiles) are significantly underestimated. Eight sensitivity simulations with a variation of the turbulent coefficient C_1 are firstly conducted, which is inspired by the analysis in Section 4.3.3, as a preliminary attempt to reveal the effect of turbulence on the cross-shore velocities and to improve the simulation results. Table 4.4 summarizes the normalized r.m.s. errors of these simulations. Apparently, a sole value of C_1 (run 1-8)

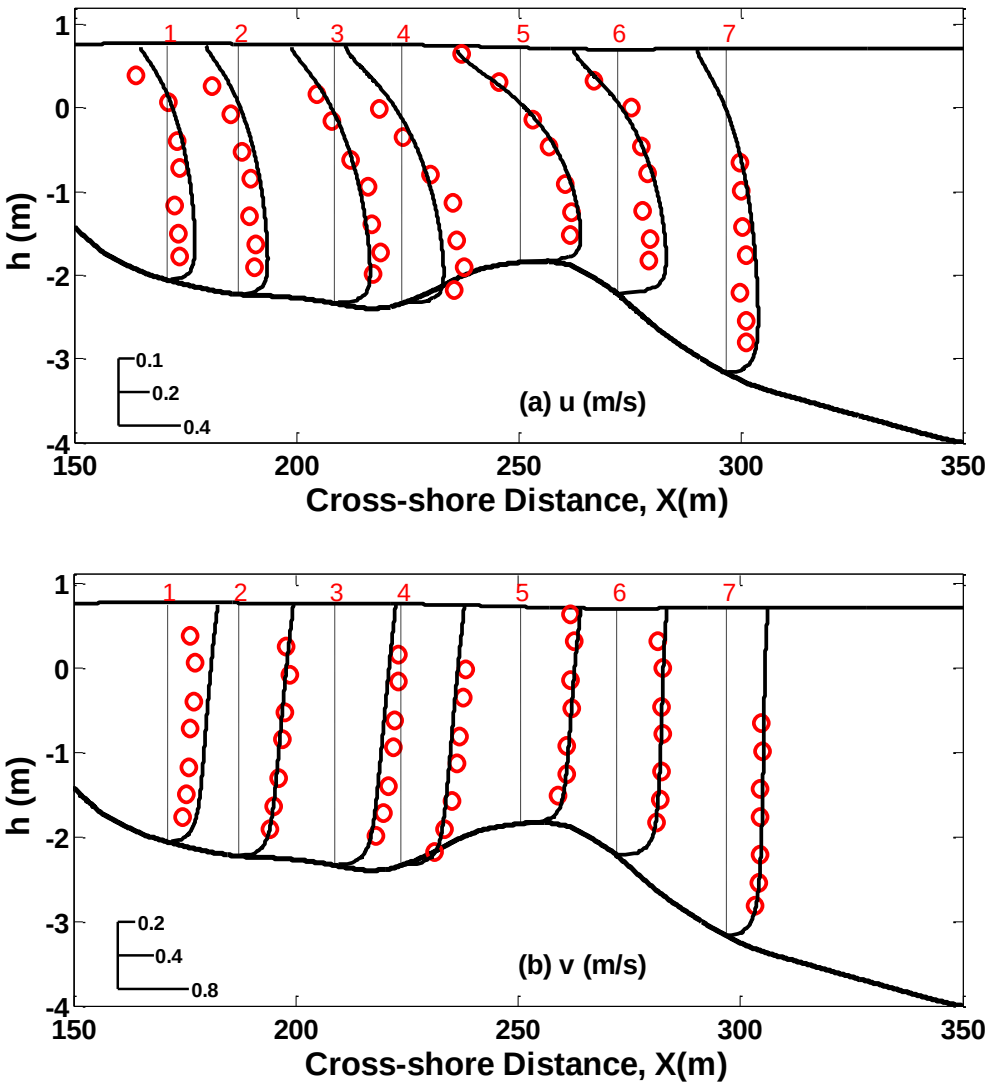

Figure 4.9: Comparison of simulation results (solid lines) with observed vertical profiles (red circles) for cross-shore (a) and alongshore (b) velocities. The vertical dashed lines indicate the profile measurement locations and zero value for each profile (data from Garcez Faria et al. [184, 19]).

cannot decrease the normalized r.m.s error at all cross-shore locations simultaneously. It is found that C1 has a best fit value of 1.10 for the 3^{rd} and 4^{th} profiles and 0.85 for the 5th profile; while in the remaining 4 profiles, 0.80 is optimum. This is in agreement with the results in Section 4.3.3, which also suggested a locally higher C_1 value for the breaking region around the bar crest. Based on the simulation results of Runs 1-8, another simulation (Run 9) was conducted with cross-shore-varying C_1, i.e. $C_1 = 1.10$ at cross-shore locations between the 3^{rd} and 4^{th} profiles and $C_1 = 0.80$ at the remainder of the locations, leading to much better results (Table 4.4).

4.4.3 Horizontal Momentum Balance

In order to understand the mechanisms responsible for these 3D model results, similar to the descriptions of Section 4.7 in Uchiyama et al. [23], the cross-shore depth-averaged and vertical variation of momentum balances are analysed and displayed in Figure 4.10 and Figure 4.11 respectively. Table 4.5 summarizes the physical meanings of relevant symbols used in the following text for representing the momentum balances.

The two-dimensional momentum balance in the cross-shore direction (Figure 4.10(a)) demonstrates a primary balance between the pressure gradient ($\boldsymbol{P}^{tot}$) and the breaking acceleration (BA) term. This is consistent with the classic surf-zone momentum balance between wave-setup and breaking acceleration (cf., Bowen et al. [28]). A secondary balance also exists between the advection and the VF terms as these two terms have similar magnitude but opposite sign at all cross-shore locations. Figure 4.10(a) also shows that these four terms are only relatively strong near the bar-crest and near the shoreline, but are negligibly small elsewhere. Similar to the balance in cross-shore direction, the alongshore momentum also demonstrates two sets of balances: a primary balance between the breaking acceleration and the bottom stress terms and a secondary one between the advection and vortex force terms. The existence of these secondary balances in cross-shore and longshore momentum are actually required by the barotropic mass balance (Uchiyama et al. [148]) which results in the anti-Stokes u flow for an alongshore-uniform, steady circulation (Figure 4.7(c) for this case and Figure 4.2(c) for plane beach case). However, it is important to point out that although the alongshore vortex force generally opposes alongshore advection at most of the cross-shore locations, due to differences in vertical structure of Stokes and Eulerian mean flows these two terms do not cancel out completely.

The contribution of the pressure gradient force is investigated in more detail. For this, the total pressure gradient force, $\boldsymbol{P}^{tot}$ (i.e. $\nabla\phi$, taken from Eq. (3.56) by excluding the vertical vortex force term K from $\nabla\phi^c$), is firstly decomposed into two terms which respectively describe the contribution from the non-WEC ($\boldsymbol{P}^c$) and WEC ($\boldsymbol{P}^{wec}$)

Table 4.5: List of symbols used for representing the momentum balances

Individual terms	Description	Expression
BA	Breaking acceleration induced by wave breaking and roller	$F_x^w = \frac{\varepsilon^{\mathrm{wcap}}+(1-\alpha_r)\varepsilon^b+\varepsilon^{\mathrm{r}}}{\rho_0\sigma}\boldsymbol{k}\cdot f^b(z)$
AD	Advection term	$-\frac{1}{D}\left(\frac{\partial u^2 D}{\partial \mathrm{x}}+\frac{\partial uvD}{\partial \mathrm{y}}+\frac{\partial u\omega^l}{\partial \mathrm{s}}\right)$
VF	Vortex Force term	$v^{st}\left(\frac{\partial v}{\partial \mathrm{x}}-\frac{\partial u}{\partial \mathrm{y}}\right)-\frac{u}{D}\left(\frac{\partial u^{st}D}{\partial \mathrm{x}}+\frac{\partial v^{st}D}{\partial \mathrm{y}}\right)+\frac{\partial}{\partial \mathrm{x}}\left[\int_s^0\left(u^{st}\frac{\partial u}{\partial\sigma}+v^{st}\frac{\partial v}{\partial\sigma}\right)ds\right]$
VM	Vertical Mixing	$\frac{\partial}{\partial \mathrm{s}}\left(\frac{K_m}{D^2}\frac{\partial u}{\partial \mathrm{s}}+\frac{\nu}{D^2}\frac{\partial u}{\partial \mathrm{s}}\right)$
PGF/$\boldsymbol{P^{tot}}$	Total pressure gradient force	$-\frac{\partial\phi^c}{\partial \mathrm{x}}=-\frac{\partial}{\partial \mathrm{x}}\left\{g\left(\zeta^c-\hat{\zeta}\right)-\left(\mathcal{P}|_{\zeta^c}-\mathcal{K}|_{\zeta^c}\right)+\int_s^0\frac{g\rho D}{\rho_0}\,ds\right\}$
$\boldsymbol{P^c}$	Non-WEC current contribution	$-\frac{\partial}{\partial \mathrm{x}}\left(g\zeta^c+\int_s^0\frac{g\rho D}{\rho_0}\,ds\right)$
$\boldsymbol{P^{wec}}$	WEC contribution	$\boldsymbol{P^{qs}}+\boldsymbol{P^{bh}}+\boldsymbol{P^{pc}}$
$\boldsymbol{P^{qs}}$	Quasi-static response	$g\frac{\partial\hat{\zeta}}{\partial \mathrm{x}}$
$\boldsymbol{P^{bh}}$	Bernoulli head	$-\frac{\partial}{\partial \mathrm{x}}\left(\mathcal{K}|_{\zeta^c}\right)$
$\boldsymbol{P^{pc}}$	Surface pressure boundary correction	$\frac{\partial}{\partial \mathrm{x}}\left(\mathcal{P}|_{\zeta^c}\right)$

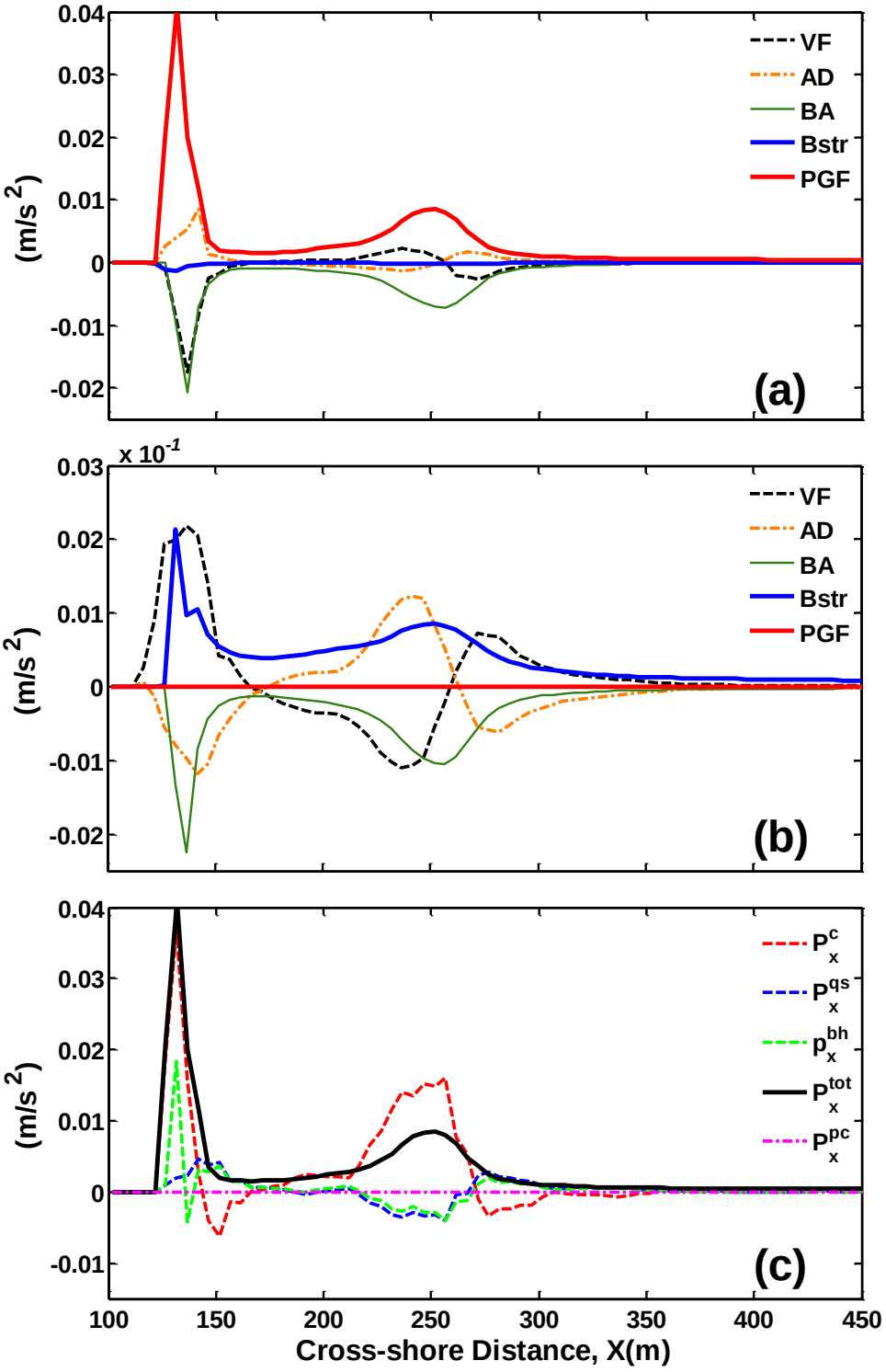

Figure 4.10: Cross-shore profiles of depth-averaged (a) cross-shore and (b) longshore momentum balance terms; (c) decomposed PGF terms in cross-shore direction as described in Eq. (4.3)

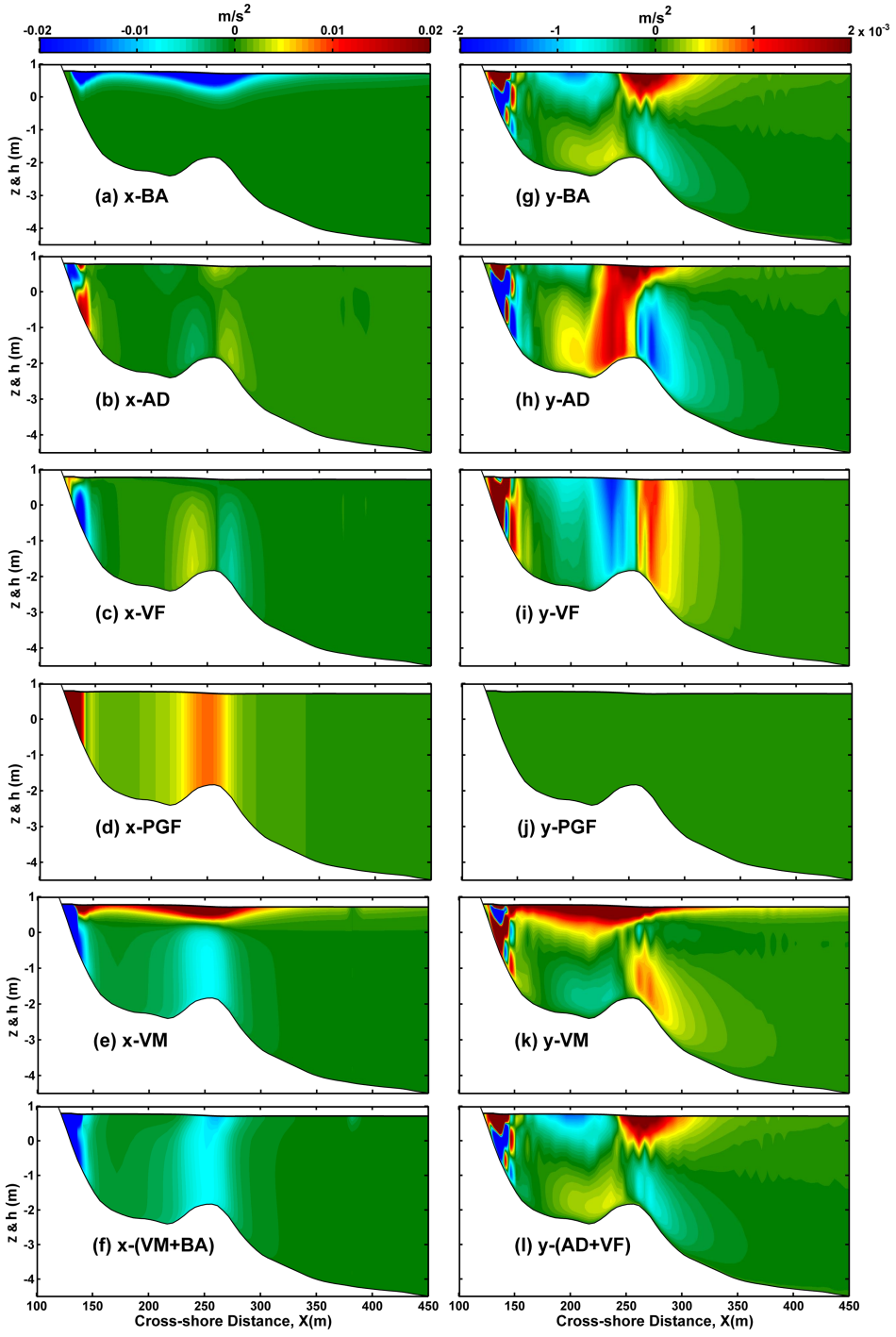

Figure 4.11: Cross-shore and vertical distribution of the terms contributing to the cross-shore (x) and longshore (y) momentum balance. Cross-shore terms: (a) x-breaking acceleration (x-BA); (b) x-Eulerian advection (x-AD); (c) x-vortex force (x-VF); (d) x-pressure gradient force (x-PGF); (e) x-vertical mixing (VM); (f) x-vertical mixing plus breaking acceleration (x-VM+BA); and alongshore terms: (g) y-breaking acceleration (y-BA); (h) y-Eulerian advection (y-AD); (i) y-vortex force (y-VF); (j) y-pressure gradient force (y-PGF); (k) y-vertical mixing (y-VM); and (l) y- advection plus vortex force (y-AD+VF)

terms. $\boldsymbol{P}^{wec}$ is further decomposed into a quasi-static response $\boldsymbol{P}^{qs}$, a Bernoulli head contribution $\boldsymbol{P}^{bh}$ and a WEC surface pressure boundary correction $\boldsymbol{P}^{pc}$ term:

$$\begin{aligned}\boldsymbol{P}^{tot} &= \boldsymbol{P}^{c} + \boldsymbol{P}^{wec} = \boldsymbol{P}^{c} + \left(\boldsymbol{P}^{qs} + \boldsymbol{P}^{bh} + \boldsymbol{P}^{pc}\right) \\ &= -\nabla_{\perp}\left(g\zeta^{c} + \int_{-h}^{z} \frac{g\rho}{\rho_0}\, dz\right) + \left(g\nabla_{\perp}\hat{\zeta} + \nabla_{\perp}\mathcal{K}|_{\ \zeta^{c}} + \nabla_{\perp}\mathcal{P}|_{\ \zeta^{c}}\right)\end{aligned} \tag{4.3}$$

Analysis of these individual components of the total pressure gradient force P_x^{tot} (Figure 4.10(c)) shows that, except for the surface pressure boundary correction term (P_x^{pc}), in the surf zone all the other three terms (i.e. P_x^{c}, P_x^{bh} and P_x^{qs}) have significant contributions to P_x^{tot}, with the non-WEC response term P_x^{c} contributing most. Outside the surf zone, however, all these terms become very small. It is important to note that in the region between the trough and crest of the bar, where high velocity shear contributes significantly to P_x^{bh} , the contribution by P_x^{bh} modifies P_x^{tot} significantly and the term thus plays an important role in this region. This is an improvement to the classical view of the barotropic cross-shore momentum balance (cf., Bowen et al. [28]; Uchiyama et al. [148]) which suggests that P_x^{tot} is primarily controlled by P_x^{c} and P_x^{qs}. As suggested by Uchiyama et al. [23], this is also the major factor that causes the difference in the wave-induced sea-level setup between the 2D (not shown here) and 3D cases.

The vertical variation of the momentum balances is shown in Figure 4.11. In the cross-shore direction, the breaking acceleration (x-BA, Figure 4.11(a)), pressure gradient (x-PGF, Figure 4.11(d)) and vertical mixing (x-VM, Figure 4.11(e)) terms are the major contributors to the momentum balance with strongest values occurring at locations where total wave dissipation is maximum, while the advection (x-AD, Figure 4.11(b)) and vortex force (VF, Figure 4.11(c)) terms are relatively weak and insignificant. Note that the VF term here is dominated by the vertical VF contribution. In this 3D cross-shore momentum balance, the VM term apparently plays an important role. It vertically transfers the surface-intensified BA down to the bottom (Figure 4.11(f)) with a near vertically-uniform distribution, and consequently it balances the nearly barotropic pressure gradient force (x-PGF, Figure 4.11(d)).

In the longshore direction, all the remaining terms (i.e., y-BA, y-AD, y-VF and y-VM) with the exception of y-PGF demonstrate significant contributions to the 3D momentum balance, in which the sum of y-BA and y-AD are balanced by the sum of y-VF and y-VM. The breaking acceleration y-BA displays a similar distribution to x-BA but is one order of magnitude smaller due to the small obliqueness of the incident waves. All of the terms of y-AD, y-VF and y-VM demonstrate evident 3D structures

which implies that it is necessary to have a fully 3D structure for the Stokes drift and VF even in shallow littoral regions like DUCK94. Similar to the longshore depth-averaged balance where vortex force balances advection, the y-VF and y-AD also seems to balance each other in this 3D budget. However, they do not completely cancel each other (Figure 4.11(l)), but instead, their sum yields a net contribution that modifies the flow pattern.

4.5 Normally Incident Waves on A Plane Beach with Shore-Parallel Breakwater

To further demonstrate the flexibility of the unstructured mesh in the present model, the laboratory experiment of Hamm et al. [7] was numerically simulated. The experiment involved regular waves propagating and breaking around a shore-parallel breakwater on a plane beach in a large scale wave tank at Sogreah Ingenierie. The layout of the plane beach with the breakwater is presented in Figure 4.12. In this test case, wave diffraction behind the breakwater induces complex three-dimensional flow patterns. The model is used to simulate the REG0107 test, which comprised detailed measurements of wave height and flow velocity (undertow) profiles at various positions around the breakwater. Figure 4.13(a) shows the model domain (a cross-shore width of 26m and an alongshore length of 60 m), measurement locations and the position of the breakwater of length 6.66 m and 0.90 m wide placed 9.3 m from the shoreline. The triangular mesh grid used in this case is shown in Figure 4.13(b), in which the mesh is locally refined behind the breakwater (with a resolution of about 0.22 m) in order to obtain comparatively high resolution results there. However, given the rather simple geometry of this case, the simulation can only be regarded as a preliminary and limited demonstration of the flexibility of the unstructured mesh, which has more added benefit for cases with a much more complicated coastline. The model settings are the same as for the ideal plane beach case (Section 4.2), except that the wave information at the offshore boundary is provided by normally incident regular waves with wave height of 0.78 m and wave period of 1.69 sec and no flow boundary conditions are utilized at the shoreline and lateral ends. The built-in feature 'OBSTACLE' of UnSWAN is utilized to simulate the wave diffraction around the breakwater with a constant transmission coefficient of 0.3 to mimic the structure porosity. The wave diffraction is approximated with a phase-decoupled refraction-diffraction approach proposed by Holthuijsen et al. [197], which however has some limitations (The SWAN Team [86]). The simulation was conducted for 1 hr before the solution converged, with a barotropic time step of 0.05 sec and a mode-splitting ration of 6.

Figure 4.14 shows the distribution of computed wave height and depth-averaged

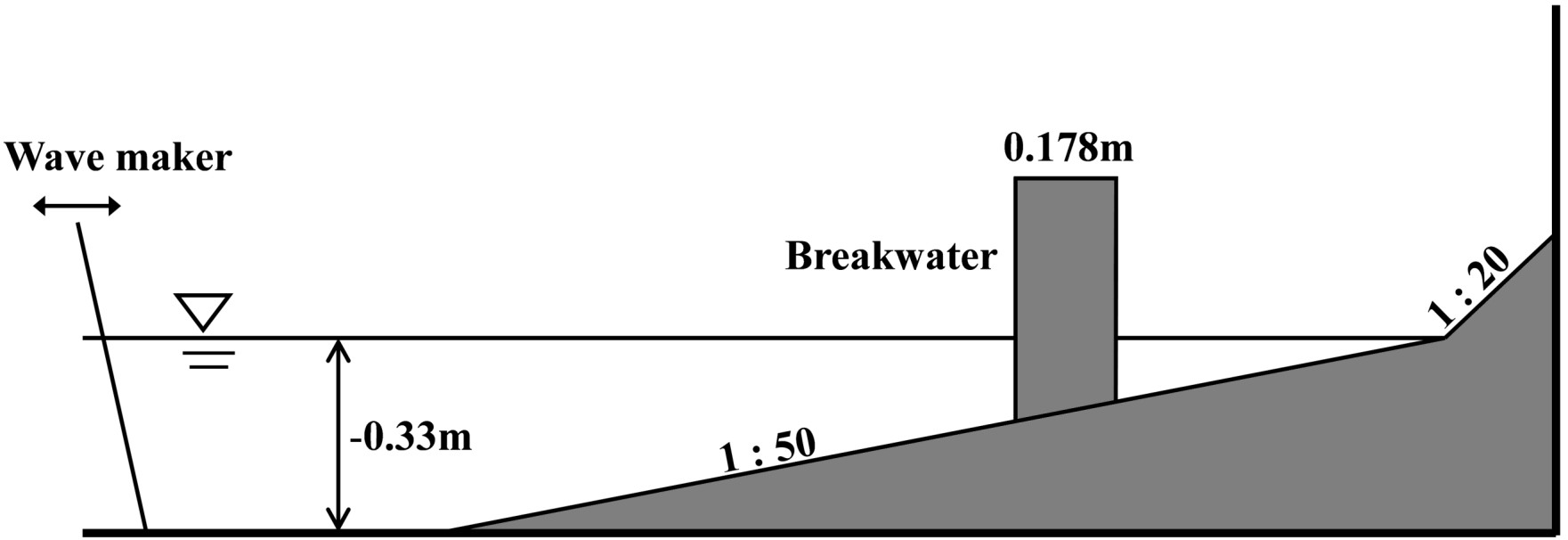

Figure 4.12: Experimental layout of Hamm et al. [7]

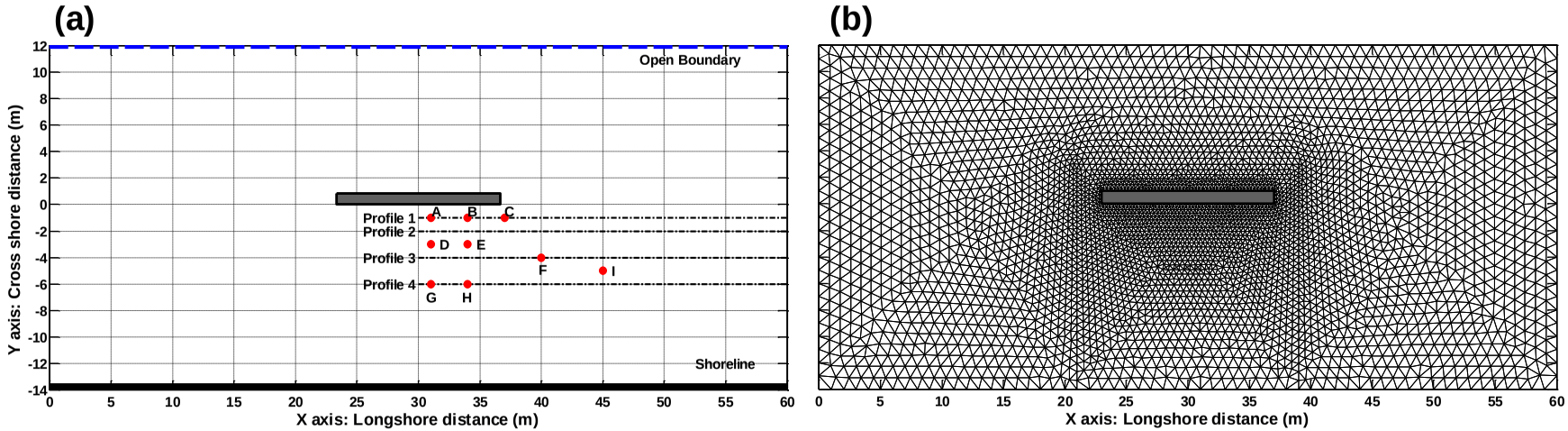

Figure 4.13: (a) Model domain and measurement profiles and points of Hamm et al. [7], the open boundary is located at Y = 12 m; (b) the horizontal unstructured triangular grids used for the simulations of the breakwater case.

flow velocity for this case. The wave diffraction as well as two large flow circulations can be seen clearly behind the breakwater. These two circulations are symmetric as the wave propagates with normal incidence to the shoreline, corresponding well with the results of Li et al [198]. Figure 4.15 shows the measured and computed wave heights, and alongshore and cross-shore depth-averaged velocity distributions along several along-shore transects behind the breakwater. As the waves propagate perpendicular to the shoreline, the computed wave height and wave induced cross-shore velocity are symmetrical along the centre of the breakwater (i.e. $X = 30$ m), while the wave-induced alongshore velocity has the same magnitude but opposite sign for each side of the $X = 30$m axis. Compared with the measurements, the model predicted wave heights are fairly good along the major part of the selected four transects. However, in the places close to the tip of the breakwater (around $X = 40$ m) in the transect 2 and 3, the simulated wave height is under-predicted which is largely attributed to reflection processes which are not properly resolved by the wave model for this case. The predicted longshore and cross-shore velocity are also found to be fairly close to the measurements in all regions, apart from the under-predicted cross-shore velocities around $X = 40$ m due to the under-predicted wave height there.

The predicted long-shore and cross-shore velocity vertical profiles are further compared with the laboratory data at several points (points A-I in Figure 4.13(a)) around the breakwater; details are shown in Figure 4.16. Similar to the depth-averaged velocities in Figure 4.15, the predicted long-shore velocity profiles agree well with the measurements at almost all positions, except for position F where the predicted profile has the correct magnitude but is of opposite sign compared to the laboratory data. This is attributed to the poorly-predicted depth-averaged longshore velocity shown at $X = 10$ m in Figure 4.15(g). The predicted cross-shore velocity profiles are also fairly good compared with measurements at most positions. The differences between the computed and measured cross-shore velocities are largely due to the discrepancies involved in the depth-averaged cross-shore velocity as shown in Figure 4.15, which in return arise because of discrepancies in the wave height. Another explanation for the discrepancies in the cross-shore velocity is the highly non-uniform flow for this experiment, which induces strong horizontal gradients and relatively large discrepancies between measured and modelled cross-shore velocities for relatively small offsets in the predicted location of the circulations (as also indicated by Rakha [199]).

Overall, the present simulation conducted by the new model system in this study successfully reproduces the complex flow structures involving a wave-induced current interacting with a shore-parallel breakwater. There are some discrepancies involved in the velocity profiles due to the under-prediction of wave height resulting from the limited performance of the wave diffraction simulation in the wave model. A better

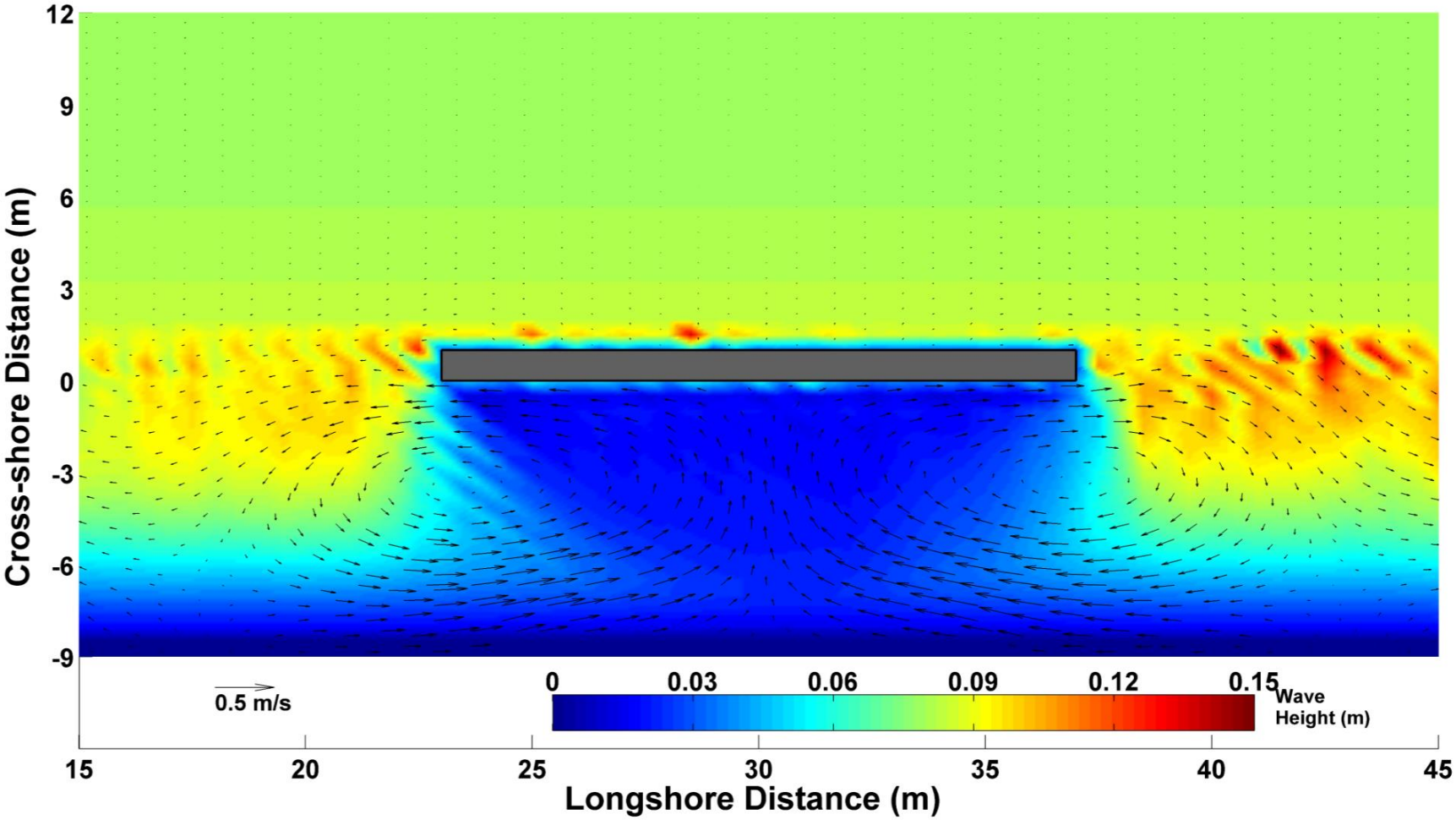

Figure 4.14: The wave height (colour) and depth-averaged velocity (vector)

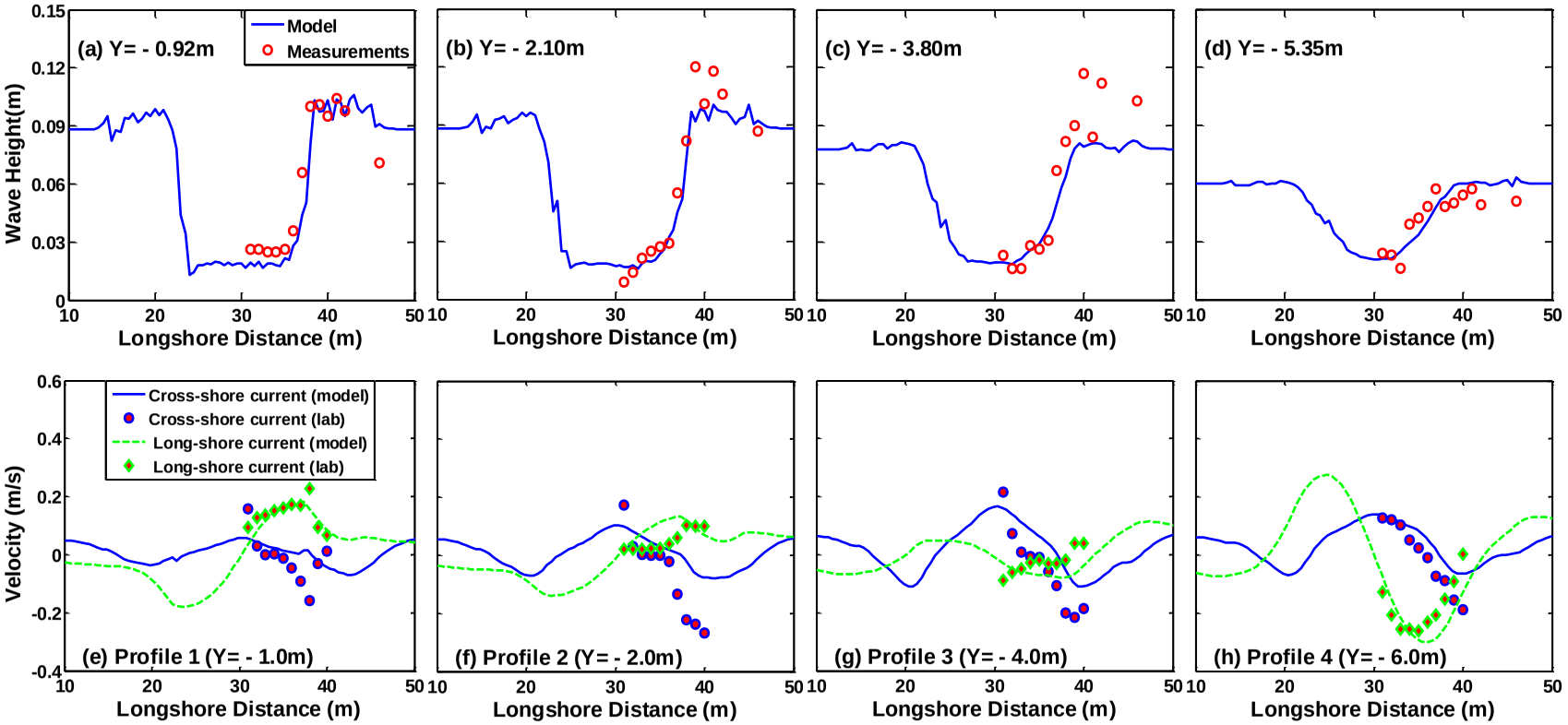

Figure 4.15: Comparison of model predicted and measured wave height (a-d), alongshore and cross-shore velocity distribution (e-h) along a number of transects in the Hamm et al. [7] experiment, test REG0107

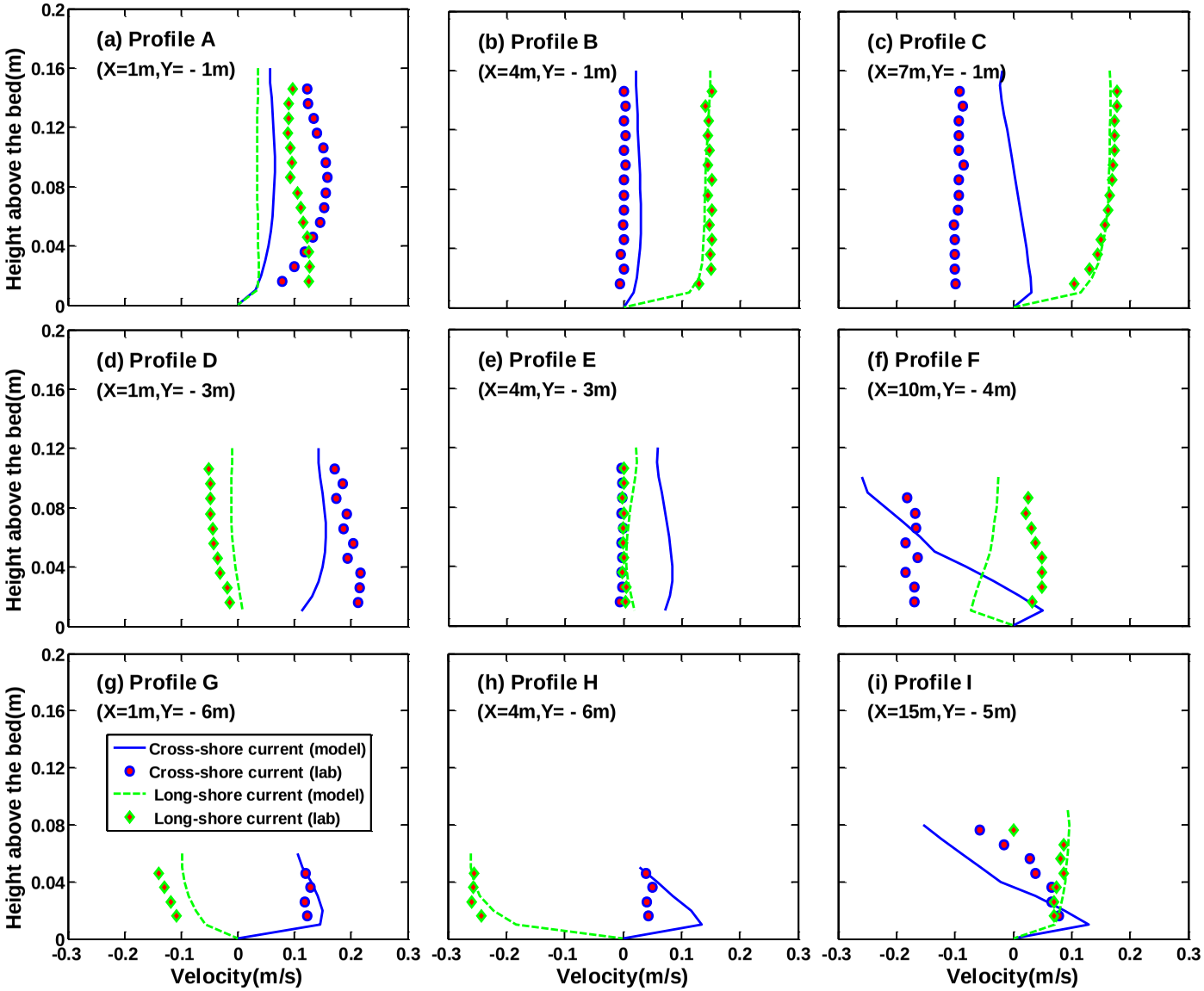

Figure 4.16: Comparison of model predicted and measured velocity vertical profiles at a number of positions in the Hamm et al. [7] experiment, test REG0107

prediction of the wave statistics would likely lead to a better prediction of the flow pattern. However, the overall qualitatively good representation of the dominant flow structures suggests the implementation of the wave-current interaction based on the VF approach is appropriate.

4.6 Conclusions

In this chapter, a detailed validation of the hydrodynamic part of the newly developed morphodynamic model system against several cases with different spatial scales and both 2D and 3D complex hydrodynamic conditions is displayed. The new morphodynamic model system is firstly validated against a theoretical case of obliquely incident waves on a planar beach. It is then applied to three test cases for both validation and dynamical interpretation: a large scale laboratory experiment of normally incident waves on a rigidized barred beach, a field experiment of obliquely incident waves on a natural sandy barred beach (Duck'94 experiment), and a 3D laboratory experiment involving normal incident waves propagating around a shore-parallel breakwater. The model predictions follow the available measurements in these tests well, suggesting robustness and efficiency in the present model for very different spatial scales and for both 2D and 3D complex hydrodynamic conditions. A general encountered difficulty in many coastal hydrodynamic simulations under breaking waves is the reproduction of Eulerian and Stokes velocities across the beach. The model results for the above applications suggest that the VF approach is capable of reproducing these balanced flow patterns for various types of beach and wave conditions.

Model simulations of the Duck 94 experiment indicate clearly that the VF is important in determining the two levels of momentum balance in both cross-shore and longshore flows. The VF method also represents the complex 3D wave dynamics and wave-driven circulation patterns around a laboratory breakwater. The simulation of the laboratory breaking wave over a barred beach indicates the importance of roller effects and of wave energy dissipation on the cross-shore mean flow (undertow) profiles. In this particular case, the empirical parameter α in Eq. (3.12) with a value of 0.75 produces the best fit with the measured data. Different values were tested for α_r (fraction of wave energy dissipation converted to roller) and for the C1 parameter that controls turbulent dissipation rates; results suggest that both parameters should vary across the breaking region for a better model accuracy. A better reproduction of the turbulent kinetic energy also leads to an improved reproduction of the undertow velocity profile.

Overall the newly developed modelling system with implementation of VF formalism

successfully resolves waves and currents in the surf zone. The modelling system provides a robust tool for better understanding of hydrodynamic processes in coastal regions, and will also be used to explore sediment transport processes and morphodynamics in the next chapter.

Chapter 5

Model Application

5.1 Introduction

In this chapter, the developed model system is applied to a laboratory mobile bed experiment. This experiment is conducted within the research project SINBAD, including breaking waves over a rigid bed profile (van der A et al. [20]) and over a mobile bed of medium-sand (van der Zanden et al. [53]). The fixed bed case has been used for model validation in Section 4.3 and the mobile bed case is tested as a model application in this chapter in detail. In this experiment, detailed measurements of hydrodynamics (water level, flow velocity and turbulent kinematic energy, etc.) and sand transport processes are obtained with a high spatial resolution, especially around the breaker bar and near the bed surface. In addition, the bed level evolutions are also recorded. With these measurements, the performance of every module (i.e. circulation module, wave module, sediment transport module and morphology evolution module) in a morphodynamic model, either as a stand alone part or a whole system, can be explicitly evaluated in detail against the measurements. The results also can be used to reveal the underlying processes in combination with the laboratory data, which make this experiment a perfect application case for the newly developed model system.

5.2 The experiment

This experiment was conducted in the large-scale CIEM wave flume in Barcelona, which is 100 m long, 3 m wide and 4.5 m deep and equipped with a wedge-type wave paddle (van der Zanden [5]). Figure 5.1 shows the setup and measurement locations of this experiment. The initial bed profile consists of a bar-trough bed configuration which can be roughly divided into four sections: an offshore-facing slope of the breaker bar (x = 35.0 to 54.8 m; $\tan(\alpha)$ = 1:10); a steeper shoreward-facing bar slope (x = 54.8 to 57.5

m; tan(α) = -1:4.7); a mildly sloping bed shoreward from the bar trough (x = 57.5 to 68.0 m; tan(α) = 1:95); and a non-mobile straight sloping beach (x = 68.0 to 80.0 m; tan(α) = 1:7.5), which is covered with geotextile and perforated concrete slabs designed to prevent erosion and promote wave energy dissipation. The coordinate system used in Figure 5.1 is defined as follows: the horizontal coordinate x is positive towards the beach with its origin at the toe of the wave paddle in its rest position; the vertical coordinate z is positive upward with $z = 0$ at the still water level. The water depth is $h_0 = 2.55\ m$ in the horizontal part of the flume, and the wave condition consists of monochromatic waves with wave period $T = 4.0\ s$ and wave height of $H_0 = 0.85\ m$ at the paddle. These conditions result in a surf similarity parameter $\xi_0 = 0.54$ (where $\xi_0 = tan(\alpha)/\sqrt{H_0/L_0}$; $tan(\alpha) = 1:10$ is the offshore bar slope and $L_0 = gT^2/2\pi$ is the deep-water wave length), which corresponds to a plunging type breaker. The mobile bed consists of sand with a medium median diameter $D_{50} = 0.24\ mm$, which has a measured settling velocity $w_s = 0.034\ m/s$.

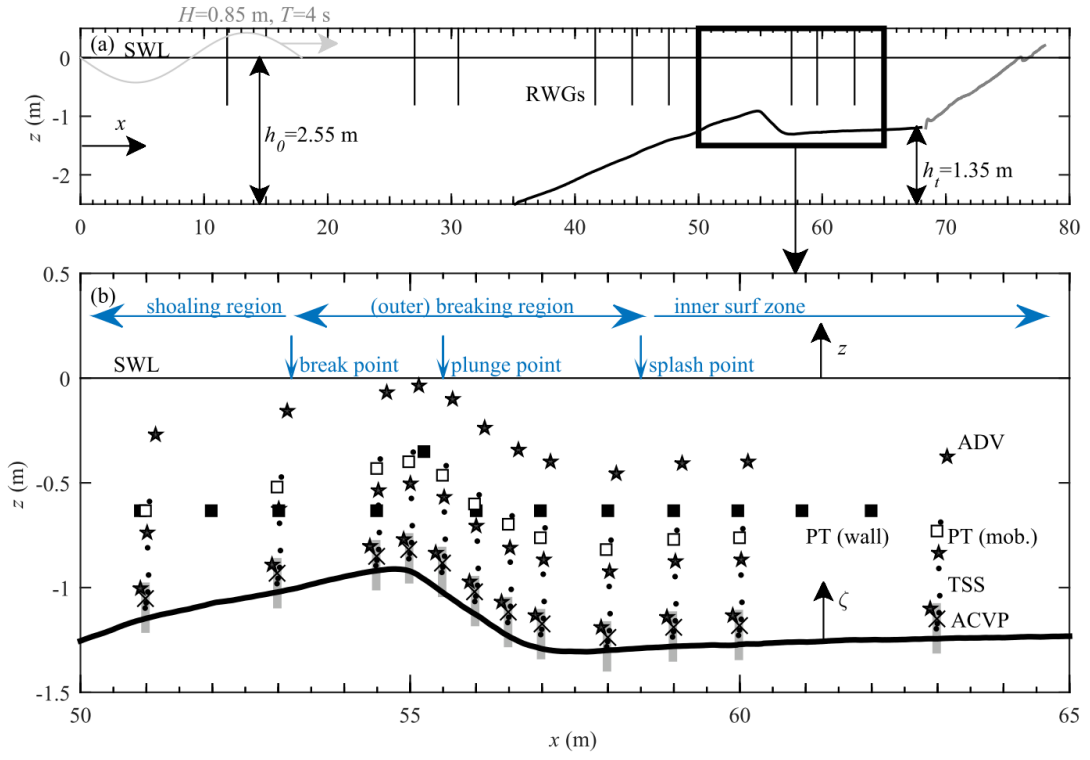

Figure 5.1: Experimental set-up and measurement locations (After van der Zanden [5]). (a) Initial bed profile (black line) and fixed beach (grey line), and locations of resistive wave gauges (RWGs, vertical black lines); (b)Measurement positions of ADVs (star symbols), mobile-frame Pressure Transducers (PT, white squares), wall-deployed PTs (black squares), Transverse Suction System nozzles (TSS, black dots), Optical Backscatter Sensor (black crosses), and measuring range of mobile-frame ACVP (grey boxes)

Starting from the initial bed profile (Figure 5.1), this experiment is run for 90 minutes, comprising of six 15-min runs, during which the bed evolved further. The bed profile is measured at the start of each experiment and after every 30-min run, namely at 0, 30, 60 and 90 min.

5.3 Model setup

In this chapter, the model testing is separated into two parts. At the first part (Section 5.4, 5.5 and 5.6), the model is applied to the condition corresponding to the third run in the experiment, e.g. 30-45 min by assuming the bed remains the same, focusing on the hydrodynamics and sediment transport processes, in which the relevant model parameters are calibrated to obtain a best model results. This is due to the fact that the bed profile evolution was very small during this 15 mins in the experiments and thus its effect on the hydrodynamics and also suspended sediment concentration can be neglected. With these calibrated model parameters, the model system is then applied to simulate the evolution of the mobile bed profile in the second part (Section 5.8), covering the experiment run during 45-60 min.

5.4 Hydrodynamics

In this section, the model simulation results regarding the wave parameters, velocities and turbulent kinetic energy are examined in detail. The values of relevant model parameters that are used in all of the following simulations are summarized in Table 5.1.

5.4.1 Wave Height and Water Surface Elevation

Figure 5.2 presents the the computed (Run I) and measured wave height and mean water level during the 30-45 min run. Overall, the predicted wave height presents a similar characteristic as that in the fixed bed test (Figure 4.3): from the offshore boundary to the shoreline, the wave height decreases first due to the bottom friction induced wave attenuation, and then increases gradually along the offshore bar slope as a result of wave shoaling until $x \approx 52$ m, where it reaches its maximum value and begins to decrease rapidly because of depth-induced wave breaking. The model accurately reproduces the location of the breaking point in this test (as a comparison, the predicted breaking point is shifted by about 1 m shoreward in the fixed bed test; see Figure 4.3), inshore(i.e. $x > 52$ m) the wave height also agrees very well with the measurement. The under-prediction in wave height on the sloping side of the bar may be due to the wave reflection

Table 5.1: Model parameters of the baseline test for the SINBAD mobile bed experiment

Variable	Value	Unit
Offshore wave height H_s	0.85	m
Offshore wave period T_p	4.0	s
Sand median diameter D_{50}	0.24	mm
Sand settling velocity w_s	0.034	m/s
Wave Roller dissipation parameter $sin\beta$	0.1	-
Wave roller parameter α_r	1.0	-
Turbulent model coefficient C_1	*	

* $C_1 = 1.10$ at $x < 53$ m and $C_1 = 1.15$ at $x > 53$ m.

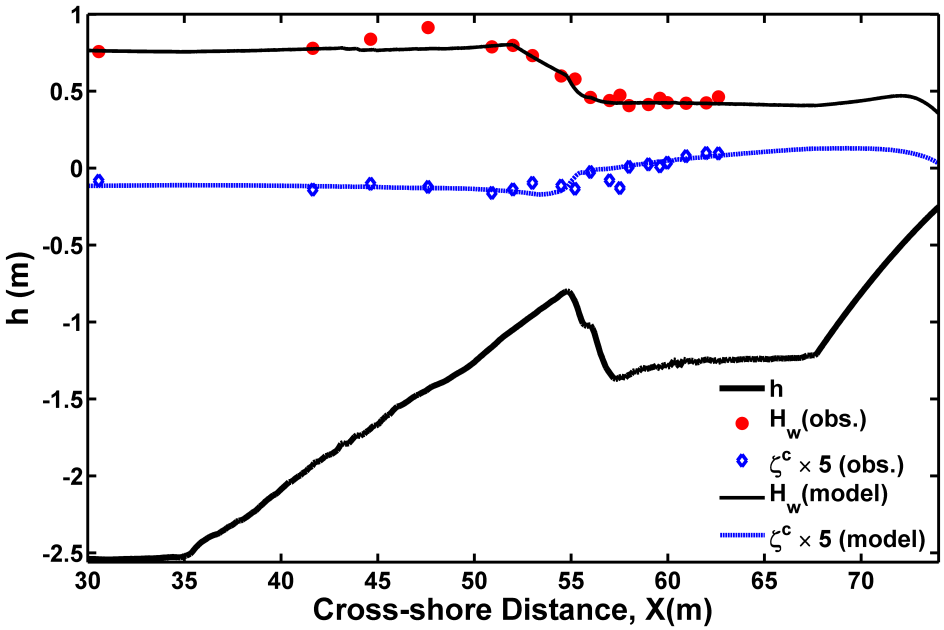

Figure 5.2: Cross-shore distribution of the significant wave height H_{sig} and five times of sea surface elevation $\zeta^c \times 5.0$ for the SINBAD mobile bed test.

and/or spurious wave generation in the laboratory, which is also seen in Figure 4.3.

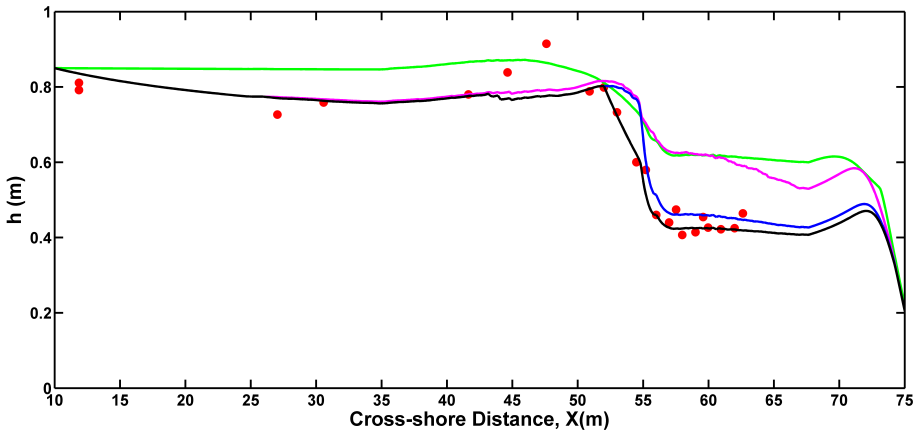

Figure 5.3: Model predicted wave height with different approaches: red nodes represent the measurement; lines represent model results simulated with the constant breaker index approach (green line), original β-kd approach (pink line), β-kd approach after the first modification (blue line) and β-kd approach after the both two modifications (black line)

It is interesting to note that the wave height gradient demonstrates two distinct sections, with a more or less constant value in each section, from the breaking point to the location where wave height keeps almost constant further shoreward (i.e. $x = 52$ m to $x = 57.5$ m). The location which separates these two sections is $x = 54.8$ m, which is exactly the peak location of the breaker bar where the bed profile slope transfers from a positive value into negative one. This results from a modification of the β-kd wave breaking approach (Salmon et al. [140]) used in this simulation. The original β-kd approach estimates the bottom slope, using in determining its breaker index parameter (i.e. $\gamma_1(\beta) = \gamma_0 + a_1 \tan\beta$ in the Eq. (5) of Salmon et al. [140]), as the magnitude of the bottom gradient taken from the computational grid (i. e. $\tan\beta = |\nabla d|$), which means it does not discriminate between forward, backward or sideways sloping profiles. However, the wave height simulated with this original β-kd approach is apparently overestimated in the surf zone (pink line in Figure 5.3). In order to achieve better agreement, two modifications are made on the original β-kd approach. In the first modification, the positive and negative slope profile is distinguished by using the expression of $\tan\beta = 0.5(\nabla d + |\nabla d|)$, i.e. the effect of negative slope in determining the $\gamma_1(\beta)$ parameter is neglected. After this modification, the predicted wave height (blue line in Figure 5.3) is much better in the area shoreward of the bed breaker bar (i.e. $x > 55$ m). However, it is still over-predicted in the area between $x = 52$ m to $x = 55$ m. The breaker index (see the Section 3.2.2) is further limited by a maximum value of 0.85 (i.e. $\gamma = \min[0.85, \gamma_1(\beta)]$) in the second modification, after which the wave height is finally well predicted (Figure 5.2; black line in Figure 5.3). For comparison, the predicted wave

height with the default constant breaker index approach ($\gamma = 0.73$) is also presented (green line in Figure 5.3), with the largest discripency among all the approaches.

Similar to Figure 4.3, the mean water level is multiplied by a factor of 5.0 to zoom in details of the inter-comparisons of the simulation and measurement. The simulated mean water level shows a continuous and nearly constant set-down of approximately 3 cm from x = 0 m (i.e. the offshore boundary) to $x \approx 54$ m, where it rapidly (within 2 m) turns into a set-up. The set-up value increases slowly throughout the inner surf zone, with a maximum value of about 2.5 cm near the end of the flume. Although the magnitude has been multiplied with a factor of 5, the discrepancy between the simulated and measured water level is still very little, indicating that the cross-shore behaviour and the quantitative set-down and set-up are well reproduced by the model. However, it should be noted that some oscillations present in the measured water level are not seen in the model results after breaking ($x > 55m$). This may results from several reasons, e.g. wave reflection and/or spurious wave generation exist in the laboratory; the bed profile evolves during the period when measurement is conducted while the bed profile keeps constant in the model simulation.

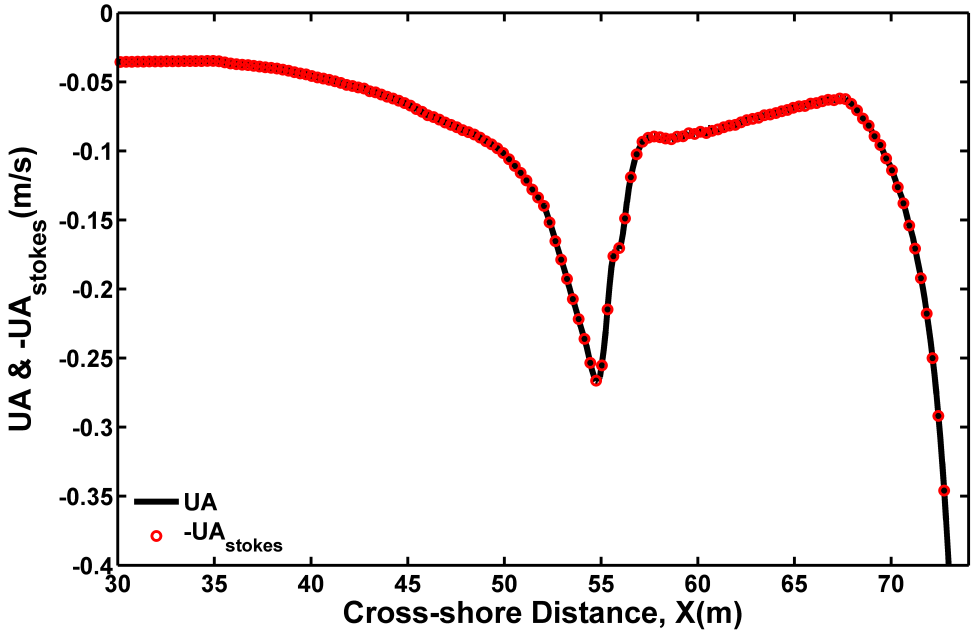

Figure 5.4: Cross-shore distribution of the depth-averaged cross-shore Eulerian velocity UA (solid line) and Stokes velocity $-UA_{stokes}$ (red circles) for the SINBAD mobile bed test.

5.4.2 Velocities

Figure 5.4 shows the simulated depth-averaged Eulerian velocity in Run I. Similar to the characteristics shown in Figure 4.3(b), it has the same magnitude but opposite sign to the depth-averaged Stokes flow, which is in good accordance with the barotropic mass conservation law. This also indicates that the model result has reached a steady state.

The simulated cross-shore and vertical distribution of the Eulerian velocity (Run I, Figure 5.5) is similar to that in the fixed bed experiment (Figure 4.3), while it is much more complicated than the plane beach condition (Figure 4.2) due to the more complex barred bathymetry. From the offshore boundary until $x \approx 48$ m, the Eulerian velocities have relatively small magnitudes ($x < 0.15$ m/s) with onshore direction in approximately the upper 1/3 water column and offshore direction in the lower 2/3 of the water body. Further shoreward from $x = 50$ m, large velocity gradients in both the horizontal and vertical direction are present in the water column around the breaker bar, leading to large onshore-directed velocities near the water surface and offshore-directed velocities near the bed. This is closely related to the enhanced mass flux resulting from the depth-induced wave breaking in this region (Figure 5.2). The Eulerian velocity has a maximum value (onshore-directed) of about 0.55 m/s near the water surface at $x \approx 57$ m, and a minimum value (offshore-directed) of about -0.5 m/s near the bed above the peak of the breaker bar (i.e. $x \approx 55$ m).

A further model-data comparison is made for the cross-shore Eulerian velocity at twelve profiles in Figure 5.6, which shows fairly good agreement between the simulated results and the measurement. For morphodynamic models, the ability to reproduce flow velocities with good accuracy is one of the most important prerequisites (see details in Section 3.4, 3.5 and 5.5) to obtain good predicted sediment transport rates and bed evolutions. A good prediction of the near bed velocities is crucial for this purpose, as they are used to calculate the bed stresses which in turn determine the amount of sediment stirred up from bed into suspension in the suspended sediment transport module and directly determine the bedload transport rate in the bedload formulation. The calculated velocity values in the first grid above the bed are used to calculate the bed shear stresses, with the assumption that the law of the wall is satisfied in these locations. In order to facilitate the comparison between the measured and model predicted velocities, the locations of the first grid above the bed used in the model at all of the twelve profiles are demonstrated with horizontal red dashed lines in Figure 5.6. Apparently, the simulated near bed velocities are also in fairly good agreement with the measurement.

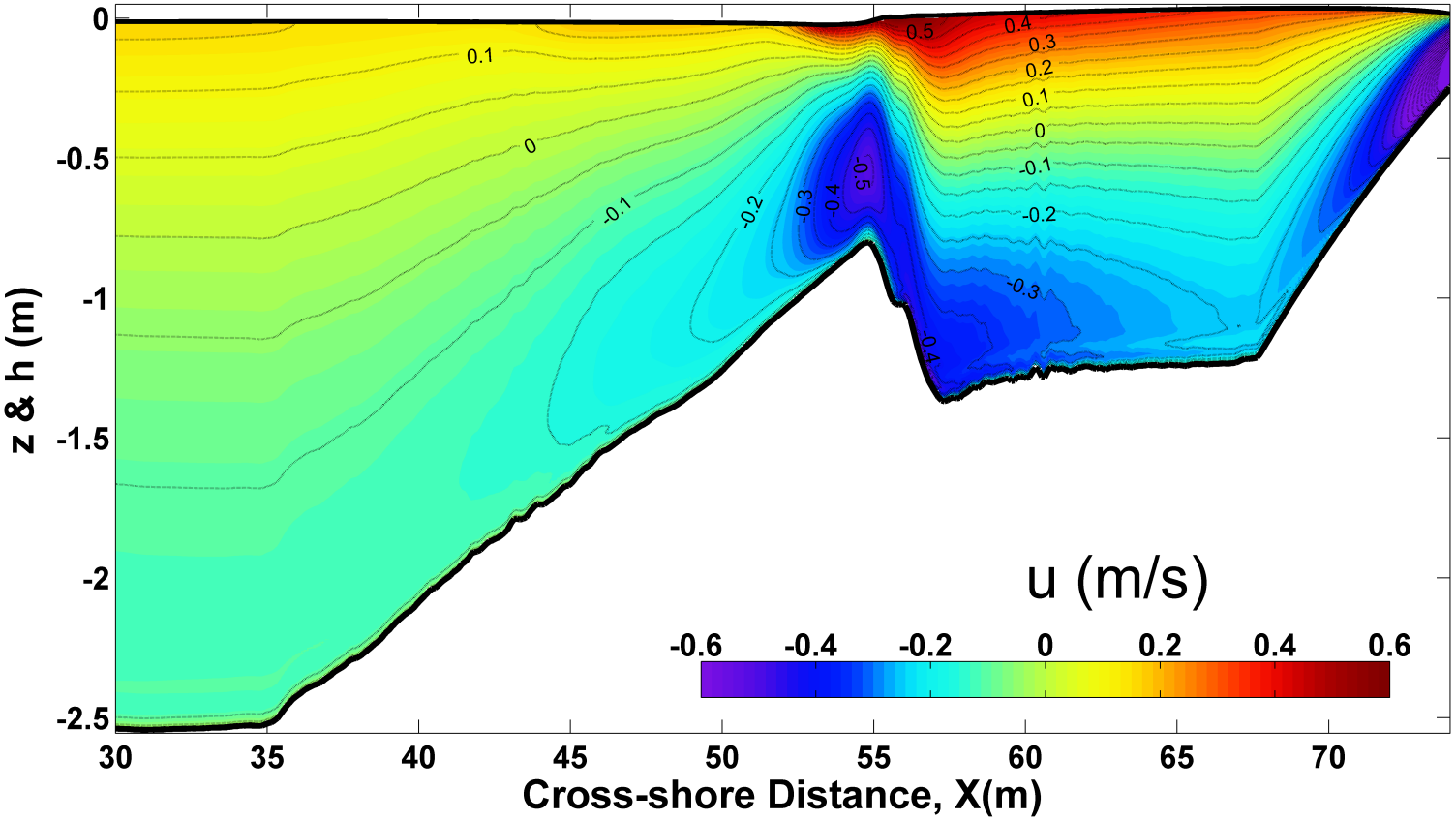

Figure 5.5: Model simulated distribution of cross-shore velocity u in the SINBAD mobile bed test; contour lines explicitly show the velocity value

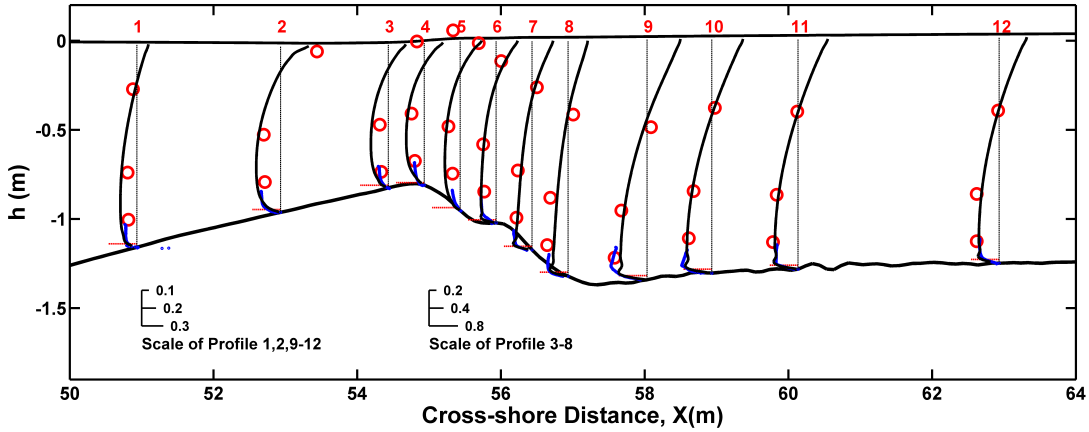

Figure 5.6: Comparison of simulation results (solid black lines) with observed vertical profiles (red circles and short near-bed blue lines) for the cross-shore velocity. The vertical black dashed lines indicate the profile measurement locations and zero value for each profile; the horizontal red dashed lines near the bed indicate the location of the first grid above the bed used in the model.

Sensitivity Analysis

Many sensitivity tests with varying parameters are conducted in order to reveal the effects of these parameters on the model's performance and obtain the optimal combinations for later simulations. Apart from the numerical tests on wave height, another two groups of sensitivity tests are conducted at this stage on the calculation of mean water level and flow velocities. The corresponding parameter values used in these tests are summarized in Table 5.2.

In Section 4.3.2, a series of numerical tests are present to explore the effects of wave roller parameter α_r (used in Eq.(3.32)), which controls the fraction of the breaking waves turned into wave rollers before dissipating, on the velocity profiles. A group of sensitivity tests are also conducted for the present SINBAD mobile bed experiment condition (with $\alpha_r = 0.0, 0.25, 0.5, 0.75, 1.0$; Figure 5.7), after which similar conclusions are obtained: without the effect of wave roller, the vertical velocity gradient is relatively too strong above the breaker bar (e.g. profile 3-5) and along the offshore slope (e.g. profile 2), while too small in the surf zone (e.g. profile 7-12); inclusion of wave roller effects improves the model performances: as the value of α_r progressively increases from 0.0 to 1.0, the vertical velocity gradients become smaller around the breaker and bigger in the surf zone, which agree better with the measurements. Among these tests, the model results with $\alpha_r = 1.0$ (Run 1.5) show the best overall agreement with the measured data.

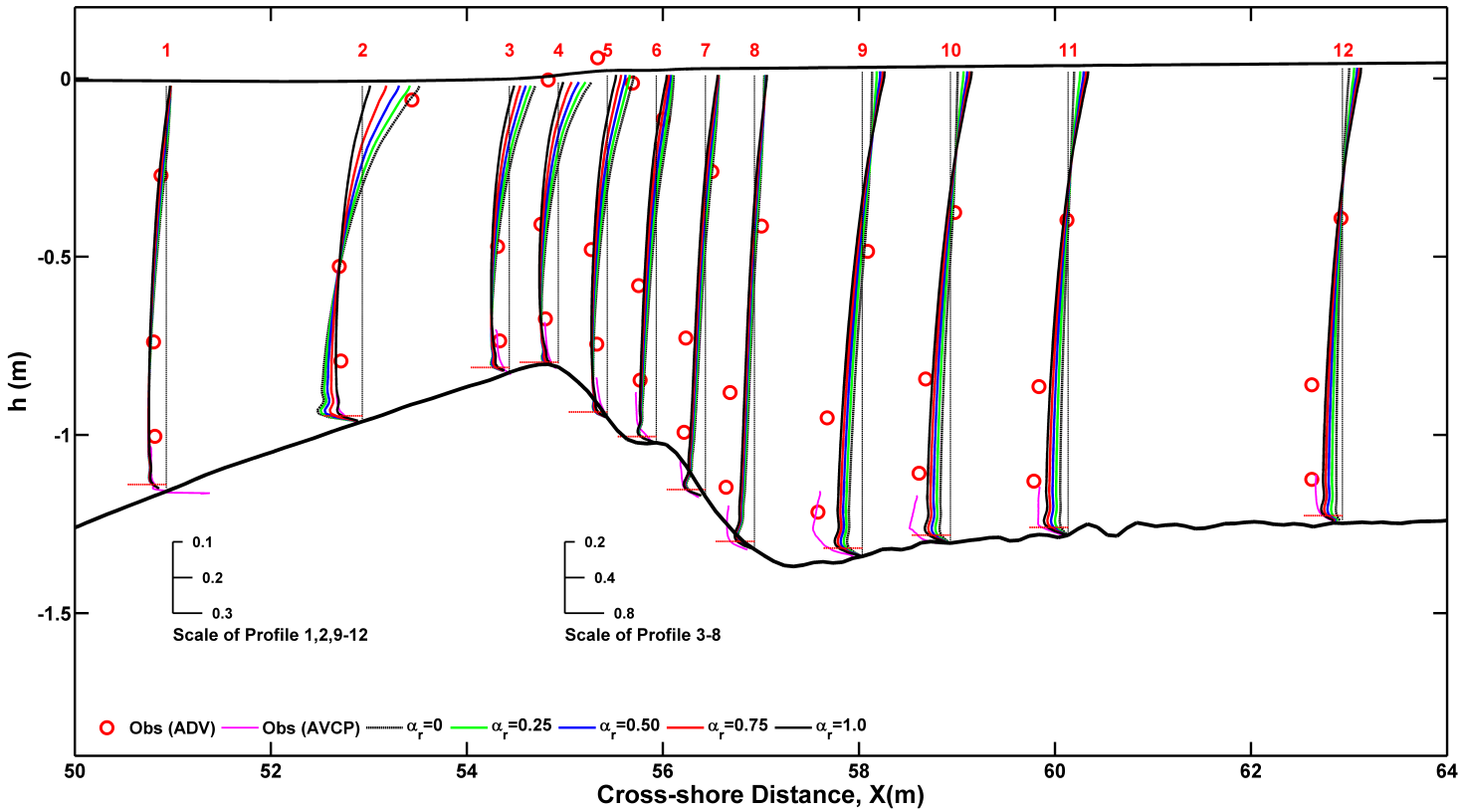

Figure 5.7: Comparison of simulation results (solid lines) with observed vertical profiles (red circles and short near-bed magenta lines) of the cross-shore velocity (u) for the sensitivity to the parameter α_r. The vertical dashed lines indicate the profile measurement locations and zero value for each profile; the horizontal red dashed lines near the bed indicate the location of the first grid above the bed used in the model.

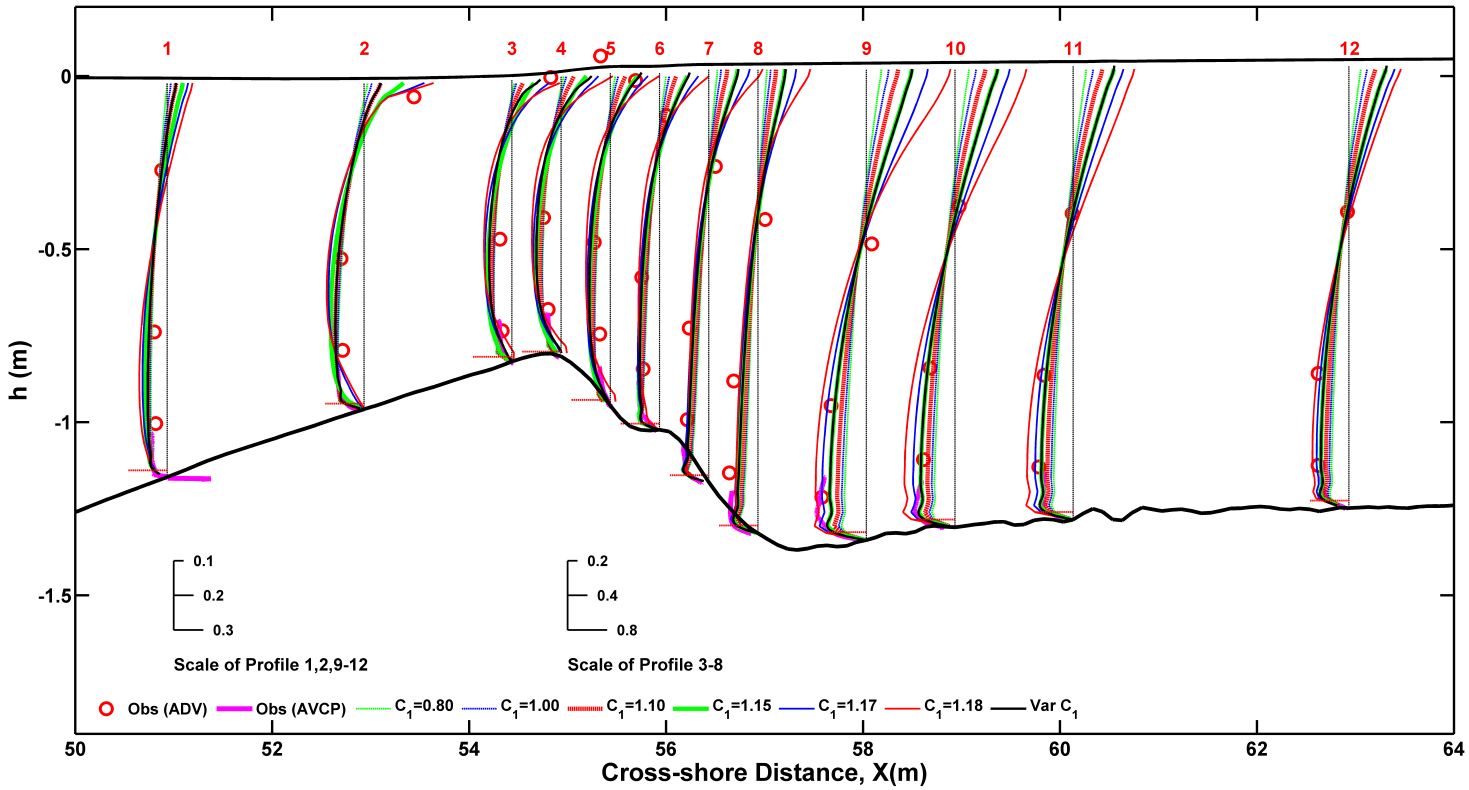

Figure 5.8: Comparison of simulation results (solid lines) with observed vertical profiles (red circles and short near-bed magenta lines) of the cross-shore velocity (u) for the sensitivity to the parameter C_1. The vertical dashed lines indicate the profile measurement locations and zero value for each profile; the horizontal red dashed lines near the bed indicate the location of the first grid above the bed used in the model

Table 5.2: Model configurations of the sensitivity tests for the parameter α_r and C_1

Group #	\	# 1					# 2					
Run #	#I	#1.1	#1.2	#1.3	#1.4	#1.5	#2.1	#2.2	#2.3	#2.4	#2.5	#2.6
α_r	1.00	0.00	0.25	0.50	0.75	1.00	1.00	1.00	1.00	1.00	1.00	1.00
C_1	*	1.00	1.00	1.00	1.00	1.00	1.00	0.80	1.10	1.15	1.17	1.18

* C_1 = 1.10 at $x < 53$ m and C_1= 1.15 at $x > 53$ m.

However, it should also be noted that the undertow velocities in the inner surf zone (e.g. profile 7-12) are underestimated in the above test with $\alpha_r = 1.0$ (Run 1.5). Given that the wave heights are well captured (Figure 5.2), the predicted surface wave dissipation is therefore expected to be reasonable. From a numerical modelling point of view, the vertical structure of flow velocity can also be affected by the turbulent eddy viscosity coefficient. To reveal the effect of turbulence on the cross-shore velocities and to improve the simulation results, five more sensitivity simulations are conducted in this section. Each of these test has a different value of turbulent coefficient C_1 (Eq.(3.57)), which equals 0.80, 1.0, 1.10, 1.15, 1.17 and 1.18 respectively. The simulated flow velocities of these tests are shown in Figure 5.8. Overall, the velocity profile at all twelve locations varies considerably with different values of C_1. As the value of C_1 progressively increases from 0.8 to 1.18, the magnitudes of the simulated velocities at profiles of 7-12, of the onshore directed flow in the upper part of water column and offshore directed undertow in the lower part of water column, also grow gradually and monotonously, leading to large vertical velocity gradients. At these locations, the best agreement is obtained with $C_1 = 1.15$. At the profiles of 1-6, similar velocity characteristics are found in the onshore directed flow in the upper part of water column. However, the changes are complicated in the offshore directed undertow. In the near bed region, the predicted undertow at these locations reaches a maximum value with $C_1 = 1.15$ and decrease gradually with larger or smaller C_1. The simulated velocities with $C_1 = 1.15$ agree best with the measurement at the profiles of 3-5; while for the profiles of 1 and 2, $C_1 = 1.10$ seems more reasonable. This is in agreement with the results in Section 4.4.2, which indicates a sole value of C_1 cannot decrease the normalized r.m.s error at all cross-shore locations simultaneously and thus suggests using a cross-shore-varying C_1 value for different locations.

These variations in C_1 indicate the differences in turbulence generation and dissipation for the region prior to wave breaking and post breaking. Apart from the surface injection that has been included in the present model, an overall increase in turbulence production coefficient after breaking point suggests stronger turbulence mixing in the water column is required in the model compare to the present one. Thus based on the above analysis, a cross-shore varying C_1 ($C_1 = 1.10$ at x $<$ 53 m and $C_1 = 1.15$ at x $>$

53 m) is finally utilized in Run I, in which better simulation results are finally obtained (Figure 5.6).

5.4.3 Turbulent Kinetic Energy

Figure 5.9 displays the comparison between the measured and model simulated TKE in Run I at the 12 profiles as shown in above section. In the upper part of the water column, the simulated TKE is apparently over-predicted at all of 12 profiles. In the lower part of the water column, reasonable well agreement is obtained at profile 1 and 3-6 while over-prediction is still clear in other profiles. This is common behaviour of RANS models, regardless of the turbulence closure model used (e.g Christensen [200]; Bakhtyar et al. [201]; Xie [188]; Jacobsen et al. [202]; Brown et al. [189], Zhou et al. [203]). Many efforts are thus made in the following sections on sensitivity analysis to identify the optimal model parameters to reduce the discrepancies.

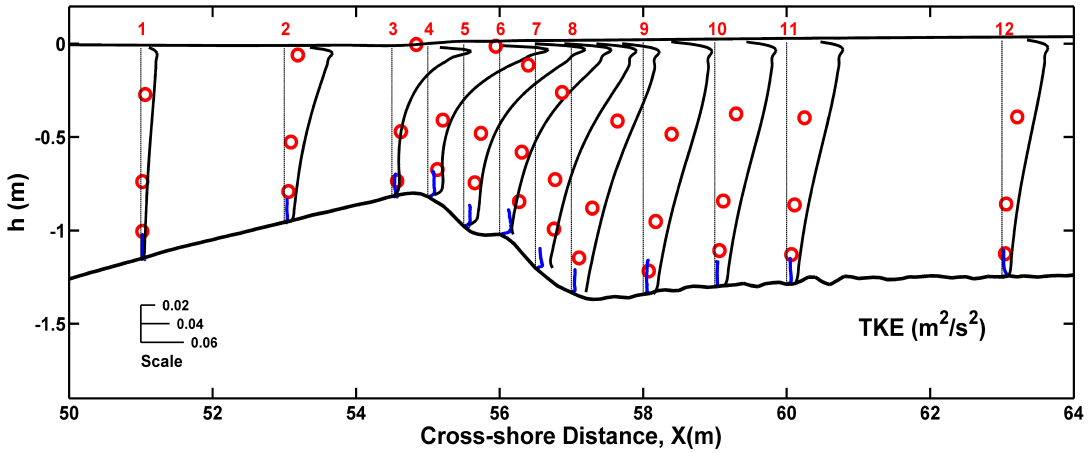

Figure 5.9: Comparison of simulation results (solid black lines) with observed vertical profiles (red circles and short near-bed blue lines) for the TKE. The vertical black dashed lines indicate the profile measurement locations and zero value for each profile.

Tests on C_1

The effect of C_1 on the simulated TKE profiles is checked and analyzed in the first step (Figure 5.10), as the six sensitivity tests (Run 2.1-2.6) in Section 5.4.2 have shown that the turbulent coefficient C_1 could largely affect the velocity profiles. With the default value of $C_1 = 1.0$, the simulated TKE is apparently over-predicted in the whole water column and at all of the profiles. As C_1 increases, the simulated TKE levels at the profiles of 2-7 gradually decrease and approach the measurements, with a locally best

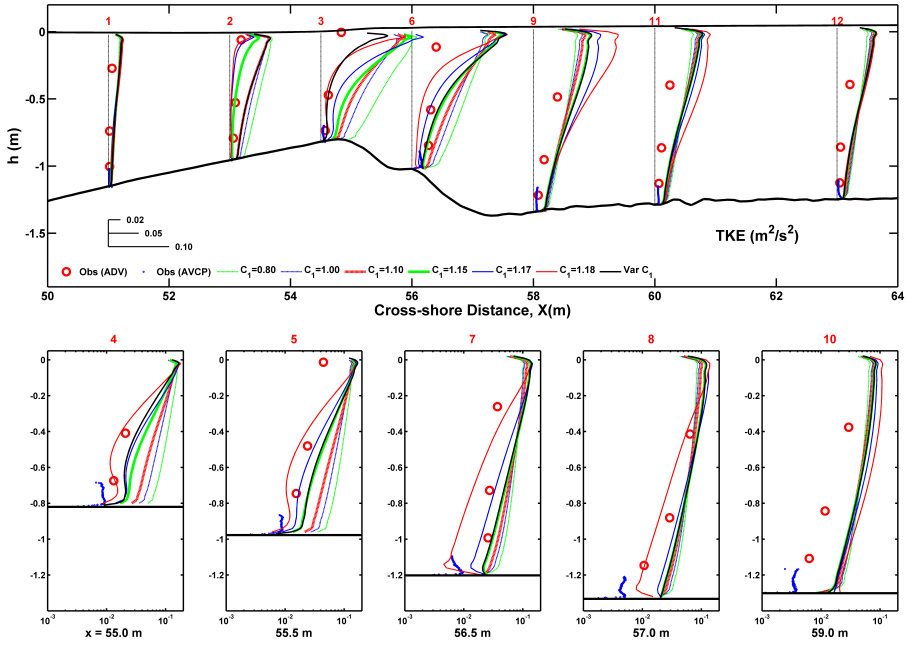

Figure 5.10: Comparison of simulation results (solid lines) with observed vertical profiles (red and blue circles) of TKE for the sensitivity to the parameter C_1. The vertical dashed lines indicate the profile measurement locations and zero value for each profile.

fit value of $C_1 = 1.15$ for profile 2, $C_1 = 1.18$ for profile 3,4 and $C_1 = 1.17$ for profiles 5-7. While for the profiles of 9-11, larger TKE values are obtained with increased value of C_1, showing a reverse tendency to that at profiles of 2-7. The locally best fit value of C_1 for TKE at profiles of 9-11 is 0.80. Overall, general increase of coefficient C_1 (from its defaults value of 1.0) improves the model performance of TKE profiles in the breaking region, but not appropriate for the other locations. In the meantime, it should also be noted that the above best fit of C_1 for TKE profiles are not consistent with that obtained from the analysis of the velocity profiles in Section 5.4.2. These results suggest that adjustment of C_1 alone will not be able to achieve the good agreement in both velocity and turbulence at the same time. Other parameters therefore need to be considered in this analysis.

Tests on D_w and H_w

Surface breaking waves enhance the turbulence in the water surface by acting as a source of TKE. In this study, this is accounted for by implementing a flux boundary condition (see Eq.(3.59)), in which the surface flux of energy injected into the surface of the water column is provided as a fraction of the surface wave dissipations, i.e. $F_k = D_w \left[(1-\alpha_r)\,\varepsilon^b + \varepsilon^{\mathrm{r}} + \varepsilon^{\mathrm{wcap}}\right]$[1]. The parameter D_w controls how much wave dissipation

[1]It should be noted that the turbulent kinetic energy under the breaking waves has strong influence on the undertow velocity profile. The total contribution of wave dissipation to the momentum balance

energy is transferred into TKE. For scenarios with breaking waves, the surface roughness height z_{0s} is the length scale of injected turbulence which is determined uniquely by the spectral properties of turbulence at the source (Umlauf and Burchard [66]). This parameter is an important factor which controls the vertical distribution of the TKE in the upper portion of the water column.

In the literature (Craig [157]; Terray et al. [118]; Govender et al. [158]; Huang et al. [159]; Feddersen and Trowbridge [160]; Feddersen [155, 156]; Paskyabi et al. [161]), a wide range of values for these two parameters had been proposed as their estimation is still a matter of scientific debated. Therefore, in various previous numerical model studies, these two parameters are taken as tuning parameters and adjusted to produce results closest to the measurements. In this section, a sensitivity analysis for these two parameters is also performed by conducting another four groups of simulations. The corresponding parameter values used in these simulations are summarized in Table 5.3.

Figure 5.11 compares the computed TKE profiles from the nine simulations, i.e. test group of #3 which includes Runs #3.1 – #3.9, against the measurements. When $D_w = 0.0$, no wave energy is transformed into surface TKE flux, thus the simulated TKE near the surface of the water column is smallest among these nine simulations. As the value of D_w increases, the contribution of wave energy as surface flux of TKE also increases accordingly, leading to a larger TKE value. However, in the major portion of the water column below, a reverse tendency is observed, i.e. as the value of D_w increases from 0.0 to 0.20, TKE value reduces in these figures. When D_w exceeds 0.2, changes in the computed TKE profile are hardly noticeable. The corresponding velocity profiles computed based on the same D_w are shown in Figure 5.13. It can be seen that at all of the twelve profiles, the vertical gradients of velocity reaches its maximum when $D_w = 0.1$; as D_w increases or decreases from 0.1, the magnitude of cross-shore velocity decreases. According to the discussion in Section 4.3.2, the vertical gradient of cross-shore velocity is proportional to the amount of wave energy dissipation that contributes to the momentum acceleration. Based on the model results shown in Figure 5.11, the vertical gradient of cross-shore velocity is also proportional to the amount of surface TKE flux. When the amount of wave energy introduced as surface flux of TKE increases, the fraction of wave energy contributing to the momentum acceleration decreases. Consequently in the process that D_w increases from 0.0 to 0.50, the opposite effects of the larger surface TKE flux and smaller wave dissipation momentum contribution on the velocity profiles balance with each other, where the vertical gradient of cross-shore velocity reaches its maximum with D_w equals 0.1 for the

needs to be kept conservative; otherwise, no consistent model results can be obtained for the velocity and TKE profiles at the same time. Therefore, the amount of wave dissipation introduced as surface flux of TKE (i.e. $F_k = D_w \left[(1-\alpha_r)\,\epsilon^b + \epsilon^r + \epsilon^{wcap}\right]$) must be subtracted from the Eq. (3.32).

Table 5.3: Model configurations of the sensitivity tests for the parameter D_w and H_w.

Group #	Run #	D_w	H_w	Group #	Run #	D_w	H_w
#3	#3.1	0.00	0.10	#5	#5.1	0.30	0.05
	#3.2	0.001	0.10		#5.2	0.30	0.10
	#3.3	0.01	0.10		#5.3	0.30	0.20
	#3.4	0.05	0.10		#5.4	0.30	0.30
	#3.5	0.10	0.10		#5.5	0.30	0.40
	#3.6	0.20	0.10		#5.6	0.30	0.50
	#3.7	0.30	0.10		#5.7	0.30	0.60
	#3.8	0.40	0.10		#5.8	0.30	0.70
	#3.9	0.50	0.10		#5.9	0.30	0.80
#4	#4.1	0.00	0.60		#5.10	0.30	0.90
	#4.2	0.001	0.60	#6	#6.1	0.001	0.05
	#4.3	0.01	0.60		#6.2	0.001	0.10
	#4.4	0.05	0.60		#6.3	0.001	0.20
	#4.5	0.10	0.60		#6.4	0.001	0.30
	#4.6	0.20	0.60		#6.5	0.001	0.40
	#4.7	0.30	0.60		#6.6	0.001	0.50
	#4.8	0.40	0.60		#6.7	0.001	0.60
	#4.9	0.50	0.60		#6.8	0.001	0.70
					#6.9	0.001	0.80
					#6.10	0.001	0.90

present case.

In Figure 5.12, the results of a similar set of sensitivity simulations, i.e. test group of #4 which have same set of D_w but a different value of $H_w = 0.6$, are displayed. Different from that shown in Figure 5.11, the simulated TKE increases monotonously with larger value of D_w in the whole water column in almost all of the twelve profiles, which is apparently in accordance with physical sense. This suggest that $H_w = 0.6$ used in this group of test (i.e. Runs $\#4.1 - \#4.9$) is more physically appropriate than the value of 0.1 that was used in Runs $\#3.1 - \#3.9$.

Similarly, a further two groups of tests (test group of #5 and #6) are performed with varying values of the parameter H_w (0.05-0.90), in which a constant value of $D_w = 0.3$ and $D_w = 0.001$ is adopted respectively. The model results against the measurements are shown in Figure 5.15 and Figure 5.16. Among the ten simulations in test group of #5 (with $D_w = 0.3$), the one with $H_w = 0.05$ obtains the smallest TKE in the whole water column at all of the twelve profiles. As the value of H_w increases, the simulated TKE shown in Figure 5.15 also increases gradually. However, when the value of D_w is taken as 0.001 (Figure 5.16), nearly constant TKEs are obtained in Runs $\#6.1 - \#6.10$, indicating that the surface roughness H_w has minor effect on the TKE profiles when the contribution of wave dissipation energy as surface flux of TKE is very small. The corresponding velocity profiles obtained in these simulations are displayed in Figures. 5.17 and 5.18.

With the above results of four groups of sensitivity simulations, the values of parameter D_w and H_w with which a simulation obtains reasonably acceptable results against the measured TKE and/or cross-shore velocities at all of the twelve profiles are summarized in Table 5.4. It can be seen that at least one set of D_w and H_w could be obtained for all of the 12 profiles, with which the modelled TKE and cross-shore velocity agree reasonably well with the measured data at the same time. A further simulation (Run II) with a cross-shore varying H_w (Figure 5.20) and a constant D_w (=0.3) is conducted, with results shown in Figure 5.19. The modelled cross-shore velocity profiles agree well with the measured data; at the same time the modelled TKE at a majority of water column are also very close to the measurements. These model parameters (e.g. wave parameters, velocity profiles, TKE, etc.) from Run II are thus utilized in calculating the sediment transport in the Section 5.5 and 5.6.

However, it should be noted that in all of the above simulations, the modelled TKE is over-predicted (to different degrees) near the water surface. Apparently, this is an issue that needs to be further studied in detail in the future. In this paper, several possible reasons are discussed in the following section as a preliminary attempt to resolve this problem.

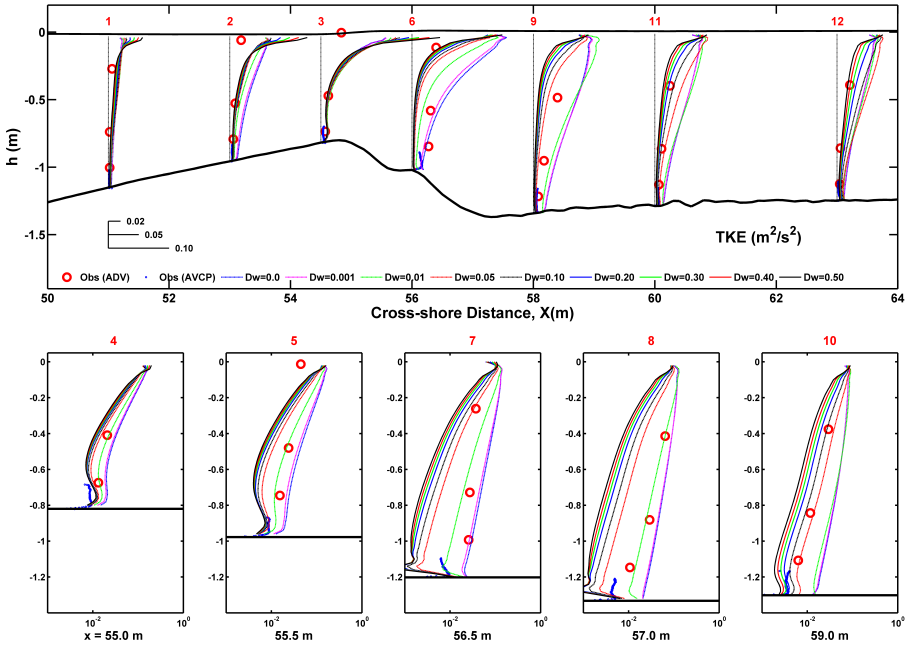

Figure 5.11: Comparison of simulation results (solid lines) with observed vertical profiles (red and blue circles) of TKE for the sensitivity to the parameter D_w. A constant value of the parameter $H_w = 0.1$ is utilized. The vertical dashed lines indicate the profile measurement locations and zero value for each profile.

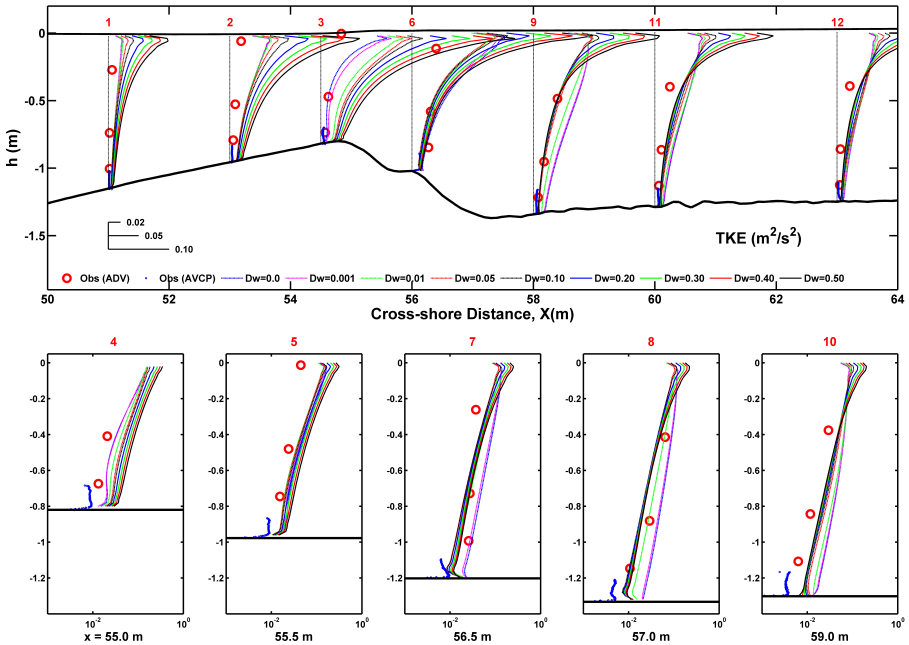

Figure 5.12: Comparison of simulation results (solid lines) with observed vertical profiles (red and blue circles) of TKE for the sensitivity to the parameter D_w. A constant value of the parameter $H_w = 0.6$ is utilized. The vertical dashed lines indicate the profile measurement locations and zero value for each profile.

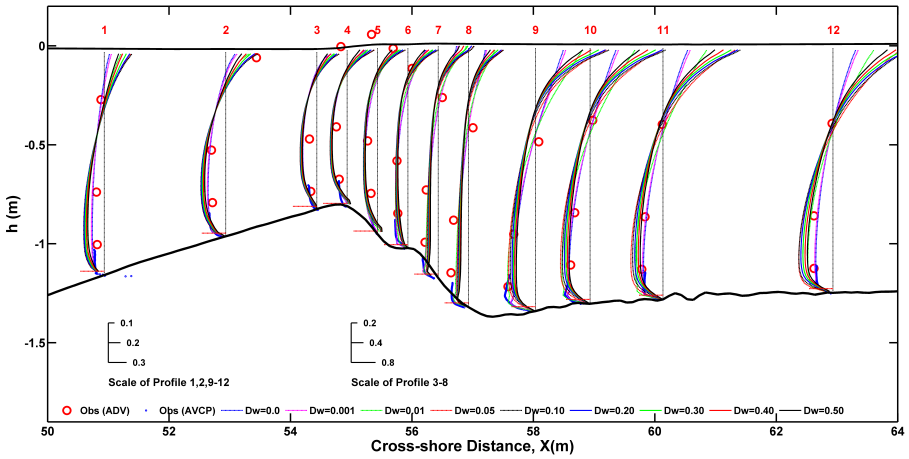

Figure 5.13: Comparison of simulation results (solid lines) with observed vertical profiles (red and blue circles) of the cross-shore velocity (u) for the sensitivity to the parameter D_w. A constant value of the parameter $H_w = 0.1$ is utilized. The vertical dashed lines indicate the profile measurement locations and zero value for each profile; the horizontal red dashed lines near the bed indicate the location of the first grid above the bed used in the model

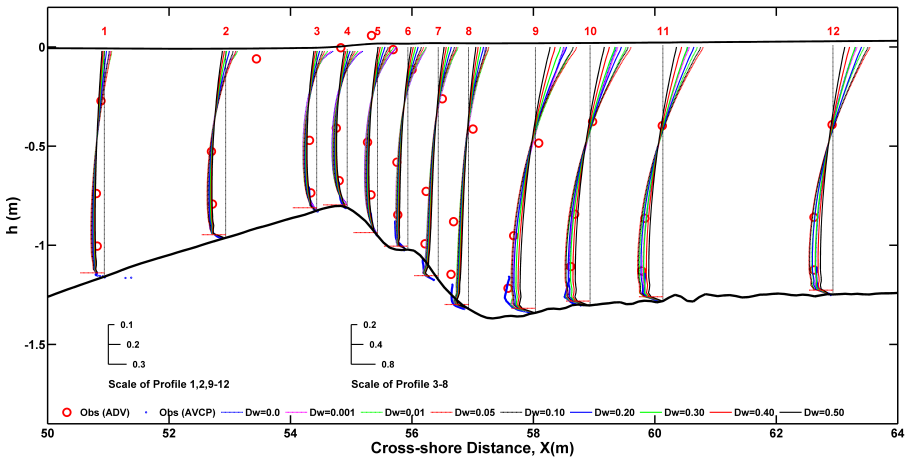

Figure 5.14: Comparison of simulation results (solid lines) with observed vertical profiles (red and blue circles) of the cross-shore velocity (u) for the sensitivity to the parameter D_w. A constant value of the parameter $H_w = 0.6$ is utilized. The vertical dashed lines indicate the profile measurement locations and zero value for each profile; the horizontal red dashed lines near the bed indicate the location of the first grid above the bed used in the model

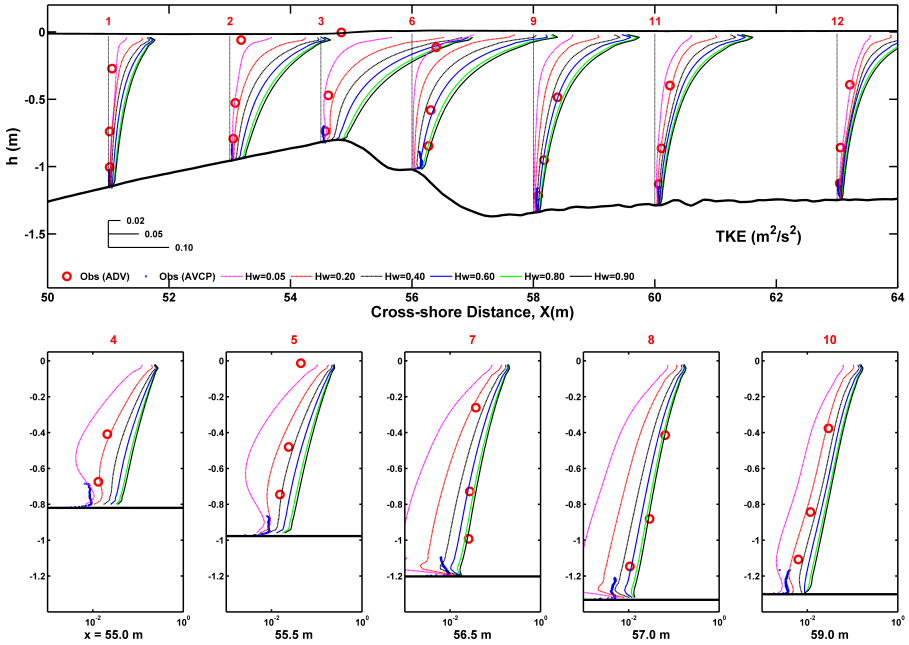

Figure 5.15: Comparison of simulation results (solid lines) with observed vertical profiles (red and blue circles) of TKE for the sensitivity to the parameter H_w. A constant value of the parameter $D_w = 0.3$ is utilized. The vertical dashed lines indicate the profile measurement locations and zero value for each profile.

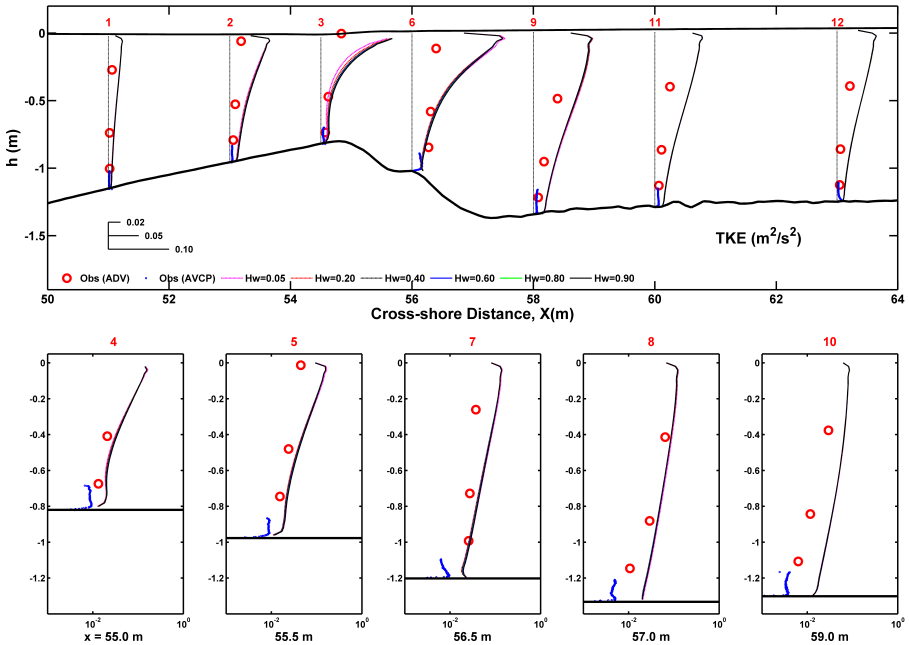

Figure 5.16: Comparison of simulation results (solid lines) with observed vertical profiles (red and blue circles) of TKE for the sensitivity to the parameter H_w. A constant value of the parameter $D_w = 0.001$ is utilized. The vertical dashed lines indicate the profile measurement locations and zero value for each profile.

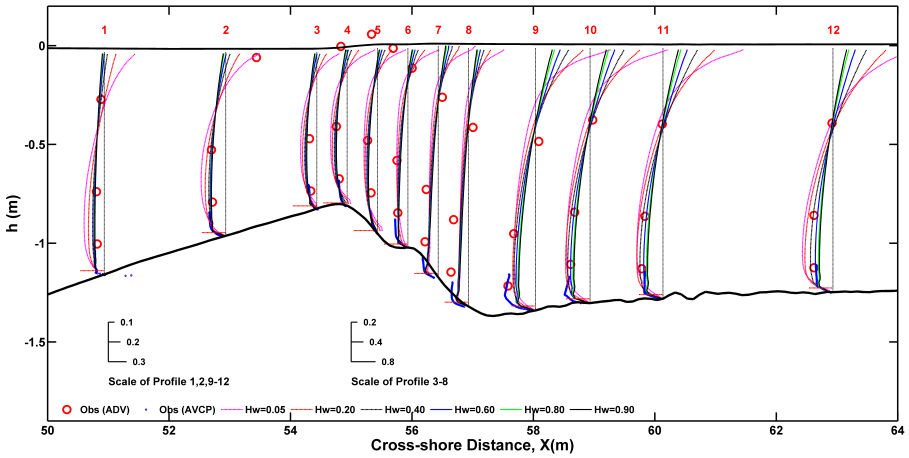

Figure 5.17: Comparison of simulation results (solid lines) with observed vertical profiles (red and blue circles) of the cross-shore velocity (u) for the sensitivity to the parameter H_w. A constant value of the parameter $D_w = 0.3$ is utilized. The vertical dashed lines indicate the profile measurement locations and zero value for each profile; the horizontal red dashed lines near the bed indicate the location of the first grid above the bed used in the model

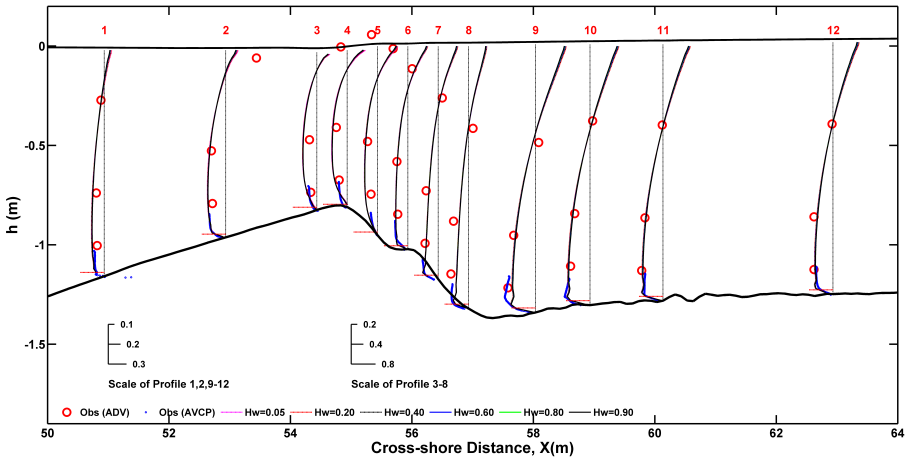

Figure 5.18: Comparison of simulation results (solid lines) with observed vertical profiles (red and blue circles) of the cross-shore velocity (u) for the sensitivity to the parameter H_w. A constant value of the parameter $D_w = 0.001$ is utilized. The vertical dashed lines indicate the profile measurement locations and zero value for each profile; the horizontal red dashed lines near the bed indicate the location of the first grid above the bed used in the model

Table 5.4: Summarization of the values of parameter D_w and H_w with which a numerical simulation obtains reasonable well results against the measured TKE or/and cross-shore velocity at the twelve profiles. These values are obtained from the modeled results of simulation Group $\#3 - \#6$

Group #	Reasonable Dw/Hw for TKE/Velocity	Profile #											
		#1	#2	#3	#4	#5	#6	#7	#8	#9	#10	#11	#12
#3	D_w for TKE	All	>=0.01	All	0.01	0.01	0.001-0.01	0.01	0.01	0.03	0.05-0.1	0.05-0.30	>0.20
$H_w = 0.1$	D_w for Velocity	0.001; >0.5	0.001; >0.5	All	All	All	All	0.001-0.01	0.001-0.01	<=0.2	0.001-0.01; >=0.3	0.001-0.01; >=0.3	0.001-0.01; >=0.5
D_w = [0.0-0.50]	D_w for TKE & Velocity	0.001;>0.5	>0.5	All	0.01	0.01	0.001-0.01	0.01	0.01	0.03	\	0.3	>=0.5
#4	D_w for TKE	\	\	<=0.001	\	\	0.001-0.30	>=0.01	>=0.01	>0.01	\	\	\
$H_w = 0.6$	D_w for Velocity	All	All	All	All	All	All	All	All	<0.2	<0.4	<0.4	<0.3
D_w = [0.0-0.50]	D_w for TKE & Velocity	\	\	<=0.001	\	\	0.001-0.30	>=0.01	>=0.01	0.01-0.2	\	\	\
#5	H_w for TKE	<=0.4	0.05-0.2	0.05-0.2	0.2	0.2-0.4	0.4-0.6	0.4-0.9	0.4-0.9	0.4-0.6	0.2-0.4	0.05-0.6	0.05-0.4
$D_w = 0.30$	H_w for Velocity	0.4-0.6	0.4-0.6	0.2-0.6	0.2-0.6	>0.2	>0.2	>0.2	>0.2	0.2-0.6	0.4-0.9	0.4-0.9	0.3-0.9
H_w = [0.05-0.90]	H_w for TKE & Velocity	0.4	\	0.2	0.2	0.2-0.4	0.4-0.6	0.4-0.9	0.4-0.9	0.4-0.6	0.4	0.4-0.6	0.3-0.4
#6	H_w for TKE	\	\	All	\	\	All	\	\	\	\	\	\
$D_w = 0.001$	H_w for Velocity	All	All	All	All	All	All	All	All	All	All	All	All
H_w = [0.05-0.90]	H_w for TKE & Velocity	\	\	All	\	\	All	\	\	\	\	\	\

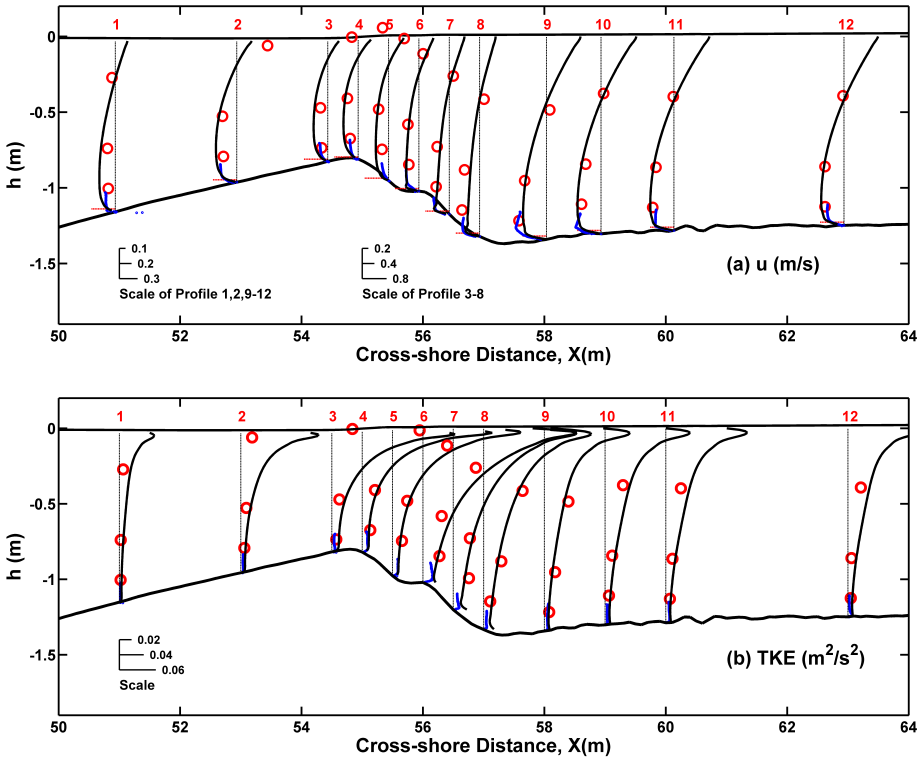

Figure 5.19: Comparison of simulation results (solid black lines) from Run II with observed vertical profiles (red circles and short near-bed blue lines) for the cross-shore velocity u (a) and the TKE (b). The vertical black dashed lines indicate the profile measurement locations and zero value for each profile; the horizontal red dashed lines near the bed indicate the location of the first grid above the bed used in the model.

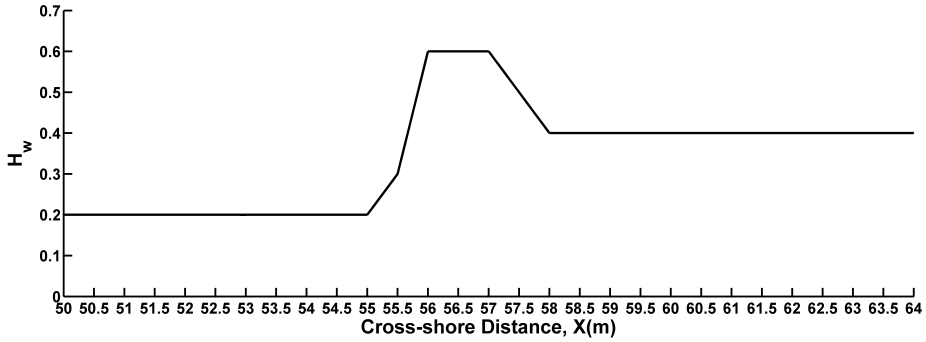

Figure 5.20: The value of cross-shore varying H_w used in Run II.

5.4.4 Discussion

As shown in above sections, although attempts have been made to identify the optimal model parameters in order to minimise the uncertainties in the model predicted turbulence characteristics, the underlying mechanism for these discrepancies requires further research into the fundamental modelling methods in turbulence generation and dissipation under breaking waves, which is beyond the scope of the present study. However, based on the present results, analysis on the model consistency and potential implications in experimental errors in these comparisons can be explored for the cases studied.

Model consistency

In the present model, the surface wave breaking induced turbulence is introduced by several mechanisms. At the surface boundary, the direct injection of the turbulence and bubbles from surface breaking waves is taken into account through the wave energy dissipation induced TKE flux. This layer has a thickness of z_0^s in which all properties including the turbulent dissipation rate are well mixed. Underneath this layer, the local turbulence level is enhanced due to the strong gradient in flow velocities, and is characterized by a shear production orders of magnitude smaller than the turbulent dissipation rate.

The shear production of TKE is parameterized by the following equation:

$$P = K_m \left[\left(\frac{\partial u}{\partial z} \right)^2 + \left(\frac{\partial v}{\partial z} \right)^2 \right] \tag{5.1}$$

which is closely related to the vertical gradient of velocity. In the turbulence closure model, Neumann-type surface boundary conditions for k and ψ (Eq.(3.60)) are used in this study to account for the surface TKE flux due to breaking waves into water column.

This boundary condition is derived based on the exact solutions of the two-equation turbulence models for TKE (k) and GLS (ψ) in the wave-enhanced layer (Umlauf and Burchard [66]), i.e.

$$\begin{aligned} k &= K(-z + z_{0s})^a \\ l &= L(-z + z_{0s}) \end{aligned} \tag{5.2}$$

where K, L and a are constants and z_{0s} is the surface roughness, under the assumption of that TKE diffusion balances dissipation in this layer. A nil TKE shear production is implied with this assumption.

However, this is not consistent with the results obtained from the model simulations: apparent non zero vertical gradients of cross-shore velocity could be observed in Figures of 5.13, 5.14, and 5.17, which indicates that the TKE shear productions are not nil at all near the water surface. This inconsistency between the model assumption and simulation results should be one of the reasons for the over-estimation of TKE near the water surface.

Uncertainties in the measured TKE

In the laboratory experiment, the measured time series signal of horizontal velocity (u_t) consists of five components:

- time-averaged contribution by the undertow ($\bar{u}$);
- orbital velocity contributions by the wave, which are found at the primary wave frequency (i.e. 0.25 Hz in this experiment) and the higher harmonics of wave (u_{orb});
- turbulent velocity contributions due to physical turbulence (u');
- high-frequency measurement noise, which can be identified using various cleaning methods (u'');
- spurious long waves that occur in the wave basin (u_{lw}).

In order to quantify the turbulent signal, all other terms that can be quantified are subtracted from the measured signal (van der Zanden [5]), i.e.

$$u' = u_t - \bar{u} - u_{orb} - u'' - u_{lw} \tag{5.3}$$

Apparently, any errors made in the quantification of the r.h.s. terms of Eq.(5.3) will contribute to the mis-estimation of the turbulent signal (u'). In both the fixed-bed

and the mobile-bed experiments, the sampling frequency of the ADVs was equal to 100 Hz and the turbulence fluctuations were measured up to frequencies of 50 Hz. The experiment staffs intercompared the ADV measurements with those of LDA (Laser Doppler Anemometer), which had an even higher sampling frequency (up to 600 Hz), and found that the agreement between the two instruments was generally good (within 10%). Only in the shoaling region there is a slight overestimation in TKE by the ADVs, which is believed to be due to acoustic noise contributions and is only significant when the physical turbulence is low (personal communication with van der Zanden). A common mistake therefore comes from the wrong quantification of the long wave signal, as other contributions (i.e. $\bar{u}$, u_{orb} and u'') can be accurately quantified.

Standing long waves are commonly produced at closed basins with the natural frequency of the basin (flume seiching), e.g. a long wave with a period of about 45 s and an amplitude of about 0.01 m existed in this laboratory experiment. Although its amplitude is small compared to the short waves, the associated velocities are of similar magnitude to u'. This long wave can be identified in the spectral domain and can be removed using a high-pass filter. However, the u_{lw} removed by this filter is closely dependant on the chosen cutoff frequency (f_c). If the adopted cut-off frequency is too high, some part of the turbulent energy must be removed as long-wave signal, leading to an underestimation of the u'. On the other hand, when the cut-off frequency is too low, there is still significant long-wave energy in the turbulence signal, resulting in an overestimation of the u'. The mis-estimation of the u' directly results in an underestimation or overestimation of measured TKE. Therefore, although the possibility is small, the overestimation of TKE in this model study may be partly due to an underestimation of the measured u'.

5.5 Suspended Sediment Transport

In the above Section 5.4, the model computed hydrodynamics (e.g. wave parameters, velocity profiles, TKE, etc.) are studied in detail. By conducting comprehensive sensitivity analysis, some relevant model parameters are also calibrated with the data. A good prediction of hydrodynamic conditions is one of the most important prerequisites to achieve accurate simulation in sediment transport rates and bed evolutions as shown in later sections. Therefore, the well predicted hydrodynamic processes obtained in Run II are utilized to calculate the suspended sediment transport in this section and the bedload transport in the next section (i.e. Section 5.6).

In the present model system, an advection-diffusion model (Eq.(3.68)) is used to calculated the transport of suspended sediment. For this kind of model, the adopted near-bed sediment boundary conditions (e.g. the sediment pickup function or the reference

concentration) are essential to the model performance, which determines the vertical sediment exchange between the bed and the suspension layers. van Rijn [204] indicated that the application of a reference concentration at a reference level close to the bed may easily lead to relatively large errors of the sediment concentrations at higher levels, therefore a prescribed pick-up rate approach instead of the reference concentration approach is applied as the bed-boundary condition for the present advection-diffusion model. Due to the high unsteadiness and complexity in the interactions between the combined flows due to waves and current and the sandy particles on the seabed, the sediment pickup rates largely rely on semi-empirical formulations so far. One of the most widely used formulations proposed by van Rijn [69] (Eq.(3.72)) is adopted in this study. Obviously, the accuracy of the predicted pickup rate by Eq.(3.72) directly depends on a reasonable estimation of the Shields parameter (θ^i). As described in the Section 2.4 and 3.3, among the three wave-current bed boundary layer models, the *mb_bbl* approach is modified and utilized in the present study. Within this model, both the maximum shear stress due to wave-current, τ_{cwmax} (see the definition in Section 3.3) and the wave-averaged one, τ_{cw}, are computed. In the literature, both variables have been used to determine the sediment motion and entrainment on the bed, e.g. Soulsby [125].

After some testing, results suggest that the maximum shear stress approach produces unrealisticly large entrainment rate near the bed and hence large discrepancies in the integrated suspended sediment transport rate in comparison with the data. Therefore, the wave-averaged shear stress (τ_{cw}) is used in the following runs. More details of these tests on the maximum shear stress are given in Appendix E. The model results using τ_{cw} are analysed and compared with the measurements in Section 5.5.1. In addition, a new approach recently proposed by van der Zanden et al. [77] for sediment entrainment under breaking waves is also examined in Section 5.5.2. The approaches used for calculating the pick-up rate in each run test and its corresponding section number are summarized in Table 5.5.

5.5.1 Suspended Sediment Concentrations

Using the τ_{cw} alone to calculate the sediment pick-up rate (Run #10.4), the predicted suspended sediment concentration profiles at the 12 locations are shown in Figure 5.21.

At profiles 1 and 2, the predicted sediment concentrations are apparently underestimated. However, the model's overall accuracy is considered to be reasonable across the 12 positions along the beach.

Previous studies in the literature suggest that breaking wave generated turbulence at the surface can penetrate through the water column and affect the bed boundary layer process, directly entrain a large amount of sediment into suspension (Nielsen [2]). In the

Table 5.5: The variable used in calculating the pick-up rate in the simulations for modeling the suspended sediment concentration.

Group #	Run #	Section #	The variables used in calculating the pick-up rate.
# 10	#10.1	E	Only τ_{cwmax}
	#10.2		$\tau_{cwmax} + k_b^{predicted}$
	#10.3		$\tau_{cwmax} + k_b^{parameterized}$
	#10.4	5.5.1	Only τ_{cw}
	#10.5	5.5.2	Only $k_b^{predicted}$

present case, a good agreement on the predicted concentration in suspension is achieved even though the wave breaking effects are not included in the pick up function explicitly. This is perhaps due to the reason that enhancement of sediment concentration may be mainly constrained in a very thin layer near the bed. For most morphodynamic models with vertical grid spacing that can not directly resolve BBL processes, it is sufficient to use a bottom boundary condition based purely on local bed shear stress induced by the local combined effect of waves and current.

It should be pointed out that the above comparison is based on computed and measured suspension concentration level, not by the bed shear stress and pick up rate directly, which reflects the difficulty in measuring these quantities even in the laboratory conditions. Taking the present simulation results (Figure 5.21) as an example, the predicted sediment concentrations at the wave breaking region is lower than the measured data near the bed; however they agree fairly well with the observations in the upper part of the water column. The predicted suspended sediment transport rate shown in Section 5.5.3 also confirms the present model's overall prediction.

To include the wave breaking effects on the near bed pick up, one can also add the additional turbulence effect on the sediment suspension, by using a generalized Shields parameter as proposed by Hsu and Liu [72], i.e. Eq. (3.77). However, as shown in Figure 5.19 the uncertainties in the computed TKE at profiles 3-12 are far too large to be used in this approach. On the other hand, by measuring the grain sizes from the bed samples, van der Zanden [5] indicated that the median sand diameter (D_{50}) decreases in time at the locations along the offshore slope of the bar (x = 51.0 to 54.0 m). This is related to two processes: one is the net removal of the coarsest grains in the mixture through selective sheet flow transport; and the other is the net deposition of fine

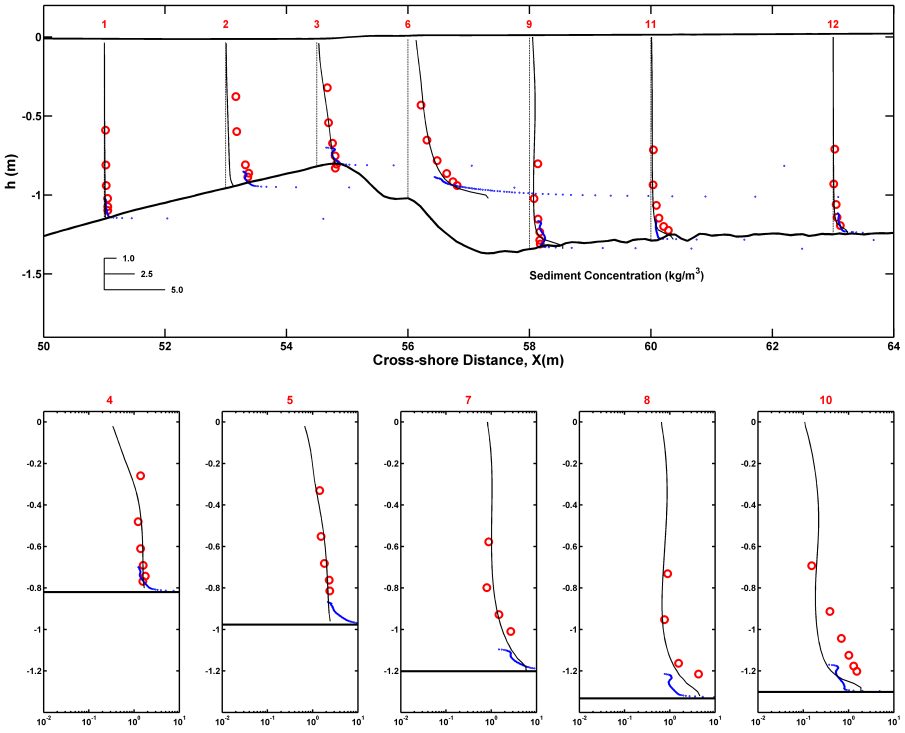

Figure 5.21: Comparison of simulation results (solid lines) with observed vertical profiles (red and blue circles) of suspended sediment concentration. The model results are from the Run #10.4. The vertical dashed lines indicate the profile measurement locations and zero value for each profile.

suspended particles that are advected offshore from the inner surf and breaking zone by the undertow. The changes in the sediment grain size can explain the underestimation of sediment concentration observed at the profiles of 1 and 2.

5.5.2 Representation of Wave Breaking Effects

Recently, van der Zanden et al. [77] proposed a new method to account for wave breaking turbulence effects in reference concentration models or pickup functions. For the sake of completeness, this method is briefly described here:

Firstly, the bed friction velocity (u_*) is parameterized to be proportional to the near-bed TKE produced by the local bed friction (k_{lf}), as follows:

$$u_*^2 = e_{lf} k_{lf} \tag{5.4}$$

where e_{lf} is a numerical coefficient.

Subsequently, substitute Eq. (5.4) into Eq. (3.77) which yields:

$$\theta_i = \frac{e_{lf}k_{lf} + e_k k_b}{(s-1)gD_{50}^i} = \frac{e_{lf}k_{lf} + e_k k_{wbr}}{(s-1)gD_{50}^i} \tag{5.5}$$

in which the second equal establishes because $k_b = k_{wbr}$, following that explained in Section E.1.

Finally, assuming $e_{lf} = e_k$, then the generalized Shields parameter could be parameterized as follows:

$$\theta_i = \frac{e_k(k_{lf} + k_{wbr})}{(s-1)gD_{50}^i} = \frac{e_k k_{nbp}}{(s-1)gD_{50}^i} \tag{5.6}$$

Instead of the bed friction velocity (u_*), Eq.(5.6) uses the total near-bed TKE (k_{nbp}) as the governing variable for calculating the Shields parameter, therefore it circumvents the uncertainties in calculating the bed shear stresses with the BBL models. In situations with other additional turbulence sources (e.g. the wave breaking produced TKE), this parameterization could also be applied as long as the TKE from those sources is included in k_{nbp}. In the absence of an additional turbulence source, $k_{nbp} = k_{lf}$, thus Eq.(5.6) returns to the original formulation proposed by van Rijn [69] provided that Eq.(5.4) is satisfied. In total, this parameterization utilizes a unified expression to predict sediment pick-up rates for situations with and without external turbulence sources. Consequently, using a cross-shore constant value of e_k could be expected.

Based on the boundary condition for bed shear produced turbulence that is commonly used in the turbulent closure models, van der Zanden et al. [77] suggest that $e_k = 0.3$ should be adopted. However, it should be noted that they used this value at the reference elevation (z_a)[2], and at the same time they indicated that the value of e_k varies greatly with distance from the bed. In this study, e_k is used at the vertical locations of the first model grid above the bed. Therefore it is kept as a tuning parameter to be adjusted to produce results closest to the available observations.

With further numerical tests, it is found that the simulated suspended sediment concentrations with a cross-shore constant e_k value of 0.05 (Figure 5.22) show an overall best agreement with the measured data (Run #10.5), suggesting that this method could be successfully used in predicting the suspended sediment concentrations in the surf zone. The present simulation results are also very close to those predicted with the

[2]The reference elevation (z_a) is typically inside the wave bottom boundary layer. Various formulations had been proposed to calculate z_a and the relevant reference concentration C_a (see those formulations in Soulsy [125]). For flat bed conditions, van Rijn [204] recommended to use a minimum value of 0.01h; while when bed forms are present, it is assumed to be equal to half of the bed form height ($z_a = 1/2\triangle$) or equal to the effective bed roughness ($z_a = k_s$) if the bed form height is unknown.

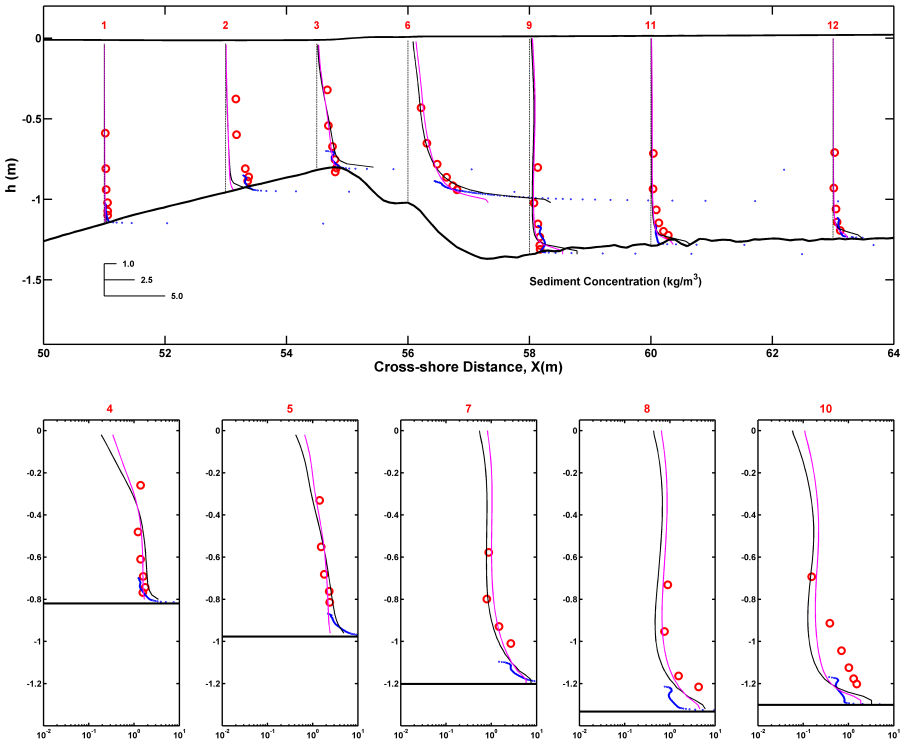

Figure 5.22: Comparison of simulation results (solid lines) with observed vertical profiles (red and blue circles) of suspended sediment concentration. The black lines are results from Run #10.5, while the magenta lines are results from Run #10.4. The vertical dashed lines indicate the profile measurement locations and zero value for each profile.

wave-averaged bed shear stress τ_{wc} (shown as magenta lines in Figure 5.22), which confirms the choice of this method to a certain degree. It is interesting to note that the concentration at profile 2 is also underestimated using the present approach, which verifies the grain size effects on the sediment entrainment at this location as discussed in Section 5.5.1.

However, the accuracy of the predicted suspended sediment transport using this parameterization relies on a reasonable estimate of the near-bed TKE (k_{nbp}). The accurate prediction of TKE in the surf zone is still a challenge for the commonly used turbulence closure models. Even with high temporal (intra-wave) and spatial (1mm vertical grid height to resolve the WBL) resolutions, the state-of-the-art CFD models have major difficulties in predicting the spatial trends and magitudes of near-bed TKE (Fernandez-Mora et al. [205]). Although a reasonably good agreement with the measured near-bed TKE is finally obtained using the present model system, it is based on the very detailed measurements of hydrodynamics in this laboratory experiment which make the complex processes of parameter calibrations possible. For most coastal engineering studies with limited amount of measured data, it may thus be particularly challenging to calibrate

the parameter settings in a way shown in above sections.

5.5.3 Suspended Sediment Transport Rate

The depth-integrated, wave-averaged suspended transport rate q_s is given by:

$$q_s = q_{s,c} + q_{s,w} = \int_{-h}^{\zeta^c} uCdz + \int_{-h}^{\zeta^c} u^{st}Cdz = \int_{-h}^{\zeta^c} u^l Cdz \tag{5.7}$$

where $q_{s,c}$ and $q_{s,w}$ are the current-related and wave-related suspended transport rate, respectively; ζ^c is the mean water level; u, u^{st} and u^l are the wave-averaged Eulerian, Stokes and Lagrangian velocities respectively; C is the suspended sediment concentration.

As the flow induced by breaking waves (undertow) is offshore directed, the suspended sediment transport is therefore expected to be in the offshore direction (negative) at all positions along the beach.

Using the predicted current velocities shown in Figure 5.19 and the sediment concentrations in Figure 5.21 and Figure 5.22, the predicted suspended sediment transport rates using the above two methods are respectively shown in Figure 5.23 and Figure 5.24. The calculated sediment transport rates (q_s) shown in these two figures have a very similar cross-shore distribution pattern, although there are some differences in terms of the specific value. At the shoaling region (i.e. $x < 53.0\ m$), q_s is nearly zero. From $x = 53.0$ to $x = 56.0\ m$, the magnitude of q_s increases strongly to a maximum value due to increasing concentrations and undertow magnitudes. In contrast, the q_s magnitudes decrease quickly from $x = 56.0$ to $x = 58.0\ m$. This is mainly the result of the decreasing sediment concentrations in this region as the magnitudes of undertow remain roughly constant (Figure 5.19). The sediment concentrations decrease along the inner surf zone (i.e. $x > 58.5\ m$), therefore the magnitude of q_s also gradually decreases in this region. At the straight sloping beach near the shoreline (x = 68.0 to 80.0 m), q_s remains zero since it was set as a fixed beach in this experiment(see the experimental setup shown in Figure 5.1)

By vertical inter- and extrapolation of the measured time averaged velocities and sediment concentrations, van der Zanden ([5], Figure 3.10) estimated the profiles of sediment fluxes over the complete water column which were then vertically integrated to compute the sediment transport rate (red diamonds in Figures of 5.23 and 5.24). It is found that the calculated q_s shown in Figure 5.23 agrees fairly well with that estimated by van der Zanden [5] on both the cross-shore distribution pattern and the specific magnitude. The pattern of calculated q_s shown in Figure 5.24 is also in reasonable agreement with that estimated by van der Zanden [5], while the specific magnitude at $x = 56\ m$ is to some extent overestimated.

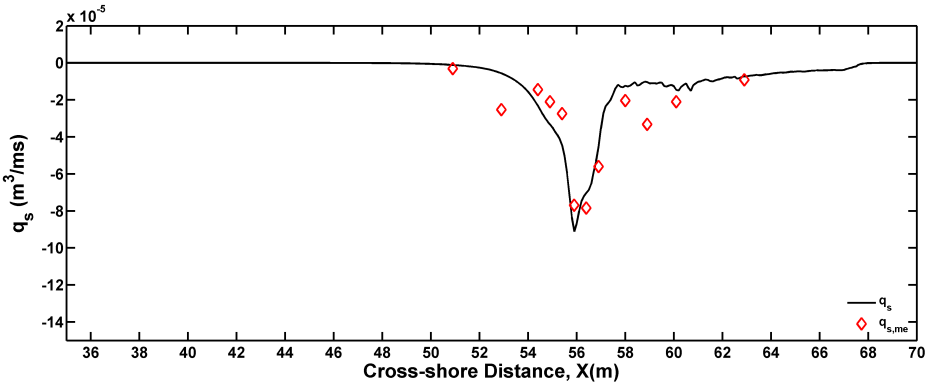

Figure 5.23: Suspended sediment transport rate q_s (black line) calculated from the sediment concentration shown in Figure 5.21. Red diamonds represent the estimated q_s from the measured suspended sediment concentration and velocity by van der Zanden [5] (i.e. the $q_{s,outer}$ showed in its Figure 3.10).

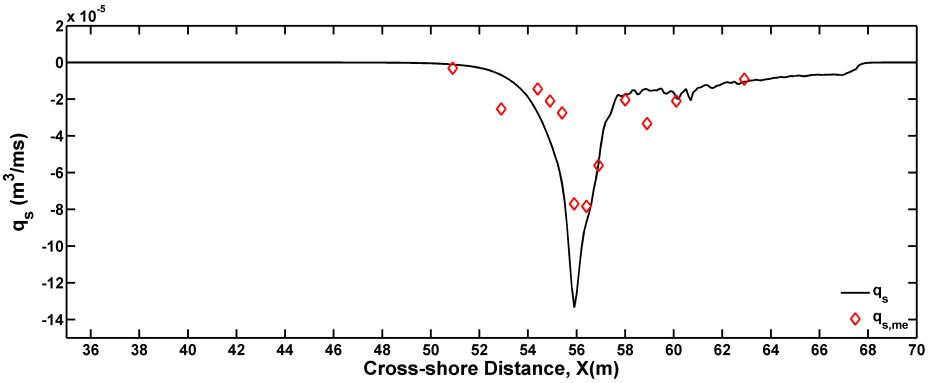

Figure 5.24: Suspended sediment transport rate q_s (black line) calculated from the sediment concentration shown in Figure 5.22. Red diamonds represent the estimated q_s from the measured suspended sediment concentration and velocity by van der Zanden [5] (i.e. the $q_{s,outer}$ showed in its Figure 3.10).

Although the sediment concentrations predicted from the simulation with the maximum bed shear stress τ_{wcmax} (Figure E.2) agree reasonably well with the measurements, the calculated sediment transport rate from the same simulation (Figure E.5) is very different from that estimated by van der Zanden [5], and is also very different from those shown in Figure 5.23 and Figure 5.24. This is because q_s, as a result of vertical integration of the sediment flux (i.e. the product of velocity and sediment concentration), accumulates the small errors in the predicted sediment concentrations at the whole water column. Therefore, q_s could be used as a more strict criterion to judge the performance of a model system in simulating the suspended sediment transport process. Apparently, the approach of using τ_{wcmax} in calculating the sediment pick-rate is not a good choice, at least for the present SINBAD mobile bed case.

5.6 Bedload Transport

In this section, the 'measured' bedload transport rate ($q_{bed,e}$) is first approximately calculated by subtracting the computed suspended transport (q_s, see Section 5.5.3) from the measured total transport rate ($q_{tot,m}$). Next, the 'measured' bedload transport rate ($q_{bed,e}$) is compared with that from three different prediction methods, i.e. the Meyer-Peter and M*ü*eller [9] (hereinafter MPM) formulation, the Soulsby and Damgaard [124] formulae and the SANTOSS model (see Section 3.5).

Unlike the suspended sediment transport, the bed load transport is affected by many different processes in the near bed region, including wave induced streaming, wave asymmetry, wave-current interactions, grain size effects and bed slop effects. The resultant transport direction therefore can be either onshore or offshore directed depending on the relative strength from each processes and their impacts to the net motions of the sediment grains.

5.6.1 Approximation of The Measured Bedload Transport Rate

As the bedload transport is confined to layers of $O(sub - mm)$ which cannot be accurately measured by most instruments, a direct measurement of the bedload transport rate in oscillatory conditions is generally very difficult. Following van der Zanden [5], the "measured" bedload transport rate ($q_{bed,e}$) is estimated as the difference between the measured total transport ($q_{tot,m}$) and suspended transport rates ($q_{s,m}$). However, it should be noted that the so-called measured suspended transport rate ($q_{s,m}$) shown in van der Zanden [5] is also an approximation, as the profiles of sediment fluxes over the complete water column are estimated by vertical inter- and extrapolation of the measured time averaged velocities and sediment concentrations.

The overall objective of the present study is to be able to simulate morphological evolution with reasonable accuracy. To minimise the uncertainties involved in the estimation of suspended load transport based on laboratory data, the computed suspended transport rates (q_s) in Section 5.5.3 is used here to derive the "measured" bedload transport.

$$q_{bed,e} = q_{tot,m} - q_s \tag{5.8}$$

The total sediment transport rate $q_{tot,m}$, due to contributions by both bedload and suspended load, is obtained from the bed profile measurements (z_{bed}) by solving the following Exner equation:

$$(1-\varepsilon_0)\frac{\partial z_{bed}}{\partial t}+\frac{\partial q_{tot,m}}{\partial x}=0 \tag{5.9}$$

i.e.

$$q_{tot,m}(x)=q_{tot,m}(x-\Delta x)-(1-\varepsilon_0)\frac{\Delta z_{bed}(x)}{\Delta t}\Delta x \tag{5.10}$$

where ε_0 is the sand porosity (=0.4 in this experiment), Δx is the horizontal resolution of z_{bed} measurements (=0.02 m) and Δt is the time interval between two consecutive profile measurements (30 mins).

The equation (5.10) can be solved if $q_{tot,m}$ is known at one x location. According to van der Zanden [5], $q_{tot,m}=0$ at the left-hand (i.e. $x=35$ m) and right-hand boundary (i.e. $x=68$ m) of the test section of this SINBAD mobile bed experiment. Therefore, two estimates of $q_{tot,m}$ (annotated $q_{tot,lhs}$ and $q_{tot,rhs}$) can be obtained. The $q_{tot,lhs}$ and $q_{tot,rhs}$ calculated from the bed profile measurements at t=30 and 60 mins are shown in Figure 5.25. It is found that these two estimates are not the same but with an approximately cross-shore constant difference. van der Zanden [5] ascribes this to the variations in the horizontally-integrated volume of the two profile measurements used to quantify Δz_{bed}. And these variations may result from sampling errors of the acoustic sensors, 3D bed forms, variations in packing density and porosity and non-uniformity of the bed profiles. Actually during this laboratory experiment, sand erodes near the walls

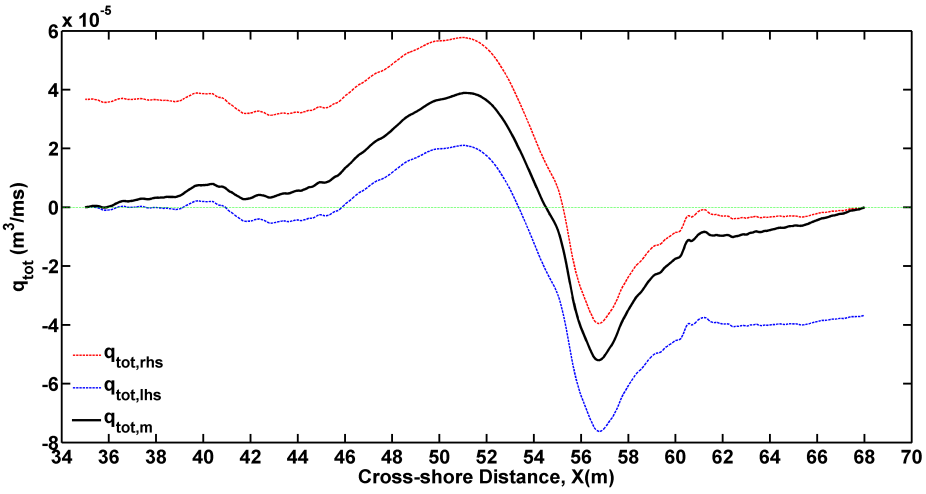

Figure 5.25: Total sediment transport rate calculated from the bed profile measurements at t=30 and 60 mins through the Eq.(5.10). Blue ($q_{tot,lhs}$) and red ($q_{tot,rhs}$) dashed lines represent the total transport rate that calculated iteratively by starting from the left- and right-hand side of the profile, respectively; while the black line ($q_{tot,m}$) is the final used total transport rate calculated as through the Eq.(5.11) the weighted average of ($q_{tot,lhs}$) and ($q_{tot,rhs}$). The green dashed line displays the zero value.

and accumulates in the center of the water flume, leading to an apparent increase in the sand volume measured along the center of the flume, i.e. the measured sand mass is not conserved (personal communication with Joep van der Zanden). Depending on the distance to each horizontal boundary of the test section, $q_{tot,lhs}$ or $q_{tot,rhs}$ is considered more accurate. Therefore, van der Zanden [5] calculated the total transport rate ($q_{tot,m}$) as the weighted average of both $q_{tot,lhs}$ and $q_{tot,rhs}$:

$$q_{tot,m}(x) = \left(\frac{x_{end} - x}{x_{end} - x_0}\right) q_{tot,lhs}(x) + \left(\frac{x - x_0}{x_{end} - x_0}\right) q_{tot,rhs}(x) \tag{5.11}$$

where $x_0 = 35$ m and $x_{end} = 68$ m are the left- and right-hand boundary of the mobile bed profile, respectively.

Using the total sediment transport rate ($q_{tot,m}$) calculated from Eq.(5.11) and the predicted suspended sediment transport rate (q_s) shown in Figure 5.24, the bedload transport rate ($q_{bed,e}$) could be easily estimated through Eq.(5.8). Generally, the estimated $q_{bed,e}$ (Figure 5.26) shows an onshore direction at $x < 56.8$ m and offshore direction at $x > 56.8$ m. However, it should be kept in mind that this $q_{bed,e}$ is only an estimation but not the real measured bedload transport, for at least two reasons: the calculated $q_{tot,m}$ from Eq.(5.11) is not accurate for the aforementioned reason and q_s is predicted by the advection-diffusion model which is also obviously not accurate. Actually, an accurately measured value of q_s does not exist. For example, the magnitude of the above estimated $q_{bed,e}$ is much overestimated between $x = 57$ m and $x = 60$ m, because the predicted magnitude of suspended sediment transport rate in this area is underestimated. Therefore $q_{bed,e}$ could only be used for qualitative but not quantitative analysis and one needs to be careful when using it to judge the model bedload transport ($q_{bed,p}$) in the following sections.

5.6.2 Bedload Transport Prediction with MPM

In this section, the MPM (Meter-Peter Müeller [9]) formulation, i.e. Eq.(2.39), is used to calculate the bedload transport rate. Similar to that discussed in Section 5.5, two kinds of bed shear stresses (i.e. maximum bed shear stress τ_{cwmax} and the wave-averaged bed shear stress τ_{cw}) could alternatively be selected to calculate the Shields parameter.

Figure 5.27 and 5.28 show the bedload transport rate ($q_{bed,p}$) predicted with τ_{cw} and τ_{cwmax} respectively (annotated $q_{bed,M1}$ and $q_{bed,M2}$). Apparently, the MPM formulation with τ_{cw} completely fails to predict the feature of bedload transport rate in this case: the predicted $q_{bed,M1}$ only has a small offshore magnitude between $x = 55.5$ m and $x = 58.0$ m; while in the majority of cross-shore locations, no predicted bedload transport is observed. Better than $q_{bed,M1}$, the predicted $q_{bed,M2}$ shows the same onshore direction

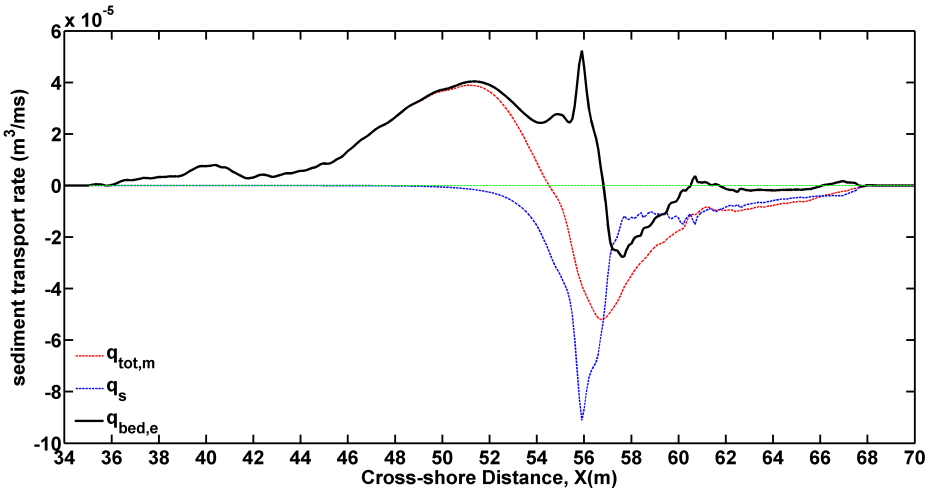

Figure 5.26: Total ($q_{tot,m}$, red dashed line), suspended (q_s, blue dashed line) and bedload ($q_{bed,e}$, black line) sediment transport rate. $q_{tot,m}$ is calculated from the bed profile measurements at t=30 and 60 mins through the Eq.(5.10); q_s is the model prediction results as that shown in Figure 5.24; $q_{bed,e}$ is estimated by the Eq.(5.8). The green dashed line displays the zero value.

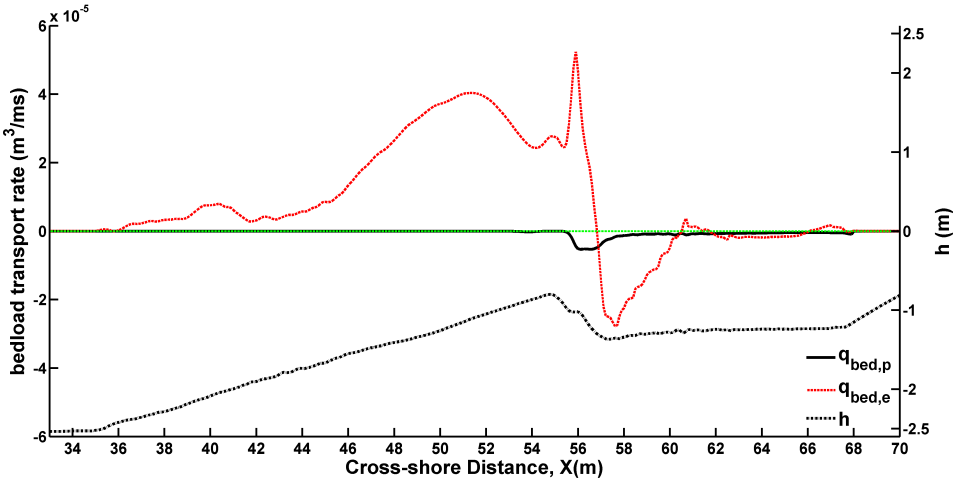

Figure 5.27: The cross-shore distribution of the bedload transport rate that estimated from Eq.(5.8) ($q_{bed,e}$,red dashed line) and that predicted by MPM formulation with τ_{cw} ($q_{bed,p}$,black line).

and similar magnitude with the estimated measurement of bedload transport ($q_{bed,e}$) along the offshore slope of the breaker bar (i.e. $x = 36.0 - 55.0$ m). This result suggests that τ_{cwmax} is more reasonable (than τ_{cw}) to be used in the bedload transport model, the bedload transport in the present case is more likely wave-dominated. However,

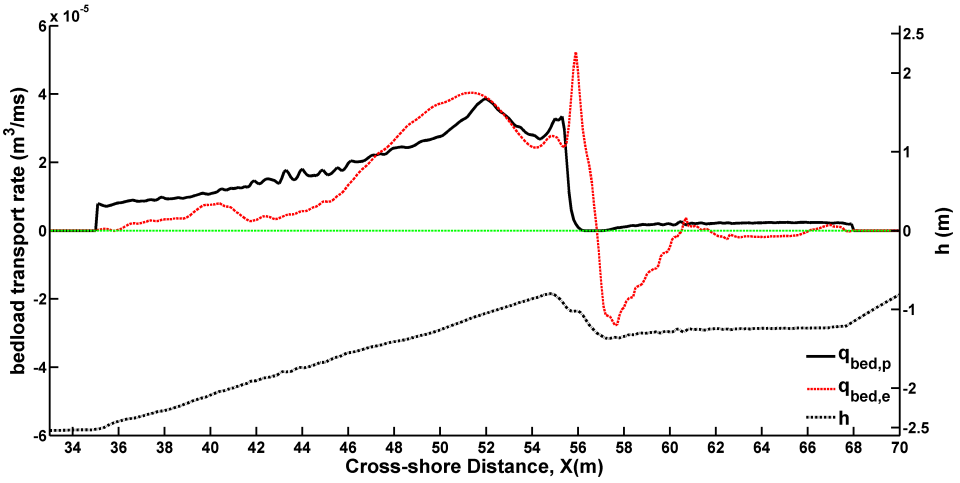

Figure 5.28: The cross-shore distribution of the bedload transport rate estimated from Eq.(5.8) ($q_{bed,e}$,red dashed line) and that predicted by MPM formulation with τ_{cwmax} ($q_{bed,p}$,black line).

shoreward of the breaker bar (i.e. $x > 57.0$ m), $q_{bed,M2}$ shows a trivial onshore directed magnitude, and fails to reproduce the right magnitude and direction (offshore) of $q_{bed,e}$.

In total, the bedload transport rate, $q_{bed,M1}$ and $q_{bed,M2}$, predicted with MPM formulation fail to reproduce the right features of measured bedload transport, suggesting that the MPM formulation is not appropriate for the SINBAD mobile bed application.

5.6.3 Bedload Transport Prediction with Soulsby and Damgaard

This section shows the predicted bedload transport rate by another parameterization, i.e. the Soulsby and Damgaard [124] formulae, which had been implemented in the original FVCOM model. Different from the MPM formulation proposed for the unidirectional flow, the formulae of Soulsby and Damgaard [124] accounts for the combined effects of mean currents and asymmetrical waves on bedload flux. Therefore it is physically more appropriate for the present SINBAD mobile bed case. However, the magnitude of predicted bedload transport rate ($q_{bed,p}$) shown in Figure 5.29 equals to zero from the offshore boundary to $x = 52.0$ m, shoreward of this location (i.e. $x = 52.0 - 68.0$ m) $q_{bed,p}$ has a small offshore directed magnitude. Consequently, the onshore directed bedload flux along the offshore and onshore slope of the breaker bar ($x = 52.0 - 57.0$ m) also failed to be reproduced.

Actually, the failure of the Soulsby and Damgaard [124] formulae in the present study is not unexpected. This approach belongs to the quasi-steady formulae which calculate intra-wave sand transport with the assumption that the instantaneous sand transport relates only to the instantaneous forcing parameters (van der A et al. [78]).

In this approach, the effect of velocity skewness that occurs under Stokes-type waves is accounted for, while the sediment transport resulting from acceleration skewness as occurs under sawtooth-shaped waves is not included. However, in the present application of the SINBAD mobile bed, waves become highly asymmetric; non-zero transport contributions resulting from the velocity and acceleration skewness are both significant. In addition, in fine sand sheet-flow conditions and rippled bed conditions (van der A, et al. [78]) the phase lag effects should also be accounted for in the practical bedload transport formulae, because this effect could significantly affect the magnitude and sometimes even the direction of the net transport rate.

Therefore, a recently proposed practical sand transport formula, which includes the effects of both velocity and acceleration skewness, phase lag effect, is incorporated in the newly developed model system (see Section 3.5). The implementation of this approach in the SINBAD mobile-bed case is discussed in Section 5.6.4.

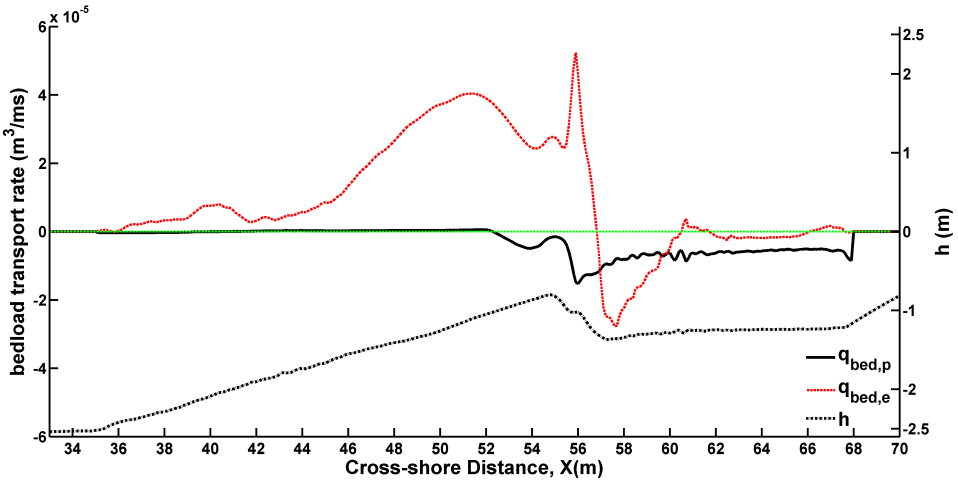

Figure 5.29: The cross-shore distribution of the bedload transport rate that estimated from Eq.(5.8) ($q_{bed,e}$,red dashed line) and that predicted by the formulation of Soulsby and Damgaard ($q_{bed,p}$,black line).

5.6.4 Bedload Transport Prediction with SANTOSS Model

SANTOSS is a recently developed practical model for net sand transport induced by non-breaking waves and currents. Its formula is especially developed for cross-shore sand transport under wave-dominated conditions and is based on the semi-unsteady, half wave-cycle concept (van der A et al. [78]). Many specific effects (processes) are included in this approach, e.g the effect of unsteady phase-lag, velocity and acceleration

skewness, progressive surface waves and bed slope. As the original SANTOSS model is developed only for non-breaking waves, to improve its results in the breaking wave conditions (e.g. the present SINBAD mobile-bed application), it is further developed with the effect of wave-breaking induced turbulence accounted for (see the details in Section 3.5.8).

In this section, the predicted bedload transport rate with all of the above mentioned effects except the wave-breaking induced turbulence is firstly analysed (Figure 5.30). Then the results with the effects of wave breaking-induced extra turbulence are presented (Figure 5.31), following a further sensitivity analysis to reveal insights into the other aforementioned effects on the bedload transport (Figure 5.34 - 5.37).

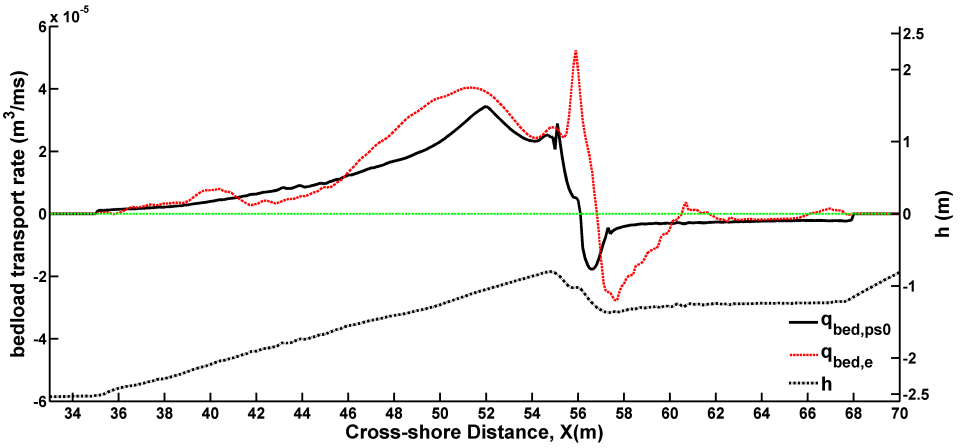

Figure 5.30: The cross-shore distribution of the bedload transport rate that estimated from Eq.(5.8) ($q_{bed,e}$, red dashed line) and that predicted by the SANTOSS model with all above mentioned effects but not the effect of wave-breaking induced turbulence ($q_{bed,ps0}$, black line).

Figure 5.30 shows the predicted bedload transport rate by the SANTOSS model with all of the above mentioned effects but not the effect of wave-breaking induced turbulence ($q_{bed,ps0}$). Along the offshore slope of the breaker bar ($x = 35.0 - 55.0$ m), $q_{bed,ps0}$ agrees fairly well with the estimated measurement value as it shows a similar magnitude and same onshore direction with $q_{bed,e}$. Inshore of the breaker bar trough ($x = 57.0 - 68.0$ m), $q_{bed,ps0}$ also shows the same offshore direction as $q_{bed,e}$ while its magnitude is much smaller than $q_{bed,e}$. However, this is more likely a result from the underestimation of suspended sediment transport (q_s) in this area, as the magnitude of q_s is smaller than that estimated from the measured suspended sediment concentration and velocity profiles by van der Zanden ([5], Figure 3.10). In addition, the magnitude of $q_{bed,ps0}$ here is very close to the bedload transport estimated from the measured data by Schnitzler [59]. Along the onshore slope of the breaker bar ($x = 55.0 - 57.0$ m),

the SANTOSS model gives a very poor result. The predicted $q_{bed,ps0}$ transforms from onshore to offshore direction at about $x = 56.1$ m, which is shifted about 0.7 m toward the offshore boundary compared to $q_{bed,e}$.

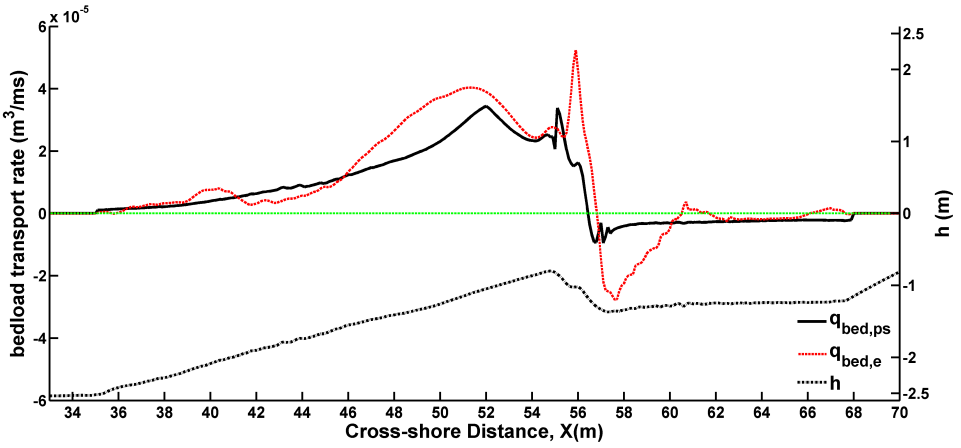

Figure 5.31: The cross-shore distribution of the bedload transport rate that estimated from Eq.(5.8) ($q_{bed,e}$, red dashed line) and that predicted by the SANTOSS model with all above mentioned effects, including the effect of wave-breaking induced turbulence ($q_{bed,ps}$, black line).

Breaking waves, especially strongly plunging waves, may directly entrain large amounts of sand from the bed (Nielsen [2]). The onshore slope of the breaker bar is just the location where wave breaking happens (the plunge point is located at $x = 55.5$ m according to van der Zanden [5]), therefore the above poor result (see Figure 5.30) is very likely because the original SANTOSS formulation is developed for the non wave-breaking conditions. Including the effect of wave-breaking induced turbulence on the sand transport with the method shown in Section 3.5.8, the predicted bedload transport is shown in Figure 5.31. The model result improves a lot along the onshore slope of the breaker bar.

Parameterization of Intra-Wave Parameters

As stated in Section 3.5.4, the parameterization process of intra-wave velocities, which provides the hydrodynamic input for the present SANTOSS model, are very important to have a good prediction of the bedload transport rate. In the present study, the analytical expression of Abreu et al. [177] and the parametrization method of Ruessink et al. [178] are utilized to predict the intra-wave parameters, e.g. peak crest and trough wave orbital velocity, orbital velocity skewness and asymmetry. It is therefore necessary

to verify the performance of these parameters against measured data.

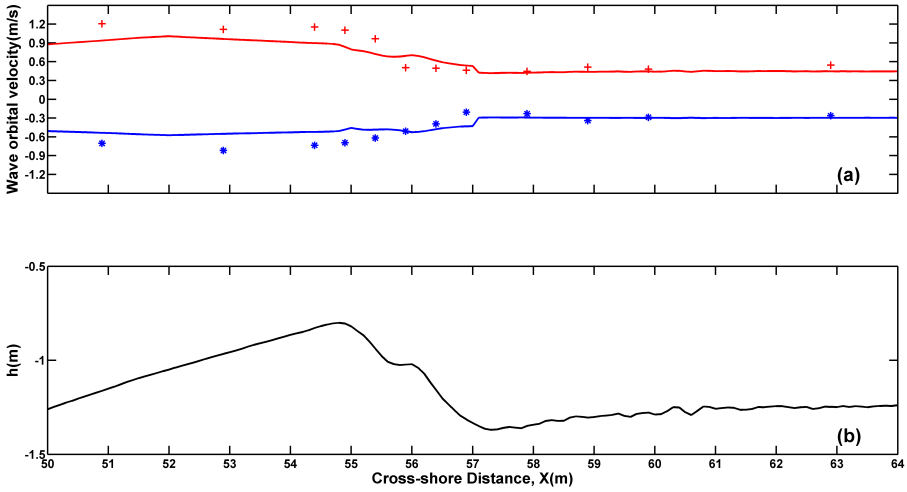

Figure 5.32: (a) Measured(stars and crosses) and model calculated (red and blue lines) peak crest (red crosses and line) and trough (blue stars and line) wave orbital velocities. Panel (b) shows the bed profile at t = 30 min.

Figure 5.32 shows that the peak crest and trough velocities are well predicted in the onshore region of the breaker bar in both the magnitude and the distribution pattern. Along the offshore slope of the breaker bar, the predicted peak velocities are to some extent underestimated. The peak orbital velocities are directly used to calculate the ripple dimensions (see Section 3.5.5), therefore this underestimation may lead to an overestimation of ripple length and ripple height according to the Eqs. (3.124) and (3.125). However, as the real ripple dimensions are not measured in the experiment, the predicted ripple length and height cannot be evaluated objectively. Further detailed CFD type simulations or dedicated experimental measurements are needed to check these parameters thoroughly.

The near-bed wave orbital velocity skewness and asymmetry predicted by the method of Ruessink et al.[178] are compared with the measurements in Figure 5.33. Measured skewness and asymmetry vary strongly in the cross-shore direction. These changes are likely due to complex behaviour of higher-order wave harmonics as waves break and de-shoal along the shoreward slope of the breaker bar (van der Zanden [5]). In addition, waves split into newly reformed surf bores and secondary crests after wave breaking. Apparently, the empirical parameterization of Ruessink et al.[178] fails to properly capture these cross-shore variations (Figure 5.33). This may be because that this parameterization is calibrated for a wide range of shoaling to inner surf zone conditions while the local wave deformation along the wave breaking region is not accounted for.

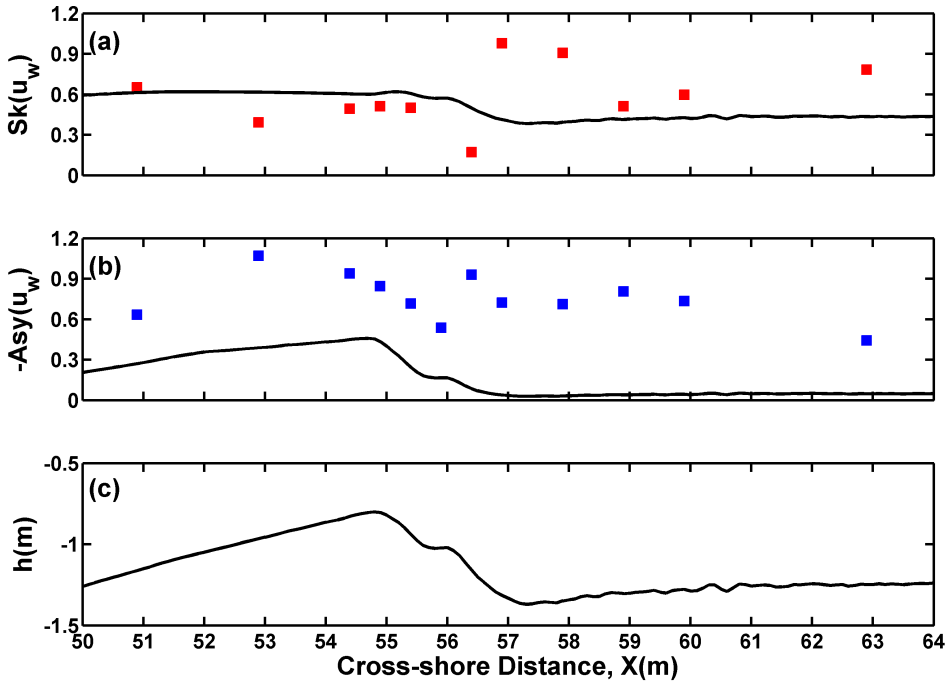

Figure 5.33: Wave orbital velocity skewness (a) and asymmetry (b) around breaker bar: measurements by ADV at $\zeta = 0.11m(squares)$ and model predictions based on local Ursell number following Ruessink et al. [178] (black lines) for t= 30-45 min. Panel (c) shows the bed profile at t = 30 min. The velocity skewness and asymmetry are respectively defined with the Eq.(B.9) and (B.10) in Appendix B.

Furthermore, it is noted that the magnitudes of velocity skewness are predicted reasonably well (Figure 5.33(a)) by this parameterization, while the magnitudes of velocity asymmetry are significantly underestimated. This is very likely due to the present study involving monochromatic waves while the field data used in the parameterization of Ruessink et al.[178] is measured under irregular short waves: the interaction between irregular short waves will likely advance breaking of the steepest wave in a sequence, leading to a lower wave asymmetry (van der Zanden [5]). In addition, the data were time-averaged (over 15 min sampling intervals) and bin-averaged (over Ursell number classes) first before being used to calibrate this parameterization, which can result in smoothing of local maximum values.

By doing a sensitivity analysis, Section 5.6.4 indicated that the contribution of velocity acceleration skewness (velocity asymmetry) to the total bedload transport rate is not as significant as that of surface progressive waves and phase-lag effects. However, the apparently underestimated magnitude of wave velocity asymmetry shown in the above analysis can significantly affect the effect of acceleration skewness on the bedload

transport. It is therefore hard to determine the real and accurate effect of acceleration skewness. Very likely its contribution is also underestimated due to the underestimation of the magnitude of the wave velocity asymmetry.

Sensitivity Analysis

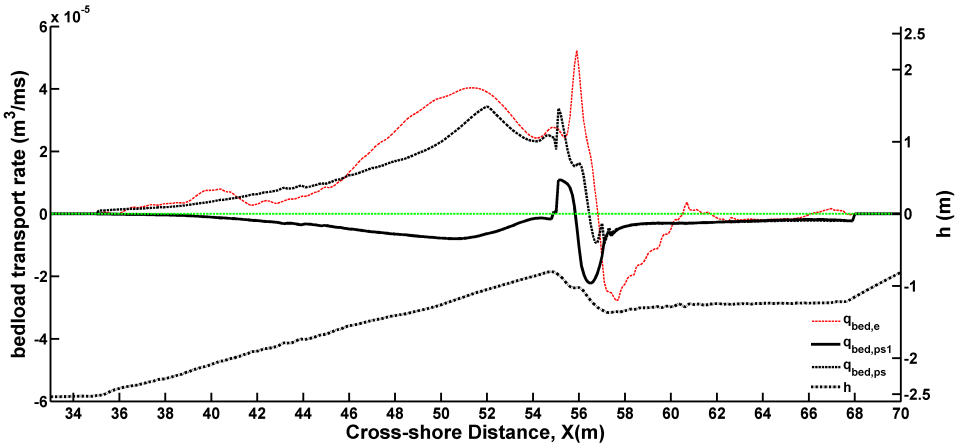

Figure 5.34: The cross-shore distribution of the bedload transport rate predicted by the SANTOSS model: with all above mentioned effects ($q_{bed,ps}$, red dashed line); with all above mentioned effects but not the effect of surface progressive waves ($q_{bed,ps1}$, black line).

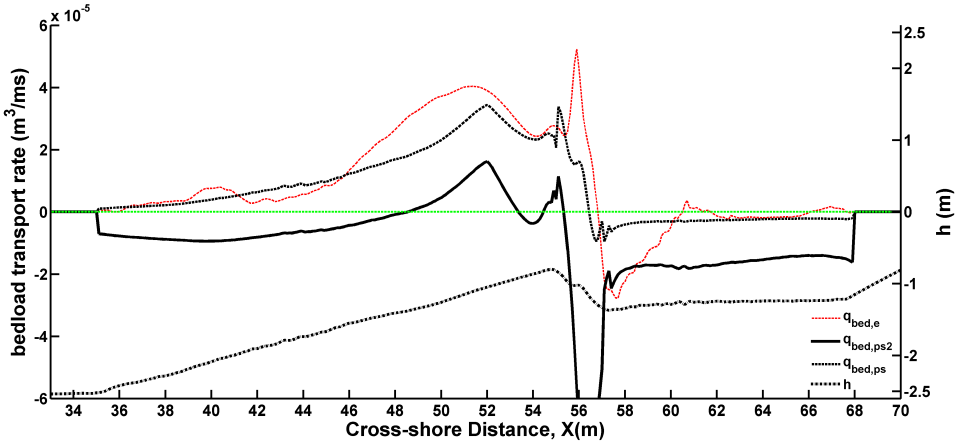

Figure 5.35: The cross-shore distribution of the bedload transport rate that predicted by the SANTOSS model: with all above mentioned effects ($q_{bed,ps}$, red dashed line); with all above mentioned effects but not the effect of phase-lag ($q_{bed,p}$, black line).

Compared with the laboratory experiment, one of the advantages of the modelling

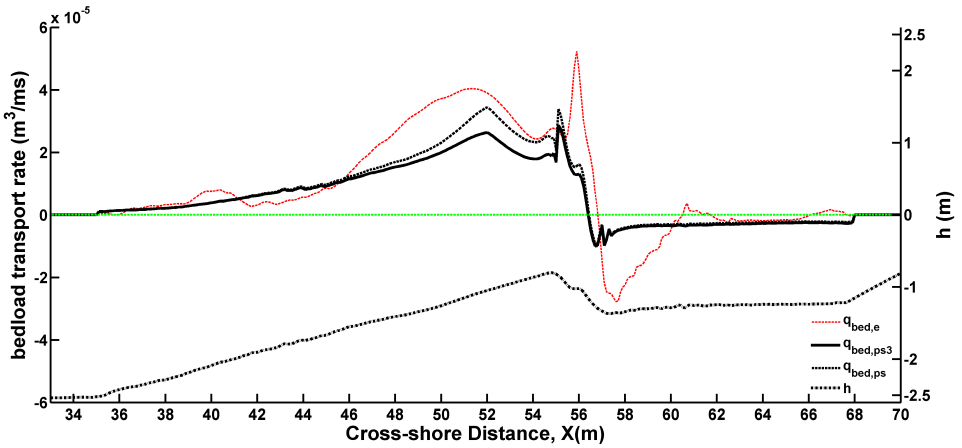

Figure 5.36: The cross-shore distribution of the bedload transport rate that predicted by the SANTOSS model: with all above mentioned effects ($q_{bed,ps}$, red dashed line); with all above mentioned effects but not the effect of acceleration skewness ($q_{bed,p}$, black line).

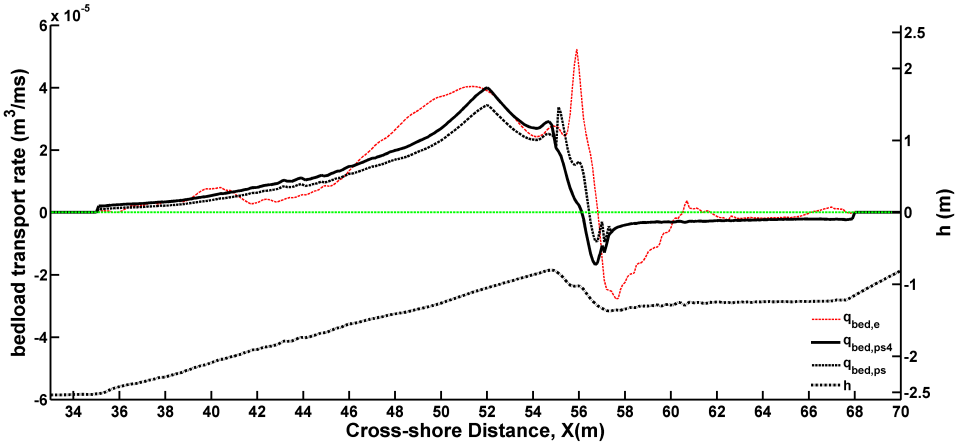

Figure 5.37: The cross-shore distribution of the bedload transport rate that predicted by the SANTOSS model: with all above mentioned effects ($q_{bed,ps}$, red dashed line); with all above mentioned effects but not the effect of bed slope ($q_{bed,p}$, black line).

simulation is that it could easily predict the effect of a specific physical process by adding (or removing) it from the model (sensitivity analysis). The predicted bedload transport rate shown in Figure 5.31 ($q_{bed,ps}$) agrees reasonably well with $q_{bed,e}$, therefore it is physically sound to study the above mentioned four effects, i.e. the effects of unsteady phase-lag, velocity and acceleration skewness, progressive surface waves and bed slope, one by one with a sensitivity analysis.

The predicted bedload transport with one of the four effects excluded are shown respectively in Figures 5.34 - 5.37. Without the effect of surface progressive waves, the predicted bedload flux ($q_{bed,ps1}$ in Figure 5.34) shows an opposite offshore direction along the offshore slope of the breaker bar. The magnitude of $q_{bed,ps1}$ is much smaller than $q_{bed,ps}$ along the onshore slope of the breaker bar. Without the phase-lag effect, the predicted $q_{bed,ps2}$ (Figure 5.35) is shifted downward, with a roughly cross-shore constant value along the offshore slope of the breaker bar and shoreward of the breaker bar trough, compared to $q_{bed,ps}$. Along the onshore slope, $q_{bed,ps2}$ has a large magnitude in the offshore direction. Therefore, the effect of both surface progressive waves and phase-lag contribute significantly to the total bedload transport rate. Without each of these two effects, the direction of bedload transport cannot be reproduced in the right way, let alone the right magnitude. In contrast with the above two effects, the contributions of acceleration skewness and bed slope to $q_{bed,ps}$ seem less significant. As shown in Figure 5.36, the predicted $q_{bed,ps3}$ without the effect of acceleration skewness shows a very close agreement with $q_{bed,ps}$, only the magnitude is slightly underestimated at $x = 50.0-55.0$ m. Different with the horizontal bed, the gravity provides a component of force on the sand grain which may increase (decrease) the amount of bedload flux if it is down the slope (up the slope). This is rightly displayed in Figure 5.37 by comparing $q_{bed,ps}$ and $q_{bed,ps4}$, which includes and excludes the effect of bed slope respectively.

On the whole, the effect of surface progressive waves and phase-lag could significantly change the characteristics of the predicted bedload transport rate; contributions of acceleration skewness and bed slope are not essential.

5.7 Total Load Transport

Based on the computed suspended load and bed load transport rates, the total load transport rate ($q_{tot,p}$) is computed and compared with the measured data ($q_{tot,m}$) in Figure 5.38. The predicted $q_{tot,p}$ has the same cross-shore distribution features as the measured $q_{tot,m}$, although there are some discrepancies in the detailed magnitude. As discussed above in Sections of 5.5 and 5.6, these discrepancies are mainly due to those in the predicted bedload transport rate. The contribution of bed load and suspended load transport to the total load is also shown in this figure.

As discussed previously, the suspended load is computed based on the wave-averaged sediment concentration and the wave-induced mean flow (undertow). The fact that the undertow is all offshore directed means that the suspended load transport is always towards offshore at all positions across the beach. However, the bed load is affected by several processes and the direction often changes from onshore to offshore depending on

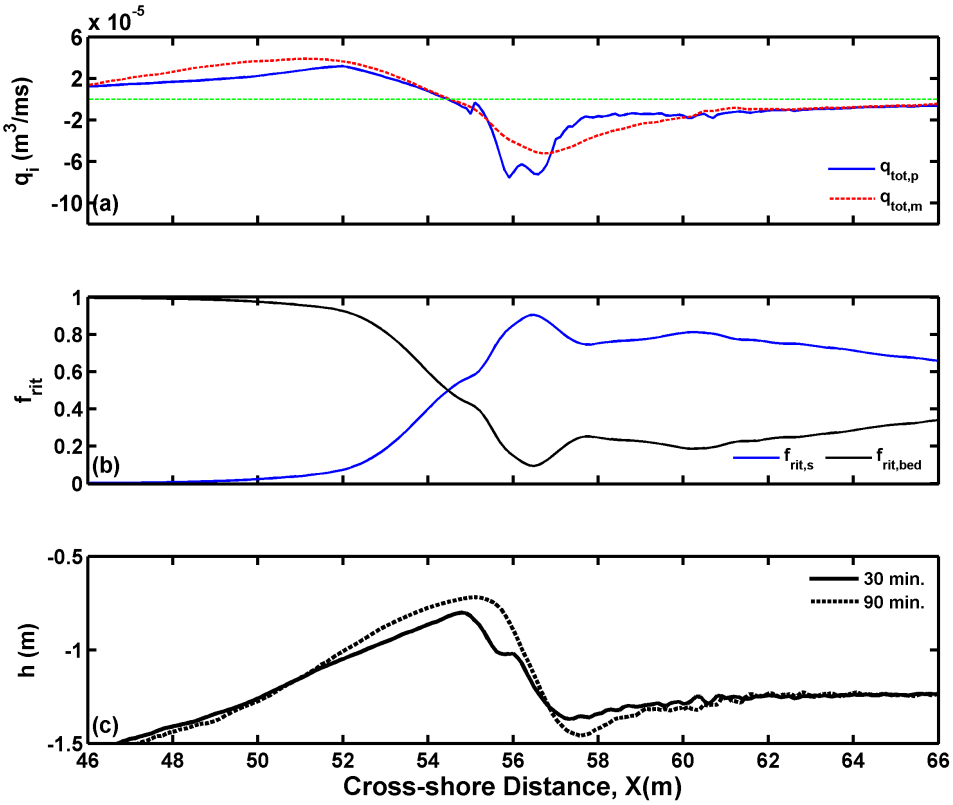

Figure 5.38: Cross-shore variation in sediment transport rates. (a) Different components of sediment transport rates: model predicted suspended transport (blue line), model predicted bedload (black line), model predicted total net transport (red line), and measured total net transport (dashed red line); (b) Relative contribution of each component to total transport, calculated as individual contribution to the sum of absolute values of the two terms (see Eq.(5.12)) (c) Measured bed profiles at $t = 0$ and $t = 90$ min.

the local balance of several different factors. In particular, along the shoaling zone, the wave undergoes strong changes in its form and the wave asymmetry, including velocity as well as acceleration skewness, dominates the near bed process, together with the wave-induced streaming and the bed load transport is typically in the onshore direction. Over the breaking bar, the local depth limits the waves height and the breaking induces strong changes in the bed boundary layer process, leading to sheet flows over a flat bed. The bed load is also affected by the grain size effects, e.g. phase lag, and often the transport direction changes to the offshore direction. In the trough of the bar, the wave height reduces and the strong current produces offshore directed bed load transport.

The overall transport direction depends on the relative strength of these two different transport modes. To quantify the relative contribution of the suspended load and

bedload to the total transport, a relative importance parameter f_{rit} is introduced as the following:

$$f_{rit,s} = \frac{|q_{s,p}|}{|q_{s,p}| + |q_{bed,p}|} \tag{5.12}$$

$$f_{rit,bed} = \frac{|q_{s,bed}|}{|q_{s,p}| + |q_{bed,p}|} \tag{5.13}$$

where $f_{rit,s}$ and $f_{rit,bed}$ respectively represent the contribution of suspended load and bedload transport rate to the total transport.

The relative importance parameters ($f_{rit,s}$ and $f_{rit,bed}$) in the present experiment are displayed in Figure 5.38(b). Across most of the offshore shoaling region ($X < 52.0$ m), the suspended load magnitude is very small and the bedload contributes to the vast majority ($> 90\%$) of total transport. From the breaking point towards the crest of the breaker bar, the magnitude of offshore-directed suspended transport increases monotonically; the relative importance of suspended load gradually approaches ($X = 53.0 - 54.5$ m) and finally exceeds ($X > 54.5m$) the bedload transport contribution, i.e. $f_{rit,s}$ increases while $f_{rit,bed}$ decreases. Parameter $f_{rit,s}$ ($f_{rit,bed}$) reaches it maximum (minimum) value at about $X = 56.5$ m; onshore of this location $f_{rit,s}$ ($f_{rit,bed}$) slightly decreases (increases) and then remains nearly constant at $X > 58.0$ m. In total, at the high end of the offshore slope and lee side of the breaker bar, bar trough and further onshore, the suspended load transport is more important in the contribution to the total transport.

It is therefore clear that in order to achieve accurate prediction of the total sediment transport across the beach, all of these different processes need to be included in the model and represented with good accuracy. In many cases, without including necessary processes, the computed transport can be in the wrong direction, even though the magnitude may be close to the measured data. The resultant beach evolution will still be very different from the reality.

5.8 Morphology Development

In the above sections (i.e. Section 5.4 to 5.7), the developed model system is applied to the SINBAD mobile bed laboratory experiment to simulate its hydrodynamic (e.g. wave parameters, mean water level, undertow and TKE, etc.) and sediment transport processes (e.g. suspended sediment concentrations, suspended load and bedload transport rates). Some relevant model parameters are calibrated, and overall fairly good and consistent simulation results are obtained for all of these processes.

All of the simulations shown in the above sections are based on the bed profile recorded at 30 min in the experiment which is assumed to be fixed in the calculation in order to achieve a converged solution. Then the comparison is made against measurements obtained during 30 min. - 45 min. (i.e. the 3rd experiment run) as the bed profile evolution is relatively small during this 15 mins and its effect on the hydrodynamics and sediment transport can thus be neglected.

With the calibrated model parameters obtained from Section 5.4 to 5.6, the model system is applied in this section to simulate evolutions of the mobile beach profiles. Section 5.8.1 presents the comparisons between the model predicted and measured bed profiles at the corresponding experiment time of 60 min. and 90 min., respectively. Similar to that shown in Section 5.6.4, the effects of progressive surface waves, unsteady phase-lag, wave orbital velocity asymmetry and bed slope on the morphology evolution are studied respectively in Section 5.8.2. Section 5.8.3 presents and discusses the cross-shore-varying contributions of suspended and bedload transport to bed profile evolutions.

5.8.1 Prediction of The Morphology Evolution

By solving the sediment continuity equation, i.e. Eq.(3.137), the bed profile in the model is allowed to evolve with time. As a result in addition to the complicated interactions between the waves, currents and sediment transport, the bed profile changes can also significantly influence the hydrodynamic and sediment transport processes, especially when they are larger than a few percent of the water depth. These processes then in turn affect the evolution of the bed profile. Overall, the simulation of morphology evolution is a very complex process which involves complicated two-way interactions between waves, currents, sediment transport and morphology changes.

Figure 5.39 presents the cross-shore evolution of the measured and model predicted bed profiles after 30 mins of experiment time (i.e. $t = 60min.$). The measured bed profile evolution shows the characteristic of small erosion at the middle part of the

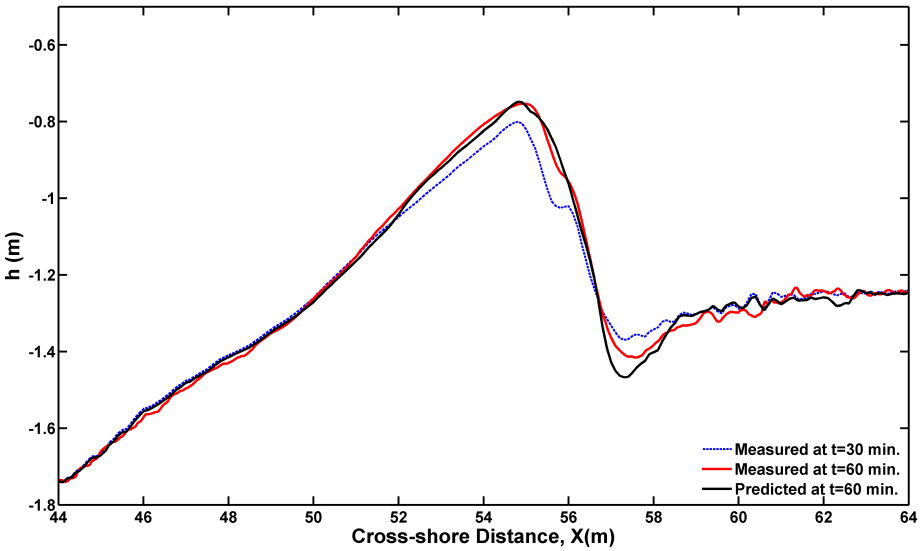

Figure 5.39: Comparison of model predicted (black line) and measured (red line) bed profiles at the experiment time of $t = 60$ min. Blue dashed line represents the measured bed profile at $t = 30$ min.

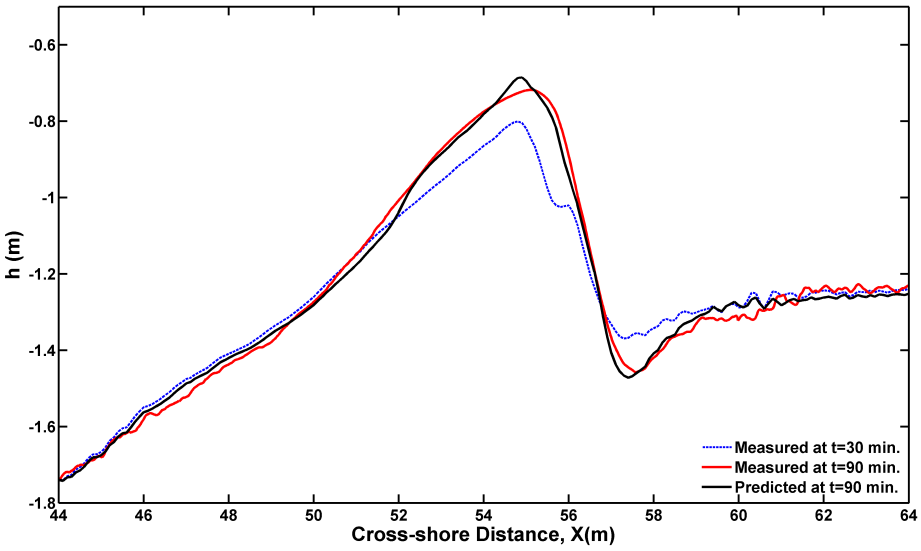

Figure 5.40: Comparison of model predicted (black line) and measured (red line) bed profiles at the experiment time of $t = 90$ min. Blue dashed line represents the measured bed profile at $t = 30$ min.

offshore bar slope ($X = 45.0 - 50.0m$), significant accumulation at the high end of the offshore and onshore slope of the breaker bar ($X = 51.5 - 56.8m$) and significant erosion

around the bar trough ($X = 57.0 - 60.0m$), leading to a steepening of both the offshore and shoreward slope of the breaker bar. Overall, the predicted bed profile at $t = 60min.$ agrees well with the measurements with all the aforementioned characteristics correctly represented in the model. At the bar trough, the bed erosion is overestimated due to a much larger total transport gradient induced by the underestimated bedload transport rate there.

The measured bed profile at $t = 90min.$ (Figure 5.40) shows similar morphology evolution characteristics as that shown at $t = 60min.$. From $t = 60min.$ to $t = 90min.$, both of the measured and model predicted breaker bar crest (bar trough) continues to grow (deepen), leading to a more steeper shoreward slope of the breaker bar. During this period, it seems that the model predicted change rate of the bed profile around the bar trough is smaller than the measurement, as the final predicted bed profile there (i.e. $X = 57.0 - 59.0m$) is very close to the measurement at $t = 90min.$ Therefore, a fairly good agreement between the model predicted and measured is finally obtained. It is further seen that the measured bar crest migrates slightly onshore at the end of experiment ($t = 90min.$), while the predicted bed profile still shows a significant bar crest at the same place. This is maybe because, toward the end of experiment, the shoreward slope gradually approaches and exceeds the natural angle of repose ($\tan\alpha \approx 0.5 - 0.7$) for sandy materials (Nielsen [130]), leading to a sediment avalanche which is not included in the present model system.

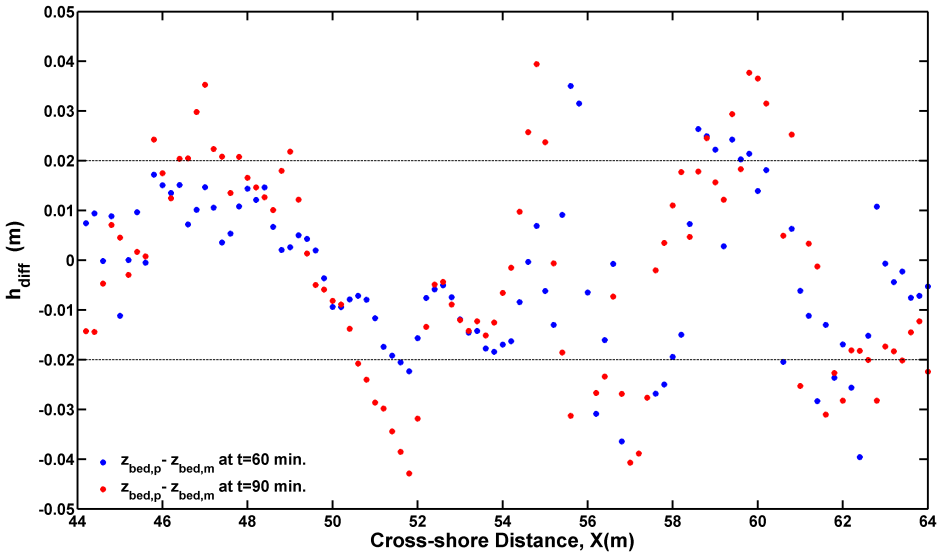

Figure 5.41: The difference between the model predicted and measured bed level at $t = 60$ min (blue stars) and $t = 90$ min (red stars).

In order to quantify model performance on the morphology evolution, the differences between the model predicted and measured bed profile are furthermore shown in Figure 5.41. In agreement with the above discussion, the predicted bed profiles at $t = 60min.$ and $t = 90min.$ agree well with the corresponding measurements. At a majority of the cross-shore locations, i.e. 78% and 60% of locations at $t = 60min.$ and $t = 90min.$ respectively, the magnitude of the differences are smaller than 0.02 m. Generally, the order of magnitude of the bed profile differences at most of the cross-shore locations at $t = 90min.$ is equal to that at $t = 60min.$, indicating that the model-measurement differences do not increase with time and those complicated processes related to the morphology evolution are correctly reproduced by the present model system. However, it is also noted that the bed profile differences increase significantly between $X = 50.0-52.0$ m, which is largely due to the discrepancies in the predicted bedload transport rate in this region.

5.8.2 The Effect of Several Bedload Processes on The Morphology Evolution

In Section 5.6.4, the effects of progressive surface waves, unsteady phase-lag, wave orbital velocity asymmetry and bed slope on the bedload transport are investigated separately. Changes in bedload transport rate are expected to have some effects on the bed profile evolution. In addition, most of the present practical morphodynamic numerical models utilize a quasi-steady formula for calculating the bedload transport rate, which cannot describe some physical processes that are only included in a semi-unsteady formulae (e.g. the phase-lag effect). Therefore, it is also meaningful to have a sensitivity study on the effects of processes on the bed profile evolution as that shown in the following section.

Figure 5.42 - 5.45 show respectively the predicted bed profile at the end of experiment time ($t = 90.min$) from four scenarios, each of which has the same setup with the simulation shown in Section 5.8.1 but excluding a specific process, e.g. the bed profile shown in Figure 5.43 is predicted without the phase-lag effect.

Generally, the differences between the bed profiles predicted from the present four scenarios and the one shown in Figure 5.40 are consistent with the predicted changes of bedload transport shown in Figure 5.34 - 5.37. After excluding the effect of surface progressive waves on the bedload transport, the predicted bed profile (Figure 5.42) shows a major discrepancy of a much deeper bar trough than the measurement. Compared with the measurement, the predicted bar crest grows too much while the bar trough deepens too much when phase-lag effect is omitted (Figure 5.43); this is also observed in Figure 5.45.

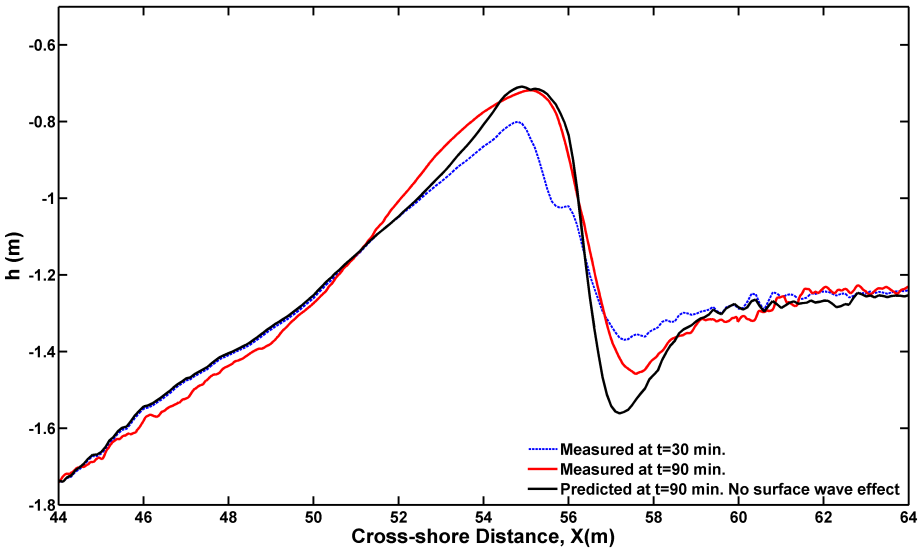

Figure 5.42: Comparison of model predicted (black line, without the effect of surface progressive waves on the bedload transport) and measured (red line) bed profiles at the experiment time of $t = 90$ min. Blue dashed line represents the measured bed profile at $t = 30$ min.

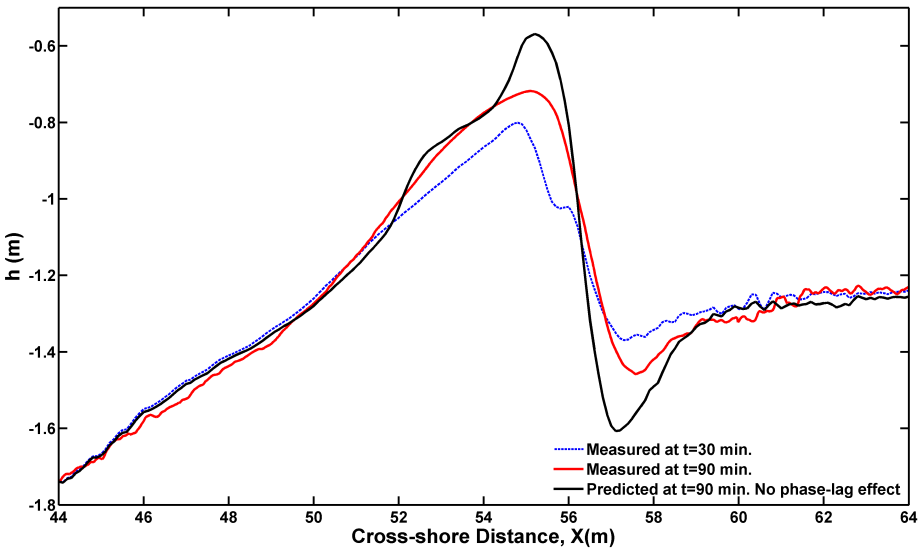

Figure 5.43: Comparison of model predicted (black line, without the phase-lag effect on the bedload transport) and measured (red line) bed profiles at the experiment time of $t = 90$ min. Blue dashed line represents the measured bed profile at $t = 30$ min.

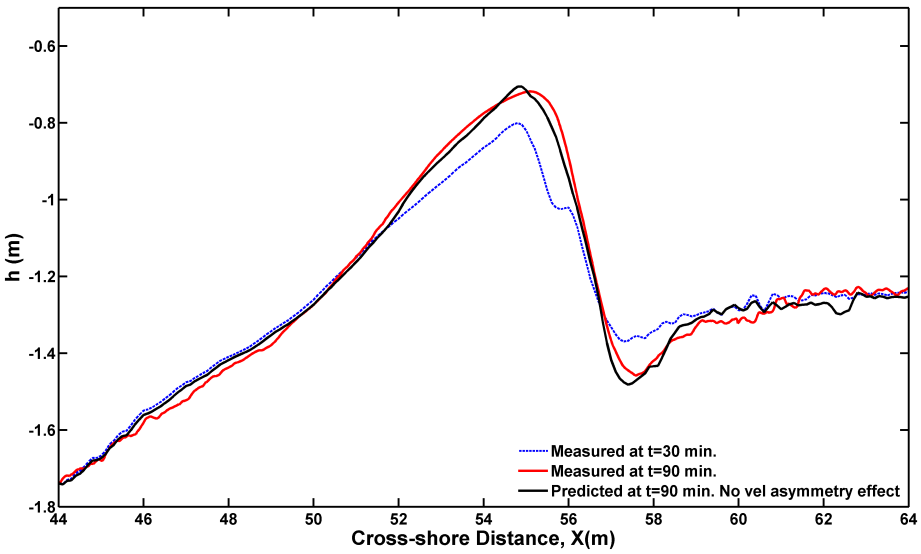

Figure 5.44: Comparison of model predicted (black line, without the effect of acceleration skewness on the bedload transport) and measured (red line) bed profiles at the experiment time of $t = 90$ min. Blue dashed line represents the measured bed profile at $t = 30$ min.

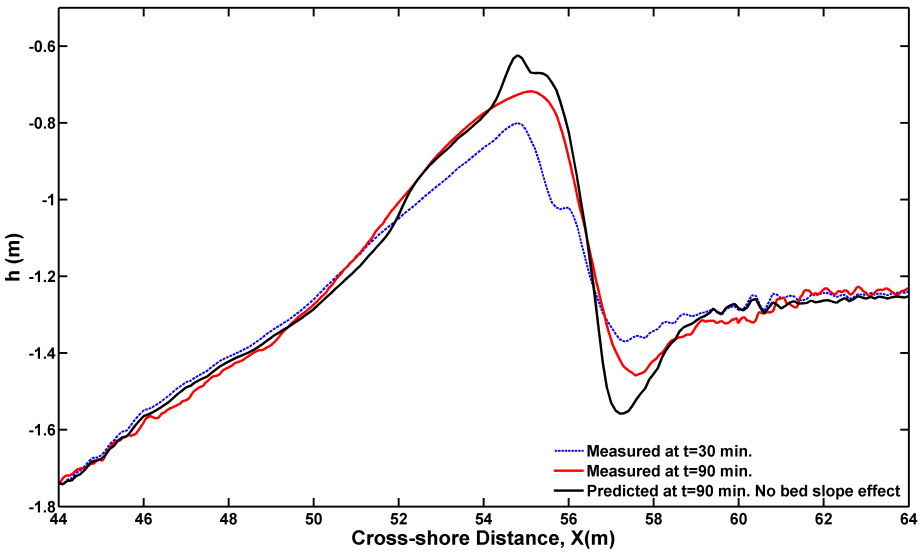

Figure 5.45: Comparison of model predicted (black line, without the effect of bed slope on the bedload transport) and measured (red line) bed profiles at the experiment time of $t = 90$ min. Blue dashed line represents the measured bed profile at $t = 30$ min.

It is interesting to further note that all of the predicted bed profiles from those four scenarios show the correct morphology evolution characteristics on the whole, i.e. the

breaker bar crest grows while the bar trough deepens during the simulation, although some discrepancies are observed on the detailed magnitude of the bed profile changes. These simulation results suggest that even if the bedload transport rate is not correctly modelled as a result of omitting some important physical processes, the primary bar evolution characteristic still can be predicted. Therefore, the decisive contribution to the bar morphodynamics in this particular case presented here is the suspended load transport. A further analysis on the contributions of suspended load and bedload transport to the bar morphodynamics is thus conducted in the following section (Section 5.8.3).

5.8.3 Contributions of Suspended Load and Bedload Transport to The Bar Morphodynamics

Following the same analysis as shown in Section 5.7, the contributions of suspended load and bedload transport to the local morphology evolution are shown in Figure 5.46. In the figure, the negative cross-shore gradients of $q_{s,p}$ and q_{bed}, divided by the sediment fraction in a loosely packed bed ($1 - \varepsilon_0$; with porosity $\varepsilon_0 = 0.40$), are calculated and shown in Figure 5.46(b). The negative sign in the gradients is chosen such that the positive values refer to net local accretion, and negative values to net erosion, of the bed. Across most of the offshore shoaling region ($X < 51.6$ m), the bed profile changes are almost fully contributed to by the bedload transport, with the nearly invisible magnitude of suspended load in these locations. Suspended transport leads to accretion of the bar crest and higher ends of the onshore bar slope ($X = 51.6 - 56.0$ m), and erosion of the bar trough ($X = 56.0 - 59.0$ m). Bedload transport leads to accretion of part of the offshore bar slope ($X = 52.0 - 54.0$ m), erosion of the bar crest and higher ends of the shoreward bar slope ($X = 54.0 - 56.0$ m), and accretion of the bar trough ($X = 56.0 - 57.8$ m). Therefore, the final bed profile changes between the bar crest and bar trough ($X = 54.0 - 58.0$ m) are results of net differences between the opposite contributions of suspended load and bedload transport. It is easy to find from the Figure 5.46(c) that, the suspended load transport contributions (the blue line in Figure 5.46(b)) to the present breaker bar morphodynamics exceed those of bedload, leading to the final morphology evolution characteristic of growth of the bar crest and deepening of the bar trough. These results confirm the results in Section 5.8.2 that the decisive contribution to the bar morphodynamics in the present case is the suspended load transport.

Since the suspended sediment transport is the decisive contribution, it is interesting to further investigate how the bed profile would evolve if the bedload transport is totally excluded in the model simulation. Two slightly different scenarios are further simulated

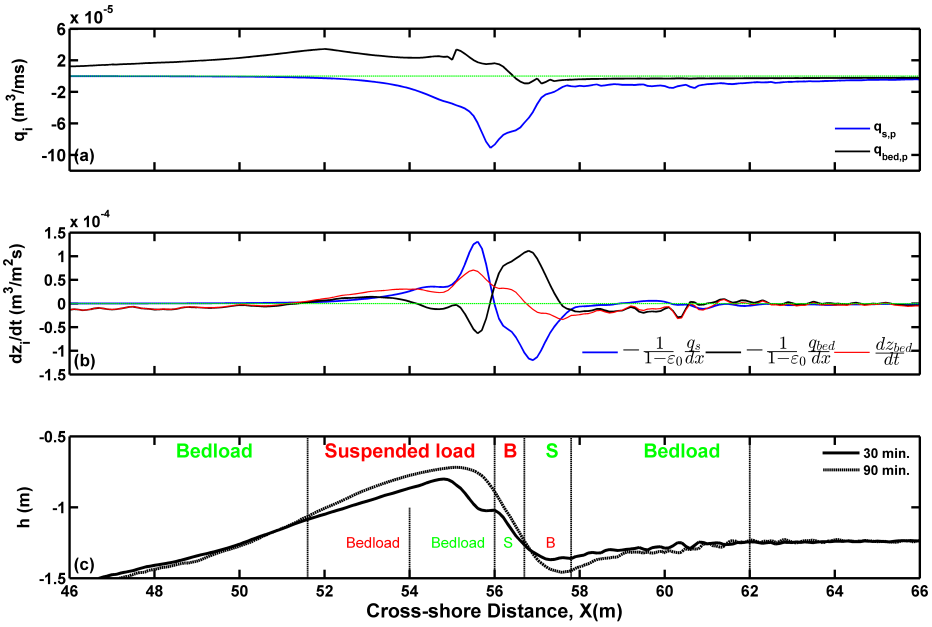

Figure 5.46: Cross-shore variation in sediment transport rates. (a) Different components of sediment transport rates: model predicted suspended transport (blue line), model predicted bedload (black line); (b) Contributions by each component to bed profile change (erosion/accretion), quantified through horizontal transport gradients divided by relative sand fraction in loosely packed bed $(1-\varepsilon_0)$: contributions by suspended load (blue line), bedload (black line) and total transport (red line); (c) A sketch indicating the dominant transport mode to the local bed level evolution (the upper big bold text), in which the red and blue colors represent local bed accretion and erosion, respectively. The impact of the other transport mode to the local bed evolution is also shown in the lower part of this figure by smaller light text. 'B' and 'S' are shorts for 'Bedload' and 'Suspended load', respectively. Measured bed profiles at $t = 0$ and $t = 90$ min are respectively represented by the black bold line and dotted line.

for this purpose. In addition to a zero bedload transport rate in both of these two scenarios, the bed level in scenario A1 is set as a constant during the whole simulation, i.e. no bed level change effect on the hydrodynamics, the accumulated bed profile change is then added to the initial bed level (the blue dashed line in Figure 5.47) at the end of experiment to represent the final predicted bed profile (the black line in Figure 5.47). The bar crest grows and bar trough deepens, however, the magnitudes of bed level change at both bar crest and trough are clearly overestimated. In addition, the measured zero change point is at about $X = 57.0$ m. But in the prediction it is shifted about 0.5 m offshore from scenario A1.

In contrast with the setting in scenario A1, the bed level is evolving instantly with time in scenario A2. The final predicted bed profile shown in Figure 5.48 is very

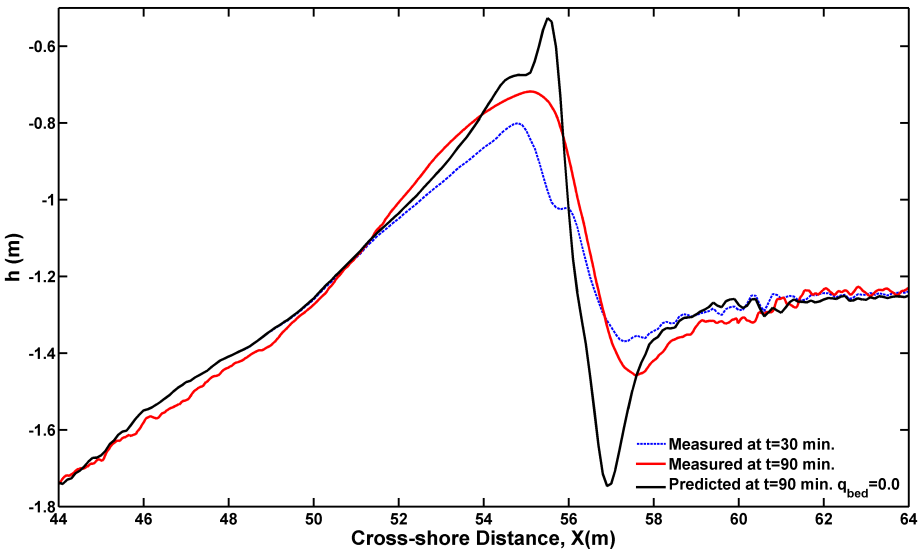

Figure 5.47: Comparison of model predicted in the scenario A1 (black line, without bedload transport component and the effect of bed profile change on the hydrodynamics) and measured (red line) bed profiles at the experiment time of $t = 90$ min. Blue dashed line represents the measured bed profile at $t = 30$ min.

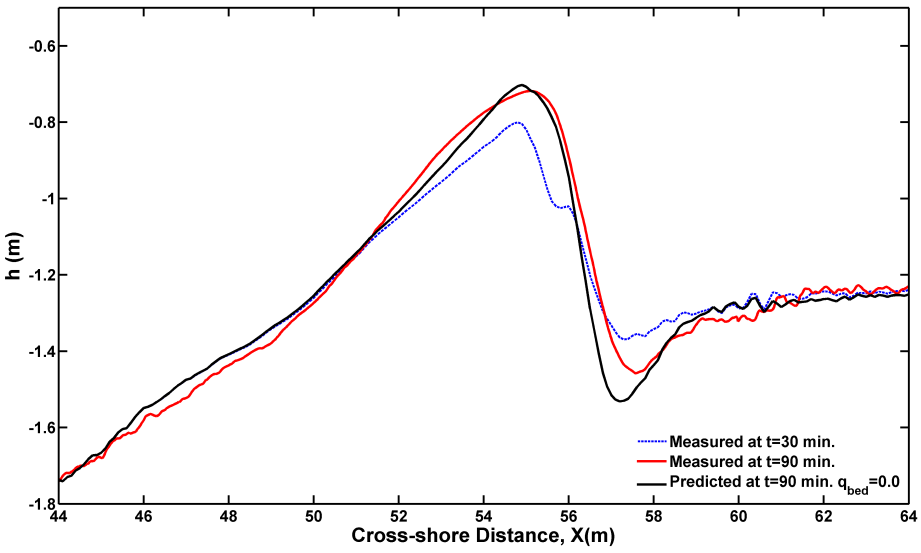

Figure 5.48: Comparison of model predicted in the scenario A2 (black line, without bedload transport component but the bed profile is evolving instantly with time) and measured (red line) bed profiles at the experiment time of $t = 90$ min. Blue dashed line represents the measured bed profile at $t = 30$ min.

different with, and much better than, that predicted from the scenario A1 (Figure 5.47), indicating that the bed level changes can significantly affect the hydrodynamics which then in turn have apparent influences on the morphology evolution.

These tests confirm that the instant feedback from the bed level change to the hydrodynamics is important to achieve realistic prediction in the beach morphology. Furthermore, the bed profile predicted from scenario A2 (the black line in Figure 5.48) is very close to the measurements, suggesting that with enough feedback information, the bed evolution can be predicted reasonably well when the bedload transport contribution is small.

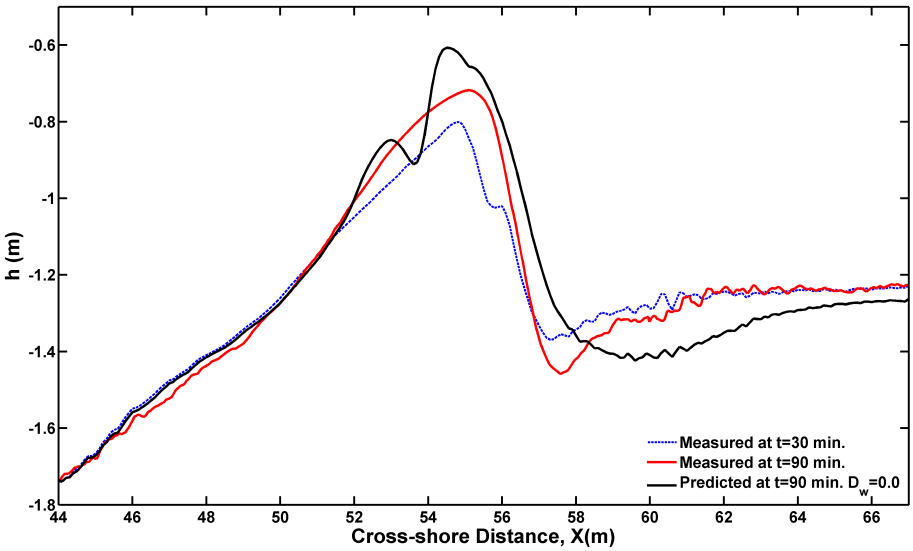

Figure 5.49: Comparison of model predicted in the scenario A3 (black line, without the wave breaking induced turbulence in the turbulent closure model) and measured (red line) bed profiles at the experiment time of $t = 90$ min. Blue dashed line represents the measured bed profile at $t = 30$ min.

From a morphological point of view, the breaking bar morphodynamics are mostly determined by the suspended sediment transport, which is in turn determined by the predicted hydrodynamics (e.g. wave parameters, undertows, TKE, etc.). Therefore, a reasonable prediction of the hydrodynamic processes are prerequisites to obtain reliable bed profile changes in the present experiment. In Section 5.4.3 and 5.4.4, much effort is made to obtain reasonable and consistent prediction results of TKE and velocity profiles at the same time. The values of parameter D_w and H_w are found to have significant effects on the TKE and velocity profiles which must be carefully calibrated. As an example of displaying the importance of reasonable predictions of the hydrodynamic processes on a proper morphodynamics simulation, another simulation (scenario A3), with the same set of parameters as that shown in Section 5.8.1 except $D_w = 0.0$ (i.e.

no contribution of surface wave dissipations to the TKE production), is further carried out. The cross-shore distribution of predicted bed profile shown in Figure 5.49 distinctly deviates the correct characteristics of observation: the whole breaker bar crest and bar trough are wrongly shifted about 1 m onshore; the magnitudes of bed level change at both the bar crest, bar trough and further onshore are overestimated too much.

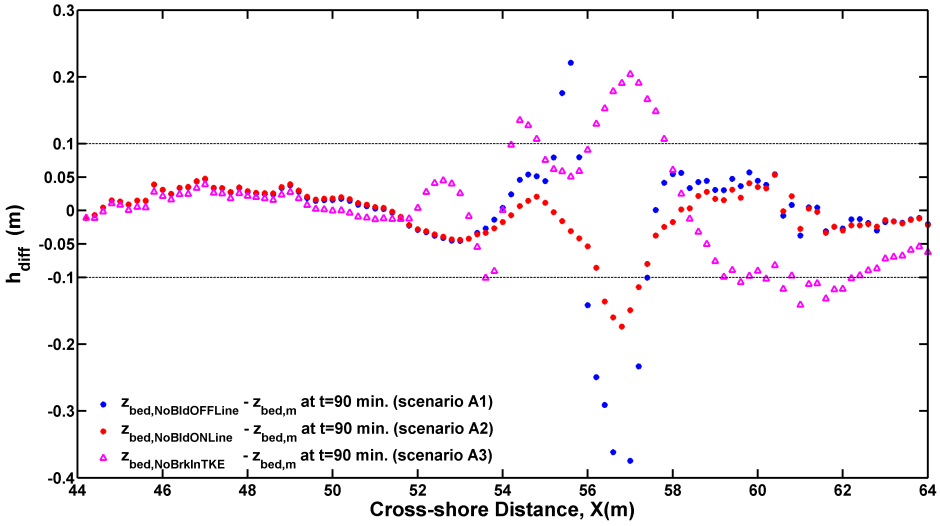

Figure 5.50: The difference between the model predicted and measured bed level at $t = 90$ min for three scenarios (see the definitions of these three scenarios in the text).

Similar to those discussed at the end of Section 5.8.1, the differences between the model predicted and measured bed profile for the above three scenarios (i.e. the scenario A1, A2 and A3) are also shown in Figure 5.50. The bed profile differences of all these three scenarios are much larger than that shown in Figure 5.41. Apparently, it is not physically reasonable to omit those processes (i.e. the wave breaking induced TKE, the bedload transport and the feedback from the bed level change to the hydrodynamics). At $X = 44 - 52$ m, the bed profile differences of these three scenarios are very close and have relatively small magnitude (< 0.05 m). This is because the bedload transport contributes most to the total load and the bed profile change (Figure 5.38), while the bed profile change is relatively very small. Further onshore (i.e. $X = 52 - 64$ m), as the suspended load contribution to the bed profile change increases, the bed profile differences from these three scenarios also become larger. Among these three scenarios, bed profile differences from scenario A3 are larger than those from A1 and A2 at most locations, suggesting again the significance of reasonable prediction of the hydrodynamic processes to obtain reliable bed profile changes in the present experiment; by contrast, bed profile differences from scenario A2 are smallest, indicating the instant feedback from the bed level change to the hydrodynamics is important to achieve realistic prediction in the beach morphology.

5.9 Conclusions

This chapter starts with a brief introduction of the mobile bed laboratory experiment conducted as one part of the SINBAD research project. During this experiment a detailed measurement of the hydrodynamics (water level, flow velocity and TKE, etc.), suspended sediment concentration and bed profiles are obtained. Therefore this experiment is an ideal application case for the model system developed in this research, as the performance of all the modules (i.e. wave module, circulation module, sediment transport module and morphology evolution module) in the model system could be explicitly presented and evaluated in detail.

Based on the treatment (time constant or evolving instantly with time) of the bed profile adopted in the simulations, the implementation of the model system shown in this chapter is separated into two parts, Part I (with constant bed profile) and Part II (with time-evolving bed profile).

All simulations in Part I (i.e. Section 5.4 - 5.6) are carried out to obtain converged solutions, based on measured bed profile of $t = 30$ min. The simulation results are further compared with the observations conducted between $t = 30 - 45$ min, assuming that the relatively small bed level changes during this 15 minutes do not significantly affect the hydrodynamics and sediment transport. The performance of the model system regarding the hydrodynamics and sediment transport processes are further analyzed and described in Part I, with the following summaries and conclusions obtained:

- The model accurately reproduces the location of breaking point in this test, inshore of which (i.e. x $>$ 52 m) the wave height agrees fairly well with the measurement (Figure 5.2). The cross-shore behaviour and the quantitative set-down and set-up are also well reproduced by the model (Figure 5.2). Further model-data comparisons show fairly good agreement between the simulated and the observed cross-shore Eulerian velocities at the twelve measurement profiles. In particular the simulated near bed velocities, which are especially important for a good prediction of sediment transport rates and bed profile evolutions, are also in good agreement with the measurement (Figure 5.6 and 5.19).

- A modification of the $\beta - kd$ wave breaking approach can significantly improve the wave height simulation results for this test case(Figure 5.3). Sensitivity analysis shows that the effect of the wave roller must be included and the model results with $\alpha_r = 1.0$ show the best overall agreement with the measured data. A cross-shore-varying value of C_1 is suggested.

- The accurate prediction of TKE in the surf zone is still a challenge for the common-

ly used turbulence closure (RANS) models; many efforts are thus made to try to improve the model results of TKE profiles in this chapter. The amount of wave dissipation introduced as surface flux of TKE (i.e. $F_k = D_w \left[(1-\alpha_r)\,\epsilon^b + \epsilon^r + \epsilon^{wcap}\right]$) must be subtracted from the Eq.(3.32); if not the total contribution of wave dissipation to the momentum balance is not conservative and no consistent model results can be obtained for the velocity and TKE profiles at the same time. Further comprehensive sensitivity analysis calibrates the values of parameter D_w and H_w. Simulated TKE and velocity profiles in a simulation with a cross-shore-varying H_w (see its cross-shore distribution in Figure 5.20) and $D_w = 0.3$ agree overall best with the observations. However, the modeled TKE is still over-predicted (with different degrees) near the water surface. This is likely a result of an inconsistency inherited from the assumption used in the turbulent closure model (see details in Section 5.4.4).

- Three methods are used to calculate the pickup rates of suspended sediment transport which describe the vertical sediment exchange between the bed load and the suspension layers. The predicted suspended sediment concentrations using the wave-averaged bed shear stress (τ_{cw}) alone without accounting for the additional wave breaking effects on the sediment concentration (method Sus-II) agree fairly well with the measurements. Although breaking waves may directly entrain large amounts of sand from the bed (Nielsen [2]), the enhancement of sediment concentration by this effect may be mainly constrained in a very thin layer near the bed in the present case and hence is not reflected in the sediment pickup process. A new method (method Sus-III) proposed by van der Zanden et al. [77] that accounts for wave breaking turbulence effects in pickup functions are also checked in this research. Simulation results show that this method could also obtain fairly good agreements with the measured suspended sediment concentration profiles, although a good prediction of the near-bed TKE is required. Calculated suspended sediment transport rates (q_s) from the Eq. (5.7) further verify the reasonability of method Sus-II and Sus-III, as the q_s calculated by these two methods are very close to that estimated from the measured q_s and undertow in van der Zanden [5].

- Both two quasi-steady bedload transport formulae, i.e. the MPM (Meter-Peter M*ü*eller [9]) and the Soulsby and Damgaard [124] formulae, fail to reproduce all of the right features of (measured) bedload transport ($q_{bed,e}$), indicating the quasi-steady formulae are not appropriate for this SINBAD mobile bed application. However, it should be noted that the MPM formulation with τ_{cwmax} provides much better q_{bed} than the same formulae with τ_{cw}, suggesting that the bedload transport in this application is wave dominated and τ_{cwmax} is more reasonable to be used in calculation. A recently developed semi-unsteady model, SANTOSS

(van der A et al. [78]), is thus used in this research. After including the extra bedload resulting from the breaking wave induced turbulence, the predicted bedload transport rate (i.e. the $q_{bed,ps}$ shown in Figure 5.31) reproduces all the important features displayed in $q_{bed,e}$, although there are some discrepancies in the detailed magnitude. Further sensitivity analysis shows that the effect of surface progressive waves and phase-lag are vitally important in determining the (right) features of $q_{bed,e}$, while the contributions of acceleration skewness and bed slope are not essential. The actual performance of the analytical expression of Abreu et al. [177] and the parametrization method of Ruessink et al. [178], which are used in this research to predict the intra-wave velocity parameters, are examined. The predicted peak crest and trough velocities agree reasonable well with the measurements. However, the near-bed wave orbital velocity skewness and asymmetry are poorly calculated, therefore the effect of acceleration skewness may be not accurately accounted for in this research. A further study on predicting the intra-wave velocity parameters is thus advised.

The model system is applied in Part II of this chapter to simulate and study the evolution of mobile bed profiles. In comparison with the bed profile at $t = 30$ min., the breaker bar crest grows while the bar trough deepens significantly at $t = 90$ min., leading to a steepening of both the offshore and shoreward slope of the breaker bar. With the calibrated model parameters obtained from Section 6.2 to 6.4 (i.e. Part I), the model predicted bed profile at the end of experiment time ($t = 90$ min.), in terms of both the cross-shore distribution features and magnitudes, agrees fairly well with the measurements. Morphology evolution is a very complex process which involves complicated two-way interactions between waves, currents, sediment transport and morphology changes. Therefore, the good simulation of this complex morphology evolution process in this research suggests the success of the developed model system to a great extent. Although the progressive surface waves, unsteady phase-lag, wave orbital velocity asymmetry and bed slope can significantly affect the predicted bedload transport rate, they don't change the main features of the bed profile in the present case. Further analysis shows that:

- The suspended load transport is more important in the contribution to the total transport at the high end of offshore slope and lee side of the breaker bar, bar trough and further onshore.
- Suspended load and bedload have opposite contributions to the final principal morphology evolution characteristics of bar crest growth and bar trough deepening. The contributions of suspended load transport exceed those by bedload; therefore it is the suspended load that decides the present bar morphodynamics.

- Even if the bedload transport is excluded from the model simulation, the principal morphology evolution characteristics still can be predicted. The effects of bed level changes on the hydrodynamics are however, important to the final beach evolution predictions.
- A reasonable prediction of the hydrodynamic processes is the prerequisite to obtain reliable bed profile changes in the present experiment application. Excluding the wave breaking induced turbulence can significantly change the correct cross-shore distribution features of the predicted bed profile.

Chapter 6

Discussion, Conclusion and Recommendations

The prediction of long term (∼100 years) and large scale (∼100km) coastal evolution, in response to either direct or indirect human interference and to natural environmental changes, is increasingly important for the understanding of the potential risk of climate changes and for effective coastal zone management. Presently, there are different types of models exist for such purpose, including the process-based model, behaviour based model and data driven model. The behaviour-based models that have been developed in recent years aim to describe the long term coastal morphology based on highly aggregated physical processes and grossly simplified concepts. They are simple to use and require very limited computing efforts. However, since many fundamental transport mechanisms that are potentially important to long term morphological changes are not accounted for by such models, such as extreme wave-induced sediment transport, selective transport of sediment mixtures, enhanced bed drag forces on non-equilibrium sediment entrainment etc., it is still difficult to apply the behaviour based model for general practice in long term prediction (Cowell et al. [206]). Similarly, the data driven model, such as ANN type of model also are limited in its application in reality due to lack of wide range of data for long period of time.

The present study belongs to the process based model. They type of models are based on detailed description of coastal processes and potentially could predict future changes due to natural forces and human interventions over medium term, e.g. in the order of 5-10 years (van Rijn [207]). However, as pointed out at the Introduction chapter, within these process models, the submodules describing hydrodynamics and sediment transport are not detailed enough for accurate and reliable long term integration as errors accumulate, including the uncertainties in the wave-breaking effects, grain size effects, wave asymmetry and etc. The present study therefore aim to improve these fundamental knowledge gap and ultimately improve the feasibility of using the process

based model for long term prediction.

The present study can be used as tool by environmental scientists, coastal engineers, national and regional authorities, environment agency and regional managers to understand and predict the erosion, transport and deposition of estuarine and coastal sediment by natural processes and anthropogenic activity. Morphological modelling systems of this kind play a critical role in the management of environments at the interface between rivers and shallow seas by engineers, including the assessment of the impact of climate change, through increased storminess and rising sea levels; beach stability; the integrity of coastal structures and the design of beach nourishment schemes; water quality; and conservation of the ecosystem.

6.1 Discussions

6.1.1 Modelling approaches

In the formulation of the present model, a number of assumptions have been adopted, including the basic wave and current modelling for combined unsteady flows, the representation of wave breaking, the sediment transport under the complex flows, and the beach morphology evolution. Notwithstanding the reasons for these assumptions, it is important to realise which processes are excluded and how these would affect the present model and results.

Wave-averaged modelling approach

The present model follows many previous works, developing the wave model based on a spectral wave model UnSWAN to simulate the wave dynamics. As discussed in the previous chapter, such an approach essentially assumes the wave dynamics can be represented through period-averaged statics and the changes within one wave period are less significant. Wave randomness and the interactions between the waves and structure or topography can be simulated through a parameterised way. Similarly, the wave-induced current is also represented by the wave-averaged momentum and mass conservations. The wave-current interaction is based on the VF theory that essentially assumes a steady representative waves. These assumptions are applicable to a large scale coastal region and are not particularly suitable to applications in small areas where the changes within wave length are significant.

Representation of wave breaking

The wave breaking in the present study is largely represented in the wave model as an energy dissipation process at the surface and extra turbulence injection in the current model, without describing the details of the surface changes within a wave period. Inevitably, several empirical parameters have to be adopted to compute the changes in wave height, current and turbulence characteristics, and the model calibration becomes critical to the model's accuracy.

Through several model testing and sensitivity analysis, recommended model parameters are identified. However, it is noted that these parameterisations are essentially based on very limited simulations for the SINBAD experiments and their generic applicability to any other conditions still requires careful considerations. Nevertheless, these studies show the distribution patterns of the values of these parameters across the beach at different locations where very different physical processes are dominant. Further study on these parameterisations can certainly improve the model's performance under a wide range of wave and current conditions.

Sediment transport modelling approach

To be consistent with the hydrodynamic modelling, the sediment transport process in the present study is also based on a wave-averaged approach. The intra-wave dynamics therefore are based on a number of parameterisations involving local wave characteristics (e.g. wave asymmetry), hydrodynamics (streaming), grain size effects (e.g. phase-lag) and bed conditions (bed slope). Most of these processes affect the sediment transport close to the bed, e.g. bed load, more significantly, in comparison to that in the suspended load. However, the details of these processes can potentially change the direction of the bed load transport and should be considered in detail to improve the accuracy of the model. In the present study, the suspended load transport is found dominant for the overall sediment motion across the beach and the model's performance in the total load transport is very good. In a different wave-current condition when the bed load contributes to the total load to a larger extend, these processes are then essential to the model's predictions.

Morphological modelling approach

Based on the mass conservation principle, the beach morphological evolution is modelled by examining the divergence in the local total sediment transport rate. Unlike the boxes approach as in the Warner et al.[47], this approach is typically used for the same sediment class, e.g. single grain size. When a mixture of sediment is taken into

account, simulations for each different sediment class will be needed and a grain sorting procedure is required to work out the total transport rate. However, the implication of such a complex transport mechanism on the transport of each individual sediment class under the same flow condition, i.e. the phase lag effects, is still unknown. It is expected that the coarse grain will be less affected but the median and fine grains could potentially change their behaviour totally under the influence of the coarse grain. Further elaboration of the multi-fractional approach and improvements might be informative in the future.

6.1.2 Sensitivity analysis justification

In Chapter 4 and Chapter 5, some sensitivity analysis of the model results against several parameters are conducted. With the detailed measurement data, these sensitivity analysis are used to both reveal the effects of these parameters on the model's performance and obtain the optimal combinations for later simulations. However, it should be noted that this kind of work must be conducted in a reasonable way. In order to justify the present sensitivity analysis study, the following two aspects are inspected, i.e. the sensitivity of model results to parameters and the adopted parameter value ranges, mainly by comparing and referring to the former work of other researchers.

Justification of the sensitivity of model results to certain parameters

The sensitivity of model results to some certain coefficients can be supported by previous studies. For example, similar sensitivity studies on the parameter α_r were conducted by Uchiyama et al. [23] and Kumar et al. [25] with similar conclusions with the present study. Many studies relevant to the parameter D_w (e.g. Govender et al. [158]; Feddersen and Trowbridge [160]; Huang et al. [159]; Feddersen [155]; Paskyabi et al. [161]) and H_w (e.g. Terray et al. [119]; Burchard [65]; Umlauf and Burchard [66]; Stips et al. [163]; Moghimi et al. [151]) can be found in the literature. Specially, it is noted that Umlauf and Burchard [66] indicated that 'It has been remarked by almost all authors that the decay coefficients are very sensitive with respect to small uncertainties in position of the virtual origin'. The so-called 'virtual origin' is $z = -z_{0s} = -H_w \cdot H_s$ in this study, thus their statement clearly indicates the sensitivity to H_w.

Although a detailed sensitivity study on the parameter C_1 has not been found in the literature, it can be justified with the specific situation the present study focuses on, i.e. the surf zone with breaking waves induced strong turbulence (see more details in the following section).

Justification of the parameter ranges used in the sensitivity studies

The parameters used for the sensitivity analysis in this study are, the parameter α_r which controls the fraction of the breaking waves turned into wave rollers, parameter C_1 that used in the generic length scale equation of the GLS turbulence closure model, parameter D_w that controls how much wave dissipation energy is transferred into TKE and parameter H_w that parameterize the surface roughness z_{0s} in relation to the significant wave height H_s. The value ranges of these parameters used in this study are justified as follows.

In terms of the parameter α_r As suggested by Uchiyama et al. [23], the parameter α_r provides some flexibility to depict different beach forms and wave breaking types (i.e. spilling, plunging, surging). The value range of α_r in this study, i.e. [0,1.0], is identical with that used by previous studies in the literature (e.g. Uchiyama et al. [23]; Kumar et al. [25]).

In terms of the parameter D_w and H_w According to the definition, D_w must be in the range of [0,1.0], and z_{0s} ($= H_w \cdot H_s$) should be no more than several times of H_s. However, no precise range had been given yet in the literature. In fact, a wide range of values had been reported in the literature, suggesting a gap between the real physical processes and the theories or models used to parameterize these processes. In various previous numerical model studies, these two parameters are generally taken as tuning parameters and adjusted with values to produce model results closest to the measurements. From literature, $D_w \approx 1.0$ is proposed for deep water white-capping (Paskyabi et al. [161]), and $D_w \approx 0.01 \sim 0.25$ for wave breaking in the surf zone (Govender et al. [158]; Huang et al. [159]; Feddersen and Trowbridge [160]; Feddersen [155]); most previous studies proposed $0 < H_w \leq 1.0$ (Terray et al. [119]; Burchard [65]; Umlauf and Burchard [66]; Stips et al.[163]; Moghimi et al. [151]), whist there are still some studies proposed $H_w > 1.0$, e.g. $H_w = 1.3$ was used by Jones and Monismith [208], and $H_w = 1.6$ by Kantha and Clayson [209]. The final adopted value ranges of these two parameters in this study, i.e. $D_w = 0.3$ and $0.2 < H_w \leq 0.6$, apparently comply with the above physical value ranges and also agree well with that proposed in the literature.

In terms of the parameter C_1 Sensitivity studies on the parameter C_1 are not available in the literature. In this study, calibration of this parameter is taken as a preliminary attempt to improve the turbulence model results in the surf zone, especially near the breaking point. As this parameter is determined in a standard situation of ho-

mogeneous turbulent shear flow in which the turbulence is assumed to be homogeneous, the divergence of any turbulent transport terms vanishes and the intricate interplay between the stabilizing effects of stratification and the destabilizing action of shear can be isolated (Umlauf and Burchard [66]), its value may not be appropriate in situations where wave breaking induced strong turbulence present, especially near the plunging point. In fact, it is found by the sensitivity analysis in the present study that with an increase value of this parameter from its default value (i.e. 1.0), the model results in the surf zone agree very well with the measurements, which indicates a very different turbulence production and dissipation under the breaking waves in comparison with equilibrium turbulence in steady flows. Further study into this will be fundamentally important to the modelling wave breaking.

By adopting the theoretical argument of Tennekes [210] and assumptions made in the above mentioned standard flow situation, Umlauf and Burchard [66] proposed $C_1 = m$ (constraint A); as $m = 1.0$ in the present study $C_1 = 1.0$ is used as the default value as suggested. However, calibrated under similar situations, the counterparts of this GLS model parameter C_1 in some other widely used turbulence closure models are actually not in absolutely accordance with the above constraint. In the literature, C_1 can be found in a range of $0.346 \cdot m$ (the model of Zeierman and Wolfshtein [211]) and $1.12 \cdot m$ (the $k - \omega$ model; Umlauf et al. [162]; Wilcox [212]).

A max value of $1.15 \cdot m$ (m=1.0 in the present study) is finally used in the simulations of the present study. Although it is slightly bigger than $1.12 \cdot m$, it can be argued that the value of $1.12 \cdot m$ are calibrated in a situation different with that the model applied in the present study. Repeat the statement above, its default value may thus not be appropriate in situations where wave breaking induced strong turbulence present. Therefore, a max value of $1.15 \cdot m$ still is thought reasonable. It should also be noted that, the value of C_1 must obey a strong constrain $C_1 < C_2$ (constraint B), deriving from the Eq. (14) of Umlauf and Burchard [66]. In this study, $C_2 = 1.22$ is adopted, thus the value of C_1 adopted in the sensitivity tests certainly obey the constraint B.

6.2 Conclusion

Through the model development and testing against a number of experimental and theoretical cases, conclusions can be drawn for both the modelling approach and the revealed hydrodynamics and sediment transport processes.

6.2.1 On Morphodynamic Model System Development

As shown in the above sections, a new fully coupled, unstructured grid, three-dimensional coastal morphodynamic model system has been developed based on the most recent progress in coastal morphodynamics. This is achieved by accomplishing the following specific objectives:

1. As a basis for the morphodynamic model system developed in the present research, a new three-dimensional coastal hydrodynamic model with fully coupled wave-current interactions on an unstructured grid is developed.

2. A new advection-diffusion (AD) suspended sediment transport module is developed for the morphodynamic model system.

3. A new bedload transport module following the SANTOSS formulae is developed for the morphodynamic model system.

4. Integration of the wave, circulation, suspended sediment and bedload transport modules into the fully coupled, three-dimensional coastal morphodynamic model system.

   By solving the sediment continuity (Exner) equation, morphology evolutions can be predicted by the present model system as a result of interactions between the hydrodynamics (waves and currents), sediment transport and the morphology itself.

5. Validation and application of the developed morphodynamic model system.

   - Firstly (see details in Chapter 4), a detailed validation of the hydrodynamic part of the developed morphodynamic model system is conducted against several applications with different spatial scales and both 2D and 3D complex hydrodynamic conditions, displaying the robustness and efficiency of the present model system.
   - Secondly (see details in Chapter 5), the developed morphodynamic model system is further applied to a laboratory mobile bed experiment, in which a detailed measurement of the hydrodynamics (water level, flow velocity and turbulent kinematic energy, etc.), sand transport processes and bed profiles are obtained with a high spatial resolution, especially around the breaker bar and near the bed. With these measurements, the performance of all the modules in the developed morphodynamic model, including the sediment transport and morphology evolution module as well as the hydrodynamic part that has been validated in Chapter 4, can be evaluated in detail, either as

a stand alone part or a whole system. Overall good agreements are obtained with the measurements in all aspects. A much more detailed conclusion has been summarized in Section 5.9.

The validations and calibrations of the model system have indicated few important findings in terms of modelling development and applications:

6. Within the hydrodynamics model, the wave-current interaction scheme, VF method, has been proven to be critical in the model's performance, which determines the two levels of momentum balance in both cross-shore and along-shore directions. The approach provides unique capability to explicitly describe the forces acting on the fluid flow from the wave oscillations. However, the α parameter for wave energy dissipation to roller and the C_1 parameter for turbulence dissipation rate are found crucial for the model accuracy, but are yet not parameterised satisfactorily due to limitation in the theory involved. The mobile bed tests clearly indicate the difficulty in the turbulence modelling based on the current approach for breaking waves. In order to achieve acceptable accuracy in both hydrodynamics and turbulence quantities, the parameter H_w and D_w have to be tuned very carefully, suggesting further investigation into the breaking wave induced turbulence and its modelling technique is clearly required.

7. Overall, the breaking waves clearly affect the hydrodynamics in both mean flow structure and the turbulence characteristics. Therefore, these additional effects have to be represented in the model properly to be able to simulate the breaking induced flows and mixing in the water column. Similarly, the mobile bed tests also suggest that the breaking simulated in the SINBAD tests enhances the turbulence level and hence the sediment suspension in the outer layer above the bed. These processes can be represented by the turbulence model with additional wave-breaking effects at the surface boundary. However, the calculation of near bed sediment pick up based on the conventional approach seems to provide sufficient sediment supply and no additional breaking effects are needed to improve the present model's prediction. The limited data from the experiment is unable to reveal whether this is due to the fact that the wave-breaking in the current case does not penetrate through the water body to reach to the bed boundary layer or due to the way the bed boundary layer process is approximated in the present model. However, it is interesting to note that based on accurate estimation of the turbulence energy level near bed surface, the sediment entrainment can also be predicted with good accuracy for breaking or non-breaking waves, which suggests an alternative to the present approach based on the shields parameter under the combined wave-current flows.

8. From the point view of modelling of total sediment transport rate, similar to the

other models in the same category, the model is capable of simulating suspended load based on wave-averaged concentration and mean flows with good accuracy. The bed load is challenging to include many different forcing factors under the varying wave forms across the beach. At different sites across the shore, different processes are playing different roles, which means the model needs to represent these processes properly to achieve good overall accuracy. Further understanding and parameterisations on intra-wave parameters (e.g. wave velocity skewness and asymmetry), grain size effects, effect of progressive surface waves, etc., are clearly needed to reduce the uncertainties in the present model.

6.2.2 On Physical Processes

Some conclusions on the physical aspects have been summarized at the end of Chapter 4 and Chapter 5. In the following, the research questions are discussed further as a supplement to those conclusions.

RQ1: How does wave breaking affect the undertow, turbulence, sediment transports and morphology evolutions?

In breaking/broken waves, the model results show that onshore mass flux contained in the roller is larger than the mass flux associated with the Stokes drift for non-breaking waves. Furthermore, the reduction in wave height results in a horizontal momentum flux gradient that drives a horizontally positive (towards the beach) time-averaged pressure gradient (set-up/set-down). The combination of mass flux increase and the positive pressure gradient leads to an increase in offshore-directed undertow velocities in the breaking region. In the presence of the breaker bar, such a process is enhanced in front of the bar and a stronger undertow can be found in the trough side of the bar.

Wave breaking leads to extra turbulence generation at the surface (the measured and predicted TKE decreases from the water surfaces downwards) and can greatly enhance TKE levels in the water column. The model results show higher values of TKE in the breaking region, especially near the surface; around the plunge point, it is almost depth-uniform over the complete water column, indicating large turbulence production at the water surface and a strong penetration into the water column down to the bed.

Breaking waves in the surf zone generate an additional sediment stirring effect, caused by the breaking-induced flows and enhanced turbulent kinetic energy in the water column. Compared with shoaling locations, much increased suspended sediment concentrations are thus found in the breaking region. The present study does not show strong effects of the wave breaking on the near bed sediment pick up, given that

the conventional approach is used without modification. However, the correlation in sediment pick up with the local generated turbulence energy can be used to estimate the sediment flux from the bed to the water column under the strong breaking scenarios.

Excluding the wave breaking induced turbulence can significantly change the cross-shore distribution of sediment concentration and transport rate , and hence the predicted bed profile. Therefore, a reasonable prediction of the hydrodynamic processes is the prerequisite to obtain reliable bed profile changes, at least for the SINBAD mobile bed experiment studied in the present research. At the same time, it is also not acceptable to detach the feedback from bed level changes on the hydrodynamics. The physical processes of hydrodynamics, sediment transport as well as the bed profile evolutions are closely related with each other; coupling between these processes is of vital importance in determining the right features of predicted results. The wave breaking to a large extend enhances such interactions and leads to much stronger interactions.

RQ2: Which processes are important in determining the dynamics of local waves, fluid flow and sediment transport under the breaking waves?

In the shoaling region, the surface waves undergo strong changes in wave form which causes considerable changes in the local flow dynamics and near bed streaming. Once wave broke, the wave height reduces drastically and a significant amount of energy is transferred into water column down below. Within the surf zone, the wave energy is dissipated continuously toward the shore. Wave rollers cause a lag in the transfer of momentum and has an important effect on the mean flow. Sensitivity analysis shows that the effect of the wave roller must be included and a cross-shore-varying value of α_r (fraction of wave energy dissipation converted to roller) is suggested.

It is found that the turbulent kinetic energy under the breaking waves has a strong influence on the undertow velocity profile. From a modelling point of view, the total contribution of wave dissipation to the momentum balance needs to be kept conservative; otherwise, no consistent model results can be obtained for the velocity and TKE profiles at the same time. Therefore, the amount of wave dissipation introduced as surface flux of TKE (i.e. $F_k = D_w \left[(1-\alpha_r)\,\epsilon^b + \epsilon^r + \epsilon^{wcap}\right]$) must be subtracted from Eq. (3.32).

The enhanced turbulence level in the water column under breaking waves increases the sediment suspension and the local concentration level considerably. The local turbulence energy within the bed boundary layer also seems dominant for the sediment pick up rate as the simulation results of the method proposed by van der Zanden et al. [77] (Section 5.5.2) show fairly good agreements with the measured suspended sediment concentration profiles. In terms of the bed load transport rate, the local wave-induced streaming, wave asymmetry, phase lag effects and bed slope are important processes to

be considered. These processes are often missing from the existing quasi-steady bedload transport formulas.

RQ3: Which transport mode, e.g. bedload and the suspended load transport, is the decisive contribution to cross-shore bar morphodynamics?

In the present study, the modelling results for the SINBAD experiment seem to suggest that the suspended load transport is more important in the contribution to the total transport at the high end of offshore slope and lee side of the breaker bar, bar trough and further onshore. At the most shoreward face of the beach, the bed load is typically the dominant transport mode in the onshore direction. Close to the bar and within the surf zone, the high turbulence induced by breaking waves causes strong sediment suspension which is particularly significant to the local sediment transport in the offshore direction in comparison with the bed load transport rate. It is found that suspended load and bedload have opposite contributions to the final principal morphology evolution characteristics of bar crest growth and bar trough deepening. For these cases simulated in the present study, even if the bedload transport is excluded from the model simulation, the principal morphology evolution characteristics still can be predicted.

However, the simulation in the present study concentrates on the SINBAD experiment only. The strong effects from the breaker bar on the waves, hydrodynamics and turbulence are particularly noted in comparison with other similar studies. The single grain size is also used in the simulation. Further investigation based on different wave-current settings and grains sizes will be helpful to confirm these results.

6.3 Suggestions for Future Work

In the present research, a novel fully coupled, unstructured grid, three-dimensional coastal morphodynamic model system is developed; its performance on the hydrodynamics, sediment transport and morphology evolution is also well demonstrated, with good agreement with the measurements. However, the developed model system is only applied to a laboratory experiment, therefore applications to a wider range of scenarios and further model developments are anticipated. Furthermore, some processes involved in coastal sand transport and associated morphodynamics are still not clear and need to be studied in detail. Suggestions for future work are therefore outlined in this section.

- Further apply the developed morphodynamic model system in field applications.

  The developed model system is applied to and entirely validated by only one

laboratory experiment (i.e. the SINBAD mobile bed experiment). Therefore it apparently needs to be further applied to more test cases, especially the field applications that have more practical objectives.

- Better prediction of turbulence.

  The accurate prediction of TKE in the surf zone is still a challenge for the commonly used turbulence closure models (e.g. the modeled TKE is still over-predicted near the water surface in the present research); many efforts are thus in need to improve the model performance. This is very likely a result of an inconsistency between the reality and assumption used in the turbulent closure model (see details in Section 5.4.4), a further study on this aspect is thus in need. Furthermore, detailed measurements in laboratory controlled conditions in both flow hydrodynamics and turbulence characteristics, as well as free surface variations are required to develop and verify a turbulence scheme's suitability in modelling wave breaking. Such comprehensive datasets are still scarce in the literature.

- Development of improved practical bedload transport formulae, especially those calibrated with measurements in breaking wave conditions.

  Although the model results of the semi-unsteady bedload transport formulae SANTOSS show much better agreements than those of two quasi-steady models in the present research, there are still some discrepancies in the detailed magnitude. Including the extra bedload resulted from the breaking wave induced turbulence improved the model results, however, this method need to be further calibrated.

- Development of better parameterization methods for the intra-wave velocity parameters.

  The actual performance of the analytical expression of Abreu et al. [177] and the parametrization method of Ruessink et al. [178], that used to predict the intra-wave velocity parameters, are examined in this research. The predicted peak crest and trough velocities agree reasonable well with the measurements. However, the near-bed wave orbital velocity skewness and asymmetry are poorly calculated. A accurate prediction of the bedload transport need a reasonable well parameterization of those intra-wave parameters, therefore a further study on predicting the intra-wave velocity parameters is thus advised.

- Better description of the bed boundary layer process.

  The current knowledge and understanding of the bed boundary layer processes is still limited. But this is critical to the representation of bed load transport accurately. Further studies into the effects of wave-induced hydrodynamics, turbulence dissipation and fluid flow-particle interactions are clearly needed. New

measurement with higher spatial and temporal resolution are also required to obtain improved data and better insight into different sediment flux components in this region.

- Better description of the surface wave roller.

  As suggested by Uchiyama et al. [23], α_r provides some flexibility to depict different beach forms and wave breaking types (i.e. spilling, plunging, surging). Sensitivity analysis suggests a cross-shore-varying of α_r should be adopted, which indicates that the dynamics behind the wave roller are still not fully understood.

- Complete the model system by accounting for more physical processes.

  The present morphodynamic model system only solves the (non-cohesive) sand transport processes; the cohesive sediment (e.g. mud) transport has very different physical characteristics, some extra physical processes (e.g. hindered settling, flocculation, etc.) need to be accounted for in the model. In addition, temperature and salinity structure and biological system can also affect the sediment transport, therefore they need to be further studied and accounted for in the model.

Appendix A

A Parallel, Computation Economical Unstructured Wave Model

As indicated in Section 3.2.1, advantages in coupling the third-generation wave model UnSWAN into FVCOM are apparent. However, there are also some potential shortages for this kind of implementations at the same time, e.g. it would be very time-consuming to apply these models in some relatively simple applications, because UnSWAN include more physical aspects explicitly, such as the three and four wave-wave interactions. Besides, UnSWAN solves an action balance equation where the action density spectrum is a function of five independent variables, wave propagation angle θ, frequency σ, and horizontal space coordinates X, Y and time t, while the circulation model only has four independent variables. All of these aspects mean the third-generation wave models need large amount of computation time. As a result, when compared with the circulation models, two orders of increase in the computation time for the coupled wave-current model should be expected, e.g. Mellor et al. [64] indicated that 86 times of computer run time are required by the SWAN wave model compare to the POM circulation model, under the same horizontal grid and length of run.

Therefore, a computation economical wave model (hereinafter wave model A) is developed in this section. This model is only regarded as a supplement to the UnSWAN model, because it constrains to a specific spectral shape (see the following description) which can not always conform to the measure spectra, thus it would lost accuracy in the prediction of integral wave properties under some circumstances; while the UnSWAN model can extend the established fully-coupled model system into the application sites where the wave model A fails to give satisfy results. Anyway, the finally established fully-coupled model system includes two different wave models after the present procedure. One of these two wave models could be selected to couple with the FVCOM model in

a specific case based on the specific situation applied, in order to take the maximum advantages that one wave model could supply and get a good balance between getting better wave model performance and reducing computation time. For its specific design and better performance in shallow water, the UnSWAN wave model is chosen to be utilized in the following application cases in this research.

A.1 Theory sketch

In this section, a computation economical, structured grid surface wave model is firstly introduced and then converted into an unstructured-grid finite-volume parallel version for use in coastal ocean regions with complex irregular geometry, which is fully compatible with the framework of Finite-Volume Coastal Ocean Model (FVCOM).

This model is previously developed by Mellor et al. [64], in which the main dependent variables are angle-dependent wave energy and frequency. The energy distribution in frequency space is parameterized using the spectrum proposed by Donelan et al. [213], which contains elements of the JONSWAP spectrum. Thus there are only four independent variables, x, y, t and θ, in this model and it doesn't need to deal with wave-wave interactions, all of which contribute to a considerable reduce in the computational effort compared to the common third-generation wave models. While, of course, distribute the wave energy in the frequency space with a specific spectral shape will affect the accuracy of the predicted wave properties. However, according to Mellor et al. [64], this model could give comparable results to the SWAN model and could fully couple the effects of depth-dependent currents on waves which are not feasible in SWAN.

The equation of directional dependent wave energy is

$$\frac{\partial E_\theta}{\partial t}+\frac{\partial}{\partial x_\alpha}\left[\left(\overline{C_{g\alpha}}+\overline{U_{A\alpha}}\right)E_\theta\right]+\frac{\partial}{\partial\theta}\left(\overline{C_\theta}E_\theta\right)+\int_{-1}^{0}\overline{S_{\alpha\beta}}\frac{\partial U_\alpha}{\partial x_\beta}D\,d\zeta=S_{\theta in}-S_{\theta Sdis}-S_{\theta Bdis} \tag{A.1}$$

where x_α denote horizontal coordinates with $x_\alpha=(x,y)$; the over bar represents spectral averages (see the following detailed equations); $E_\theta=\int_0^\infty E_{\sigma,\theta}(x,y,t,\sigma,\theta)\,d\sigma$ is the directional kinematic energy; θ is the wave propagation direction relative to the east-ward direction, σ is the intrinsic frequency; C_g, C_θ represent group velocity and refraction speed respectively, and the C_θ is defined as

$$C_\theta=\frac{g}{2c\ cosh^2kD}\left(sin\theta\frac{\partial D}{\partial x}-cos\theta\frac{\partial D}{\partial y}\right)+\frac{k_\alpha}{k}\left(sin\theta\frac{\partial U_{A\alpha}}{\partial x}-cos\theta\frac{\partial U_{A\alpha}}{\partial y}\right) \tag{A.2}$$

where $U_{A\alpha}$ is the Doppler (or advective) velocity, express as

$$U_{A\alpha} = kD \int_{-1}^{0} U_\alpha \left[\frac{1}{2}(F_{cs}F_{cc} + F_{ss}F_{sc}) + F_{cs}F_{ss} \right] \, d\zeta \tag{A.3}$$

and $S_{\alpha\beta}$ is the wave radiation stress, which could be calculated with the following expression:

$$S_{\alpha\beta} = kE \left(\frac{k_\alpha k_\beta}{k^2} F_{cs}F_{cc} - \delta_{\alpha\beta}F_{sc}F_{ss} \right) + \delta_{\alpha\beta}E_D \tag{A.4}$$

in which F_{cs}, F_{cc}, F_{sc}, F_{ss} are depth-dependent functions:

$$\begin{aligned} F_{cs} &= \frac{coshkD(1+\zeta)}{sinhkD} \\ F_{cc} &= \frac{coshkD(1+\zeta)}{coshkD} \\ F_{sc} &= \frac{sinhkD(1+\zeta)}{coshkD} \\ F_{ss} &= \frac{sinhkD(1+\zeta)}{sinhkD} \end{aligned} \tag{A.5}$$

and the E_D is a modified delta function, defined as $E_D = 0$ if $\zeta \neq 0$ and $\int_{-1}^{0} E_D D d\zeta = E/2$.

In the left hand of the Eq. (A.1), the first two terms represent the wave energy propagation in time and horizontal space, whereas the third term denotes the change of wave energy propagation direction. The fourth term accounts for the current effects on wave energy, its explicit form is

$$\begin{aligned} &\int_{-1}^{0} \overline{S_{\alpha\beta}} \frac{\partial U_\alpha}{\partial x_\beta} D \, d\zeta = k_p E_\theta D \\ &\left[cos^2\theta \int_{-1}^{0} \frac{\partial U}{\partial x} F_1 d\zeta - \int_{-1}^{0} \frac{\partial U}{\partial x} F_2 d\zeta + cos\theta sin\theta \int_{-1}^{0} \left(\frac{\partial U}{\partial y} + \frac{\partial V}{\partial x} \right) F_1 d\zeta \right. \\ &\left. + sin^2\theta \int_{-1}^{0} \frac{\partial V}{\partial y} F_1 d\zeta - \int_{-1}^{0} \frac{\partial V}{\partial y} F_2 d\zeta \right] + \left(\frac{\partial U}{\partial y} + \frac{\partial V}{\partial x} \right) \frac{E_\theta}{2} \end{aligned} \tag{A.6}$$

in which k_p is the wave number where frequency is peak frequency. The three terms on the right hand of the Eq. (A.1), $S_{\theta in}$, $S_{\theta Sdis}$, and $S_{\theta Bdis}$ are the wind input term, wave dissipation terms due to wave processes at the surface and bottom respectively.

The spectrally averaged terms in Eq. (A.1) are defined in the following equations. For a detailed description on how these formulations are derived, one can refer into Mellor et al. [64].

$$\begin{aligned}
&\frac{\overline{C_g}}{C} = \frac{\int_0^\infty (C_g/C) E_{\sigma,\theta} d\sigma}{\int_0^\infty E_{\sigma,\theta} d\sigma} \\
&\overline{C_\theta} = \frac{g F_{c\theta}}{2c\ cosh^2 kD} \left(sin_\theta \frac{\partial D}{\partial x} - cos_\theta \frac{\partial D}{\partial y} \right) + \frac{k_\alpha}{k} \left(sin_\theta \frac{\partial \overline{U_{A\alpha}}}{\partial x} - cos_\theta \frac{\partial \overline{U_{A\alpha}}}{\partial y} \right) \\
&\overline{U_{A\alpha}} = \int_{-1}^{0} U_\alpha F_3 d\sigma \\
&\overline{S_{\alpha\beta}} = k_p E_\theta \left(\frac{k_\alpha k_\beta}{k^2} F_1 - \delta_{\alpha\beta} F_2 \right) + \delta_{\alpha\beta} E_{D\theta}
\end{aligned} \tag{A.7}$$

The relevant temporarily defined function in Eq. (A.7) are given as:

$$\begin{aligned}
&F_{c\theta}(k_p D) = E_T^{-1} \int_0 \infty E_\sigma \frac{c_[theta}{c_p} \left(\frac{cosh\ k_p D}{cosh\ kD} \right)^2 d\sigma \\
&F_1(k_p D, \zeta) = E_T^{-1} \int_0 \infty E_\sigma (k/k_p) F_{cs} F_{cc} d\sigma \\
&F_2 = E_T^{-1} \int_0 \infty E_\sigma (k/k_p) F_{sc} F_{ss} d\sigma \\
&F_3 = E_T^{-1} \int_0 \infty E_\sigma kD \left[\frac{1}{2} (F_{cs} F_{cc} + F_{ss} F_{sc}) + F_{cs} F_{ss} \right] d\sigma \\
&E_T = \int_{-\pi} \pi E_\theta d\theta \\
&E_{D\theta} = 0 \text{ if } \zeta \neq 0 \text{ and } \int_{-1}^{0} E_{D\theta} D d\zeta = E_\theta / 2.
\end{aligned} \tag{A.8}$$

Besides the above wave energy equation, the frequency is also a function of prop-

agation direction and horizontal space and time, which is solved with the following equation.

$$\frac{\partial \sigma_\theta}{\partial t} + \left(\overline{C_{g\alpha}} + \overline{U_{A\alpha}}\right) \frac{\partial \sigma_\theta}{\partial x_\alpha} = - \frac{\partial \sigma_\theta}{\partial k} \left(\frac{k_\alpha k_\beta}{k} \frac{\partial \overline{U_{A\alpha}}}{\partial x_\alpha} \right) + \frac{\partial \sigma_\theta}{\partial D} \left(\frac{\partial D}{\partial t} + \overline{U_{A\alpha}} \frac{\partial D}{\partial x_\alpha} \right) + \sigma_p (\sigma_p - \sigma_\theta) \sqrt{f_{spr}} \tag{A.9}$$

where $\partial \sigma_\theta / \partial k = \overline{C_g}$, $\partial \sigma_\theta / \partial D = (\sigma_\theta / D)(n - 1/2)$, $f_{spr} = S_{\theta in} / \int_{-\pi/2}^{\pi/2} S_{\theta in} d\theta$ and $n = 1/2 + kD/sinh2kD$. In regions of θ that are wind driven ($f_{spr} > 0$), the last term in the equation has the effect of nudging σ_θ toward θ_p. θ_p is provided by

$$\frac{U_{10} \sigma_p}{g} = \left(\frac{0.0022 \; U_{10}^4}{g E_{TW}} \right)^{0.303} \tag{A.10}$$

where E_{TW} is defined as the integral of the portion of E_θ that is wind driven. For the wind driven portion of E_θ, σ_p will be determined as a function of E_{TW} and U_{10} by Eq. (A.10); for other portions of E_θ or for light or no winds, frequency is determined by Eq. (A.9).

A.2 Discretization approach

In order to couple this wave model into the FVCOM circulation model, the wave energy equation (Eq. (A.7)) is firstly split into three equations, following the discrete approach proposed by Hsu et al. [103].

$$\frac{\partial E_\theta}{\partial t} + \frac{\partial}{\partial x_\alpha} \left[\left(\overline{C_{g\alpha}} + \overline{U_{A\alpha}} \right) E_\theta \right] = 0 \tag{A.11}$$

$$\frac{\partial E_\theta}{\partial t} + \frac{\partial}{\partial \theta} \left(\overline{C_\theta} E_\theta \right) = 0 \tag{A.12}$$

$$\frac{\partial E_\theta}{\partial t} = S_{\theta in} - S_{\theta Sdis} - S_{\theta Bdis} - \int_{-1}^{0} \overline{S_{\alpha\beta}} \frac{\partial U_\alpha}{\partial x_\beta} D \; d\zeta \tag{A.13}$$

The first equation (Eq. (A.11)) describes the wave energy propagation in the horizontal space, and is solved by a second-order accuracy explicit finite-volume upwind

advection scheme, same with the method for solving horizontal advection terms used in FVCOM. The second equation (Eq. (A.12)) is solved numerically by using the Multi-dimensional Positive Definite Advection Transport Algorithm (MPDATA) proposed by Smolarkiewicz [214] with or without the Flux Corrected Transport (FCT) term, which is used in FVCOM as an optional numerical approach for resolving the vertical advection terms. This approach provides an optimal control of an artificial numerical error by adding an anti-diffusion term used to reduce the diffusion incurred by a pure upwind differencing. Here, a detailed description of the explicit finite-volume method is given, while, for the other numerical method, please refer to the research papers given above.

In this model system, the horizontal mesh is composed of non-overlapping, unstructured triangular grids, which include three nodes, a centroid and three sides (Figure A.1). The wave energy E_θ and frequency σ_θ, same with the other scalar variables in the FVCOM model, are placed at the nodes of the mesh. And these variables are calculated via a net flux through the so-called TCEs (the dark shaded area Ω in Figure A.1; see also its definition in Section 2.5).

Rewrite the Eq. (A.11) into a flux-conservative form,

$$\frac{E_\theta^{n+1} - E_\theta^n}{\Delta t} + \nabla_\perp \cdot \left(\vec{C} E_\theta\right) = 0 \tag{A.14}$$

where $\vec{C} = \overrightarrow{C_g} + \overrightarrow{U_A}$.

Integrate this equation on a given area of TCE and time, yields

$$\int_{\Delta t}\int_{\Delta S} \left\{ \frac{E_\theta^{n+1} - E_\theta^n}{\Delta t} + \nabla_\perp \cdot \left(\vec{C} E_\theta\right) \right\} dS dt = 0 \tag{A.15}$$

i.e.

$$\begin{aligned} E_\theta^{n+1} &= E_\theta^n - \frac{\Delta t}{\Omega} \iint_\Omega \nabla_\perp \cdot \left(\vec{C} E_\theta\right) d\Omega \\ &= E_\theta^n - \frac{\Delta t}{\Omega} \oint_l C_n E_{\theta l} dl \\ &= E_\theta^n - \frac{\Delta t}{\Omega} \sum_{i=1}^{l_{\Omega,n}} (C_{n,i}\ E_{\theta l_{\Omega},i}\ \Delta l_{\Omega,i}) \end{aligned} \tag{A.16}$$

where $l_{\Omega,i}(i = 1, l_n)$ is the perimeter of Ω and l_n is the number of edges of Ω; $C_{n,i}$ is the component of $\vec{C} = \overrightarrow{C_g} + \overrightarrow{U_A}$ normal to $l_{\Omega,i}$ at the middle point of edge $l_{\Omega,i}$ (more specifically, the blue node in the Figure A.1).

Using the second-order approximated upwind scheme (for sake of simplicity, the subscripts θ is omitted in the following equations),

$$E_l = \begin{cases} E_{lA} & , \text{ if } C_n > 0 \\ E_{lB} & , \text{ if } C_n < 0 \end{cases} \tag{A.17}$$

where

$$\begin{aligned} E_{lA} &= E_A + \nabla E_A \cdot \boldsymbol{\Delta r_A} \\ E_{lB} &= E_B + \nabla E_B \cdot \boldsymbol{\Delta r_B} \end{aligned} \tag{A.18}$$

Integrating the Eq. (A.18) in the areas of Ω_A (Figure A.1),

$$\begin{aligned} E_{lA} &= E_A + \frac{\boldsymbol{\Delta r_A}}{\Omega_A} \iint_{\Omega_A} \nabla E_A \, \mathrm{d}\Omega_A \\ &= E_A + \frac{\boldsymbol{\Delta r_A}}{\Omega_A} \iint_{\Omega_A} \left(\frac{\partial E_A}{\partial x} \ , \ \frac{\partial E_A}{\partial y} \right) \mathrm{d}\Omega_A \\ &= E_A + \frac{\boldsymbol{\Delta r_A}}{\Omega_A} \left(\oint_{l_{\Omega_A}} E_{l_{\Omega_A}} \, \mathrm{d}y_{l_{\Omega_A}} \ , \ \oint_{l_{\Omega_A}} -E_{l_{\Omega_A}} \, \mathrm{d}x_{l_{\Omega_A}} \right) \\ &= E_A + \frac{\boldsymbol{\Delta r_A}}{\Omega_A} \left(\sum_{j=1}^{l_{\Omega_A,n}} [E_{l_{\Omega_A},j} \ \Delta x_{\Omega_A,j}] \ , \ \sum_{j=1}^{l_{\Omega_A,n}} [-E_{l_{\Omega_A},j} \ \Delta y_{\Omega_A,j}] \right) \end{aligned} \tag{A.19}$$

Similarly,

$$\begin{aligned} E_{lB} &= E_B + \frac{\boldsymbol{\Delta r_B}}{\Omega_B} \iint_{\Omega_B} \nabla E_B \, \mathrm{d}\Omega_B \\ &= E_B + \frac{\boldsymbol{\Delta r_B}}{\Omega_B} \iint_{\Omega_B} \left(\frac{\partial E_B}{\partial x} \ , \ \frac{\partial E_B}{\partial y} \right) \mathrm{d}\Omega_B \\ &= E_B + \frac{\boldsymbol{\Delta r_B}}{\Omega_B} \left(\oint_{l_{\Omega_B}} E_{l_{\Omega_B}} \, \mathrm{d}y_{l_{\Omega_A}} \ , \ \oint_{l_{\Omega_B}} -E_{l_{\Omega_B}} \, \mathrm{d}x_{l_{\Omega_A}} \right) \\ &= E_B + \frac{\boldsymbol{\Delta r_B}}{\Omega_B} \left(\sum_{j=1}^{l_{\Omega_B,n}} [E_{l_{\Omega_B},j} \ \Delta x_{\Omega_B,j}] \ , \ \sum_{j=1}^{l_{\Omega_B,n}} [-E_{l_{\Omega_B},j} \ \Delta y_{\Omega_B,j}] \right) \end{aligned} \tag{A.20}$$

In the above equations, the E_A and E_B are the wave energy at nodes A and B, Ω_A and Ω_B are the shaded areas in Figure A.1 with the node A and node B in the central, $l_{\Omega_A,j}(j = 1, l_{\Omega_A,n})$ and $l_{\Omega_B,j}(j = 1, l_{\Omega_B,n})$ are the perimeters of Ω_A and Ω_B; $l_{\Omega_A,n}$ and $l_{\Omega_B,n}$ are the number of edges of Ω_A and Ω_B; and $\boldsymbol{\Delta r_A}$ and $\boldsymbol{\Delta r_B}$ are the distance verctors from node A and node B to the blue point in Figure A.1.

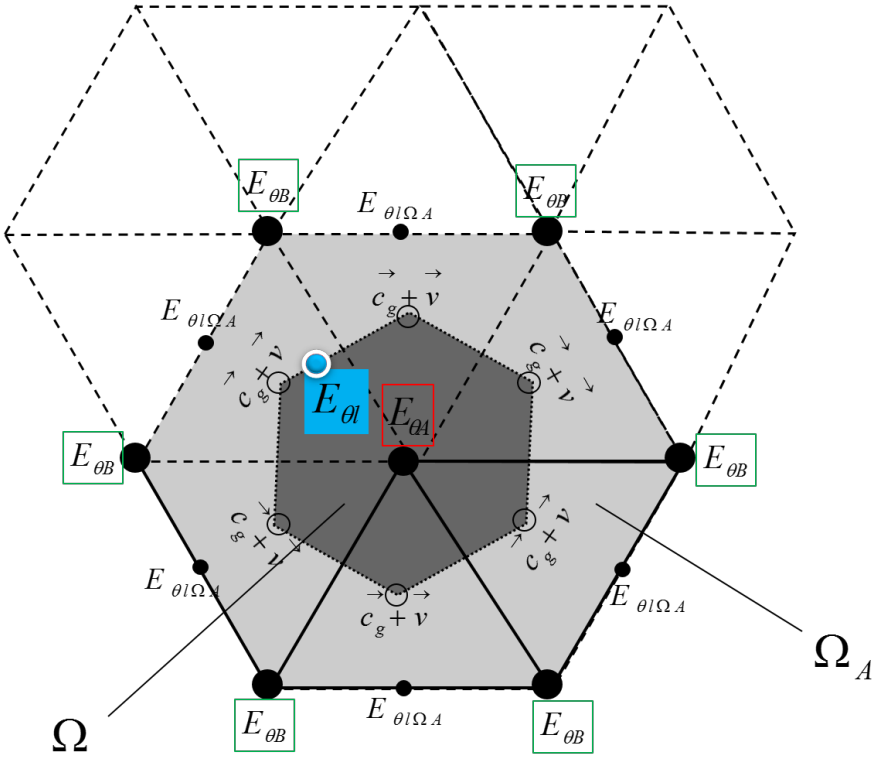

Figure A.1: Schematic of the model horizontal unstructured grid

In Figure A.2, a grid stencil for the direction space is proposed. The range of the wave angle is $-\pi$ to π, different from that of the SWAN model, 0 to 2π. And a cyclic boundary condition is used to connect the branch cut at $-\pi$ to π.

Apart from the above discretization schemes, several open boundary conditions (OBC) are also designed for the wave energy and frequency of this wave model. For example, the clamped boundary condition, in which the wave properties (wave energy or wave height, wave direction, wave period and peak wave frequency) in the open boundary is specified by the user via the external files or control parameters; the no-gradient boundary condition, in which the wave properties are specified as the same value at the interior nodes. These interior nodes should satisfy certain requirements: connected to the open boundary nodes and the line links an interior node and its corresponding open boundary node should be perpendicular to the open boundary. Specially, in some ideal applications, the cyclic boundary condition may need, thus, a cyclic open boundary condition is also developed for the unstructured-gird finite-volume approach in this wave model.

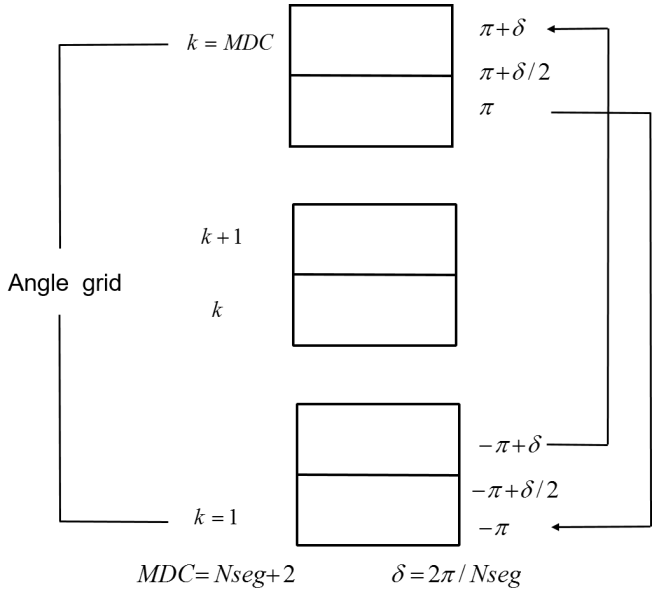

Figure A.2: Schematic of the angle grid and the cyclic boundary conditions

A.3 Parallelization

Nowadays, most of the practical applications needs large amount of computation time and resources. So whether a numerical model possesses the ability of running in large parallel high-performance clusters has been a very significant standard on whether this model could be used widely or not. In order to make full use of the multiple processors of high-performance computers and at the same time reduce the computation time, this wave model code is parallelized using the Single Processor Multiple Data (SPMD) approach, and using the Massage Passing Interface (MPI) to define the inter-processor communications. As shown in the Figure A.3, the computation domain is firstly decomposed into N equal subdomains by using the METIS graph partitioning library, where N is the number of processors. Because there are some variables located in the center nodes of the triangles in FVCOM, this decomposition is not based on the vertices of the triangles but triangle-sized cells, i.e. the triangle-sized cells are not duplicated in different computer processors, while some vertexes are shared with two adjacent processors. This should be an intrinsic characteristic unique to the FVCOM model framework.

After the global domain is decomposed, each processor would have been assigned a unique subdomain in which to set up integrations. However, at the computation stage, before the next time step, the data on the interior boundaries of the adjacent subdomains must be exchanged to preserve the correctness of the flux. In order to facilitate this kind of information exchange, the interior nodes of neighboring processors along the

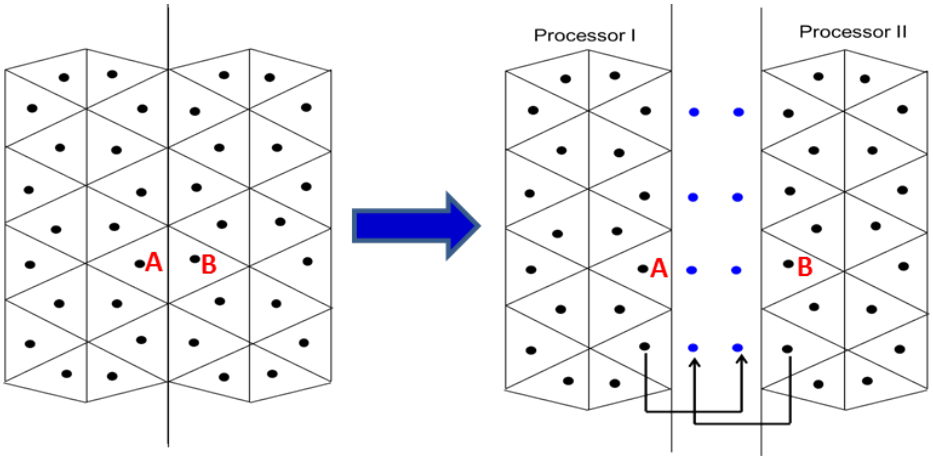

Figure A.3: A schematic diagram of the cell-centered portioning approach.

interprocessor boundaries are mapped to the corresponding halo nodes of the exchange partners and vice-versa. So the variables in one sub-domain include the information computed by its adjacent domains on other processors. For example, the computation of flux of cell A in the processor I, one of whose edges residing on the interprocessor boundaries, would require the information from the cell B. Located and computed in the sub-domain of processor II, the cell B are then regarded as the halo cells of the processor I. By using the standard MPI (Message Passing Interface) library, the information on halo nodes and cells could be provided by interprocessor communication. In Figure A.3, the blue nodes are the so-called halo nodes which are used to exchange information from another adjacent processors. At the asked time of outputting computation results, before proceeding with later integration, the residing data in the local subdomains are collected to an aggregate array, residing in the master processor, corresponding to the global node/element numbering defined by the grid input file and then be written to the external file.

Appendix B

Wave skewness and asymmetry

B.1 Analytical expression of wave orbital velocity

The analytical formulation of Abreu et al.[177] that reproduces the near-bed wave orbital velocity is as follows:

$$u_w(t) = u_{orb}^w \sqrt{1-r^2} \frac{\left[\sin(\omega t) + \frac{r\sin\phi}{1+\sqrt{1-r^2}}\right]}{1 - r\cos(\omega t + \phi)} \tag{B.1}$$

u_{orb}^w is the orbital velocity amplitude, $w(= 2\pi/T_p)$ is the angular angular frequency, ϕ is the waveform parameter ($-\pi \leq \phi \leq 0$) and r is the parameter of skewness ($-1 < r \leq 1$). The corresponding acceleration time series is given by:

$$a(t) = \omega u_{orb}^w \sqrt{1-r^2} \frac{\left[\cos(\omega t) - r\cos\phi - \frac{r^2}{1+\sqrt{1-r^2}}\sin\phi\sin(\omega t + \phi)\right]}{\left[1 - r\cos(\omega t + \phi)\right]^2} \tag{B.2}$$

B.2 Parameterizations for the parameter of waveform (ϕ) and skewness (r)

In order to utilize the analytical expression of Abreu et al. [177] to estimate the near-bed wave orbital velocities, Ruessink et al.[178] proposed a parameterization method for calculating the parameter of waveform (ϕ) and skewness (r). This parameterization method could be separated into three steps:

Firstly, the Ursell number is calculated as a function of wave height (H_s), wave period (T_p) and water depth (h) with the following equation:

$$U_r = \frac{3}{8}\frac{H_s k}{(kd)^3} \tag{B.3}$$

Based on the analysis of a large group of measured filed data, Ruessink et al. [178] then suggested a fitting curve for the total non-linearity parameter B and the phase ψ, in the form of a Boltzman sigmuoid function and a tanh-function respectively, as the following:

$$B = p1 + \frac{p2}{1 + exp\left(\frac{p3 - logU_r}{p4}\right)} \tag{B.4}$$

$$\psi = -90^\circ - 90^\circ \tanh(\frac{p5}{U_r^{p6}}) \tag{B.5}$$

in which $p1 - p6$ are six calibration parameters with advised values of $p1 = 0.0$, $p2 = 0.857$, $p3 = -0.471$, $p4 = 0.297$, $p5 = 0.815$ and $p6 = 0.672$.

In the third step, the parameter of skewness (r) is determined via its relation to the parameter B as

$$\begin{aligned} B &= \frac{3b}{\sqrt{2(1-b^2)}} \\ b &= \frac{r}{1+\sqrt{1-r^2}} \end{aligned} \tag{B.6}$$

and the parameter of waveform (ϕ) is determined via its relation to the parameter ψ as

$$\phi = -\psi - \frac{\pi}{2} \tag{B.7}$$

Via the Eqs. (B.3) - (B.7), the parameter of waveform (ϕ) and skewness (r) used in the analytical expression of Abreu et al. [177] can be determined from the wave parameters of H_s, T_p and water depth (h). However, it is also noted that it is difficult to obtain the parameter r form a known parameter B from the Eq. (B.6). Veen [179] thus proposed a simple fitting curve as

$$r = 0.0517B^3 - 0.4095B^2 + 1.0853B - 0.0099 \tag{B.8}$$

The wave orbital velocity skewness ($Sk(u_w)$) and velocity asymmetry ($Asy(u_w)$) are two common used parameters to measure the skewness and asymmetry of the wave

motion. They can be calculated from the wave orbital velocity time series via following formulas:

$$Sk(u_w) = \frac{\overline{(u_w)^3}}{\sigma_{u_w}^3} \tag{B.9}$$

$$Asy(u_w) = \frac{\overline{\hbar(u_w)^3}}{\sigma_{u_w}^3} \tag{B.10}$$

where σ_{u_w} is the standard deviation of orbital velocity u_w, $\hbar(u_w)$ is the Hilbert transform of u_w.

The relations of $Sk(u_w)$, $Asy(u_w)$ and parameters of B and ψ are given as:

$$\begin{aligned} Sk(u_w) &= B\cos\psi \\ Asy(u_w) &= B\sin\psi \end{aligned} \tag{B.11}$$

Appendix C

Adaption of the SANTOSS model in the current dominated flow

In the original version of SANTOSS model (van der A et al.[78], Veen [179], Schnitzler [59]), the duration of the crest half-cycle (i.e. crest period, T_c) is determined as the part of wave period (T) with the positive velocity, and the duration of the trough half-cycle (i.e. trough period, T_t) is determined as the part of wave period (T) with the negative velocity. In the absent of current, the velocity used to determine the crest/trough periods is the wave orbital velocity ($\vec{u}_w(t)$ in Eq.(3.104)); while in the present of current, the velocity is the combined wave and current velocity ($\vec{u}(t)$ in Eq.(3.104)).

In the current dominated situations, especially when the magnitude of the current is close to or exceeds the absolute value of the maximum (minimum) wave orbital velocity, the wave and current combined velocity $\vec{u}_w(t)$ could be positive or negative during the whole wave period (T). In these cases, the crest period (T_c) or the trough period (T_t) is equal to zero according to the definition. Some adaption thus are adopted by Veen [179] and Schnitzler [59] to seek realistic predictions, e.g. adaption of the codes to prevent the situations of dividing by zeros, adaption of the codes to get a smooth transition from the normal cases to the cases with only a crest (or trough) period. The details are showed in this section for the sake of completeness.

The first adaption aims for keeping the direction of the representative velocity at each half-cycle same with its respective half cycle, i.e. to ensure the representative velocity at the crest half cycle is positive while at the trough half cycle is negative. Take the a simple situation in crest half cycle for example: when $(\tilde{u}_{c,r} + |u_\delta|cos\varphi) < 0 < (\hat{u}_c + |u_\delta|cos\varphi)$, according to the above definition for crest period, $T_c > 0$; however, as the representative velocity $(\tilde{u}_{c,r} + |u_\delta|cos\varphi) < 0$, the transport in this crest period is in the opposite direction of the wave crest direction, which is wrong apparently. Therefore, the representative combined wave-current velocity vectors for each half cycle

are changed from the Eqs. (3.113) and (3.114) to the following:

$$\vec{u}_{c,r} = \{u_{c,rx}, u_{c,ry}\} = \begin{cases} \{\ \tilde{u}_{c,r} + |u_\delta| cos\varphi, |u_\delta| sin\varphi\} & \text{, if } \tilde{u}_{c,r} + |u_\delta| cos\varphi > 0 \\ \{\ 0.001, |u_\delta| sin\varphi\} & \text{, if } \tilde{u}_{c,r} + |u_\delta| cos\varphi \leq 0 \end{cases} \tag{C.1}$$

$$\vec{u}_{t,r} = \{u_{t,rx}, u_{t,ry}\} = \begin{cases} \{-\tilde{u}_{t,r} + |u_\delta| cos\varphi, |u_\delta| sin\varphi\} & \text{, if } -\tilde{u}_{t,r} + |u_\delta| cos\varphi < 0 \\ \{-0.001, |u_\delta| sin\varphi\} & \text{, if } -\tilde{u}_{t,r} + |u_\delta| cos\varphi \geq 0 \end{cases} \tag{C.2}$$

For the cases where the crest period is very small, the sand entrained in the crest period (ω_c) is then transported in the trough period ($\omega_c t$). And when the crest period equal to zero, all the sediment is then transported only in the trough period. This is adapted by changing the Eqs. (3.80) as follows:

$$\Omega_{ct} = \begin{cases} 0 & \text{, if } P_c \leq 1 \text{ and } T_c > 0.001 \\ (1 - \frac{1}{P_c})\Omega_c & \text{, if } P_c > 1 \text{ and } T_c > 0.001 \\ \Omega_c & \text{, if } T_c \leq 0.001 \end{cases} \tag{C.3}$$

Similarly, the Eqs. (3.82) is changed into the following:

$$\Omega_{tc} = \begin{cases} 0 & \text{, if } P_t \leq 1 \text{ and } T_t > 0.001 \\ (1 - \frac{1}{P_t})\Omega_t & \text{, if } P_t > 1 \text{ and } T_t > 0.001 \\ \Omega_t & \text{, if } T_t \leq 0.001 \end{cases} \tag{C.4}$$

The non-dimensional transport rate is then changed for the cases with crest or trough periods equal to zero. Under these circumstances the non-dimensional transport rate in the trough (crest) period depends only on the sand entrained and transported during the trough (crest) period and the dimensionless transport in the crest (trough) period is zero. Thus

$$\overrightarrow{\Phi}_c = \frac{\overrightarrow{\theta_c}}{\sqrt{\theta_c}} \left(\Omega_{cc} + \frac{T_c}{2T_{cu}} \Omega_{tc} \right) \tag{C.5}$$

is replaced by

$$\overrightarrow{\Phi}_c = \begin{cases} \frac{\overrightarrow{\theta_c}}{\sqrt{\theta_c}} \left(\Omega_{cc} + \frac{T_c}{2T_{cu}} \Omega_{tc} \right) & \text{, if } T_c > 0 \text{ and } T_t > 0 \\ \frac{\overrightarrow{\theta_c}}{\sqrt{\theta_c}} \left(\Omega_{cc} \right) & \text{, if } T_c > 0 \text{ and } T_t \leq 0 \\ 0.0 & \text{, if } T_c \leq 0 \text{ and } T_t > 0 \end{cases} \tag{C.6}$$

and

$$\overrightarrow{\Phi}_t = \frac{\overrightarrow{\theta_t}}{\sqrt{\theta_t}} \left(\Omega_{tt} + \frac{T_t}{2T_{tu}} \Omega_{ct} \right) \tag{C.7}$$

is replaced by

$$\overrightarrow{\Phi}_t = \begin{cases} \frac{\overrightarrow{\theta_t}}{\sqrt{\theta_t}} \left(\Omega_{tt} + \frac{T_t}{2T_{tu}} \Omega_{ct} \right) & \text{, if } T_c > 0 \text{ and } T_t > 0 \\ \frac{\overrightarrow{\theta_t}}{\sqrt{\theta_t}} \left(\Omega_{tt} \right) & \text{, if } T_c \leq 0 \text{ and } T_t > 0 \\ 0.0 & \text{, if } T_c > 0 \text{ and } T_t \leq 0 \end{cases} \tag{C.8}$$

When strong currents are present, the combined wave-current velocity could be only positive or negative during the whole wave period, the zero crossings ($t_{0_{pn}}$ and $t_{0_{np}}$) are thus not present and the durations defined by the Eqs.3.118 - 3.123 are not appropriate any more. Therefore, the following definitions are used as supplement definitions when strong currents are present.

$$T_c = \begin{cases} T & \text{, if } (|u_\delta| cos\varphi - \hat{u}_t) > 0 \\ 0 & \text{, if } (|u_\delta| cos\varphi + \hat{u}_c) < 0 \end{cases} \tag{C.9}$$

$$T_{cd} = \begin{cases} t_{u_{min}} - t_{u_{max}} & \text{, if } (|u_\delta| cos\varphi - \hat{u}_t) > 0 \\ 0 & \text{, if } (|u_\delta| cos\varphi + \hat{u}_c) < 0 \end{cases} \tag{C.10}$$

$$T_{cu} = \begin{cases} T_c - T_{cd} & \text{, if } (|u_\delta| cos\varphi - \hat{u}_t) > 0 \\ 0 & \text{, if } (|u_\delta| cos\varphi + \hat{u}_c) < 0 \end{cases} \tag{C.11}$$

$$T_t = \begin{cases} 0 & \text{, if } (|u_\delta| cos\varphi - \hat{u}_t) > 0 \\ T & \text{, if } (|u_\delta| cos\varphi + \hat{u}_c) < 0 \end{cases} \tag{C.12}$$

$$T_{td} = \begin{cases} 0 & \text{, if } (|u_\delta| cos\varphi - \hat{u}_t) > 0 \\ t_{u_{min}} - t_{u_{max}} & \text{, if } (|u_\delta| cos\varphi + \hat{u}_c) < 0 \end{cases} \tag{C.13}$$

$$T_{tu} = \begin{cases} 0 & \text{, if } (|u_\delta| cos\varphi - \hat{u}_t) > 0 \\ T_t - T_{td} & \text{, if } (|u_\delta| cos\varphi + \hat{u}_c) < 0 \end{cases} \tag{C.14}$$

Appendix D

Comparison of the new and original methods used to define the periods of crest/trough half-cycles in SANTOSS model

The original and new methods used to definite the periods of crest/trough half-cycles in the SANTOSS model are very similar in style. Both of these two methods definite the duration of the crest half-cycle (i.e. crest period, T_c) as the part of wave period (T) with the positive velocity and the duration of the trough half-cycle (i.e. trough period, T_t) as the part of wave period (T) with the negative velocity. The difference between these two methods is on the kind of velocity used to make the definition: the original method uses the combined wave and current velocity (i.e. $\vec{u}(t)$ in Eq.(3.104)), while the new method utilizes the wave orbital velocity (i.e. $\vec{u}_w(t)$ in Eq.(3.104)), Therefore, these two methods are identical at the situations when only waves are present while a mean current is absent.

In the SANTOSS model, the representative wave orbital velocities for the crest and trough half-cycles are defined as the root mean square velocity of a sinusoidal flow with the amplitude of $\hat{u}_c$ and $\hat{u}_t$ respectively, as given by Eqs. (3.111) and (3.112). Using a constant value to represent the time-varying wave orbital velocities in a half-cycle, this approach presumes that the sediment transport rate induced by this constant velocity equal to the time-averaged value induced by the original wave orbital velocity in a half-cycle. This can be depicted as that the area covered by the rectangle box with red dotted line is roughly equal to the blue shadowed area of sinusoid shown in Figure D.1. When only waves are present, the Figure D.1 applies to both the original and new methods as these two methods are identical in these situations.

When a strong mean current is present, apparent difference appear between the new

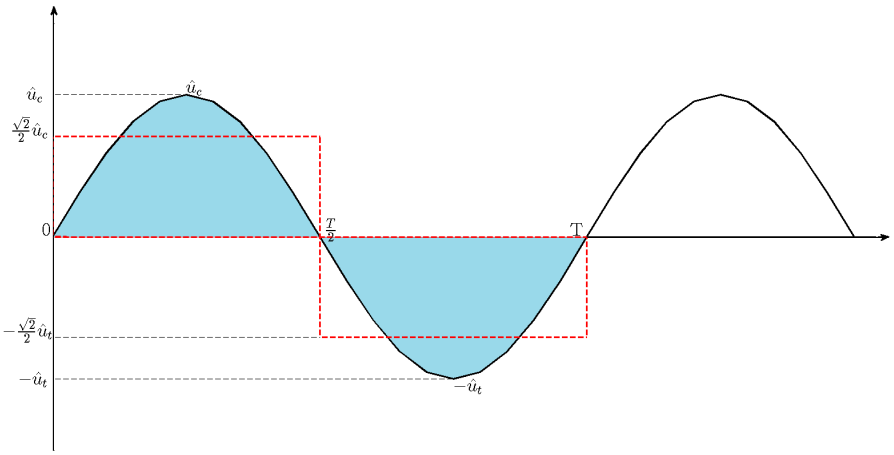

Figure D.1: A sketch on the method used to definite the crest and trough periods for SANTOSS model in situations when only waves are present. For the sake of simplicity, the wave orbital velocity is represented with a sinusoidal function.

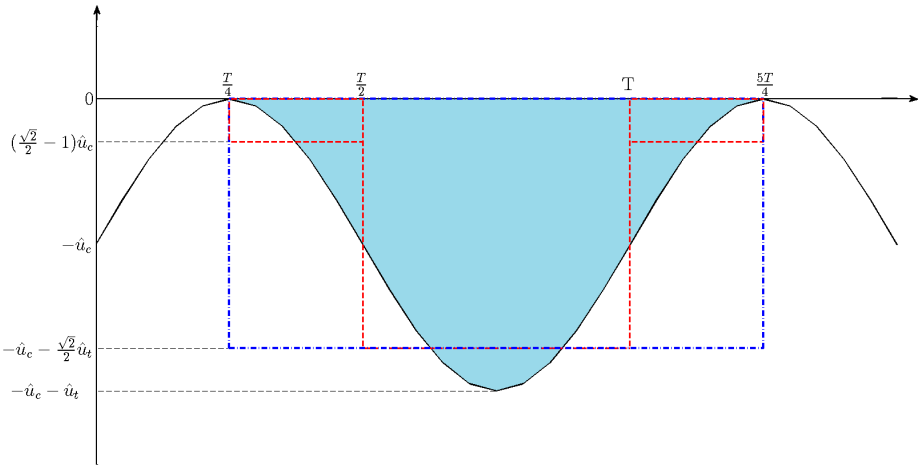

Figure D.2: A sketch on the method used to definite the crest and trough periods for SANTOSS model in situations when both wave and mean current are present. For the sake of simplicity, the wave orbital velocity is represented with a sinusoidal function.

and original methods. Without loss of generality, the mean current is assumed with a magnitude of $\hat{u}_c$ and a opposite direction to the wave prorogation direction . According to the original definition, the crest period is zero as the combined wave-current velocity in the whole wave cycle is no more than zero. The resulting area using this definition is represented by the area of rectangle in blue dotted lines (hereinafter Area1, Figure D.2).

While based on the new definition method, both the crest and trough periods exist, and the resulting area is represented as the rectangle areas in red dotted lines (hereinafter Area2) in the Figure D.2. Apparently, the Area2 is more close to target area (i.e. the blue shadowed area) while the Area1 is too much bigger. Suppose the wave shown in Figure D.2 is onshore directed, a much bigger Area1 implies that the offshore directed sediment transport rate can be much overestimated when using the original definition method. Therefore, it is thought that the new definition method is physically more reasonable. In addition, those supplemental adaptions shown in Appendix C proposed for the original method are not needed any more after applying this new definition method. The code structure is thus more concise and efficient.

Appendix E

Using the Maximum Bed Shear Stress (τ_{cwmax}) in pick-up function

Using the maximum bed shear stress (τ_{cwmax}) alone to calculate the sediment pick-up rate (Run #10.1), the predicted suspended sediment concentration profiles at the 12 locations are compared with the measured data in Figure E.1. Inside the surfzone (e.g. at locations of profiles 4-11), the modeled suspended sediment concentration profiles are apparently under-estimated, indicating that the calculated bed shear stress (i.e. Shields parameters) at these locations are also much underestimated. Sediment transport is usually caused by bottom friction, induced by near-bed shear flow and surface waves. However, the breaking waves may directly entrain large amounts of sand from the bed in the surf zone (Nielsen [2]). And the formulations using the Shields parameters directly calculated from waves and currents as the driving force for the sand suspension (e.g. Nielsen [68]; van Rijn [69, 70, 57]) may have limited predictive capabilities when applied to the wave breaking region (Aagaard and Jensen [71]). Therefore, it is thought that the underestimation of sediment concentration maybe a result of lacking the effect of wave breaking induced turbulence. In order to include wave breaking effects on the sediment suspension, three methods are adopted in the developed model system. These three methods and the computed results are described in detail in the following text.

E.1 Enhance Shields Parameter with The Predicted Near-Bed TKE

To account for the additional turbulent suspension that induced by breaking waves in the surf zone, Hsu and Liu [72] introduced a generalized Shields parameter, i.e. Eq.3.77, which obtained reasonable well agreement with the measured data. In this approach, the breaking wave turbulence energy (k_b) is used to parameterized the effects of breaking waves on the sediment suspension, and a numerical coefficient e_k is proposed

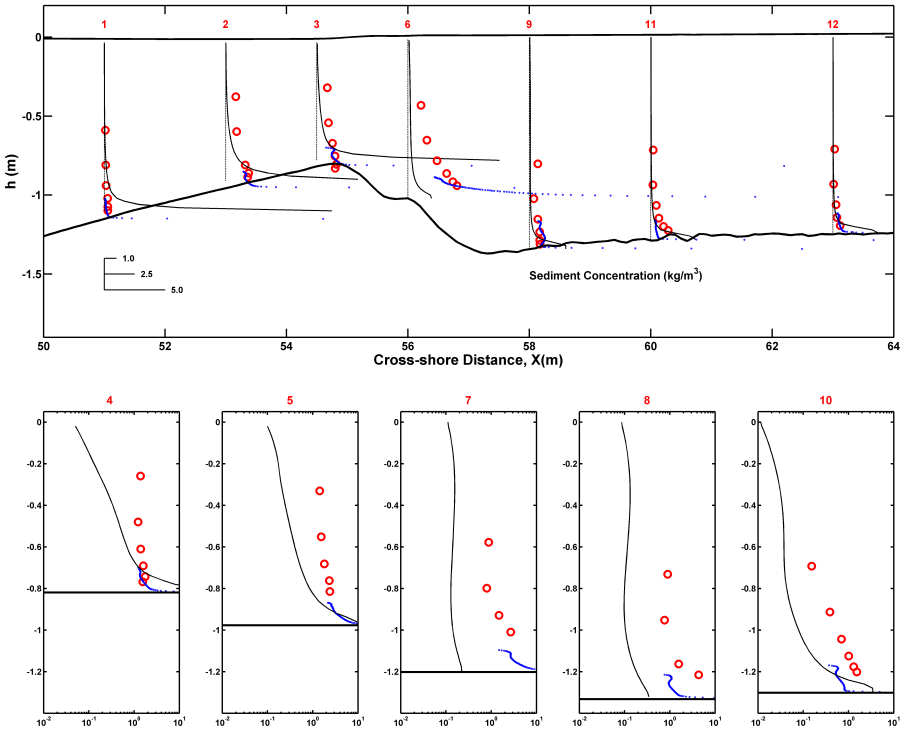

Figure E.1: Comparison of simulation results (solid lines) with observed vertical profiles (red and blue circles) of suspended sediment concentration. The model results are from the Run #10.1. The vertical dashed lines indicate the profile measurement locations and zero value for each profile.

to determine sediment suspension efficiency. Following Hsu and Liu [72], the model predicted near-bed TKE (i.e. model calculated TKE at the first grid point above the bed, hereafter as k_{nbp}) is adopted as the k_b in this study, which could dynamically adjust the intensity of wave breaking induced turbulence on the near-bed sediment pickup rate; and the coefficient e_k is taken as a tuning parameter to be adjusted to produce closer results to available observations.

In the surf zone where depth-induced wave breaking happens, the near-bed TKE is mainly composed of two parts, one part is produced by the local bed friction (hereafter as k_{lf}) while the other part comes from the process that surface wave breaking induced turbulence invades the bottom layer (hereafter as k_{wbr}). Physically speaking, the value of k_b used in the Eq.3.77 should be equal to k_{wbr}. However, for a modeling study it is very difficult or even impossible to separate k_{wbr} from the predicted total near-bead TKE (k_{nbp}), therefore the model predicted k_{nbp} is used as k_b as stated in the above paragraph. Outside of surf zone where waves have not break, no wave breaking induced turbulence exist and thus its effect on the sediment suspension should also be nil. However, the predicted near bed TKE is not nil at areas where waves doesn't break. To be consistent with the physical reality, the value of the coefficient e_k outside of surf zone must be

taken as zero. This is also in accordance with the model results. Figure E.1 shows that the magnitude of the model predicted suspended sediment concentrations at profiles 1 and 2 are already agree well with the measurements, suggesting that there is no need to increase the magnitude of the calculated Shields parameter. Therefore a cross-shore varying value of the coefficient e_k should be adopted.

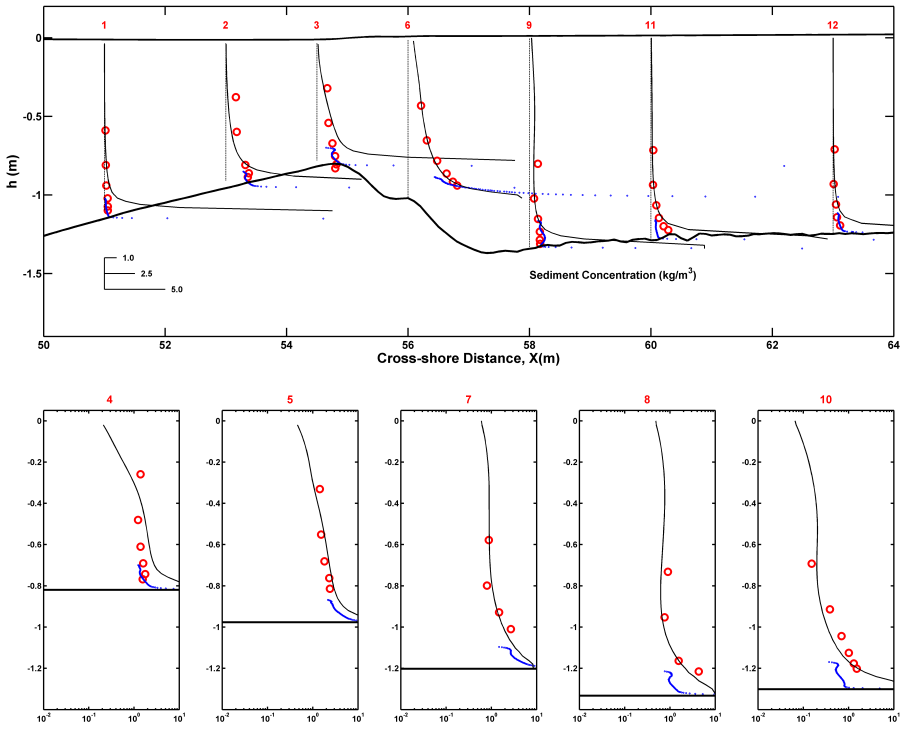

Figure E.2: Comparison of simulation results (solid lines) with observed vertical profiles (red and blue circles) of suspended sediment concentration. The model results are from the Run #10.2. The vertical dashed lines indicate the profile measurement locations and zero value for each profile.

After several numerical attempts, the predicted suspended sediment concentration profiles finally agree fairly well with the measured data (Figure E.2), by calibrating the value of the coefficient e_k to take the effect of breaking wave turbulence into account in calculating the pickup function (Run #10.2). The cross-shore varying value of the finally used e_k is displayed in Figure E.3, which could also be represented with a simple piecewise function, i.e.

$$e_k = \begin{cases} 0 & , \ X < 55.5 \\ (x - 55.5) * 0.05 & , \ 55.5 \leq X \leq 56.5 \\ 0.05 & , \ X > 56.5 \end{cases} \tag{E.1}$$

Although a more complicated distribution of e_k could lead to better agreement with

the measurements (this could be seen from results of one numerical attempt, but not shown here), the present simple distribution (Figure E.3) apparently has more practical significance for modelling and /or coastal engineering studies, as in most cases there are not so much detailed measurements as that used in the present process of calibration. The value of 0.05 is consistent with that used in the study of Hsu and Liu [72].

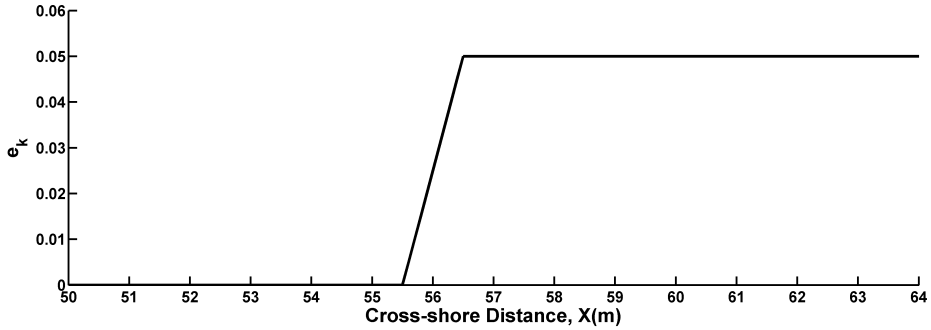

Figure E.3: The value of cross-shore varying e_k.

E.2 Enhance Shields Parameter with Wave Dissipation Energy

To calculate the magnitude of the near-bed TKE, Roelvink and Stive [181] proposed an exponential decay model with a depth length scale proportional to H_{rms}, as follows:

$$k_b = \frac{(\epsilon_r/\rho)^{2/3}}{exp(D/H_{rms}) - 1} \tag{E.2}$$

where ϵ_r is the roller energy dissipation rate that defined in Section 3.2.1, D is the water depth and H_{rms} is the root mean square wave height.

As stated in Section 5.4.3, there are still some problems in accurately predicting the TKE in the wave breaking regions with the present model system. Many studies using various turbulence closure models have also reported similar problems. The calculated wave parameters by a widely used third-generation wave model (e.g. the UnSWAN used in this study), however, generally agree fairly well with observations. Therefore by using the wave model calculated parameters (e.g. wave height and roller energy dissipation) to parameterize the magnitude of the near-bed TKE, the present parameterization (Eq.E.2) does not rely on detailed numerical predictions of wave breaking generated turbulence dynamics which thus it is more simple and more robust.

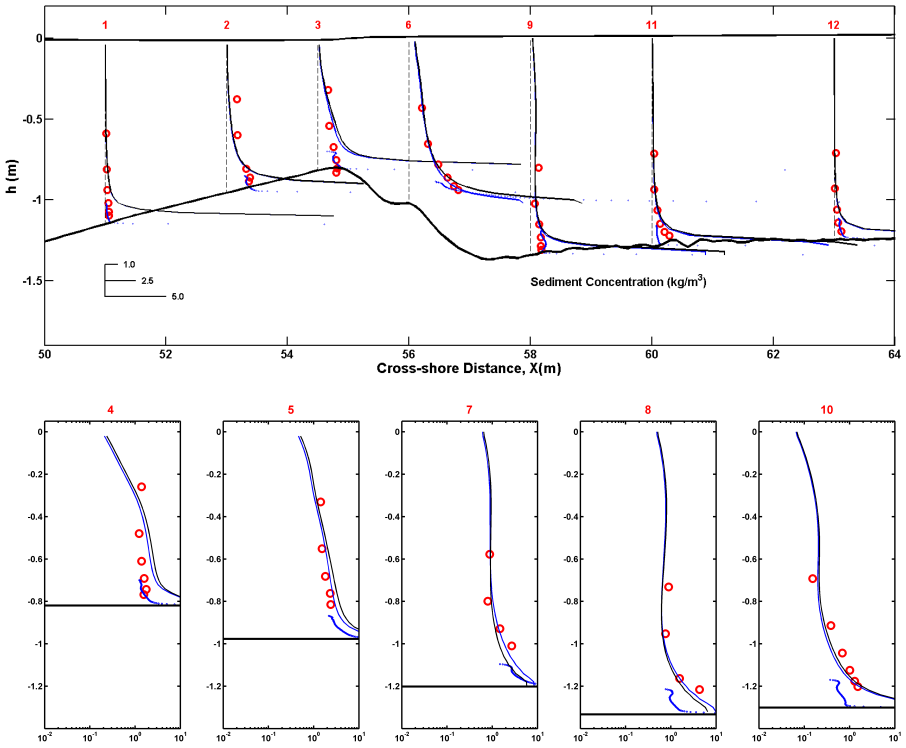

Figure E.4: Comparison of simulation results (solid lines) with observed vertical profiles (red and blue circles) of suspended sediment concentration. The black lines are results from Run #10.3 with k_b calculated from Eq.E.2, while the blue lines are results from Run #10.2 using the model predicted near-bed TKE. The vertical dashed lines indicate the profile measurement locations and zero value for each profile.

Using this parameterization and the same set of e_k value as given by Eq.E.2 (Run #10.3), the model calculated suspended sediment concentration profiles are shown in Figure E.4 (black lines). To facilitate the comparison, the suspended sediment concentration profiles shown in Section E.1 are re-plotted in Figure E.4 (with blue lines). Interestingly, the sediment concentration profiles predicted with the above two methods are very close with each other and all agree fairly well the observations, indicating that both of these two methods could be successfully used in accurately predicting the suspended sediment transport.

E.3 Suspended Sediment Transport Rate

Similar to that shown in Section 5.5.3, the predicted suspended sediment transport rate is also computed and compared with the measured data in this section (Figure E.5).

The suspended sediment transport rate is calculated by using the Eq (5.7) with the predicted current velocities shown in Figure 5.19 and the sediment concentrations in Figure E.2.

Although the sediment concentrations predicted from the simulation with the maximum bed shear stress τ_{wcmax} (Figure E.2) agree reasonable well with the measurements, the calculated sediment transport rate from the same simulation (Figure E.5) are very different with that estimated by van der Zanden [5], and are also very different with those shown in Figure 5.23 and Figure 5.24. This is because q_s, as a result of vertical integration of the sediment flux (i.e. the product of velocity and sediment concentration), accumulates the small errors lie in the predicted sediment concentrations at the whole water column. Therefore, q_s could be used as a more strict criterion to judge the performance of a model system in simulating the suspended sediment transport process. Apparently, the approach of using τ_{wcmax} in calculating the sediment pick-rate is not a good choice, at least for the present SINBAD mobile bed case.

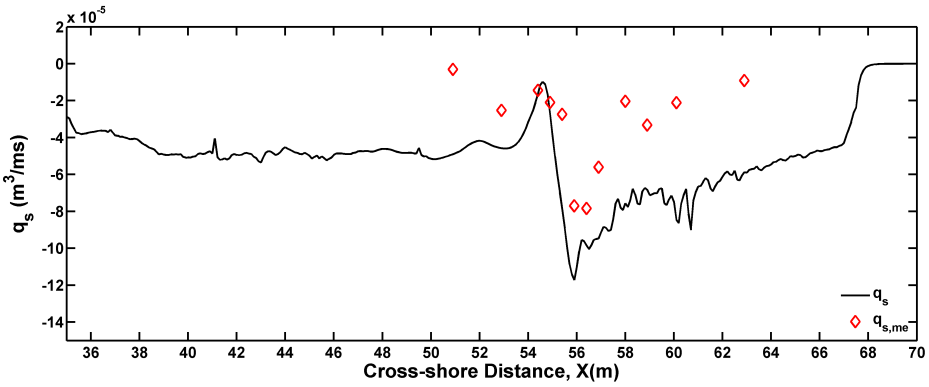

Figure E.5: Suspended sediment transport rate q_s (black line) calculated from the sediment concentration shown in Figure E.2. Red diamonds represent the estimated q_s from the measured suspended sediment concentration and velocity by Joep [5] (i.e. the $q_{s,outer}$ showed in its Figure 3.10).

Appendix F

Publications

Peng Zheng, Ming Li, Dominic A van der A, Joep van der Zanden, Judith Wolf, Xueen Chen, and Caixia Wang. A 3D unstructured grid nearshore hydrodynamic model based on the vortex force formalism. Ocean Modelling, 116:48–69, 2017.

<Model study of a laboratory mobile barred bed evolution I : the model development and the hydrodynamics> *under preparation*

<Model study of a laboratory mobile barred bed evolution II : the sediment transport and bed evolution> *under preparation*

Bibliography

[1] G. Mellor, "The three-dimensional current and surface wave equations," *Journal of Physical Oceanography*, vol. 33, no. 9, pp. 1978–1989, 2003.

[2] P. Nielsen, "Field measurements of time-averaged suspended sediment concentrations under waves," *Coastal Engineering*, vol. 8, no. 1, pp. 51 – 72, 1984.

[3] B. T. Grasmeijer, "Process-based cross-shore modelling of barred beaches," Ph.D. dissertation, Utrecht University, 2002.

[4] J. Fredsoe and R. Deigaard, *Mechanics of coastal sediment transport.* World Scientific Publishing Co Inc, 1992, vol. 3.

[5] J. van der Zanden, "Sand transport processes in the surf and swash zones," Ph.D. dissertation, University of Twente, 12 2016.

[6] M. Zijlema, "Computation of wind-wave spectra in coastal waters with SWAN on unstructured grids," *Coastal Engineering*, vol. 57, no. 3, pp. 267 – 277, 2010.

[7] C. P. L. Hamm, M. Mory, "Hydrodynamic measurements around a detached breakwater in a 3D wave basin," Sogreah Ingenierie, techreport, 1995.

[8] T. O'Donoghue, J. Doucette, J. van der Werf, and J. Ribberink, "The dimensions of sand ripples in full-scale oscillatory flows," *Coastal Engineering*, vol. 53, no. 12, pp. 997 – 1012, 2006.

[9] E. Meyer-Peter and R. Müller, "Formulas for bedload transport," in *Proceedings of 2nd meeting of the International Association for Hydraulic Structures Research*, 1948, pp. 39–64.

[10] C. Small and R. J. Nicholls, "A global analysis of human settlement in coastal zones," *Journal of Coastal Research*, vol. 19, no. 3, pp. 584–599, 2003.

[11] A. Giardino, J. Mulder, J. de Ronde, and J. Stronkhorst, "Sustainable development of the Dutch coast: present and future," *Journal of Coastal Research*, pp. 166–172, 2011.

[12] L. C. van Rijn, J. S. Ribberink, J. V. D. Werf, and D. J. Walstra, "Coastal sediment dynamics: recent advances and future research needs," *Journal of Hydraulic Research*, vol. 51, no. 5, pp. 475–493, 2013.

[13] L. H. Holthuijsen, *Waves in oceanic and coastal waters*. Cambridge university press, 2010.

[14] O. Phillips, "On the dynamics of unsteady gravity waves of finite amplitude Part 1. the elementary interactions," *Journal of Fluid Mechanics*, vol. 9, no. 2, pp. 193–217, 1960.

[15] M. S. Longuet-Higgins, "Mass transport in water waves," *Philosophical Transactions of the Royal Society of London A: Mathematical, Physical and Engineering Sciences*, vol. 245, no. 903, pp. 535–581, 1953.

[16] J. S. Ribberink and A. A. Al-Salem, "Sheet flow and suspension of sand in oscillatory boundary layers," *Coastal Engineering*, vol. 25, no. 3, pp. 205 – 225, 1995.

[17] I. Svendsen, "Mass flux and undertow in a surf zone," *Coastal Engineering*, vol. 8, no. 4, pp. 347 – 365, 1984.

[18] R. B. Nairn, J. A. D. Roelvink, and H. N. Southgate, "Transition zone width and implications for modelling surfzone hydrodynamics," in *Coastal Engineering 1990*. ASCE, 1990.

[19] A. F. Garcez Faria, E. B. Thornton, T. C. Lippmann, and T. P. Stanton, "Undertow over a barred beach," *Journal of Geophysical Research: Oceans*, vol. 105, no. C7, pp. 16 999–17 010, 2000.

[20] D. A. van der A, J. van der Zanden, T. O'Donoghue, D. Hurther, I. Cáceres, S. J. McLelland, and J. S. Ribberink, "Large-scale laboratory study of breaking wave hydrodynamics over a fixed bar," *Journal of Geophysical Research: Oceans*, vol. 122, no. 4, pp. 3287–3310, 2017.

[21] E. L. Gallagher, S. Elgar, and R. T. Guza, "Observations of sand bar evolution on a natural beach," *Journal of Geophysical Research: Oceans*, vol. 103, no. C2, pp. 3203–3215, 1998.

[22] B. Ruessink, J. Miles, F. Feddersen, R. Guza, and S. Elgar, "Modeling the alongshore current on barred beaches," *Journal of Geophysical Research: Oceans*, vol. 106, no. C10, pp. 22 451–22 463, 2001.

[23] Y. Uchiyama, J. C. McWilliams, and A. F. Shchepetkin, "Wave–current interaction in an oceanic circulation model with a vortex-force formalism: Application to the surf zone," *Ocean Modelling*, vol. 34, no. 1, pp. 16 – 35, 2010.

[24] P. Zheng, M. Li, D. A. van der A, J. van der Zanden, J. Wolf, X. Chen, and C. Wang, "A 3D unstructured grid nearshore hydrodynamic model based on the vortex force formalism," *Ocean Modelling*, vol. 116, pp. 48–69, 2017.

[25] N. Kumar, G. Voulgaris, J. C. Warner, and M. Olabarrieta, "Implementation of the vortex force formalism in the coupled ocean-atmosphere-wave-sediment transport (COAWST) modeling system for inner shelf and surf zone applications," *Ocean Modelling*, vol. 47, pp. 65 – 95, 2012.

[26] J. Wolf and D. Prandle, "Some observations of wave–current interaction," *Coastal Engineering*, vol. 37, no. 3, pp. 471–485, 1999.

[27] M. Longuet-Higgins and R. Stewart, "Radiation stresses in water waves; a physical discussion, with applications," *Deep Sea Research and Oceanographic Abstracts*, vol. 11, no. 4, pp. 529 – 562, 1964.

[28] A. J. Bowen, D. L. Inman, and V. P. Simmons, "Wave 'set-down' and set-up," *Journal of Geophysical Research*, vol. 73, no. 8, pp. 2569–2577, 1968.

[29] K. Hasselmann, "On the mass and momentum transfer between short gravity waves and larger-scale motions," *Journal of Fluid Mechanics*, vol. 50, no. 1, p. 189–205, 1971.

[30] A. D. D. Craik and S. Leibovich, "A rational model for Langmuir circulations," *Journal of Fluid Mechanics*, vol. 73, no. 3, p. 401–426, 1976.

[31] C. Garrett, "Generation of Langmuir circulations by surface waves-a feedback mechanism," *Journal of Marine Research*, vol. 103, pp. 117–135, 1976.

[32] O. M. Phillips, *The dynamics of the upper ocean.* Cambridge university press, 1977.

[33] J. A. Smith, "Wave–current interactions in finite depth," *Journal of Physical Oceanography*, vol. 36, no. 7, pp. 1403–1419, 2006.

[34] G. Mellor, "Some consequences of the three-dimensional current and surface wave equations," *Journal of Physical Oceanography*, vol. 35, no. 11, pp. 2291–2298, 2005.

[35] ——, "Wave radiation stress," *Ocean Dynamics*, vol. 61, no. 5, pp. 563–568, May 2011.

[36] ——, "A combined derivation of the integrated and vertically resolved, coupled wave–current equations," *Journal of Physical Oceanography*, vol. 45, no. 6, pp. 1453–1463, 2015.

[37] F. Ardhuin, N. Rascle, and K. Belibassakis, "Explicit wave-averaged primitive equations using a generalized Lagrangian mean," *Ocean Modelling*, vol. 20, no. 1, pp. 35 – 60, 2008.

[38] G. L. Mellor, "The depth-dependent current and wave interaction equations: a revision," *Journal of Physical Oceanography*, vol. 38, no. 11, pp. 2587–2596, 2008.

[39] A.-C. Bennis, F. Ardhuin, and F. Dumas, "On the coupling of wave and three-dimensional circulation models: Choice of theoretical framework, practical implementation and adiabatic tests," *Ocean Modelling*, vol. 40, no. 3, pp. 260 – 272, 2011.

[40] D. G. Andrews and M. McIntyre, "An exact theory of nonlinear waves on a Lagrangian-mean flow," *Journal of Fluid Mechanics*, vol. 89, no. 4, pp. 609–646, 1978.

[41] S. Moghimi, K. Klingbeil, U. Gräwe, and H. Burchard, "A direct comparison of a depth-dependent radiation stress formulation and a vortex force formulation within a three-dimensional coastal ocean model," *Ocean Modelling*, vol. 70, pp. 132–144, 2013.

[42] F. Ardhuin, A. D. Jenkins, and K. A. Belibassakis, "Comments on "the three-dimensional current and surface wave equations"," *Journal of Physical Oceanography*, vol. 38, no. 6, pp. 1340–1350, 2008.

[43] H. Aiki and R. J. Greatbatch, "The vertical structure of the surface wave radiation stress for circulation over a sloping bottom as given by thickness-weighted-mean theory," *Journal of Physical Oceanography*, vol. 43, no. 1, pp. 149–164, 2013.

[44] F. Ardhuin, N. Suzuki, J. C. McWilliams, and H. Aiki, "Comments on "a combined derivation of the integrated and vertically resolved, coupled wave–current equations"," *Journal of Physical Oceanography*, vol. 47, no. 9, pp. 2377–2385, 2017.

[45] Y. P. Sheng and T. Liu, "Three-dimensional simulation of wave-induced circulation: Comparison of three radiation stress formulations," *Journal of Geophysical Research: Oceans*, vol. 116, no. C5, pp. n/a–n/a, 2011, c05021.

[46] J. Wang and Y. Shen, "Development and validation of a three-dimensional, wave-current coupled model on unstructured meshes," *Science China Physics, Mechanics and Astronomy*, vol. 54, no. 1, pp. 42–58, Jan 2011.

[47] J. C. Warner, C. R. Sherwood, R. P. Signell, C. K. Harris, and H. G. Arango, "Development of a three-dimensional, regional, coupled wave, current, and sediment-transport model," *Computers & Geosciences*, vol. 34, no. 10, pp. 1284–1306, 2008.

[48] N. Kumar, G. Voulgaris, and J. Warner, "Implementation and modification of a three-dimensional radiation stress formulation for surf zone and rip-current applications," *Coastal Engineering*, vol. 58, no. 12, pp. 1097 – 1117, 2011.

[49] J. C. McWilliams, J. M. Restrepo, and E. M. Lane, "An asymptotic theory for the interaction of waves and currents in coastal waters," *Journal of Fluid Mechanics*, vol. 511, p. 135–178, 2004.

[50] N. Suzuki, B. Fox-Kemper, P. E. Hamlington, and L. P. Van Roekel, "Surface waves affect frontogenesis," *Journal of Geophysical Research: Oceans*, vol. 121, no. 5, pp. 3597–3624, 2016.

[51] P. A. Newberger and J. S. Allen, "Forcing a three-dimensional, hydrostatic, primitive-equation model for application in the surf zone: 1. formulation," *Journal of Geophysical Research: Oceans*, vol. 112, no. C8, pp. n/a–n/a, 2007, c08018.

[52] ——, "Forcing a three-dimensional, hydrostatic, primitive-equation model for application in the surf zone: 2. application to DUCK94," *Journal of Geophysical Research: Oceans*, vol. 112, no. C8, pp. n/a–n/a, 2007, c08019.

[53] J. van der Zanden, D. A. van der A, D. Hurther, I. Cáceres, T. O'Donoghue, and J. S. Ribberink, "Near-bed hydrodynamics and turbulence below a large-scale plunging breaking wave over a mobile barred bed profile," *Journal of Geophysical Research: Oceans*, vol. 121, no. 8, pp. 6482–6506, 2016.

[54] J. van der Zanden, D. van der A, D. Hurther, I. Cáceres, T. O'Donoghue, S. Hulscher, and J. Ribberink, "Bedload and suspended load contributions to breaker bar morphodynamics," *Coastal Engineering*, vol. 129, pp. 74 – 92, 2017.

[55] J. van der Zanden, D. van der A, D. Hurther, I. Cáceres, T. O'Donoghue, and J. Ribberink, "Suspended sediment transport around a large-scale laboratory breaker bar," *Coastal Engineering*, vol. 125, pp. 51 – 69, 2017.

[56] L. C. van Rijn, "Unified view of sediment transport by currents and waves. I: initiation of motion, bed roughness, and bed-load transport," *Journal of Hydraulic Engineering*, vol. 133, no. 6, pp. 649–667, 2007.

[57] ——, "Unified view of sediment transport by currents and waves II: suspended transport," *Journal of Hydraulic Engineering*, vol. 133, no. 6, pp. 668–689, 2007.

[58] J. S. Ribberink, J. J. van der Werf, T. O'Donoghue, and W. N. Hassan, "Sand motion induced by oscillatory flows: Sheet flow and vortex ripples," *Journal of Turbulence*, vol. 9, p. N20, 2008.

[59] B. Schnitzler, "Modeling sand transport under breaking waves," Master's thesis, University of Twente, July 2015.

[60] C. M. Dohmen-Janssen, "Grain size influence on sediment transport in oscillatory sheet flow; phase lags and mobile-bed effects," Ph.D. dissertation, Delft University of Technology, 1999.

[61] J. Groeneweg and G. Klopman, "Changes of the mean velocity profiles in the combined wave–current motion described in a GLM formulation," *Journal of Fluid Mechanics*, vol. 370, p. 271–296, 1998.

[62] H. Xia, Z. Xia, and L. Zhu, "Vertical variation in radiation stress and wave-induced current," *Coastal Engineering*, vol. 51, no. 4, pp. 309 – 321, 2004.

[63] H. Huang, C. Chen, G. W. Cowles, C. D. Winant, R. C. Beardsley, K. S. Hedstrom, and D. B. Haidvogel, "FVCOM validation experiments: comparisons with ROMS for three idealized barotropic test problems," *Journal of Geophysical Research: Oceans*, vol. 113, no. C7, pp. n/a–n/a, 2008, c07042.

[64] G. L. Mellor, M. A. Donelan, and L.-Y. Oey, "A surface wave model for coupling with numerical ocean circulation models," *Journal of Atmospheric and Oceanic Technology*, vol. 25, no. 10, pp. 1785–1807, 2008.

[65] H. Burchard, "Simulating the wave-enhanced layer under breaking surface waves with two-equation turbulence models," *Journal of Physical Oceanography*, vol. 31, no. 11, pp. 3133–3145, 2001.

[66] L. Umlauf and H. Burchard, "A generic length-scale equation for geophysical turbulence models," *Journal of Marine Research*, vol. 61, no. 2, pp. 235–265, 2003.

[67] S. M. Durski, S. M. Glenn, and D. B. Haidvogel, "Vertical mixing schemes in the coastal ocean: Comparison of the level 2.5 Mellor-Yamada scheme with an enhanced version of the K profile parameterization," *Journal of Geophysical Research: Oceans*, vol. 109, no. C1, pp. n/a–n/a, 2004, c01015.

[68] P. Nielsen, "Suspended sediment concentrations under waves," *Coastal Engineering*, vol. 10, no. 1, pp. 23 – 31, 1986.

[69] L. C. van Rijn, "Sediment pick-up functions," *Journal of Hydraulic Engineering*, vol. 110, no. 10, pp. 1494–1502, 1984.

[70] ——, "Sediment transport, part II: suspended load transport," *Journal of Hydraulic Engineering*, vol. 110, no. 11, pp. 1613–1641, 1984.

[71] T. Aagaard and S. G. Jensen, "Sediment concentration and vertical mixing under breaking waves," *Marine Geology*, vol. 336, pp. 146 – 159, 2013.

[72] T.-J. Hsu and P. L.-F. Liu, "Toward modeling turbulent suspension of sand in the nearshore," *Journal of Geophysical Research: Oceans*, vol. 109, no. C6, pp. n/a–n/a, 2004, c06018.

[73] A. Okayasu, K. Fujii, and M. Isobe, "Effect of external turbulence on sediment pickup rate," *Coastal Engineering Proceedings*, vol. 1, no. 32, p. 14, 2011.

[74] M. P. Ravindra Jayaratne and T. Shibayama, "Suspended sediment concentration on beaches under three different mechanisms," *Coastal Engineering Journal*, vol. 49, no. 04, pp. 357–392, 2007.

[75] N. Kobayashi and B. D. Johnson, "Sand suspension, storage, advection, and settling in surf and swash zones," *Journal of Geophysical Research: Oceans*, vol. 106, no. C5, pp. 9363–9376, 2001.

[76] K. Spielmann, D. Astruc, and O. Thual, "Analysis of some key parametrizations in a beach profile morphodynamical model," *Coastal Engineering*, vol. 51, no. 10, pp. 1021 – 1049, 2004.

[77] J. van der Zanden, M. Fernandez Mora, D. van der A, D. Hurther, I. Caceres, T. O'Donoghue, and J. Ribberink, "Inclusion of wave breaking turbulence in reference concentration models," in *Proceedings Coastal Dynamics 2017, Helsingør, Denmark*, 2017, pp. 629–641.

[78] D. A. van der A, J. S. Ribberink, J. J. van der Werf, T. O'Donoghue, R. H. Buijsrogge, and W. M. Kranenburg, "Practical sand transport formula for non-breaking waves and currents," *Coastal Engineering*, vol. 76, pp. 26 – 42, 2013.

[79] D. A. van der A, T. O'Donoghue, and J. S. Ribberink, "Measurements of sheet flow transport in acceleration-skewed oscillatory flow and comparison with practical formulations," *Coastal Engineering*, vol. 57, no. 3, pp. 331 – 342, 2010.

[80] A. Watanabe and S. Sato, *A sheet-flow transport rate formula for asymmetric, forward-leaning waves and currents*. World Scientific Publishing Company, 2012, pp. 1703–1714.

[81] B. Camenen and M. Larson, "A total load formula for the nearshore," in *Coastal Sediments' 07*. ASCE, 2007, pp. 56–67.

[82] J. J. van der Werf, J. S. Doucette, T. O'Donoghue, and J. S. Ribberink, "Detailed measurements of velocities and suspended sand concentrations over

full-scale ripples in regular oscillatory flow," *Journal of Geophysical Research: Earth Surface*, vol. 112, no. F2, pp. n/a–n/a, 2007, f02012.

[83] P. A. da Silva, A. Temperville, and F. S. Santos, "Sand transport under combined current and wave conditions: A semi-unsteady, practical model," *Coastal Engineering*, vol. 53, no. 11, pp. 897–913, 2006.

[84] L. C. van Rijn, "Unified view of sediment transport by currents and waves. III: graded beds," *Journal of Hydraulic Engineering*, vol. 133, no. 7, pp. 761–775, 2007.

[85] N. Booij, R. C. Ris, and L. H. Holthuijsen, "A third-generation wave model for coastal regions: 1. model description and validation," *Journal of Geophysical Research: Oceans*, vol. 104, no. C4, pp. 7649–7666, 1999.

[86] T. S. Team, "SWAN scientific and technical documentation: SWAN Cycle III version 41.10," Delft University of Technology, Tech. Rep., 2016.

[87] O. M. Phillips, "On the generation of waves by turbulent wind," *Journal of fluid mechanics*, vol. 2, no. 5, pp. 417–445, 1957.

[88] J. W. Miles, "On the generation of surface waves by shear flows," *Journal of Fluid Mechanics*, vol. 3, no. 2, pp. 185–204, 1957.

[89] K. Hasselmann, "On the spectral dissipation of ocean waves due to white capping," *Boundary-Layer Meteorology*, vol. 6, no. 1, pp. 107–127, Mar 1974.

[90] A. J. van der Westhuysen, "Advances in the spectral modelling of wind waves in the nearshore," Ph.D. dissertation, Delft University of Technology, 2007.

[91] G. Komen, K. Hasselmann, and K. Hasselmann, "On the existence of a fully developed wind-sea spectrum," *Journal of physical oceanography*, vol. 14, no. 8, pp. 1271–1285, 1984.

[92] W. E. Rogers, P. A. Hwang, and D. W. Wang, "Investigation of wave growth and decay in the SWAN model: three regional-scale applications," *Journal of Physical Oceanography*, vol. 33, no. 2, pp. 366–389, 2003.

[93] G. P. van Vledder and D. P. Hurdle, "Performance of formulations for whitecapping in wave prediction models," in *Proc. OMAE. 02 21st Int. Conf. on Offshore Mechanics and Artic Engineering*, 2002, pp. 1–9.

[94] K. Hasselmann, "Measurements of wind wave growth and swell decay during the Joint North Sea Wave Project (JONSWAP)," *Dtsch. Hydrogr. Z.*, vol. 8, p. 95, 1973.

[95] K. Hasselmann and J. Collins, "Spectral dissipation of finite depth gravity waves due to turbulent bottom friction," *J. mar. Res.*, vol. 26, pp. 1–12, 1968.

[96] O. S. Madsen, Y.-K. Poon, and H. C. Graber, "Spectral wave attenuation by bottom friction: theory," in *Coastal Engineering 1988*. ASCE, 1989, pp. 492–504.

[97] S. Weber, "Surface gravity waves and turbulent bottom friction," Ph.D. dissertation, University of Utrecht, 1989.

[98] J. A. Battjes and J. P. F. M. Janssen, "Energy loss and set-up due to breaking of random waves," in *Coastal Engineering 1978*. ASCE, 1978.

[99] L. Bertotti and L. Cavaleri, "Accuracy of wind and wave evaluation in coastal regions," in *Coastal Engineering 1994*. ASCE, 1995, pp. 57–67.

[100] J. I. Collins, "Prediction of shallow-water spectra," *Journal of Geophysical Research*, vol. 77, no. 15, pp. 2693–2707, 1972.

[101] Y. Eldeberky and J. Battjes, "Parameterization of triad interactions in wave energy models," in *Proceedings Coastal Dynamics'95*. ASCE, 1995, pp. 140–148.

[102] J. Qi, C. Chen, R. C. Beardsley, W. Perrie, G. W. Cowles, and Z. Lai, "An unstructured-grid finite-volume surface wave model (FVCOM-SWAVE): Implementation, validations and applications," *Ocean Modelling*, vol. 28, no. 1, pp. 153 – 166, 2009, the Sixth International Workshop on Unstructured Mesh Numerical Modelling of Coastal, Shelf and Ocean Flows.

[103] T.-W. Hsu, S.-H. Ou, and J.-M. Liau, "Hindcasting nearshore wind waves using a FEM code for SWAN," *Coastal Engineering*, vol. 52, no. 2, pp. 177–195, 2005.

[104] J. P. Boris and D. L. Book, "Flux-corrected transport. i. SHASTA, a fluid transport algorithm that works," *Journal of computational physics*, vol. 11, no. 1, pp. 38–69, 1973.

[105] J. Crank and P. Nicolson, "A practical method for numerical evaluation of solutions of partial differential equations of the heat-conduction type," in *Mathematical Proceedings of the Cambridge Philosophical Society*, vol. 43. Cambridge University Press, 1947, pp. 50–67.

[106] W. Group, "The WAM model—a third generation ocean wave prediction model," *Journal of Physical Oceanography*, vol. 18, no. 12, pp. 1775–1810, 1988.

[107] H. L. Tolman, "User manual and system documentation of WAVEWATCH-III version 2.22," NOAA/NWS/NCEP/MMAB, Tech. Rep. 222, 2002.

[108] C. Chen, H. Liu, and R. C. Beardsley, "An unstructured grid, finite-volume, three-dimensional, primitive equations ocean model: application to coastal ocean and estuaries," *Journal of Atmospheric and Oceanic Technology*, vol. 20, no. 1, pp. 159–186, 2003.

[109] Z. Lai, C. Chen, G. W. Cowles, and R. C. Beardsley, "A nonhydrostatic version of FVCOM: 1. validation experiments," *Journal of Geophysical Research: Oceans*, vol. 115, no. C11, pp. n/a–n/a, 2010, c11010.

[110] ——, "A nonhydrostatic version of FVCOM: 2. mechanistic study of tidally generated nonlinear internal waves in Massachusetts Bay," *Journal of Geophysical Research: Oceans*, vol. 115, no. C12, pp. n/a–n/a, 2010, c12049.

[111] J. Smagorinsky, "General circulation experiments with the primitive equations: I. the basic experiment*," *Monthly weather review*, vol. 91, no. 3, pp. 99–164, 1963.

[112] G. L. Mellor and T. Yamada, "Development of a turbulence closure model for geophysical fluid problems," *Reviews of Geophysics*, vol. 20, no. 4, pp. 851–875, 1982.

[113] B. Galperin, L. Kantha, S. Hassid, and A. Rosati, "A quasi-equilibrium turbulent energy model for geophysical flows," *Journal of the Atmospheric Sciences*, vol. 45, no. 1, pp. 55–62, 1988.

[114] G. Mellor and A. Blumberg, "Wave breaking and ocean surface layer thermal response," *Journal of Physical Oceanography*, vol. 34, no. 3, pp. 693–698, 2004.

[115] L. H. Kantha and C. A. Clayson, *Numerical models of oceans and oceanic processes*. Academic press, 2000, vol. 66.

[116] ——, "An improved mixed layer model for geophysical applications," *Journal of Geophysical Research: Oceans*, vol. 99, no. C12, pp. 25 235–25 266, 1994.

[117] G. L. Mellor and T. Yamada, "A hierarchy of turbulence closure models for planetary boundary layers," *Journal of the Atmospheric Sciences*, vol. 31, no. 7, pp. 1791–1806, 1974.

[118] E. Terray, M. Donelan, Y. Agrawal, W. Drennan, K. Kahma, A. J. Williams, P. Hwang, and S. Kitaigorodskii, "Estimates of kinetic energy dissipation under breaking waves," *Journal of Physical Oceanography*, vol. 26, no. 5, pp. 792–807, 1996.

[119] E. Terray, W. Drennan, and M. Donelan, "The vertical structure of shear and dissipation in the ocean surface layer," Dept of Applied Ocean Physics and Engineering, Woods Hole Oceanographic Institution, Tech. Rep., 1999.

[120] S. D. Smith, R. J. Anderson, W. A. Oost, C. Kraan, N. Maat, J. De Cosmo, K. B. Katsaros, K. L. Davidson, K. Bumke, L. Hasse, and H. M. Chadwick, "Sea surface wind stress and drag coefficients: The hexos results," *Boundary-Layer Meteorology*, vol. 60, no. 1, pp. 109–142, Jul 1992.

[121] R. Ariathurai and K. Arulanandan, "Erosion rates of cohesive soils," *Journal of the Hydraulics Division*, vol. 104, no. 2, pp. 279–283, 1978.

[122] P. Colella and P. R. Woodward, "The Piecewise Parabolic Method (PPM) for gas-dynamical simulations," *Journal of Computational Physics*, vol. 54, no. 1, pp. 174 – 201, 1984.

[123] X.-D. Liu, S. Osher, and T. Chan, "Weighted essentially non-oscillatory schemes," *Journal of Computational Physics*, vol. 115, no. 1, pp. 200 – 212, 1994.

[124] R. L. Soulsby and J. S. Damgaard, "Bedload sediment transport in coastal waters," *Coastal Engineering*, vol. 52, no. 8, pp. 673 – 689, 2005.

[125] R. Soulsby, *Dynamics of marine sands: a manual for practical applications*. Thomas Telford, 1997.

[126] J. Malarkey and A. G. Davies, "A non-iterative procedure for the Wiberg and Harris (1994) oscillatory sand ripple predictor," *Journal of Coastal Research*, vol. 19, no. 3, pp. 738–739, 2003.

[127] P. L. Wiberg and C. K. Harris, "Ripple geometry in wave-dominated environments," *Journal of Geophysical Research: Oceans*, vol. 99, no. C1, pp. 775–789, 1994.

[128] P. L. Wiberg and D. M. Rubin, "Bed roughness produced by saltating sediment," *Journal of Geophysical Research: Oceans*, vol. 94, no. C4, pp. 5011–5016, 1989.

[129] W. D. Grant and O. S. Madsen, "Movable bed roughness in unsteady oscillatory flow," *Journal of Geophysical Research: Oceans*, vol. 87, no. C1, pp. 469–481, 1982.

[130] P. Nielsen, *Coastal bottom boundary layers and sediment transport*. World Scientific Publishing Co Inc, 1992, vol. 4.

[131] O. S. Madsen, "Spectral wave-current bottom boundary layer flows," in *Coastal Engineering 1994*. ASCE, 1995, pp. 384–398.

[132] R. Styles and S. M. Glenn, "Modeling stratified wave and current bottom boundary layers on the continental shelf," *Journal of Geophysical Research: Oceans*, vol. 105, no. C10, pp. 24 119–24 139, 2000.

[133] P. L. Wiberg and J. M. Nelson, "Unidirectional flow over asymmetric and symmetric ripples," *Journal of Geophysical Research: Oceans*, vol. 97, no. C8, pp. 12 745–12 761, 1992.

[134] M. J. Stive and H. J. De Vriend, "Shear stresses and mean flow in shoaling and breaking waves," in *Coastal Engineering 1994*. ASCE, 1995, pp. 594–608.

[135] A. J. H. M. Reniers, J. A. Roelvink, and E. B. Thornton, "Morphodynamic modeling of an embayed beach under wave group forcing," *Journal of Geophysical Research: Oceans*, vol. 109, no. C1, pp. n/a–n/a, 2004, c01030.

[136] Y. Tajima and O. S. Madsen, "Modeling near-shore waves, surface rollers, and undertow velocity profiles," *Journal of Waterway, Port, Coastal, and Ocean Engineering*, vol. 132, no. 6, pp. 429–438, 2006.

[137] J. Grue and J. Kolaas, "Experimental particle paths and drift velocity in steep waves at finite water depth," *Journal of Fluid Mechanics*, vol. 810, 2017.

[138] J. H. G. M. Alves and M. L. Banner, "Performance of a saturation-based dissipation-rate source term in modeling the fetch-limited evolution of wind waves," *Journal of Physical Oceanography*, vol. 33, no. 6, pp. 1274–1298, 2003.

[139] A. J. van der Westhuysen, M. Zijlema, and J. A. Battjes, "Nonlinear saturation-based whitecapping dissipation in SWAN for deep and shallow water," *Coastal Engineering*, vol. 54, no. 2, pp. 151 – 170, 2007.

[140] J. Salmon, L. Holthuijsen, M. Zijlema, G. van Vledder, and J. Pietrzak, "Scaling depth-induced wave-breaking in two-dimensional spectral wave models," *Ocean Modelling*, vol. 87, pp. 30 – 47, 2015.

[141] A. Okayasu, T. Shibayama, and N. Mimura, "Velocity field under plunging waves," in *Coastal Engineering 1986*. ASCE, 1987, pp. 660–674.

[142] K. A. Haas and J. C. Warner, "Comparing a quasi-3D to a full 3D nearshore circulation model: SHORECIRC and ROMS," *Ocean Modelling*, vol. 26, no. 1, pp. 91 – 103, 2009.

[143] A. Reniers, E. Thornton, T. Stanton, and J. Roelvink, "Vertical flow structure during Sandy Duck: observations and modeling," *Coastal Engineering*, vol. 51, no. 3, pp. 237 – 260, 2004.

[144] R. Soulsby and A. Davies, "Bed shear-stresses due to combined waves and currents," *Advances in Coastal Morphodynamics*, pp. 4–20, 1995.

[145] G. Klopman, "Stokes transport," *WL-Delft Hydraulics Report H*, vol. 840, 1994.

[146] Z. Xu and A. J. Bowen, "Wave- and wind-driven flow in water of finite depth," *Journal of Physical Oceanography*, vol. 24, no. 9, pp. 1850–1866, 1994.

[147] S. J. Lentz, M. Fewings, P. Howd, J. Fredericks, and K. Hathaway, "Observations and a model of undertow over the inner continental shelf," *Journal of Physical Oceanography*, vol. 38, no. 11, pp. 2341–2357, 2008.

[148] Y. Uchiyama, J. C. McWilliams, and J. M. Restrepo, "Wave-current interaction in nearshore shear instability analyzed with a vortex force formalism," *Journal of Geophysical Research: Oceans*, vol. 114, no. C6, pp. n/a–n/a, 2009, c06021.

[149] S. A. Thorpe, "On the determination of kv in the near-surface ocean from acoustic measurements of bubbles," *Journal of Physical Oceanography*, vol. 14, no. 5, pp. 855–863, 1984.

[150] Y. Agrawal, E. Terray, M. Donelan, P. Hwang, A. J. Williams, W. Drennan, K. Kahma, and S. Krtaigorodskii, "Enhanced dissipation of kinetic energy beneath surface waves," *Nature*, vol. 359, no. 6392, pp. 219–220, 1992.

[151] S. Moghimi, J. Thomson, T. Özkan Haller, L. Umlauf, and S. Zippel, "On the modeling of wave-enhanced turbulence nearshore," *Ocean Modelling*, vol. 103, pp. 118 – 132, 2016, waves and coastal, regional and global processes.

[152] P. D. Craig and M. L. Banner, "Modeling wave-enhanced turbulence in the ocean surface layer," *Journal of Physical Oceanography*, vol. 24, no. 12, pp. 2546–2559, 1994.

[153] L. Umlauf, H. Burchard, and K. Bolding, *GOTM-scientific documentation: version 3.2.* Institut für Ostseeforschung, 2005.

[154] J. C. Warner, C. R. Sherwood, H. G. Arango, and R. P. Signell, "Performance of four turbulence closure models implemented using a generic length scale method," *Ocean Modelling*, vol. 8, no. 1, pp. 81 – 113, 2005.

[155] F. Feddersen, "Observations of the surf-zone turbulent dissipation rate," *Journal of Physical Oceanography*, vol. 42, no. 3, pp. 386–399, 2012.

[156] ——, "Scaling surf zone turbulence," *Geophysical Research Letters*, vol. 39, no. 18, pp. n/a–n/a, 2012, l18613.

[157] P. D. Craig, "Velocity profiles and surface roughness under breaking waves," *Journal of Geophysical Research: Oceans*, vol. 101, no. C1, pp. 1265–1277, 1996.

[158] K. Govender, G. P. Mocke, and M. J. Alport, "Dissipation of isotropic turbulence and length-scale measurements through the wave roller in laboratory spilling

waves," *Journal of Geophysical Research: Oceans*, vol. 109, no. C8, pp. n/a–n/a, 2004, c08018.

[159] Z.-C. Huang, S.-C. Hsiao, H.-H. Hwung, and K.-A. Chang, "Turbulence and energy dissipations of surf-zone spilling breakers," *Coastal Engineering*, vol. 56, no. 7, pp. 733 – 746, 2009.

[160] F. Feddersen and J. H. Trowbridge, "The effect of wave breaking on surf-zone turbulence and alongshore currents: a modeling study," *Journal of Physical Oceanography*, vol. 35, no. 11, pp. 2187–2203, 2005.

[161] M. B. Paskyabi, I. Fer, and A. D. Jenkins, "Surface gravity wave effects on the upper ocean boundary layer: Modification of a one-dimensional vertical mixing model," *Continental Shelf Research*, vol. 38, pp. 63 – 78, 2012.

[162] L. Umlauf, H. Burchard, and K. Hutter, "Extending the k-ϵ turbulence model towards oceanic applications," *Ocean Modelling*, vol. 5, no. 3, pp. 195 – 218, 2003.

[163] A. Stips, H. Burchard, K. Bolding, H. Prandke, A. Simon, and A. Wüest, "Measurement and simulation of viscous dissipation in the wave affected surface layer," *Deep Sea Research Part II: Topical Studies in Oceanography*, vol. 52, no. 9, pp. 1133 – 1155, 2005, observations and modelling of mixed layer turbulence: Do they represent the same statistical quantities?

[164] F. Feddersen and A. J. W. III, "Direct estimation of the reynolds stress vertical structure in the nearshore," *Journal of Atmospheric and Oceanic Technology*, vol. 24, no. 1, pp. 102–116, 2007.

[165] M. Z. Li and C. L. Amos, "SEDTRANS96: the upgraded and better calibrated sediment-transport model for continental shelves," *Computers & Geosciences*, vol. 27, no. 6, pp. 619–645, 2001.

[166] M. Dibajnia and A. Watanabe, "Sheet flow under nonlinear waves and currents," *Coastal Engineering 1992*, pp. 2015–2028, 1992.

[167] ——, "A transport rate formula for mixed-size sands," in *Proceedings of the 25th International Conference on Coastal Engineering, ASCE*, 1996, pp. 3791–3804.

[168] ——, "Transport rate under irregular sheet flow conditions," *Coastal Engineering*, vol. 35, no. 3, pp. 167 – 183, 1998.

[169] D. van der A, T. O' Donoghue, and J. Ribberink, *Sheet flow sand transport processes in oscillatory flow with acceleration skewness*. World Scientific, 9 2009, pp. 1–13.

[170] B. G. Ruessink, T. J. J. van den Berg, and L. C. van Rijn, "Modeling sediment transport beneath skewed asymmetric waves above a plane bed," *Journal of Geophysical Research: Oceans*, vol. 114, no. C11, pp. n/a–n/a, 2009, c11021.

[171] W. M. Kranenburg, J. S. Ribberink, J. J. L. M. Schretlen, and R. E. Uittenbogaard, "Sand transport beneath waves: The role of progressive wave streaming and other free surface effects," *Journal of Geophysical Research: Earth Surface*, vol. 118, no. 1, pp. 122–139, 2013.

[172] J. S. Ribberink, "Bed-load transport for steady flows and unsteady oscillatory flows," *Coastal Engineering*, vol. 34, no. 1, pp. 59–82, 1998.

[173] D. Swart, "Predictive equations regarding coastal transports," in *Coastal Engineering 1976*. ASCE, 1977, pp. 1113–1132.

[174] D. A. van der A, T. O'Donoghue, A. G. Davies, and J. S. Ribberink, "Experimental study of the turbulent boundary layer in acceleration-skewed oscillatory flow," *Journal of Fluid Mechanics*, vol. 684, p. 251–283, 2011.

[175] M. Longuet-Higgins, "The mechanics of the boundary layer near the bottom in a progressive wave," in *Proceedings of the 6th International Conference on Coastal Engineering, Berkeley (CA), ASCE*, vol. 184, 1958, p. 193.

[176] P. Nielsen, "Sheet flow sediment transport under waves with acceleration skewness and boundary layer streaming," *Coastal Engineering*, vol. 53, no. 9, pp. 749 – 758, 2006.

[177] T. Abreu, P. A. Silva, F. Sancho, and A. Temperville, "Analytical approximate wave form for asymmetric waves," *Coastal Engineering*, vol. 57, no. 7, pp. 656 – 667, 2010.

[178] B. Ruessink, G. Ramaekers, and L. Van Rijn, "On the parameterization of the free-stream non-linear wave orbital motion in nearshore morphodynamic models," *Coastal Engineering*, vol. 65, pp. 56–63, 2012.

[179] R. Veen, "The implementation and testing of the SANTOSS sand transport model in Delft3D," Master's thesis, University of Twente, 2014.

[180] R. A. Bagnold, *An approach to the sediment transport problem from general physics*. US government printing office, 1966.

[181] J. A. Roelvink and M. J. F. Stive, "Bar-generating cross-shore flow mechanisms on a beach," *Journal of Geophysical Research: Oceans*, vol. 94, no. C4, pp. 4785–4800, 1989.

[182] L. Wu, C. Chen, P. Guo, M. Shi, J. Qi, and J. Ge, "A FVCOM-based unstructured grid wave, current, sediment transport model, i. model description and validation," *Journal of Ocean University of China*, vol. 10, no. 1, pp. 1–8, Mar 2011.

[183] J. Dietrich, M. Zijlema, J. Westerink, L. Holthuijsen, C. Dawson, R. Luettich, R. Jensen, J. Smith, G. Stelling, and G. Stone, "Modeling hurricane waves and storm surge using integrally-coupled, scalable computations," *Coastal Engineering*, vol. 58, no. 1, pp. 45 – 65, 2011.

[184] A. F. Garcez Faria, E. B. Thornton, T. P. Stanton, C. V. Soares, and T. C. Lippmann, "Vertical profiles of longshore currents and related bed shear stress and bottom roughness," *Journal of Geophysical Research: Oceans*, vol. 103, no. C2, pp. 3217–3232, 1998.

[185] H. Michaud, P. Marsaleix, Y. Leredde, C. Estournel, F. Bourrin, F. Lyard, C. Mayet, and F. Ardhuin, "Three-dimensional modelling of wave-induced current from the surf zone to the inner shelf," *Ocean Science*, vol. 8, no. 4, pp. 657–681, 2012.

[186] A. Roland and F. Ardhuin, "On the developments of spectral wave models: numerics and parameterizations for the coastal ocean," *Ocean Dynamics*, vol. 64, no. 6, pp. 833–846, Jun 2014.

[187] E. R. Smith and N. C. Kraus, "Laboratory study of wave breaking over bars and artificial reefs," *Journal of Waterway, Port, Coastal, and Ocean Engineering*, vol. 117, no. 4, pp. 307–325, 1991.

[188] Z. Xie, "Two-phase flow modelling of spilling and plunging breaking waves," *Applied Mathematical Modelling*, vol. 37, no. 6, pp. 3698 – 3713, 2013.

[189] S. Brown, D. Greaves, V. Magar, and D. Conley, "Evaluation of turbulence closure models under spilling and plunging breakers in the surf zone," *Coastal Engineering*, vol. 114, pp. 177 – 193, 2016.

[190] P. Lin and P. L.-F. Liu, "A numerical study of breaking waves in the surf zone," *Journal of Fluid Mechanics*, vol. 359, p. 239–264, 1998.

[191] E. D. Christensen, D.-J. Walstra, and N. Emerat, "Vertical variation of the flow across the surf zone," *Coastal Engineering*, vol. 45, no. 3, pp. 169 – 198, 2002, surface and Swash Zone Mechanics.

[192] S. Shao, "Simulation of breaking wave by SPH method coupled with k-ϵ model," *Journal of Hydraulic Research*, vol. 44, no. 3, pp. 338–349, 2006.

[193] C. E. Long, "Index and bulk parameters for frequency-direction spectra measured at cerc field research facility, June 1994 to August 1995," US Army Corps of Engineers Waterways Experiment Station, Techreport, 1996.

[194] S. Elgar, R. T. Guza, B. Raubenheimer, T. H. C. Herbers, and E. L. Gallagher, "Spectral evolution of shoaling and breaking waves on a barred beach," *Journal of Geophysical Research: Oceans*, vol. 102, no. C7, pp. 15 797–15 805, 1997.

[195] E. L. Gallagher, W. Boyd, S. Elgar, R. Guza, and B. Woodward, "Performance of a sonar altimeter in the nearshore," *Marine Geology*, vol. 133, no. 3, pp. 241 – 248, 1996.

[196] F. Feddersen, R. T. Guza, S. Elgar, and T. H. C. Herbers, "Alongshore momentum balances in the nearshore," *Journal of Geophysical Research: Oceans*, vol. 103, no. C8, pp. 15 667–15 676, 1998.

[197] L. Holthuijsen, A. Herman, and N. Booij, "Phase-decoupled refraction–diffraction for spectral wave models," *Coastal Engineering*, vol. 49, no. 4, pp. 291 – 305, 2003.

[198] M. Li, P. T. Fernando, S. Pan, B. A. O'Connor, and D. Chen, "Development of a quasi-3d numerical model for sediment transport prediction in the coastal region," *Journal of Hydro-environment Research*, vol. 1, no. 2, pp. 143 – 156, 2007.

[199] K. Rakha, "A Quasi-3D phase-resolving hydrodynamic and sediment transport model," *Coastal Engineering*, vol. 34, no. 3, pp. 277 – 311, 1998.

[200] E. Christensen, "Large eddy simulation of spilling and plunging breakers," *Coastal Engineering*, vol. 53, no. 5-6, pp. 463 – 485, 2006.

[201] R. Bakhtyar, A. Yeganeh-Bakhtiary, D. A. Barry, and A. Ghaheri, "Two-phase hydrodynamic and sediment transport modelling of wave-generated sheet flow," *Advances in Water Resources*, vol. 32, no. 8, p. 1267 – 1283, 2009.

[202] N. Jacobsen and J. Fredsøe, "Formation and development of a breaker bar under regular waves. Part 2: Sediment transport and morphology," *Coastal Engineering*, vol. 88, p. 55 – 68, 2014.

[203] Z. Zhou, T.-J. Hsu, D. Cox, and X. Liu, "Large-eddy simulation of wave-breaking induced turbulent coherent structures and suspended sediment transport on a barred beach," *Journal of Geophysical Research*, vol. 112, p. 207–235, 2017.

[204] L. C. van Rijn, *Principles of sediment transport in rivers, estuaries and coastal seas*. Aqua publications Amsterdam, 1993, vol. 1006.

[205] A. Fernandez-Mora, J. Ribberink, J. van der Zanden, J. van der Werf, and N. Jacobsen, "Rans-vof modeling of hydrodynamics and sand transport under full-scale non-breaking and breaking waves," *Coastal Engineering Proceedings*, vol. 1, no. 35, p. 29, 2017.

[206] P. J. Cowell, M. J. F. Stive, A. W. Niedoroda, D. J. P. Swift, H. J. de Vriend, M. C. Buijsman, R. J. Nicholls, P. S. Roy, G. M. Kaminsky, J. Cleveringa, C. W. Reed, and P. L. de Boer, "The coastal-tract (part 2): Applications of aggregated modeling of lower-order coastal change," *Journal of Coastal Research*, vol. 19, no. 4, pp. 828–848, 2003.

[207] L. van Rijn, D. Walstra, B. Grasmeijer, J. Sutherland, S. Pan, and J. Sierra, "The predictability of cross-shore bed evolution of sandy beaches at the time scale of storms and seasons using process-based profile models," *Coastal Engineering*, vol. 47, no. 3, pp. 295 – 327, 2003.

[208] N. L. Jones and S. G. Monismith, "The influence of whitecapping waves on the vertical structure of turbulence in a shallow estuarine embayment," *Journal of Physical Oceanography*, vol. 38, no. 7, pp. 1563–1580, 2008.

[209] L. H. Kantha and C. A. Clayson, "On the effect of surface gravity waves on mixing in the oceanic mixed layer," *Ocean Modelling*, vol. 6, no. 2, pp. 101 – 124, 2004.

[210] H. Tennekes, *Two- and three-dimensional turbulence: Predictability and other problems.* World Scientific, Singapore, 1989, pp. 20–35.

[211] S. Zeierman and M. Wolfshtein, "Turbulent time scale for turbulent-flow calculations," *AIAA*, vol. 24, no. 10, pp. 1606–1610, 1986.

[212] D. C. Wilcox, "Reassessment of the scale-determining equation for advanced turbulence models," *AIAA*, vol. 26, no. 11, pp. 1299–1310, 1988.

[213] M. A. Donelan, J. Hamilton, and W. H. Hui, "Directional spectra of wind-generated waves," *Philosophical Transactions of the Royal Society of London. Series A, Mathematical and Physical Sciences*, vol. 315, no. 1534, pp. 509–562, 1985.

[214] P. K. Smolarkiewicz, "A fully multidimensional positive definite advection transport algorithm with small implicit diffusion," *Journal of Computational Physics*, vol. 54, no. 2, pp. 325–362, 1984.